

AD-784 191

DEVELOPMENT AND EXPERIMENTAL VERIFICATION OF PROCEDURES TO DETERMINE NONLINEAR LOAD-DEFLECTION CHARACTERISTICS OF HELICOPTER SUBSTRUCTURES SUBJECTED TO CRASH FORCES. VOLUME I. DEVELOPMENT OF SIMPLIFIED ANALYTICAL TECHNIQUES TO PREDICT TYPICAL HELICOPTER AIRFRAME CRUSHING CHARACTERISTICS AND THE FORMULATION OF DESIGN PROCEDURES

G. Wittlin, et al

Lockheed-California Company

Prepared for:

Army Air Mobility Research and
Development Laboratory

May 1974

DISTRIBUTED BY:

NTIS

National Technical Information Service
U. S. DEPARTMENT OF COMMERCE
5285 Port Royal Road, Springfield Va. 22151

Unclassified

SECURITY CLASSIFICATION OF THIS PAGE (When Data Entered)

REPORT DOCUMENTATION PAGE		READ INSTRUCTIONS BEFORE COMPLETING FORM
1. REPORT NUMBER USAAMRD-TR-74-12A	2. GOVT ACCESSION NO.	3. RECIPIENT'S CATALOG NUMBER AD 784 191
4. TITLE (and Subtitle) DEVELOPMENT AND EXPERIMENTAL VERIFICATION OF PROCEDURES TO DETERMINE NONLINEAR LOAD-DEFLECTION CHARACTERISTICS OF HELICOPTER SUBSTRUCTURES SUBJECTED TO CRASH FORCES - VOLUME I		5. TYPE OF REPORT & PERIOD COVERED Final report
		6. PERFORMING ORG. REPORT NUMBER
7. AUTHOR(s) G. Wittlin K. C. Park		8. CONTRACT OR GRANT NUMBER(s) Contract DAAJ02-73-C-0051
9. PERFORMING ORGANIZATION NAME AND ADDRESS Lockheed-California Company Burbank, California 91503		10. PROGRAM ELEMENT, PROJECT, TASK AREA & WORK UNIT NUMBERS Task 1F162205AH88
11. CONTROLLING OFFICE NAME AND ADDRESS Eustis Directorate U. S. Army Air Mobility R&D Laboratory Fort Eustis, Virginia 23604		12. REPORT DATE May 1974
		13. NUMBER OF PAGES 252
14. MONITORING AGENCY NAME & ADDRESS (if different from Controlling Office)		14. SECURITY CLASS. (of this report) Unclassified
		15a. DECLASSIFICATION/DOWNGRADING SCHEDULE
16. DISTRIBUTION STATEMENT (of this Report) Approved for public release; distribution unlimited.		
17. DISTRIBUTION STATEMENT (of the abstract entered in Block 20, if different from Report)		
18. SUPPLEMENTARY NOTES Volume I of a two-volume report		
19. KEY WORDS (Continue on reverse side if necessary and identify by block number) Aircraft Tolerances (physiology) Crash resistance Helicopters Dynamics Energy absorbers Structural properties Mathematical models		
20. ABSTRACT (Continue on reverse side if necessary and identify by block number) The results of a study to develop simplified design procedures for determining nonlinear load-deflection characteristics for helicopter airframe structures are presented. A literature survey is performed in which 60 technical reports and papers are evaluated with regard to their applicability to crashworthiness analysis and designer-oriented procedures.		

DD FORM 1473 EDITION OF 1 NOV 65 IS OBSOLETE

1 JAN 73
Reproduced by
NATIONAL TECHNICAL
INFORMATION SERVICE
U. S. Department of Commerce
Springfield, VA

Unclassified

SECURITY CLASSIFICATION OF THIS PAGE (When Data Entered)

4. Continued.

DEVELOPMENT OF SIMPLIFIED ANALYTICAL TECHNIQUES TO PREDICT TYPICAL HELICOPTER AIRFRAME CRUSHING CHARACTERISTICS AND THE FORMULATION OF DESIGN PROCEDURES

20. Continued.

Studies using an existing 31 lumped mass model of the UH-1H helicopter are performed to determine the sensitivity of responses to changes in the load-deflection representation for the engine and transmission mounts, landing gear and fuselage. Simplified techniques are used to predict the load-deflection curve for the crushing of a segment of the lower fuselage under impact conditions. The predictions include elastic behavior, failure load and post-failure behavior. The structural segment selected for analysis and test is a section supported on four edges, representative of the transmission pylon support.

Twelve specimens were fabricated and tested. The specimens are 46 inches long by 18 inches wide by 6.125 inches or 12.125 inches deep. The 6.125-inch-deep specimens are approximately half size (except for thickness) and are varied in detail design (number of angles, spacing of angles, lightening holes). Static and dynamic tests were performed. The predicted load-deflection curves are compared to the test load-deflection curves and show good agreement with regard to peak failure load, failure point, energy absorbed, and shape. The results of the tests show that for this type of fuselage structure, static tests provide load-deflection data which is similar to data that can be obtained from dynamic tests, but more economically.

Program KRASH is refined to facilitate its use by designers. In particular, the input data is reordered, some inputs are standardized and more general load-deflection curve characteristics are possible. The capacity of the program is increased to 80 lumped masses, 100 internal beams and 120 load-deflection tables. The refined program was run to demonstrate capability to treat a three-dimensional impact velocity, mass penetration into an occupiable space, and simplified rotor blade contact. Specimen test data is also used to refine the 31 mass UH-1H model.

The analytical techniques developed herein are presented in the form of design charts, nomographs, curves, tables and equations and form the basis of a structural crashworthiness design manual. The design procedures are outlined in a step-by-step process including examples. Included in the design procedures are design modeling guidelines for such typical structural elements as columns, beams, honeycomb panels and frangible tubes.

Volume II contains supporting analytical and test data and a literature matrix categorization. A description of refined program KRASH is provided which shows the new input-output format, listing, and sample problems.

EUSTIS DIRECTORATE POSITION STATEMENT

The Eustis Directorate technical monitor for this effort was Mr. G. T. Singley III of the Military Operations Technology Division.

The conclusions submitted by the contractor are considered to be valid.

The report is divided into two volumes. Volume I contains a description of the survey of technical publications, investigation of the sensitivity of the simulated structural response to load-deflection variations, sub-structure test program, refinement of KRASH, structural crashworthiness design procedures, and results obtained. Volume II contains abstracts of literature reviewed, supporting analytical and test data, a description of the refined KRASH computer program, and a user's guide for the computer program.

ACCESSION for	
NTIS	Write Section <input checked="" type="checkbox"/>
DIC	Print Section <input type="checkbox"/>
SEARCHED	<input type="checkbox"/>
INDEXED	<input type="checkbox"/>
BY	
DISTRIBUTION/AVAILABILITY CODES	
Dist.	AVAIL. and/or SPECIAL
A	

DISCLAIMERS

The findings in this report are not to be construed as an official Department of the Army position unless so designated by other authorized documents.

When Government drawings, specifications, or other data are used for any purpose other than in connection with a definitely related Government procurement operation, the United States Government thereby incurs no responsibility nor any obligation whatsoever; and the fact that the Government may have formulated, furnished, or in any way supplied the said drawings, specifications, or other data is not to be regarded by implication or otherwise as in any manner licensing the holder or any other person or corporation, or conveying any rights or permission, to manufacture, use, or sell any patented invention that may in any way be related thereto.

Trade names cited in this report do not constitute an official endorsement or approval of the use of such commercial hardware or software.

DISPOSITION INSTRUCTIONS

Destroy this report when no longer needed. Do not return it to the originator.

PREFACE

This report was prepared by the Lockheed-California Company under U.S. Army Contract DAAJ02-73-C-0051 (Project LF262205AH88). The work was administered under the direction of the Eustis Directorate, U.S. Army Air Mobility Research and Development Laboratory, Fort Eustis, Virginia, with G.T. Singley, III, acting as Project Engineer.

The Lockheed-California Company Program Manager was G. Wittlin. K.G. Park developed the analytical procedures. The design procedures were developed by both G. Wittlin and K.C. Park. Supporting effort was provided by R. Matlock (test) and M.A. Gamon (program KRASH refinements).

TABLE OF CONTENTS

	<u>Page</u>
PREFACE	iii
LIST OF ILLUSTRATIONS	viii
LIST OF TABLES	xv
INTRODUCTION	1
Background	1
Program Objectives	5
Report Format	6
SURVEY OF TECHNICAL PUBLICATIONS	7
General Discussion	7
Evaluation	7
Simplified Analytical Techniques	7
Experimental Data	8
Design Procedures and Guidelines	13
Load-Deflection Data	13
Energy Absorption	16
Methods of Analysis	19
Strain Rate Effects	19
Inertia Effects	20
LOAD-SENSITIVITY STUDY	21
General	21
Load-Deflection Variations	21
Engine	21
Transmission	27
Landing Gear	27
Fuselage	31
Results	31
Engine	31
Transmission	37
Landing Gear	37
Fuselage	37

	<u>Page</u>
SUBSTRUCTURE ANALYSIS	42
Objective	42
Methods of Analysis	42
Procedure	49
Prediction of Failure Loads for Stiffened Panels	49
Post-Failure Analysis of Stiffened Panels	55
Calculation of Plastic Hinge Moment (M_p)	58
Main Beam and Bottom Skin Analysis	60
Total Load Deflection	62
Column Effect on the Failure Strength of Stiffened Panels	63
General Application of the Procedure	67
Predicted Subelement and Total Load-Deflection Curves	67
SUBSTRUCTURE TEST PROGRAM	76
Test Program Objectives	76
General	76
Test Specimens	77
Installation	80
Instrumentation	88
Test Sequence	88
Photography	91
Results	91
CORRELATION	111
General	111
Comparison of Test and Analysis Load-Deflection Curves	111
Comparison of Test and Analysis Energy Absorption	118
Remarks on the Initial Analytical Assumptions	122
Plastic Hinge Formation	122
Empirical Corrections to the Post-Failure Load-Deflection Curve	125
Failure Deflection	127
Determination of the Deflection Value at Failure	127
Strain Data and Failure Modes	132
PROGRAM "KRASH" REFINEMENT	137
General	137
Program "KRASH" Input Format Revisions	138
Three-Dimensional Impact and Mass Penetration	139
Case Description	139
Results	139
Rotor Blade Contact	141
Case Description	141
Results	141

	<u>Page</u>
Test Data Load-Deflection Curve	141
Case Description	141
Results	143
DESIGN PROCEDURES	145
Specification of Crashworthiness Capability	145
General Approach	146
Detail Approach	150
Detail Design Procedure and Illustrative Sample Calculations	150
Structural Element Modeling Guidelines	185
RESULTS OF THE PROGRAM	203
Literature Survey and Critique	203
Load-Sensitivity Study	203
Substructure Analysis	204
Substructure Test Program	206
Correlation Between Test and Analysis	210
Program "KRASH" Refinement	211
Design Procedures	213
CONCLUSIONS	215
REFERENCES	216
LIST OF SYMBOLS	225

LIST OF ILLUSTRATIONS

<u>Figure</u>		<u>Page</u>
1	Load-Deflection and Energy-Absorbed Results for Static and Dynamic Fuselage Bumper Tests (Reference 1)	4
2	Plate Stringer Compression Panels Load-Deflection Test Data (Reference 4).	9
3	The Effects of Impact Speed on Dynamic Force-Deflection Relationship of Curved Box-Beam Columns (Reference 38) . .	11
4	Structural Behavior Typical of Solid Cross-Section Beams of Ductile Material (Reference 39)	12
5	Structural Behavior Typical of Built-Up Beams (Reference 39)	12
6	General Arrangement of the UH-1H Helicopter	22
7	31 Lumped Mass Helicopter Model Representation (Reference 1)	23
8	Engine Axial and Bending Load-Stroke Curves	26
9	Left Side, Looking Inboard, View of Engine Mount	27
10	Transmission Axial and Bending Load-Stroke Curves	29
11	Landing-Gear Bending and Rotational Load-Stroke Curves . .	30
12	Fuselage External Crushing Load-Deflection Curves	32
13	Fuselage External Crushing Load-Deflection Curves	32
14	Engine-Mount Axial Load and Energy Absorbed Versus Deflection Curves	34
15	Engine-Mount Bending Load and Energy Absorbed Versus Deflection Curves	35
16	Transmission-Mount Axial Load and Energy Absorbed Versus Deflection Curves	38
17	Landing Gear Load and Energy Absorbed Versus Deflection Curves	40
18	Model Specimen of Lower Fuselage Substructure	43
19	Drawing For Specimens 1 and 2.	45

<u>Figure</u>		<u>Page</u>
20	UH-1H Lower Fuselage Bulkhead and Stiffener Arrangement	47
21	Various Failure Modes of Short Riveted Panels (Reference 12)	50
22	Effect of Rivet Tensile Strength, Pitch, and Diameter Upon Compressive Strength of Short, Riveted, Aluminum-Alloy Z-Panels, 2117-T4 Rivets (Reference 12) . .	52
23	Effect of Rivet Tensile Strength, Pitch, and Diameter Upon Compressive Strength of Short, Riveted, Aluminum-Alloy Z-Panel, Various Rivet Materials (Reference 12) . .	53
24	Method of Determining Number of Flanges	54
25	Method of Determining Effective Width	56
26	Plastic Hinge Mechanisms and Effective Cross Section To Determine Plastic Moment	57
27	Approximate Yield Function for Combined Bending and Axial Force (Reference 101).	59
28	Lumped Model of Bottom Skin and Main Beams	61
29	Critical Stress Versus L'/ρ Ratio	64
30	Failure Stress Versus Slenderness Ratio of Stiffened Panels	65
32	Chart for Determining $(\rho/\rho_w)^2$	66
33	Stiffeners With Various Corners	68
34	Various Stiffener Configurations	69
35	Bulkhead Load-Deflection Curve for Specimens 1 through 6	72
36	Side Skin Load-Deflection Curves for Specimen 1.	72
37	Side Skin Load-Deflection Curve for Specimens 2, 3 and 4 .	73
38	Side Skin Load-Deflection Curve for Specimens 5 and 6 . .	73
39	Main Beam and Bottom Skin Load-Deflection Curve for Specimens 1 and 6	74

<u>Figure</u>		<u>Page</u>
40	Predicted Total Load-Deflection Curve for Specimen 1 . . .	74
41	Predicted Total Load-Deflection Curve for Specimens 5 and 6	75
42	Predicted Total Load-Deflection Curve for Specimens 2, 3 and 4	75
43	Typical 6.125-Inch-Deep Test Specimen (Specimens 1-9)	78
44	Typical 12.125-Inch-Deep Test Specimen (Specimens 10-12)	78
45	UH-1H Lower Fuselage Bulkhead and Stiffener Arrangement	81
46	Drawing for Specimens 1 and 2 (All Dimensions in Inches)	83
47	Baldwin Universal Static Testing Machine	85
48	Static Test Setup	85
49	Frame Structure Test Tower for Dynamic Tests	86
50	Dynamic Test Setup With Load Cells for Specimens 7 and 8	87
51	Strain Gage Locations (All Dimensions in Inches)	89
52	Load Versus Deflection, Test 1	93
53	Load Versus Deflection, Test 2	93
54	Load Versus Deflection, Test 3	94
55	Load Versus Deflection, Test 4	94
56	Load Versus Deflection, Test 5	95
57	Load Versus Deflection, Test 6	95
58	Load Versus Deflection, Test 7	96
59	Load Versus Deflection, Test 8	96
60	Load Versus Deflection, Test 9	97

<u>Figure</u>		<u>Page</u>
61	Load Versus Deflection, Test 10	97
62	Load Versus Deflection, Test 11	98
63	Load Versus Deflection, Test 12	98
64	Setup for Specimen 12	99
65	Post-Test Condition of Specimen 1	100
66	Post-Test Condition of Specimen 2	100
67	Post-Test Condition of Specimen 3	101
68	Post-Test Condition of Specimen 4	101
69	Post-Test Condition of Specimen 5	102
70	Post-Test Condition of Specimen 6	102
71	Comparison of Post-Test Damage for Specimens 5 and 6 (End View)	103
72	Comparison for Post-Test Damage for Specimens 5 and 6 (Top View)	103
73	Post-Test Condition of Specimen 7	104
74	Post-Test Condition of Specimen 8	104
75	Post-Test Condition of Specimen 9	105
76	Comparison of Post-Test Damage to Specimens 7, 8 and 9 (Top View)	105
77	Comparison of Post-Test Damage for Specimens 7, 8 and 9 (Side View)	107
78	Post-Test Condition of Specimen 10	107
79	Post-Test Condition of Specimen 11	108
80	Post-Test Condition of Specimen 12	108
81	Comparison of Post-Test Damage for Specimens 10 and 11 (Top View)	109

<u>Figure</u>		<u>Page</u>
82	Comparison of Post-Test Damage for Specimens 10 and 12 (Side View)	109
83	Predicted Versus Test Load-Deflection Curves for Specimen 1	113
84	Predicted Versus Test Load-Deflection Curves for Specimen 2	113
85	Predicted Versus Test Load-Deflection Curves for Specimen 3	116
86	Predicted Versus Test Load-Deflection Curves for Specimen 4	116
87	Predicted Versus Test Load-Deflection Curves for Specimen 5	117
88	Predicted Versus Test Load-Deflection Curve for Specimen 6	117
89	Predicted Versus Test Load-Deflection Curves for Specimen 7	119
90	Predicted Versus Test Load-Deflection Curves for Specimen 8	119
91	Predicted Versus Test Load-Deflection Curves for Specimen 9	120
92	Predicted Versus Test Load-Deflection Curves for Specimen 10	120
93	Predicted Versus Test Load-Deflection Curve for Specimen 11	121
94	Predicted Versus Test Load-Deflection Curves for Specimen 12	121
95	Sensitivity Factor for Asymmetric Hinge Formation Versus Deflection as a Function of Column Length	124
96	Post-Failure Load - Deflection Curves	125
97	Comparison of Analysis with Experimental Data from Reference 4	128

<u>Figure</u>		<u>Page</u>
98	Variation of Stiffness with Load (Reference 107)	129
99	Load Versus Strain for Specimen No. 1	133
100	Observed Deformation Modes of Stiffened Panels	135
101	Three-Dimensional Impact and Mass Penetration Model	140
102	Rotor Blade Contact Model	142
103	Test Specimen Data Load-Deflection Curve	143
104	Simplified Load-Deflection Categories	149
105	Structure Used in Example	151
106	Assumed Deformation Mode	152
107	Determination of K_1	156
108	Compressive-Buckling Coefficient for Flat Rectangular Plates (Reference 12)	157
109	Determination of K_w	174
110	Nomograph To Determine Beam Bending Loads	175
111	Nomograph To Determine Beam Deflections	176
112	Load-Deflection Curve Obtained by Asymptotic Matching	180
113	Load-Deflection Curve for Bulkhead, Sample Problem	181
114	Load-Deflection Curve for the Side Stiffener Web, Sample Problem	182
115	Load-Deflection Curve for the Main Beam and Bottom Skin, Sample Problem	183
116	Composite Load-Deflection Curve, Sample Problem	184
117	Stress Ratio versus Lateral Deflection Curve for Axially Loaded Column	189
118	Load versus Deflection Curve for Axially Loaded Column	190

<u>Figure</u>		<u>Page</u>
119	Critical Load Factor for Thin Walled Column with Cross-Section of Unequal Angles	193
120	Load-Deformation Characteristics for Compressively Loaded Honeycomb Panel (Reference 113)	194
121	Variation of Stress With Angle of Applied Load (Reference 112)	197
122	Thickness versus Energy Absorbing Capacity for Nonstandard Aluminum Honeycombs (Reference 112)	198
123	Cross-Section of Frangible Tube Energy Absorber (Reference 34)	200
124	Frangible Tube Energy Curve (Reference 34)	201
125	Comparison of Static and Dynamic Test Results	208
126	Percentage of Structural Springback Versus Impact Velocity	209
127	Comparison of Test and Analysis Results	212

LIST OF TABLES

<u>Table</u>		<u>Page</u>
I	UH-1H Structural Element Types and Locations	3
II	Load-Deflection Data	14
III	Matrix of Structural Element Load-Deflection Categories and Load Type	15
IV	Comparison of "One-Shot" Load-Limiting Devices For 1000-To-4000-Pound Loads (Reference 2, Table 3-1)	17
V	Comparative Summary of Absorption Energies (Reference 33)	18
VI	Correlation Study Analytical Model Grid Point Identification (Reference 1)	24
VII	Engine-Mount Axial and Bending KR Changes	25
VIII	Transmission-Mount Axial and Bending KR Changes	28
IX	Landing-Gear Bending and Rotational KR Changes	28
X	Fuselage External Crushing Load-Stroke Characteristics	33
XI	Engine Mount Axial Load Sensitivity Study Results	36
XII	Engine Mount Bending Load Sensitivity Study Results	36
XIII	Transmission-Mount Axial Load Sensitivity Study Results	39
XIV	Landing Gear Load Sensitivity Study Results	39
XV	Fuselage Load Sensitivity Study Results	41
XVI	Values of n , m , g , β_g as Function of Stiffened Panel Configuration (Reference 12)	70
XVII	Specimen Design Configuration, Dimensions and Types of Tests Performed*	79
XVIII	Strain Gage Locations	90
XIX	Test Results	92
XX	Summary of Comparison Between Test Results and Predicted Values	112

<u>Table</u>		<u>Page</u>
XXI	Comparison of Test and Analytically Obtained Failure Deflections	130
XXII	Summary of Test Specimen Stiffener Response	136
XXIII	Comparison of Results Using Test Specimen Data With Previous Correlation Analysis and Test Results	144
XXIV	Core Radius	191
XXV	Reduced Column Length as a Function of End Fixity	191
XXVI	Typical Values of K_T and F_C (Reference 34)	199

INTRODUCTION

BACKGROUND

To date, research into the determination of load-deflection characteristics for structural elements has been concentrated on the elastic region. Literally thousands of tests have been run on as many specimens which have varied in material, size, shape, loading, and end fixity. Semiempirical procedures for determining yield inputs, elastic curve and types of failure have been generated for all kinds of conceivable structures. By comparison, there is a sparsity of data available for structural behavior beyond the elastic regime. This, of course, is not to say that no useful information has been developed. A development program could be undertaken to obtain the same type of data to support analysis for nonlinear behavior as has already been accomplished on linear behavior of structural elements. However, before such a program is undertaken, the following factors should be considered:

- The cost in manpower, material and time would be very great.
- The data can be obtained by performance of proof of crash-worthy design tests as a modest addition to the standard laboratory structural tests that are conducted to qualify an airframe.

Reference (1) provides a program by which an iterative process is used to incorporate improved crashworthy characteristics into helicopters during the early design phase. Since large deformations are involved (beyond the elastic range) in determining the energy absorbed by the structure during a crash, the nonlinear response of the various significant structural parts comprising the airframe is needed. In addition, because of the large number of different structures used in airframe construction, the designer needs the data in some orderly form that categorizes the response characteristics.

The Crash Survival Design Guide (Reference 2) provides valuable information which, if applied properly, will enhance occupant survivability in a severe yet potentially survivable crash. The design guide, as currently constituted, presents in detail aircraft crash kinematics, survivable impact envelopes, airframe crashworthiness principles, seat design, restraint system design, occupant environment design, and additional applicable data. However, the design guide does not describe the following significant items:

- procedures by which crashworthiness capability can be evaluated
- design criteria as a function of the aircraft design configuration and operational usage

- load deflection determination procedures in the nonlinear regime for various types of structural elements used in airframe design

In the last decade, there have been significant efforts to develop crashworthy seats (pilot, troop and gunner). The capabilities of these seats can be greatly enhanced if the structure below the seat, namely, the landing gear and airframe, can be designed to absorb additional energy. Another pertinent factor that must be considered in crashworthy design, whether it be the airframe, seats or major mass items, is that aircraft differ in design configurations, in usage and, consequently, in impact environment and dynamic response characteristics.

Until recently it has been difficult to assess aircraft crashworthiness capability. However, the development of digital computer programs (references 1 and 82) has served to provide basic analytical tools. Program KRASH (reference 1), in particular, has proved to be capable of predicting structural and occupant response during combined velocity (vertical-lateral and longitudinal) impact. Program KRASH provides a foundation from which the practical application of a consistent crashworthiness approach can evolve. The recent study described in reference 1 established that an analytical method is available which is a useful tool for the designer, if guidelines for the determination of nonlinear load-deflection characteristics of structural elements used in aircraft design are provided. The development of simplified methods to obtain this type of data will result in the establishment of procedures which can readily be applied to various airframes to evaluate their crashworthiness capability. Furthermore, designers of aircraft will have the means to improve airframe crashworthiness in an orderly manner to a desired level, with a minimum incremental weight and cost increase. Since the development of procedures applicable to crash analysis is primarily intended for designers, with special emphasis on the preliminary design, special consideration is given to simplified expressions which have general application as opposed to rigorous approaches which are oriented toward unique design or loading conditions.

There are many different types of structural elements used in the various sections of a helicopter. The structure is designed to take loads acting in different directions; consequently, different modes of failure occur such as buckling, tension, compression, bearing and shear. Table I gives a sampling of the types of structural elements and their locations in a UH-1H helicopter. Some useful load-deflection information, both linear and nonlinear, has been developed over a period of time for many of the different types of structural elements used in a helicopter. In particular, much experimental and analytical effort has been expended to determine elastic responses of columns, struts, stringers, longerons, honeycomb panels and beams to dynamic and static loads.

While research has been oriented predominately in the linear regime, the results provide valuable information (i.e., the yield points, the elastic curve and buckling behavior) for establishing the characteristics of certain structures when the nonlinear region is encountered.

1. Honeycomb panel	Main beams, bulkheads, skin, fuel cell, door, etc.
2. Torque box (beams)	Fuselage mid section
3. Simply supported beam	Lift link (transmission)
4. Cantilevered beam	Fwd. of f.s. 155, aft of f.s. 211
5. Tension rod	Fuselage (f.s. 211 to 243)
6. Flanged webs	Bulkheads, main beam
7. Frames	Cabin, tail boom
8. Stanchions, columns	Cabin
9. Strut, bipod, tripod	Engine mount
10. Bulkheads	Fuselage, tail boom
11. Stringers	Tail boom
12. Longerons	Tail boom
13. Rib spar	Vertical fin
14. Torsion tube	Horiz. stabilizer, engine-transmission
15. Panel (flat, curved)	Fuselage
16. Skin stiffeners	Fuselage, tail boom
17. Tubular (curved, flat)	Landing gear, troop seats
18. Rubber mounts	Transmission
19. Beam stiffeners	Main beam

An important consideration in defining the energy absorption characteristics of structural elements in the nonlinear region is to establish the significance of rate of loading. To this end, the energy absorption characteristics of a typical aircraft substructure (P2V-4 fuselage bumper) were obtained under static and dynamic loading conditions (Reference 1). The results of these tests are compared in Figure 1. The dynamic test results show good agreement in the deformation of the shell structure when compared to the static test data. The results obtained from the tests of the fuselage bumper are significant in that the dynamic test of the bumper indicates that for some typical aircraft structure, a simple static test will suffice.

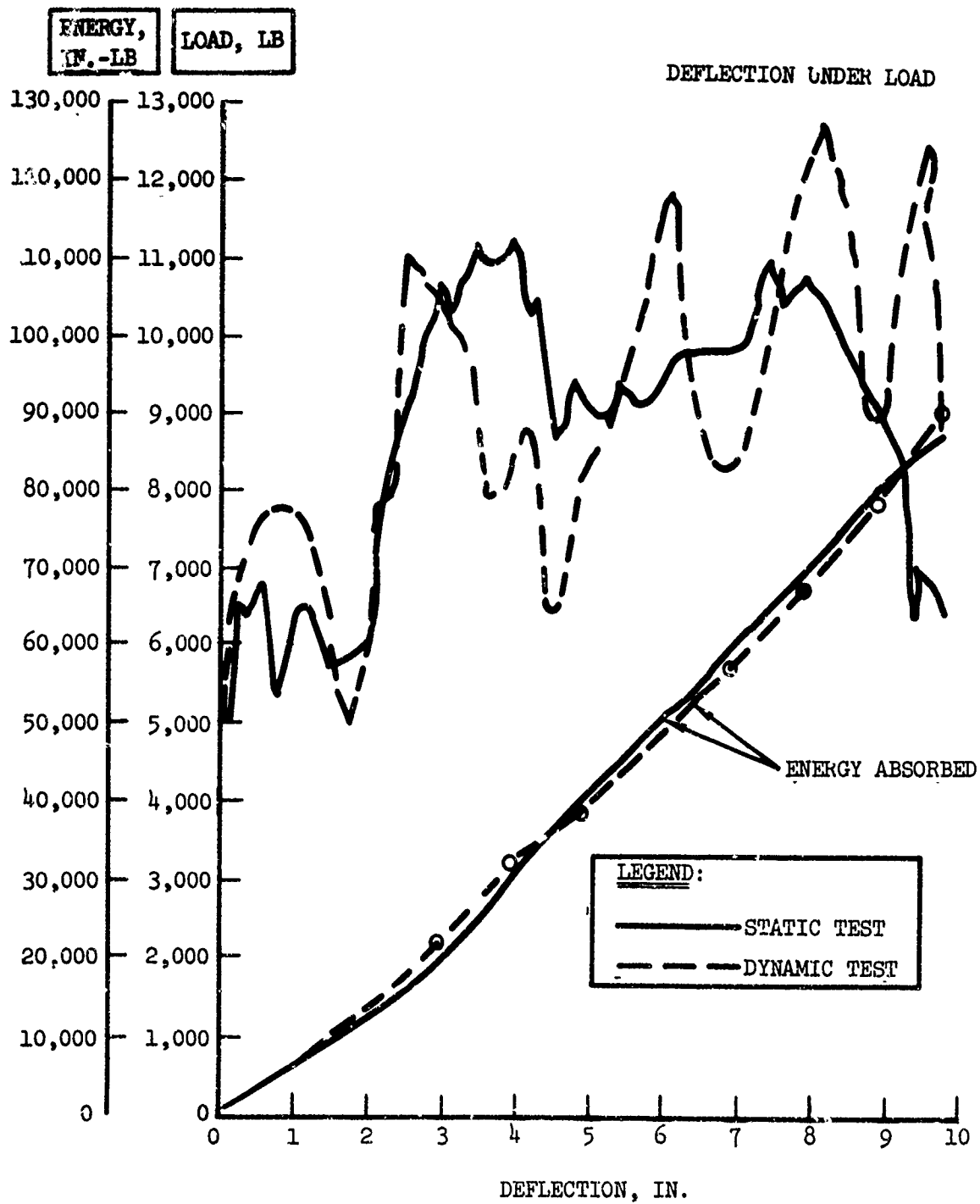


Figure 1. Load-Deflection and Energy-Absorbed Results for Static and Dynamic Fuselage Bumper Tests (Reference 1).

Some structures, on the other hand, will behave differently under dynamic loading conditions than under a static load environment. However, if static tests can be performed in lieu of dynamic tests to obtain load-deflection characteristics, then significant savings can be realized in future programs. What is needed is an approach which recognizes that existing linear and nonlinear load deformation data can formulate a basis for establishing guidelines which will help designers, during the preliminary design stage of a vehicle's development, to determine the amount of energy absorption necessary to achieve a crashworthy design. The exact load-deflection curve of the element which deforms plastically, although desirable, is not essential to a crashworthiness analysis. More important is the understanding of the gross behavior in the plastic region, i.e., constant load-carrying capacity as compared to instantaneous loss of load-carrying capability.

From an economic point of view, it is more efficient to optimize for the incorporation of crashworthiness features early in the design stage. However, during preliminary design it is doubtful if sufficient design details, which influence the exact plastic deformation shape of structural elements, will be available. The availability of simple procedures to predict energy absorption and load-deformation characteristics will allow the designer to initiate valuable cost, weight and geometry trade-off studies. The development of these procedures will require some testing of typical specimens. This testing should, as a minimum, verify the validity of proposed procedures for providing pertinent nonlinear load-deformation data.

PROGRAM OBJECTIVES

The objectives of the program are as follows:

- To develop simplified analytical techniques by which nonlinear load-deflection characteristics of typical structural elements can be obtained.
- To verify with tests that these simple analytical techniques are valid for crashworthiness analysis.
- To provide designers with simplified techniques with which to perform crashworthiness studies during the preliminary design phase.
- To simplify data input requirements of computer program KRASH.

To achieve the objectives, the results of the study will determine:

- (1) The pertinent structural element load-deflection characteristics that are to be modeled in order to obtain acceptably accurate structural and occupant responses.

- (2) The accuracy with which typical airframe structure load-deflection characteristics can be predicted using simplified analytical procedures.

REPORT FORMAT

The table of contents conveys the general plan of the report. Background information is presented initially to provide a proper perspective in relation to the objectives of the program. Volume I is presented in chronological order of the program milestones and includes:

- Survey of Technical Publications
- Load Sensitivity Studies
- Substructure Analysis
- Substructure Test Program
- Correlation
- Program KRASH Refinement
- Design Procedures

The program results are presented in summary form prior to the conclusions.

Volume II contains supporting data for the details presented in Volume I. Volume II contains abstracts for the 60 technical reports and publications reviewed during the program. Included in the literature survey section is a matrix categorization of the reports by subject and applicable area of interest. The test data is presented in its entirety, including accelerometer, load cell, strain gage deflection, and time (or scan) histories for each of the twelve tests. Supporting data for analysis and design procedures is also presented. Program KRASH refinements which include standardization of input, modified input format, and user's guide are included.

SURVEY OF TECHNICAL PUBLICATIONS

GENERAL DISCUSSION

Technical publications were reviewed and their contents categorized in accordance with the various aspects of developing improved crashworthiness criteria and concepts to assist in future reference as needed. A review and evaluation of 60 publications are presented herein. A complete listing of publications which comprise the literature survey is presented in Volume II. The literature is reviewed with regard to the impact on developing designer-oriented crashworthiness design procedures. In particular, emphasis is placed in the following areas:

- Simplified analytical techniques
- Experimental data
- Design procedures and guidelines
- Load-deflection data
- Energy absorption
- Methods of analysis
- Strain-rate sensitivity
- Inertia effects

EVALUATION

All documents reviewed are evaluated for their applicability to each of the subject areas listed above, the contribution of each is briefly stated, and a composite summary of the pertinent aspects is recorded.

Volume II, which provides additional literature survey information, consists of a summary or abstract for each report and a literature survey subject index which contains a matrix categorization of the contents of the technical reports. The matrix categorization lists the reports by number and associates each report with an area of specific content or applicability. All report numbers in this section refer to the reference numbers as they are listed under Literature Cited.

Simplified Analytical Techniques

The determination of load deformation characteristics of aircraft structure will enhance the ability of the designer to predict structure and occupant responses during severe yet survivable crashes. However, it is important that this data is presented in a manner which will aid the designer in developing the desired level of crashworthiness in the airframe structure. The data presented in the literature provides analytical procedures and/or empirical data which is applicable to a great many types of structural ele-

ments. Unfortunately, much of the data in its present form is not directly applicable for the following reasons:

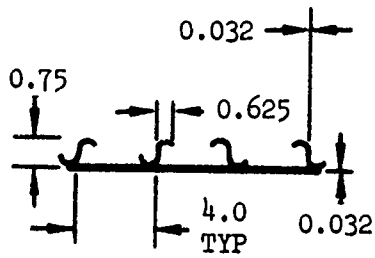
- (1) The analytical techniques require computer programs in order to formulate solutions.
- (2) The empirical data is not related to analytical procedures.
- (3) The data is for structural elements under a unique loading condition or boundary condition.
- (4) The data neglects effects of inertia loads, strain rate, wave propagation and/or geometry changes.

There are several references, most notably 5, 6, 7, 9, 12, 18, 24 and 30, which provide information that can be incorporated into procedures that could serve as guidelines for designers. Several of the aforementioned references are texts (6, 7, 8, 9, 24, 30) which, although primarily limited to elastic and plastic behavior, cover a wide range of structural elements such as beams, columns, plates, rings, arches and composite structure. The data in these references provide basic information regarding yield point loads and methods by which the effects of plasticity, crippling and buckling can be taken into account.

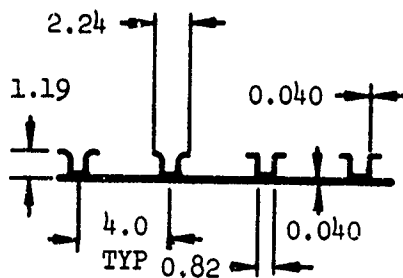
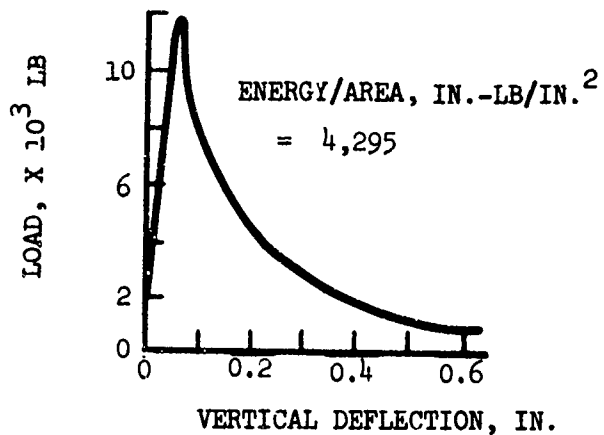
Experimental Data

References 1, 4, 17, 19, 26, 28, 32, 33 and 35 present results of tests. The data is generally in the form of load versus deflection, force versus time and stress versus strain. Reference 1 static and dynamic test results showed that for some typical aircraft structure, the load deflection characteristics are the same for both static and dynamic loading conditions. Figure 1 shows a comparison of the results of the static and dynamic tests described in Reference 1.

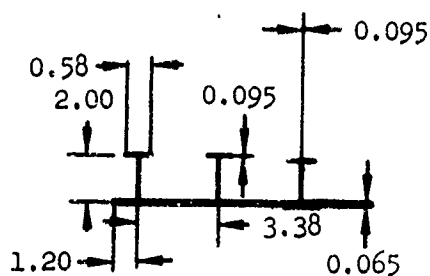
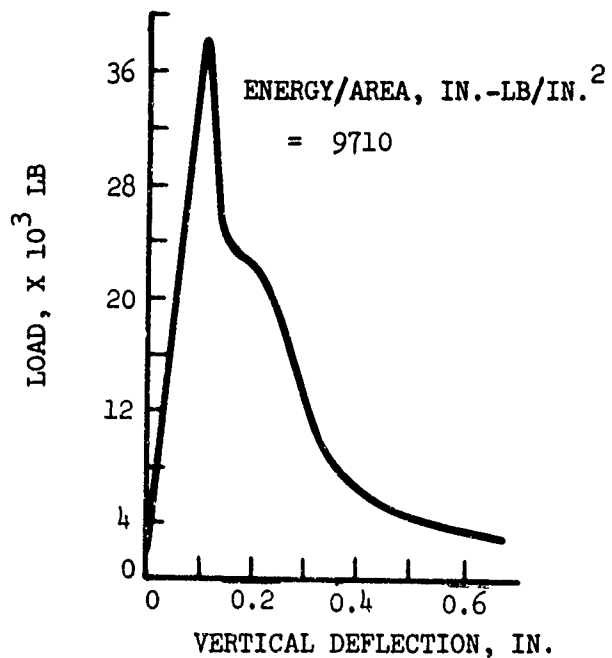
In Reference 4, load deflection curves for plate stringer panel configurations are presented. The results of these panel tests, illustrated in Figure 2, show the energy to area ratio of the three configurations. Of particular importance is the relative absorption capabilities of the panels and their respective modes of failure. For example, the integrally machined panels produce a reasonably efficient energy-area ratio, but the load stroke performance is poor because the mode of failure is an explosive fracture in which the riser splits completely off the skin. In addition, the peak load of this latter configuration is much higher than the peak load for the other panels, which could result in higher transmitted loads. Reference (4) also presents load-deflection data for the lower frame of a typical fuselage segment obtained from drop tests. This test data is compared to analysis and is shown to differ substantially. Reference 10 presents data regarding buckling characteristics of perfect and imperfect circular cylindrical shells subjected to dynamic axial loading.



(a) ROLLED ZEE STRINGER



(b) ROLLED HAT STRINGER



(c) INTEGRALLY STIFFENED RISER

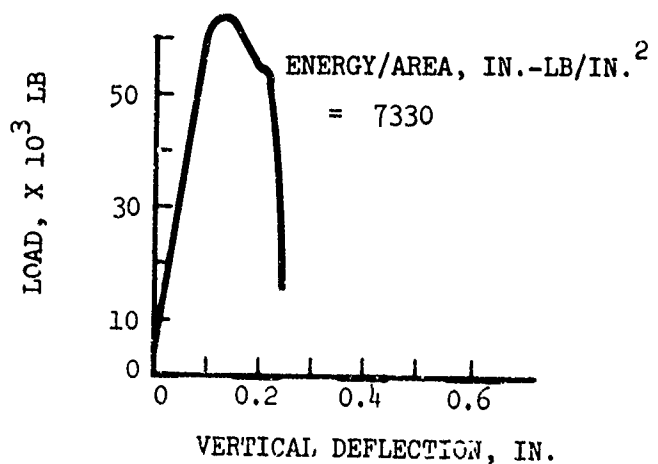


Figure 2. Plate Stringer Compression Panels Load-Deflection Test Data (Reference 4).

Close agreement was found between theory and experiment for both dynamic buckling strength and buckling mode shapes.

Reference 17 presents data for simple structures like a clamped beam, circular ring, circular plate and hemisphere. The data is limited to deflection time histories and is for a specific material, loading condition, boundary condition and size of structure. In Reference 19, a comparison is made of experimental data with the results of a theoretical investigation of the plastic deformation of cantilevered beams subjected to impulsive loading. The test results for this particular study followed the general trend predicted by rigid-plastic theory. A conclusion drawn from the results is that an increase in yield stress with strain rate is the primary cause of the discrepancy between theory and experiment.

Reference 26 presents results of an experimental investigation into the use of frangible metal tubing as an energy absorber. Tests were performed using a 1/5 scale model of a proposed manned spacecraft, and impact velocities reached 30 fps vertical and combined vertical (13.5 fps) and horizontal (18 fps). Results are presented as curves of force versus displacements. References 27, 32, 33, 34 and 35 present data for a one-shot energy absorber. References 32 through 35 provide data accumulated over a period of years for the Lockheed developed Dynasorb. The device has been tested for ground impact conditions as high as 112 fps. Materials tested include aluminum alloy 2024-T3, brass, copper, magnesium AZ-31B-F, steel (1015), steel (4130), and titanium. Energy curves showing load versus displacement are presented.

Reference 29 presents results of experimental investigations of thin webbed plate-girder beams to determine shear loads required to cause web rupture and flange rivet failure. In all, twenty-seven beams were tested. Reference 38 discusses the impact response of curved box-beam columns with large global and local deformations. Of significance are load-deflection curves for steel and aluminum under static and dynamic loading conditions (Figure 3). This paper concludes that the consideration of cross-section changes is necessary and important in predicting the impact response of beam columns with thin-walled box sections subjected to large deformation. The effects of strain rate sensitivity and strain wave propagation on the load-deflection curve are discussed.

Reference 39 presents stress-strain curves for aluminum honeycomb and two foamed plastic structures. The characteristics of these three materials are examined to ascertain how they can be applied for human protection against accelerations encountered at low impact speeds (30 fps). Reference 41 presents data regarding modes of failures of multiweb beams. The ultimate strength and buckling characteristics of multiweb beams have been investigated both experimentally and theoretically. The three primary types of instability that occur are (1) local buckling, (2) wrinkling, and (3) inter-rivet buckling. It is noted that beams of solid cross sections typically exhibit large plastic deformations as shown in Figure 4, while built-up

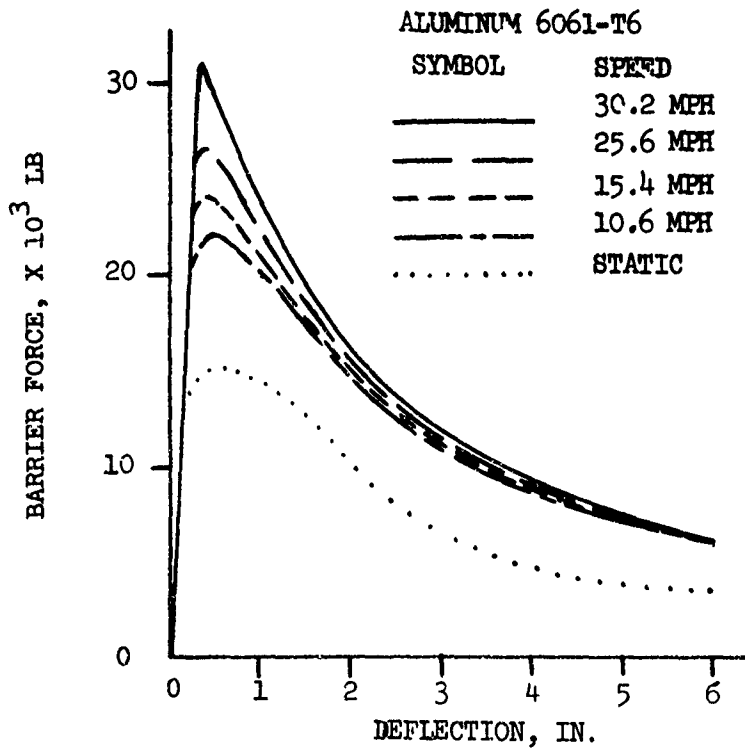
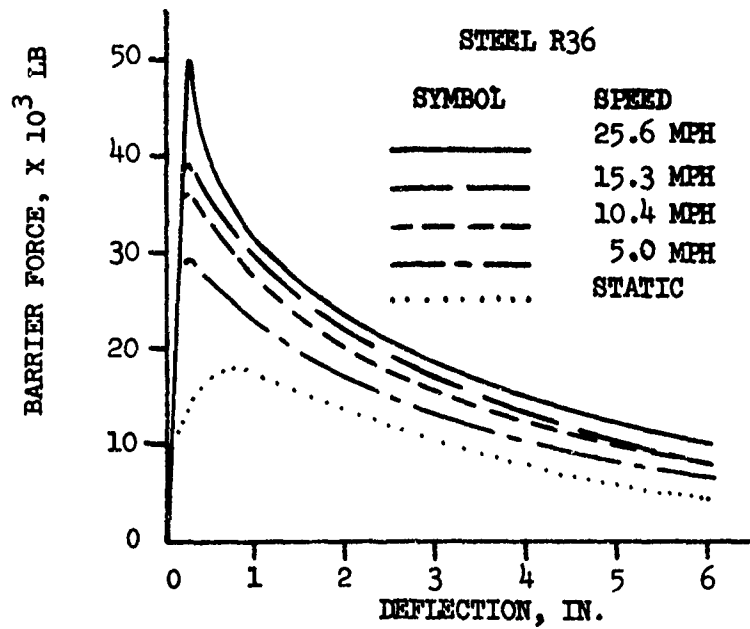


Figure 3. The Effects of Impact Speed on Dynamic Force-Deflection Relationship of Curved Box-Beam Columns (Reference 38).

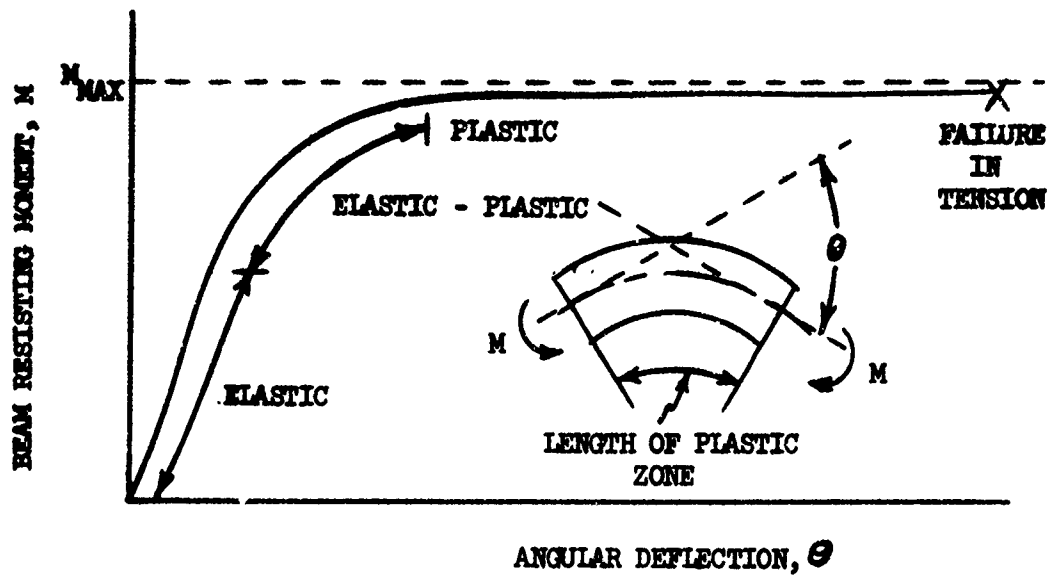


Figure 4. Structural Behavior Typical of Solid Cross-Section Beams of Ductile Material (Reference 39).

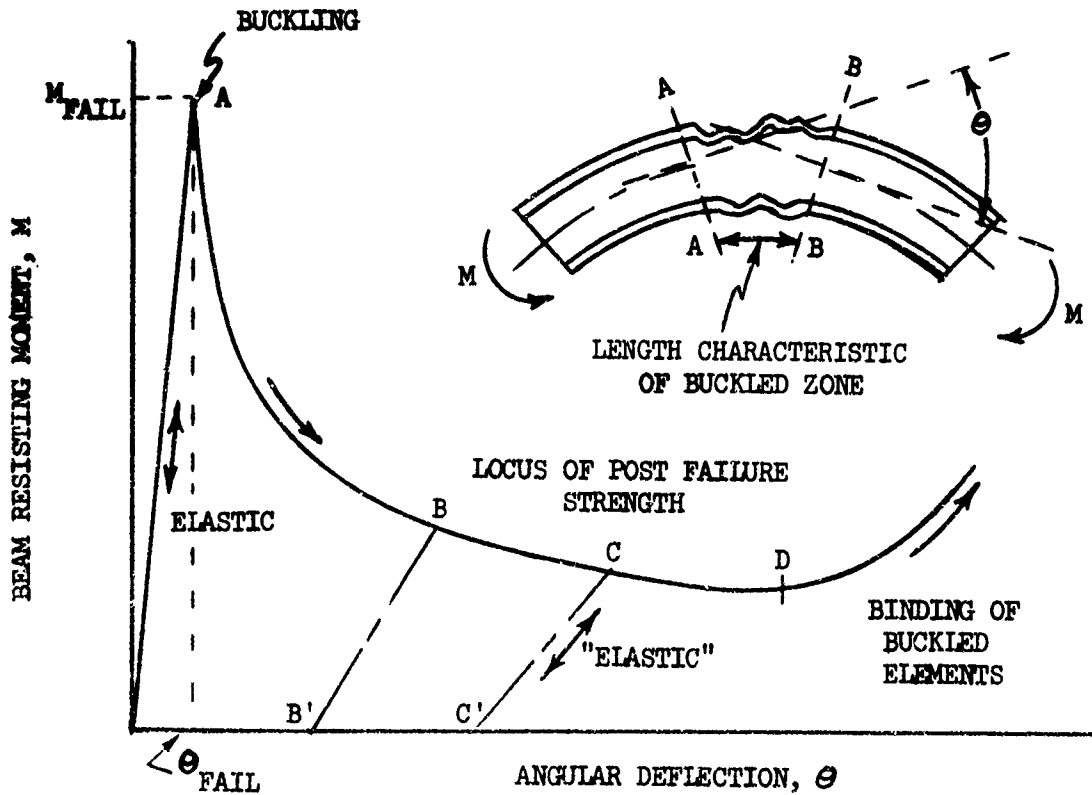


Figure 5. Structural Behavior Typical of Built-Up Beams (Reference 39).

sheet beams exhibit structural behavior similar to that shown in Figure 5.

Design Procedures and Guidelines

To perform a crash analysis of an aircraft requires the use of verified analytical tools, in addition to the definition of the crash environment and human tolerance considerations. Potentially, the greatest payoff with regard to efficiency of design in performing crash analysis exists during the preliminary design stages. However, during the initial stages of design, little data is available other than basic concepts, configuration and sizing. Thus, the designer is faced with the formidable task of incorporating crashworthy design features which are compatible with the crash environment, aircraft operational requirements, cost, weight and geometry constraints while working with preliminary design data. Of use to the designer are several categories of information. For example, design principles which include techniques and considerations for improving crashworthiness capability provide one set of guidelines. References 2, 3 and 4 are particularly useful in this respect. Reference 1 outlines an approach which, based on current available data and techniques, provides an opportunity to assess the trade-off between the level of crashworthiness capability versus incremental increase in cost and weight to achieve improved crashworthiness capability. It also presents a systematic approach for ascertaining crashworthiness capability which can incorporate the data compiled by various agencies and studies over the years. In addition, Reference 1 provides a verified analytical method which can form the basis of a designer-oriented tool.

References 6, 7, 12, 13, 29, 30 and 34, some of which are texts, provide procedures by which load deflection characteristics of various types of structures in the elastic range can be obtained. In addition, these references show how the effects of plasticity and crippling can be incorporated. These latter references present data for a variety of types of aircraft structures and include changes in geometry and boundary conditions for the different structures. In general, the data presented from the publications in the literature is not oriented toward design type personnel; accordingly, little in the way of procedures and/or guidelines is made available.

Load-Deflection Data

Although much effort has been expended to obtain structural characteristics of structural elements, only a small percentage of published data provides load-deflection data that can be directly incorporated by designers. Table II shows a cross section of data available from the references that are included in the literature evaluation. The load-deflection data provides some useful data to the designer, in that characteristic trends can be associated with different types of structural elements. Table III presents a matrix of structural element load-deflection categories and load types. The table indicates, to some degree, how the

TABLE II. LOAD-DEFLECTION DATA

Structural Element Type	Test Data		Load-Defl. Curves		Load Category*	Loading	Reference
	Static	Dynamic	Static	Dynamic			
Shell segment on bulkhead support	X	X	X	X	1	Compression of skin (bending and tension on bulkheads)	1
Metal tube or stranded cable	X	X	X	X	2	Tension	2
Inversion tube	X	X	X	X	2	Tension (outside-in) Compression (inside-out)	2
Tube flaring					2	Compression	2
Honeycomb					2	Compression (buckling of membrane columns)	2, 39
Plate stringer							
a) rolled zee	X			X	3	Compression	4
b) rolled hat	X			X	3	Compression	4
c) integrally machined stiffener	X			X	3	Compression (skin buckling and bending of risers)	4
Box beam-column	X	X	X	X	3	Compression	36
Foamed plastic		X		**	2	Compression	39
Frangible tube	X	X	X	X	*** 1,2	Compression	25, 26, 32, 33, 35

* LOAD CATEGORIES

1. Increasing load with increase in deflection
2. Constant load with increase in deflection
3. Decreasing load with increase in deflection

** Data in form of stress versus strain and load versus time
 *** Inadequate control ring design results in load increase versus deflection

TABLE III. MATRIX OF STRUCTURAL ELEMENT LOAD-DEFLECTION CATEGORIES AND LOAD TYPE

Load Type	Load Categories *		
	1	2	3 **
Compression	Skin-Stringer	Frangible Tube	Sheet Skin
	Coil Spring	Telescoping Tube	Flat and Curved Plate
	Stiffened Cylinder	Honeycomb	Axially Loaded Cylinder
		Multiple Cell Structure	Slender Long Column
	Short Column	Stringer Shell Segment	
		Beam	
Tension	Bulkhead	Inversion Tube	Short Elongation Strap
	Stiffener	Stainless Steel Strap	Sheet Skin
		Stranded Cable	Stringer

* LOAD CATEGORIES

1. Increasing load with increase in deflection
2. Constant load with increase in deflection
3. Decreasing load with increase in deflection

** Compression members tend to fail as a result of the lateral bending induced by the compression load, an action which is commonly called buckling.

selection of a structural element design can influence the loads that will be experienced in an aircraft. This information, without additional data such as energy-absorption efficiency, linear load-deflection curves, and yield points for specific design configurations, although a contribution, is inadequate for crashworthiness design. References 6, 7 and 30 present some valuable data concerning various types of structural elements up to the point of failure and including plasticity effects. Of particular importance in this data is that nondimensional graphs are presented; these allow one to easily determine load capability for different geometry or end constraints. Reference 6 includes discussions of plastic bending, buckling of flanges and webs, lateral buckling of beams, buckling of beams in combined axial compression and bending, buckling of frames, and a general method for computing elastic-plastic displacements. Reference 7 presents discussions and tables of data for determining load and deflection for beams and frames, including simultaneous axial and transverse loading, variable cross sections and curved sections, flat plates (ultimate strength, large deflections, nonuniform loading), columns (eccentric loading, combined compression and bending), and buckling of bars, columns, flat and curved plates. Reference 30 provides a discussion of the design of members in tension (skin, stringers, spar caps), bending (beams), torsion (shafts), compression (columns, flat plates, curved sheets), and shear (webs). Included in this reference are design equations, nondimensional buckling design curves, and a discussion of the manner in which local crippling failures can be analyzed.

Energy Absorption

From a crashworthiness design efficiency standpoint, it is desirable to have structural elements which exhibit a load-deflection curve that is approximately flat (zero slope) beyond the elastic limit, provided the maximum transmittal load does not subject the occupant to an intolerable acceleration magnitude. There are many load-limiting devices which can be incorporated for crashworthiness considerations. However, the selection of a particular device requires that a trade-off be made between performance, weight, space and cost. Table IV, obtained from Reference 2, compares several "one-shot" load-limiting devices for 1000-to-4000-pound loads. Included is a comparison of the pertinent design factors for eight different devices. "Long-term reliability" refers to the ability of the device to perform its function without benefit of maintenance throughout the life of the aircraft, while "specific energy" indicates the amount of energy that can be absorbed per pound of weight of the device.

References 1, 3, 4, 17, 25, 26, 27, 32, 33, 34 and 35 also present data related to structural element energy-absorption requirements or capability. Table V (Reference 33), for example, compares energy absorption efficiencies for several different materials and methods.

References 32 through 35 discuss the Lockheed Dynasorb frangible tube energy absorber which has been tested using a 3400-pound simulated vehicle structure with a ground impact velocity of 112 feet/second.

TABLE IV. COMPARISON OF "ONE SHOT" LOAD-LIMITING DEVICES FOR 1000- TO 4000-POUND LOADS (REFERENCE 2, TABLE 2-1)

Device Description	Energy-Absorption Process	Operation Sketch	Tension or Compression	Specific Energy (ft-lb/lb)	Space Required	Long-Term Reliability	Ability To Sustain Rebound Loads	Potential Applications
PLATE AND ROD								
Strap/Rod over Die or Roller	Metal Bending and Friction		T	Not Known	Average	Fair to Good	Poor	Cargo Restraint
ROLLER AND STRAP OR ROD								
Basic Metal Tube or Plate	Elongation of Metal		T	3400-4500	Minimum	Good to Excellent	Poor ^a to Fair	Forward or Lateral Seat Braces
Basic Stranded Cable ^b	Elongation of Stainless Steel		T	3000-4500	Minimum	Excellent	Zero	Cargo Restraint ^b
"S" Shaped Bar ^c	Bending and Shear		T	1400-2400	Good	Excellent	Poor	Seat Pan Downward Support Cargo Restraint ^c
Rod Pull-Through Tube ^d	Hoop Tension and Friction		T and C	600 ^d	Minimum	Good	Good	Seat Legs or Braces ^e
INSIDE-OUT								
Inversion Tube ^d	Hoop Tension/Compression and Bending		T and C	1200-2000	Average	Excellent	Excellent	Seat Legs or Braces ^d
OUTSIDE-IN								
Tube Flaring	Hoop Tension, Friction and Bending		C	30,000 ^h	Average	Good	Fair ^a	Seat Pan Downward Support
HONEYCOMB CYLINDER								
Honeycomb Compression ^f	Buckling of Membrane "Columns"		C	2500-3500	Average	Good	Poor ^a to Fair	Seat Legs or Landing Gear ^f
Tension Pulley ^g	Shear and Bending of Sheave Housing		T		Excellent	Good to Excellent	Zero	Cargo or Troup Seat
Bar Through Die ^h	Torsion		T and C	746 ^j	Average	Good	Fair	Seat Legs or Braces or Landing Gears
Wire Through Platen ⁱ	Metal Bending and Friction		T	591 ^j	Average	Fair to Good	Zero	Cargo Restraint
Rolling Torus ^k	Cyclic Bending and Shear		T and C	1453 ^j	Average	Good to Excellent	Excellent	Seat Legs or Landing Gear

(a) This device could be rated higher if an integral rebound device were incorporated into the design.
 (b) Currently being marketed by American Chain & Cable Company.
 (c) Royal Netherlands Aircraft Factories Fokker did the initial development of this device in 1963.
 (d) Development conducted by General Motors Research Laboratories, Warren, Michigan.
 (e) A device utilizing a compressed tube rather than the expanding tube shown is being marketed by the Aerotherm Company, Bantam, Connecticut.
 (f) This device is being used by the Sikorsky Aircraft Company in their S-58, S-61, and S-62 helicopter landing gears.
 (g) This value is based on the compressed tube device tested. This value could be doubled in a more efficient design.
 (h) This maximum value from Reference 12 does not consider end fitting weights; a value of 6000-8000 ft-lb/lb is comparable to the other devices. A device similar to this manufactured by Boeing-Vertol demonstrated specific energy of 737 ft-lb/lb.
 (i) This device is manufactured by Hardman Tool & Engineering Company.
 (j) Reference 18.
 (k) This device is manufactured by ARDE.
 (l) This device is manufactured by All-American Engineering Company.
 (m) This device is manufactured by ARA, Aerospace Research Associates.

TABLE V. COMPARATIVE SUMMARY OF ABSORPTION ENERGIES (REFERENCE 33)

Material or Method	Maximum Efficiency (in. lb/lb) *
Buckling Column (short)	4800
Fabric Gas Bags	72,000
Metal Gas Bags	135,000
Metal Honeycomb	130,000
Paper Honeycomb	25,000
Plastic Foam	50,000
Balsa Wood	285,000
Frangible Tubes	370,000
Stainless Steel Tension Strap	260,000
Lockheed Roll-Up Tubes With Ring Control **	450,000

NOTE: * Tabulated data are experimental values (either published information or Lockheed determined).

** Trade name "Dynasorb"

Methods of Analysis

The several methods of analysis that are available for determining load-deflection data for typical structural elements include:

- Classical static plastic analysis
- Dynamic mode approximations
- Finite differences
- Finite elements

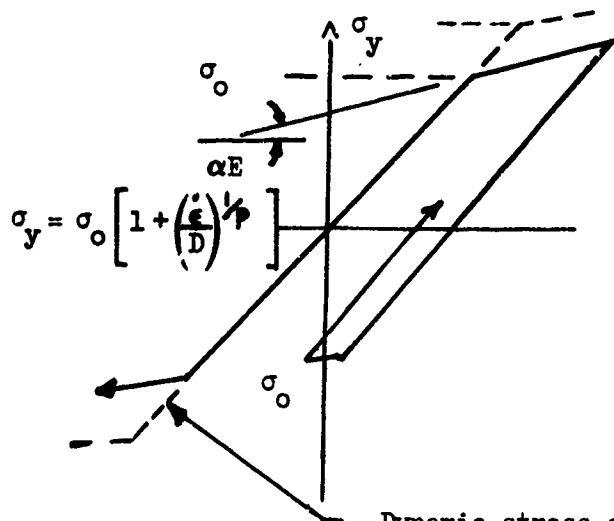
Classical static plastic analysis is applicable to most structures except wherein instability and/or buckling occurs. Beam and simple-shell type structures are generally analyzed by this method. The dynamic mode approximation technique is described in References 45 and 61. This approach is relatively simple to apply; however, it does have the following limitations:

- A constant acceleration is assumed throughout the dynamic deformation. Therefore, the use of load-deflection characteristics obtained by this approach would not accurately reflect the actual acceleration response of the structure.
- This technique is not applicable to structure which exhibits instability and/or buckling characteristics.
- For complex structures it is difficult to define a unique mode shape which is kinematically and dynamically admissible.

Finite difference and finite-element techniques are discussed in References 17, 38, 52 and 63. These approaches give reasonable load-deformation information for simple structures. However, for complex structures, these numerical methods are not yet considered as reliable or as economical as experimental techniques. Analytical techniques and numerical methods for stability analysis and post-failure analysis presented in References 15 and 64 through 71 are primarily concerned with the technique itself rather than the application of the technique to practical problems. The analytical approaches presented in the literature are devoid of methods by which designers can make direct use of the analytical procedures.

Strain Rate Effects

If materials exhibit strain-rate sensitivity, then the effect on the load-stroke characteristics for the structure will be a change in the yield and ultimate loads. For cases in which structural materials exhibit strain rate sensitivity, an approximate accounting for this effect can be made. Several references, including 5, 19, 31, 36, 37, 38, 40, 43, 44 and 46, discuss strain rate effects. There is no universally validated and accepted strain rate law. One approximation described in Reference 38 and used in several publications is shown on the next page.



σ_0 = static value of yield point

σ_y = yield point

D, p = constants of the structural material

ϵ = strain

$\dot{\epsilon}$ = strain rate

Dynamic stress-strain based on average strain rate

The approximation regards the effect of strain rate as raising the yield point (σ_y) above the static yield value (σ_0) with the associated strain hardening portion of the curve kept parallel to the static strain hardening curve.

In Reference 18 is presented a simplified method for solving impulsively loaded structure for rate-sensitive materials. The results of the study indicate that good approximations to the exact solution may be found by utilizing a rate-insensitive material with constant yield stress equal to the initial dynamic yield stress.

Inertia Effects

If inertia forces for a particular type of structure are important, then the load-deflection characteristics for the structure under dynamic loading conditions can differ from the load-deflection characteristics under static loading conditions. References 1, 8, 24, 29, 38, 40 and 43 present data related to inertia effects. In Reference 1 the load-deflection curves are obtained under dynamic loading and compared to a previously obtained static load-deflection curve for the same specimen type. The load-deflection curve for the specimen is also obtained analytically using an existing finite element program.

If the higher modes of the frequency components dominate the response initially such as to cause failure before the fundamental mode can respond, then the effects of inertia should be considered in the load-deflection curves.

Reference 38 shows the effects of impact speed on the dynamic force deflection relationship for steel and aluminum curved box-beam columns.

LOAD-SENSITIVITY STUDY

GENERAL

The results of the study described in Reference 1 show that an analytical procedure is capable of predicting the responses of airframe structure during crash conditions. The results of the study also indicate that the trade-off between cost and weight increase versus improved crashworthiness capability is an integral part of the iterative process for determining a crashworthy design. Although the computer program developed in Reference 1 provides an acceptable analytical tool for determining crashworthiness capability during preliminary design, refinements can be made which will make the program more designer oriented. The purpose of the load sensitivity studies is to ascertain how accurate the modeling representation of the structure has to be in order to obtain sufficiently accurate results for preliminary design usage. It is important to bear in mind that during a preliminary design, the structural data that is generally available is related to concepts, sizing, and location, whereas very little in the way of detail construction is known.

The load sensitivity studies make use of the 31 lumped mass model of the UH-1H helicopter described in Reference 1. The general arrangement of the UH-1H is shown in Figure 6. The basic math model internal springs, external springs and lumped masses are noted. The detailed lumped mass model and the mass representation geometry are shown in Figure 7 and Table VI, respectively. For detailed information regarding the model, see pages 81-93, Volume I of Reference 1. For information regarding the related theory including coordinate systems, see pages 25-86, Volume II of Reference 1.

LOAD-DEFLECTION VARIATIONS

Engine

The changes in the engine-mount stiffness factors and load-deflection curves are shown in Table VII and Figure 8, respectively. The load-deflection curve is obtained from the expression

$$K = \int_{j=1}^{j=n} (KR_j) \cdot (DX_j) \text{ versus } X$$

where

- K = stiffness, lb/in.
 DX_j = incremental distance, in.
 KR_j = stiffness reduction factors; i.e., for the first row in Table VII, the KR vs DX curve appears as shown in the sketch accompanying Table VII.
 X = distance, in.

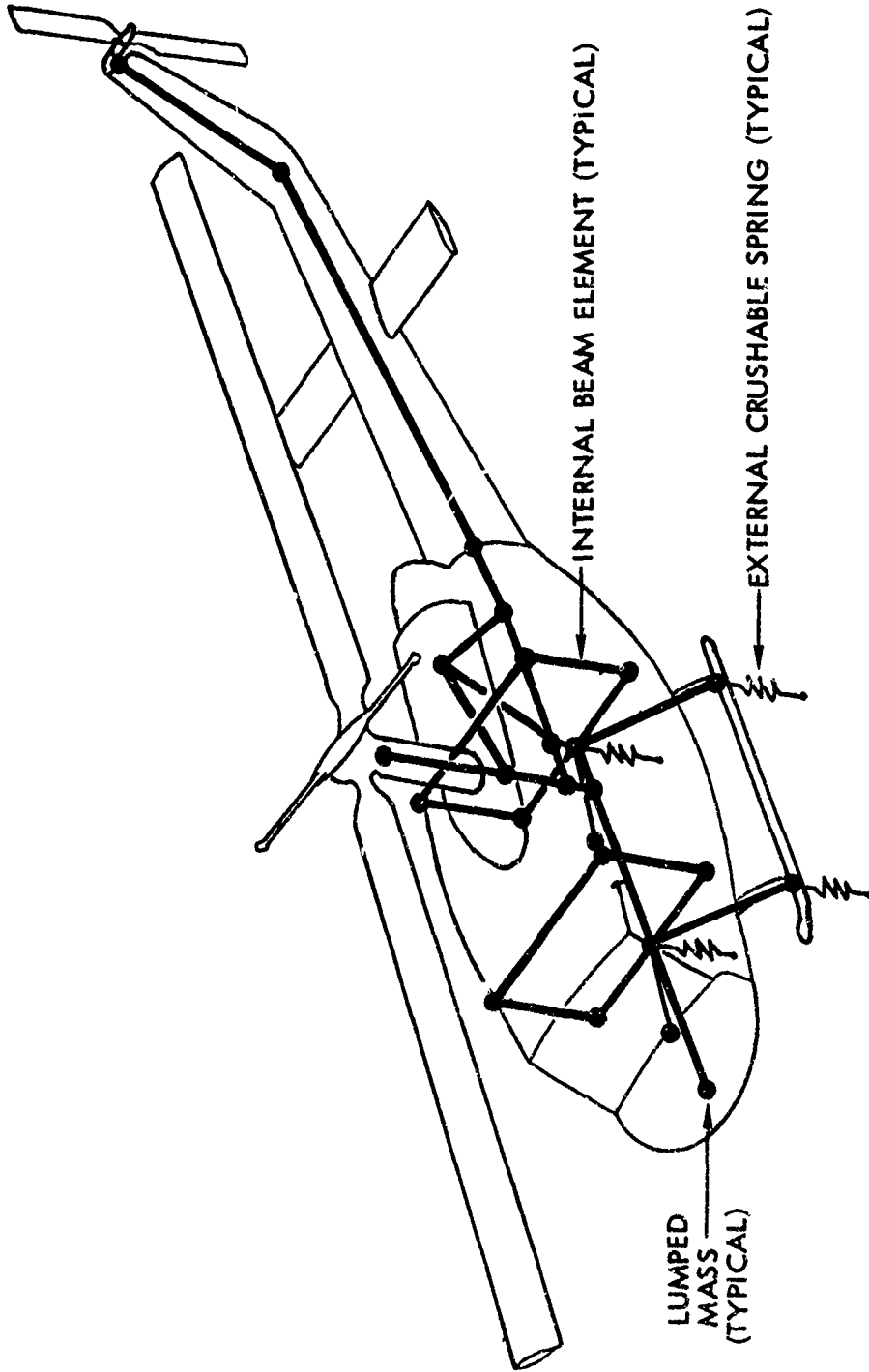


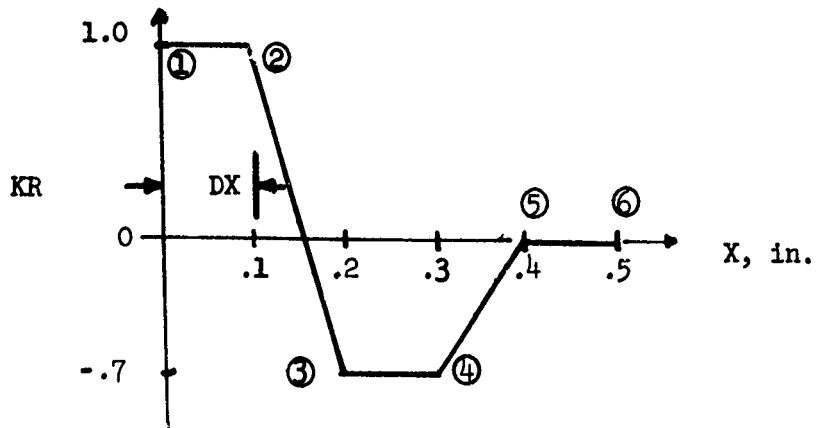
Figure 6. General Arrangement of the UH-1H Helicopter.

TABLE VI. CORRELATION STUDY ANALYTICAL MODEL GRID POINT IDENTIFICATION (REFERENCE 1)

Number	Approximate Location			Spring Length (in.)	Mass Weight (lb)	Simulated Mass Item
	FS	BL	WL			
1	460	0	132		139	Tail Rotor
2	404	0	72		85	Tail Boom
3	241	0	47.5		62	Aft Fuselage and Tail Boom
4	211	0	38.5		172	Aft Fuselage Section, Aft Base for Engine Struts
5	163	0	38.5		278	Aft Fuselage Section, Fwd Base for Engine Struts, PAX*
6	141	0	38.5		932	Pylon Support Structure, PAX*
7	187	0	79		731	Engine
8	136	0	90		1412	Main Rotor, Blade, Hub and Transmission
9	141	0	67		90	Pylon Support Structure
10	163	0	22	17	257	Lwr Fuselage, Center, PAX*
11	141	0	22	17	1823	Lwr Fuselage, Fuel Tank Location; Passengers
12	71.6	-45	22	17	175	Lwr Fuselage, Right Side
13	71.6	45	22	17	175	Lwr Fuselage, Left Side
14	163	-50.8	-14	2.25	23	Aft Landing Gear, Right Side
15	163	50.8	-14	2.25	24	Aft Landing Gear, Left Side
16	71.6	0	22	17	950	Lwr Fuselage Structure, Center, Pilot, Co-Pilot, PAX*
17	71.6	-50.8	-14	2.25	24	Fwd. Landing Gear, Right Side
18	71.6	50.8	-14	2.25	24	Fwd. Landing Gear, Left Side
19	23	0	22		307	Nose Structure
20	163	-45	76		31	Aft Top Cabin Structure, Right Side
21	163	45	22		31	Aft Top Cabin Structure, Left Side
22	163	-45	22	17	166	Lwr Fuselage Structure, Right Side
23	163	45	76	17	166	Lwr Fuselage Structure, Left Side
24	71.6	-45	76		28.5	Fwd Top Cabin Structure, Right Side
25	71.6	45	76		28.5	Fwd Top Cabin Structure, Left Side
26	163	0	22		55	Troop Seat, Aft
27	71.6	0	22		70	Pilot/Co-Pilot Seat Forward
28	163	0	41		120	10 Hz Man - Weight of Upper Torso - Aft
29	73	0	41		120	10 Hz Man - Weight of Upper Torso - Fwd.
30	163	0	41		120	8 Hz Man - Weight of Upper Torso (DRI) - Aft
31	73	0	41		120	8 Hz Man - Weight of Upper Torso (DRI) - Fwd.

*PAX denotes passenger.

The KR versus X curve is depicted below:



There are six KR values for each element. The first KR value corresponds to a zero deflection. The incremental deflections (DX) are equally spaced. The KR values shown in the sketch above are for the base axial case (31-52) shown in Table VII.

For a linear spring, KR = 1
 For a constant force, KR = 0
 For a decreasing force, KR < 0

TABLE VII. ENGINE-MOUNT AXIAL AND BENDING KR CHANGES

Case Identification	DX (in.)	KR Values at DX_j					
		①	②	③	④	⑤	⑥
AXIAL							
Base	.1	1.0	1.0	-.7	-.7	0	0
E1	.1	1.0	.8	0	-.5	-.25	0
E2	.1	1.0	.8	0	0	0	0
E3	.1	1.0	.6	.5	.4	.3	.2
BENDING							
Base	.0667	1.	1.	1.	1.	0	0
EB1	.1	1.	1.	1.	0	-1.	-.8
EB2	.1	1.	1.	1.	0	1.	.8
EB3	.1	1.	1.	1.	0	-.5	-.4
EB4	.1	1.	1.	1.	0	.5	.4
K _{axial}		= 5.64×10^4 lb/in.					
K _{bending}		= 1.12×10^5 lb/in.					

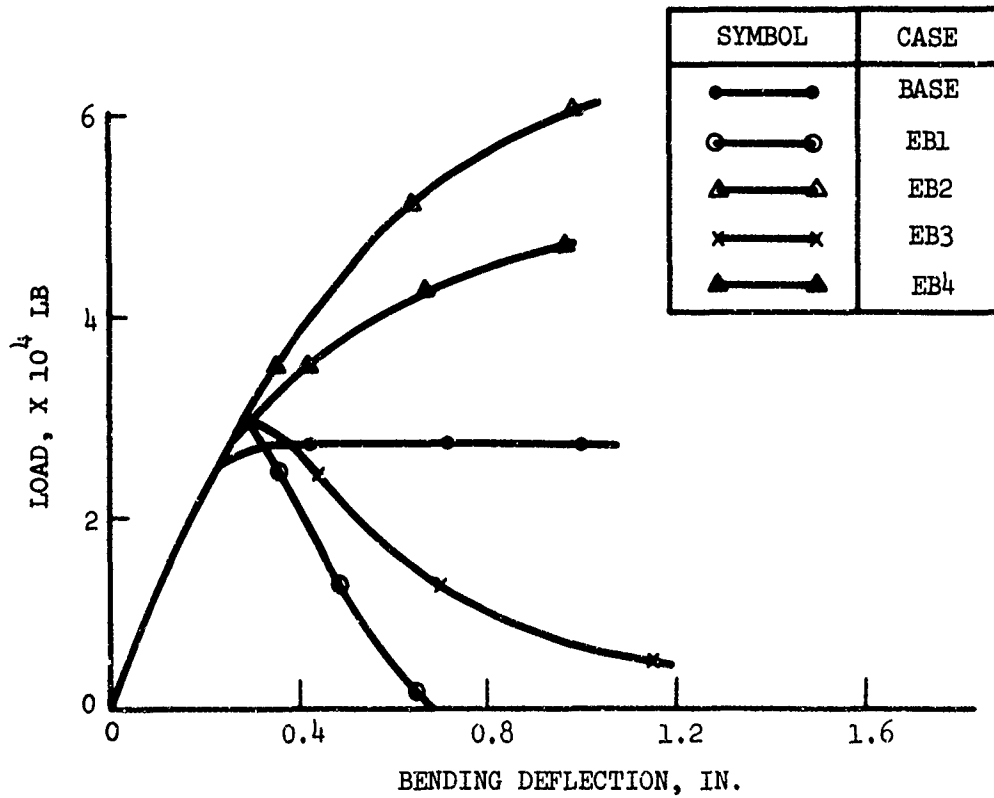
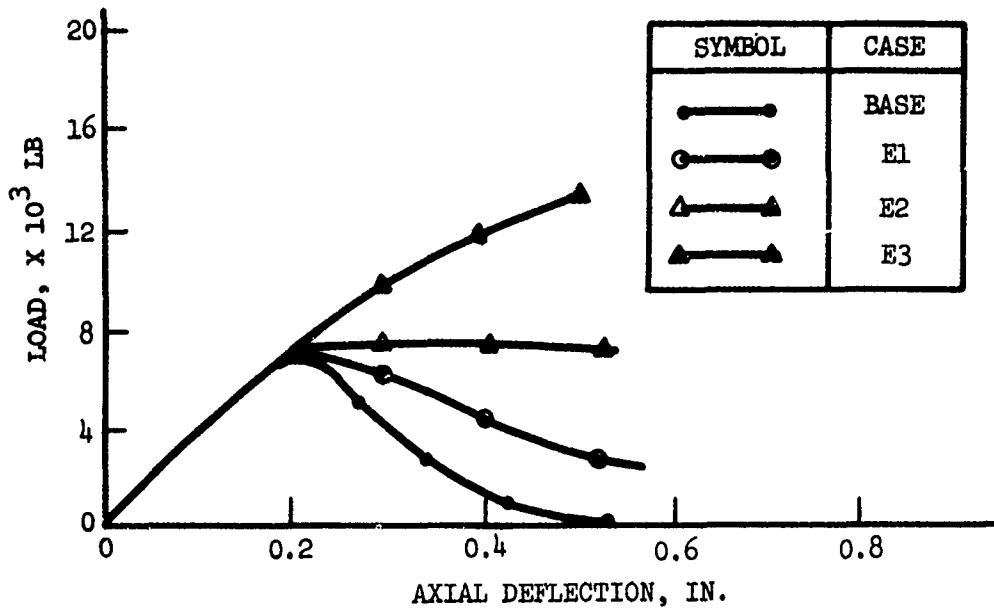


Figure 8. Engine Axial and Bending Load-Stroke Curves.

The engine mount is a bipod arrangement; thus, the vertical force is influenced primarily by the member axial and vertical forces and the angle of the mount. A left side, looking inboard, view of the engine mount arrangement is shown in Figure 9.

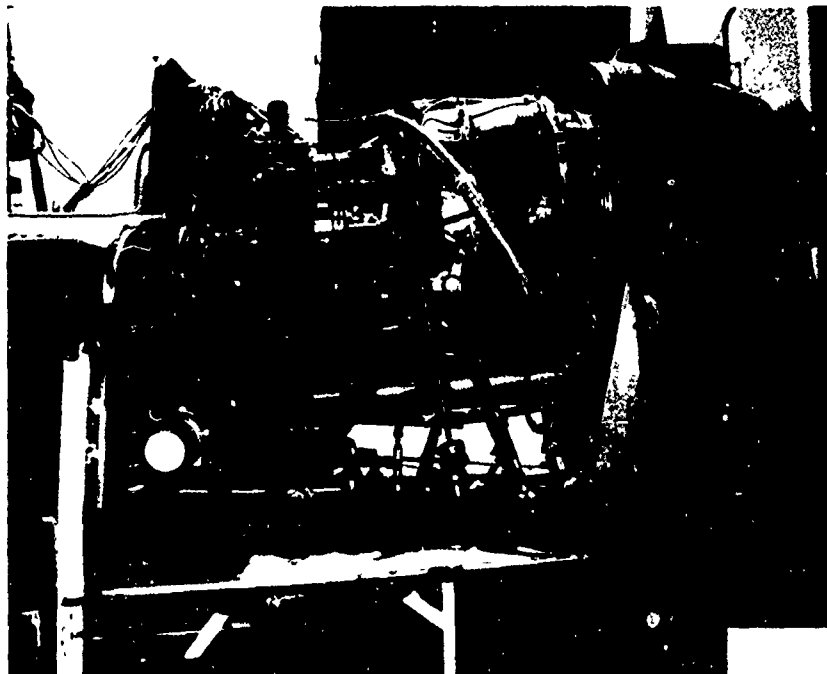


Figure 9. Left Side, Looking Inboard, View of Engine Mount.

Transmission

The transmission mount is a near-vertical member; therefore, the vertical response is influenced primarily by the member axial (vertical) stiffness. The changes in the transmission-mount stiffness reduction factors and, consequently, the load-deflection curve are shown in Table VIII. The associated load-deflection curves ($K \int (KR) (DX) vs X$) for the transmission mount, members 8 - 9, are shown in Figure 10.

Landing Gear

The changes in the landing skid stiffness reduction factors are shown in Table IX. The associated load-deflection curves for the forward landing skid (members 16 - 17 and 16 - 18) and the aft landing skid (members 10 - 14 and 10 - 15) are shown in Figure 11.

TABLE VIII. TRANSMISSION-MOUNT AXIAL AND BENDING KR CHANGES							
Case Identification	DX (in.)	KR Value at DX _j					
		①	②	③	④	⑤	⑥
<u>AXIAL</u>							
Base	.48	.00785	.00785	1.	1.	0.	0
T ₁	.48	.00785	.00785	1	1	.5	0
T ₂	.48	.00785	.00785	1	1	-.25	-.25
T ₃	.48	.00785	.00785	1	1	-.5	-.5
T ₄	.48	.00785	.00785	1	1	-.1	-1.
<u>BENDING</u>							
Base	.25	1.	1.	1.	1.	0.	0.
TB1	.5	1.	1.	1.	1.	-1.	0.
TB2	.4	1.	1.	1.	-1.	-1.	-1.
K axial =		2×10^5 lb/in.					
K bending =		1.9×10^4 lb/in.					

TABLE IX. LANDING-GEAR BENDING AND ROTATIONAL KR CHANGES							
Case Identification	DX (in.)	KR Value at DX _j					
		①	②	③	④	⑤	⑥
<u>BENDING</u>							
Base	4.0	1	1	1	1	-3.3	-3.3
SB1	4.0	1	1	1	1	1.0	1.0
SB2	4.0	1	1	1	1	0.	0.
SB3	4.0	1	1	1	1	0	-2.0
SB4	4.0	1	1	1	1	-1.	-2.5
<u>ROTATION</u>							
Base	.02	1	1	1	1	-3.3	-3.3
SR1	.005	1	1	1	1	2.0	-3.3
SR2	.005	1	1	1	1	0.	0.
K bending =		2.7×10^3 lb/in.					
K rotation =		2.17×10^6 in-lb/rad					

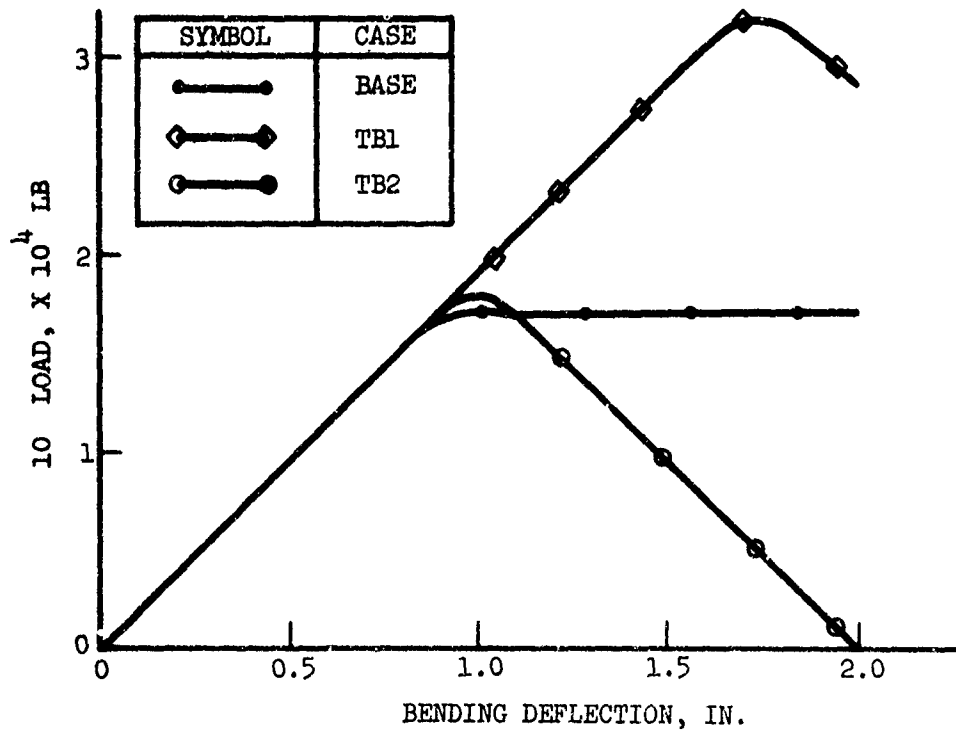
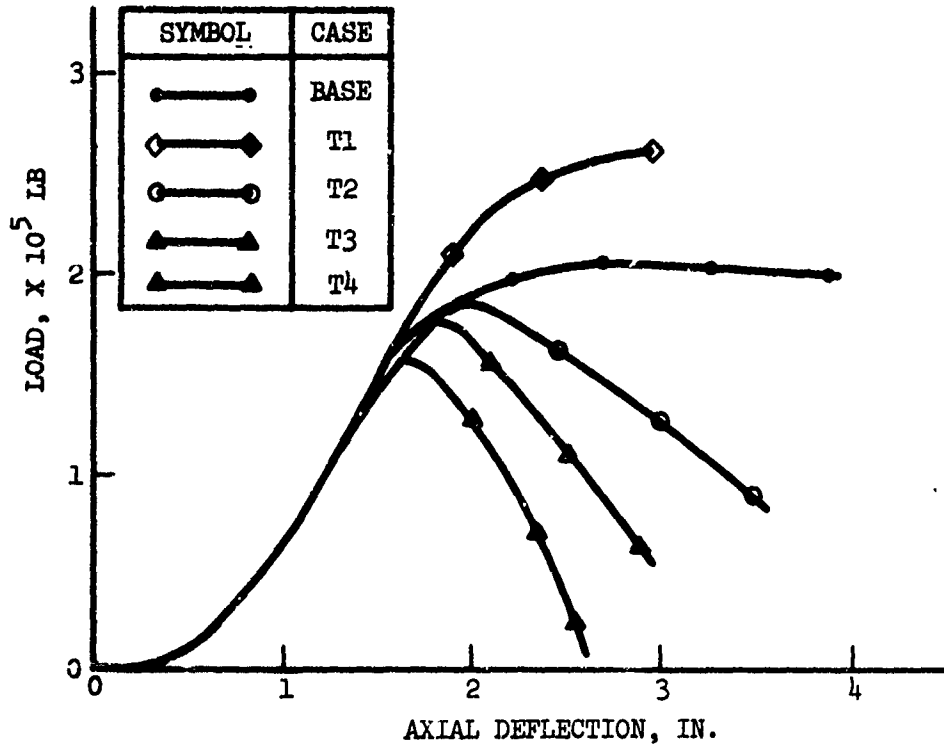


Figure 10. Transmission Axial and Bending Load-Stroke Curves.

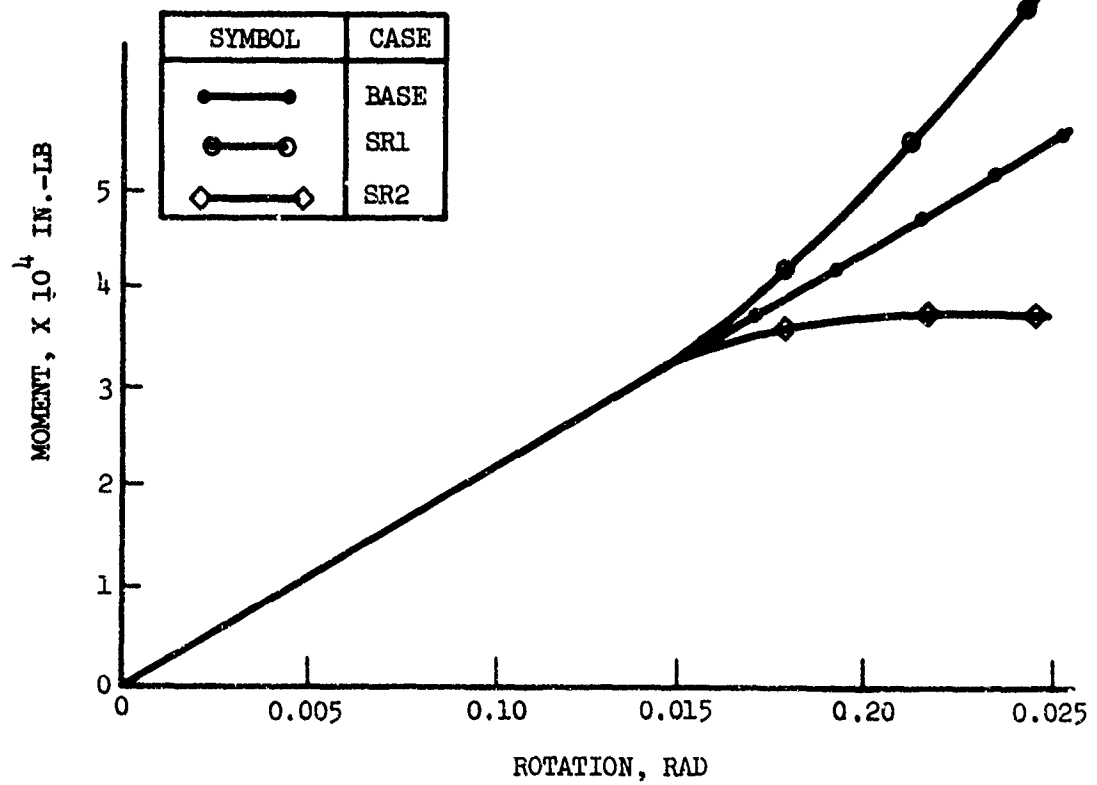
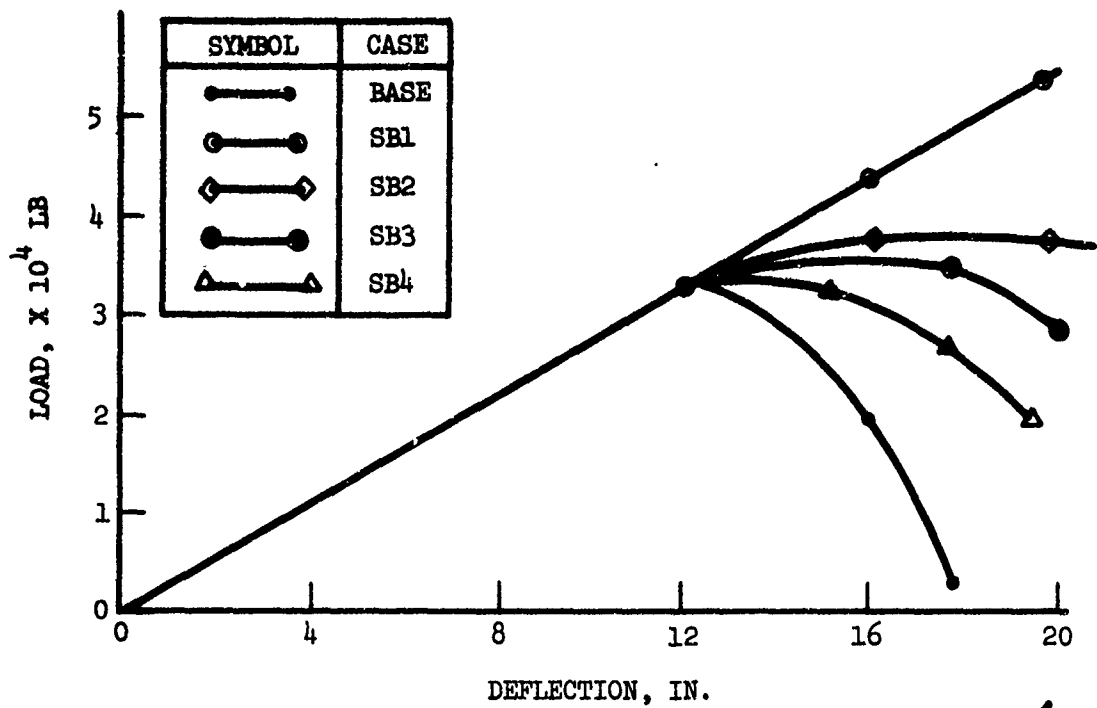


Figure 11. Landing-Gear Bending and Rotational Load-Stroke Curves.

The effective bending stiffness of the landing skids can be approximated from the expression

$$K = \frac{(K_{33})(K_{55}) - (K_{35})^2}{K_{55}} = K_{33} - \frac{(K_{35})^2}{K_{55}}$$

where K_{33} = bending stiffness (load due to deflection)

K_{55} = rotational stiffness (torque due to rotation)

K_{35} = load due to rotation

In program KRASH, stiffness reduction factors are input separately for all the diagonal terms, i.e., K_{11} , K_{22} , K_{33} , K_{44} , K_{55} , K_{66} . The stiffness reduction factor for each diagonal term applies for all the K values in the respective column (the stiffness reduction factor for K_{33} = the stiffness reduction factor for K_{13} , K_{23} , K_{43} , K_{53} , K_{63}).

Fuselage

The changes in the fuselage external spring load-deflection curves are shown in Figures 12 and 13. The parameters that are varied include the load level, stroke and the rate of loading. Figures 12 and 13 represent the load-deflection curves for masses 10 and 16 (forward); the load level for the external springs from masses 11 (mid), 12, 13, 22, and 23 (sides) are equal to half the load level of masses 10 and 16.

Crushing load-stroke characteristics are given in Table X.

RESULTS

Load sensitivity studies using computer program KRASH and the existing 31 lumped mass model are shown in Figures 14 through 17 for the load and energy absorbed versus deflection for the engine (axial), engine (bending), transmission (axial), and landing gear (bending), respectively. The results, shown in Tables XI through XV, compare the peak load and peak responses for the base case versus the various load-deflection changes for the structural elements.

Engine

The results of the engine load-sensitivity runs are shown in Figures 14 and 15 and Tables XI and XII. For large changes in axial load-stroke, the response is fairly insensitive. For example, case E1 versus the base case shows a potential inaccuracy of 12% if the shape of the buckled load-stroke curve is not represented exactly. If the load-stroke curve is considered flat (E2), then a 20% error would be introduced.

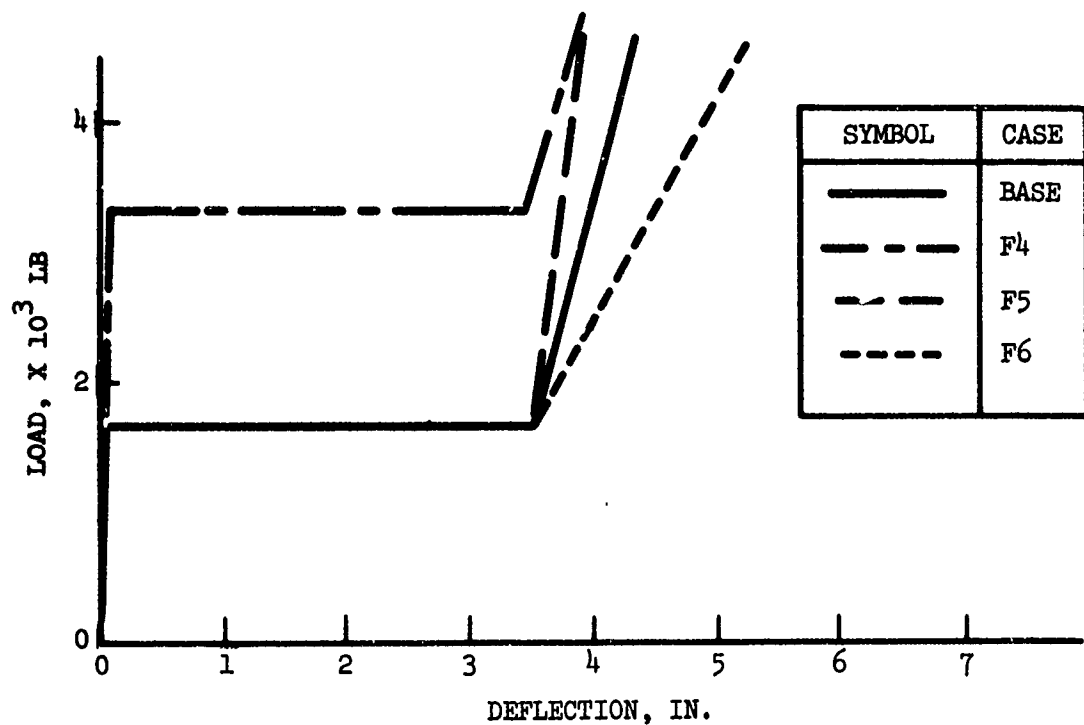


Figure 12. Fuselage External Crushing Load-Deflection Curves.

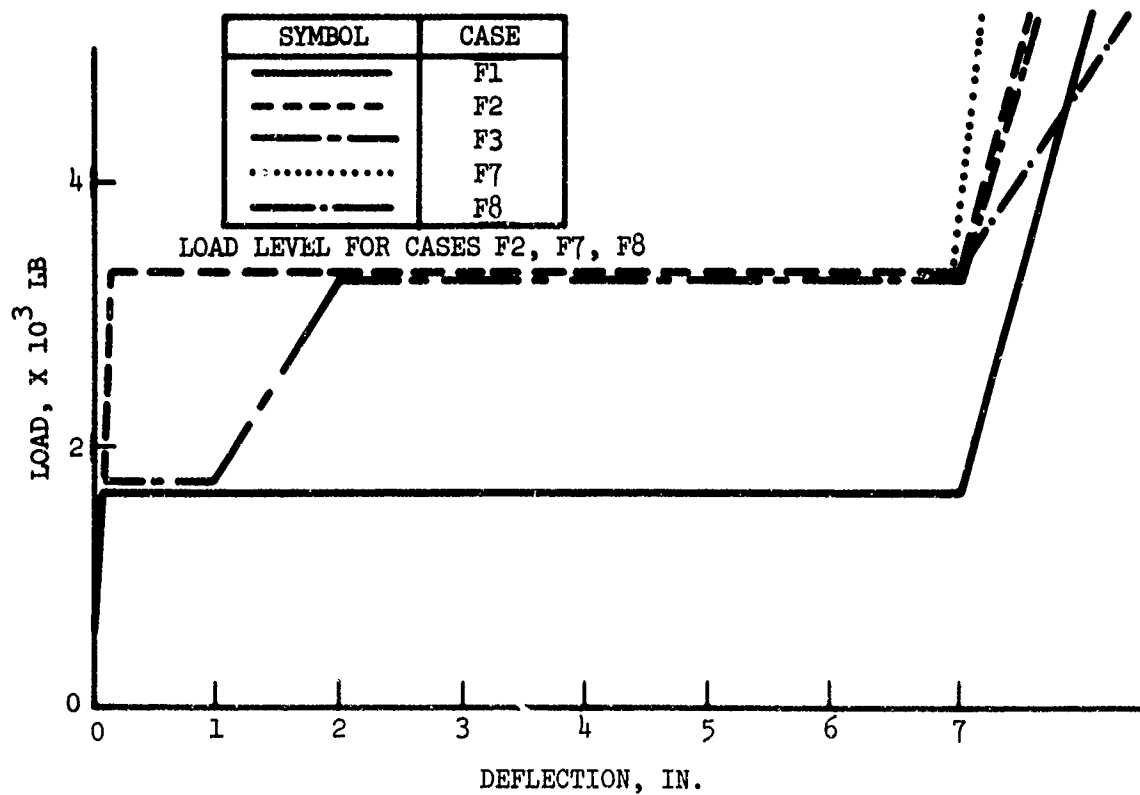
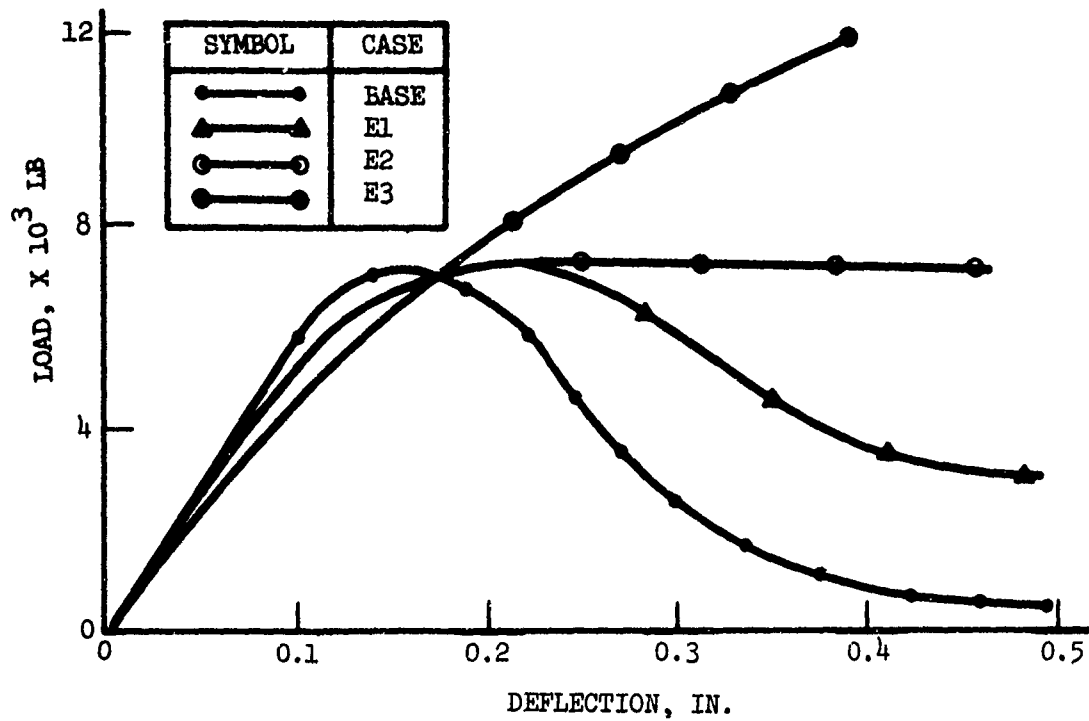


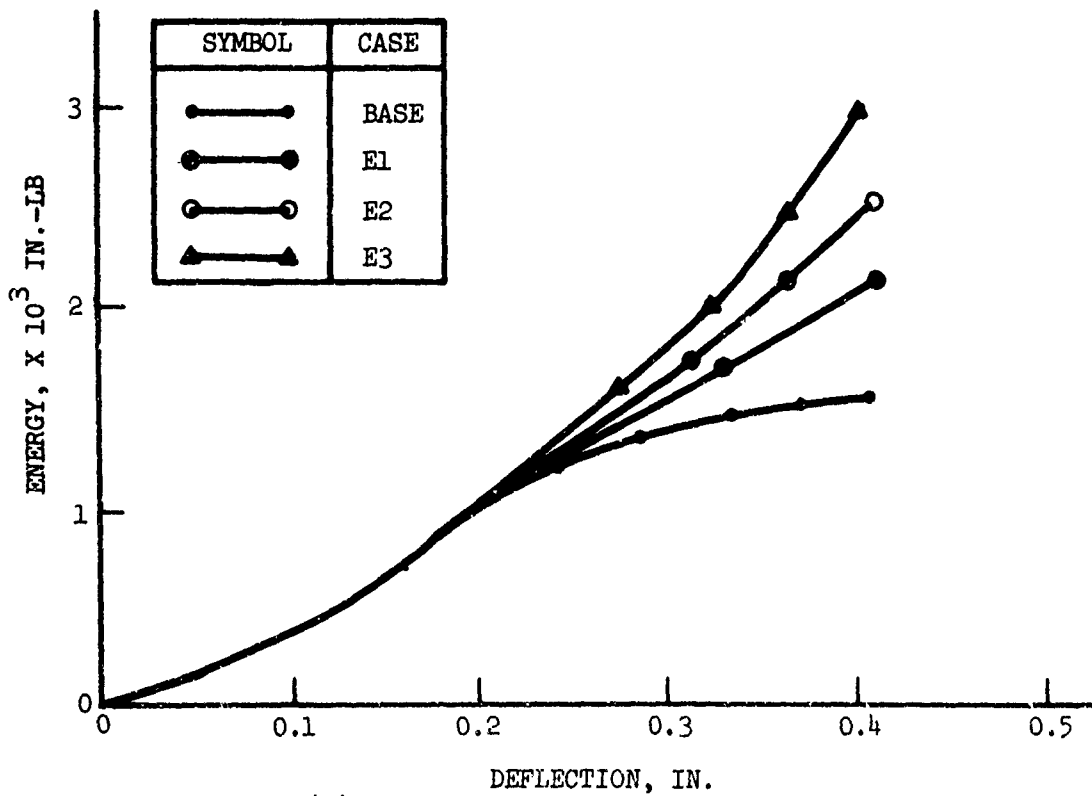
Figure 13. Fuselage External Crushing Load-Deflection Curves.

TABLE X. FUSELAGE EXTERNAL CRUSHING LOAD-STROKE CHARACTERISTICS			
Case	Load Level * (Lb)	Crushing Distance* (In.)	Bottoming Stiffness* (Lb/In.)
BASIC	1.65×10^4	3.5	3.3×10^4
F1	1.65×10^4	7	3.3×10^4
F2	3.3×10^4	7	3.3×10^4
F3	1.65 to 3.3×10^4	7	3.3×10^4
F4	3.3×10^4	3.5	3.3×10^4
F5	1.65×10^4	3.5	6.6×10^4
F6	1.64×10^4	3.5	1.65×10^4
F7	3.3×10^4	7	6.6×10^4
F8	3.3×10^4	7	1.65×10^4

* Values shown are for masses 10 (aft) and 16 (fwd).
All other external springs are changed in the same proportion.



(a) LOAD VERSUS DEFLECTION



(b) ENERGY ABSORBED VERSUS DEFLECTION

Figure 14. Engine-Mount Axial Load and Energy Absorbed Versus Deflection Curves.

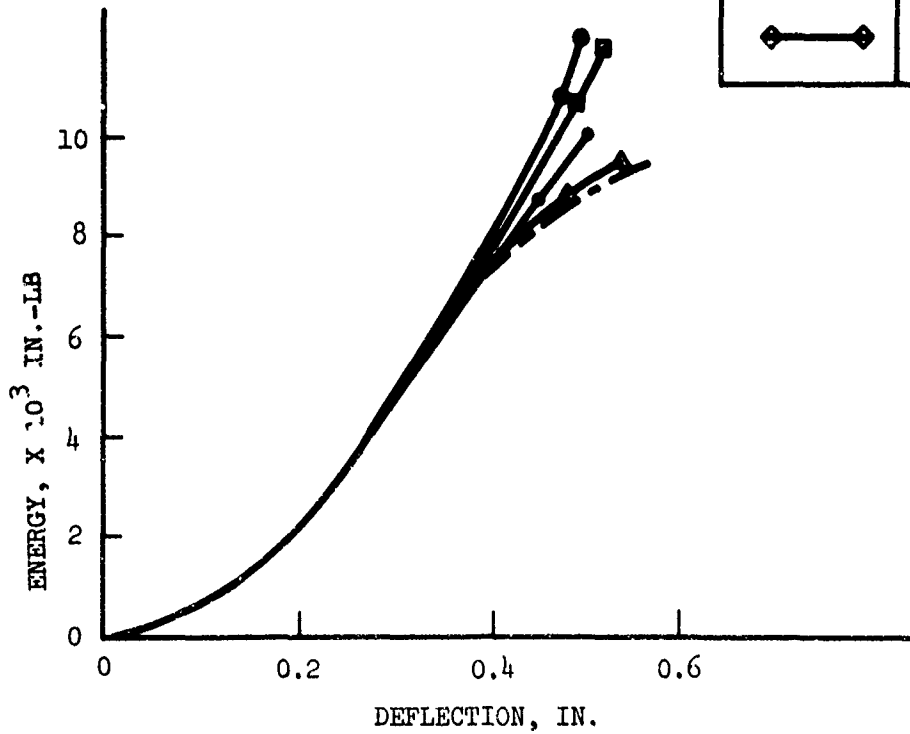
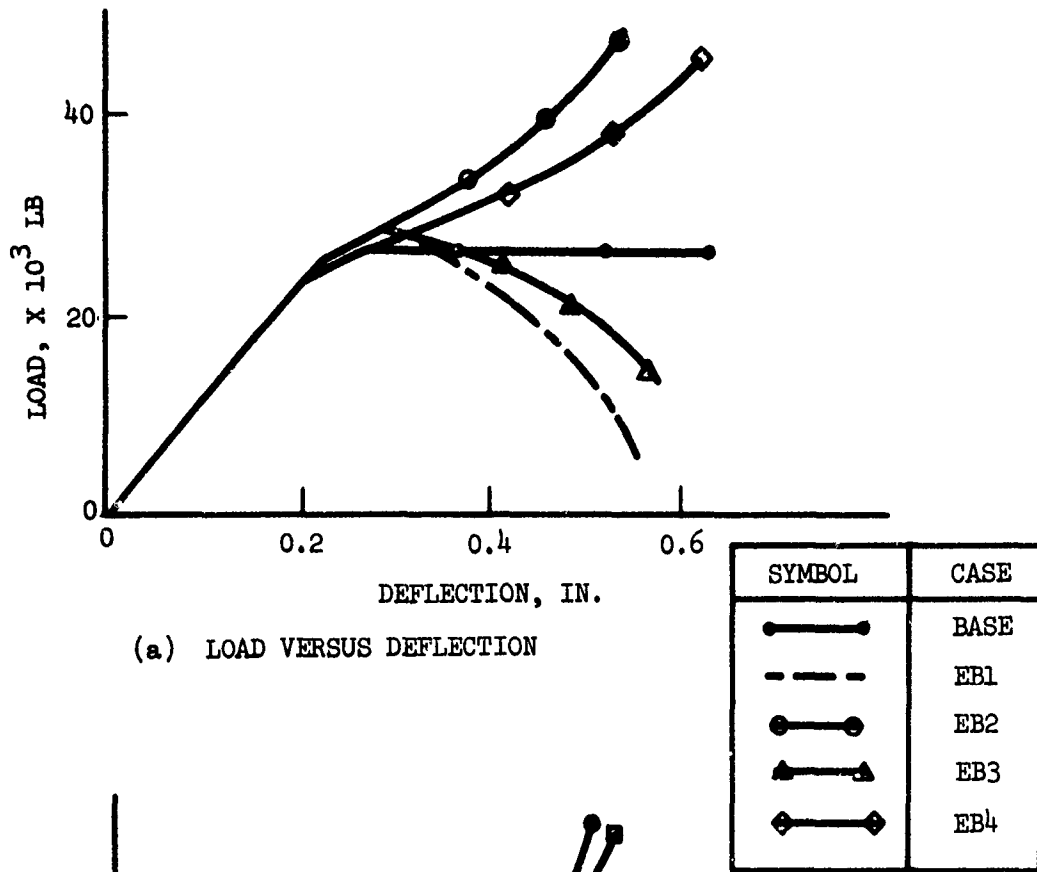


Figure 15. Engine-Mount Bending Load and Energy Absorbed Versus Deflection Curves.

TABLE XI. ENGINE MOUNT AXIAL LOAD SENSITIVITY STUDY RESULTS				
Condition	Peak Load (lb) @ Time Δ_{max} .	Peak Response (G's) @ Time Δ_{max} .	Percent Change	
			Load	Response
Base	500 *	49	-	-
E1	2,500 *	55	400	12
E2	7,200	60	1400	20
E3	12,000	72	2400	44

* Peak Load = 7200 lb (Figure 14) at $\Delta = .15''$ to $.2''$. However peak response occurs later in run when axial load drops off ($\Delta = .6''$) and is influenced by bending forces.

TABLE XII. ENGINE MOUNT BENDING LOAD SENSITIVITY STUDY RESULTS				
Condition	Peak Load (lb) Time @ $\Delta = .38''$	Peak Response (G's) Time @ $\Delta = .38''$	Percent Change	
			Load	Response
Base	26,000	47	-	-
EB1	24,000	46	-7.6	-2.1
EB3	25,000	47	-3.8	0
EB4	30,000	49	+15.4	+4.2
EB2	32,000	50	+23.	+6.4

Condition	Peak Load (lb) Time @ $\Delta = .5''$	Peak Response (G's) Time @ $\Delta = .5''$	Percent Change	
			Load	Response
Base	26,000	50	-	-
EB1	12,000	30	-54	-40
EB3	20,000	40	-23	-20
EB4	36,000	60	+38	+20
EB2	45,000	72	+73	+44

Transmission

The results of the transmission-mount axial load-sensitivity runs are shown in Figure 16 and Table XIII. A comparison of the percentage of change in load and corresponding percentage of change in response indicates that the latter parameter is far less sensitive than the former parameter. Conditions T2, T3 and T4 represent situations in which the load-carrying capability will decrease. While they vary considerably in load vs deflection beyond the failure point, the effect on the peak response varies from 25% to 36.5%, as compared to the basic. Conditions T and T1 represent conditions in which the rate of load increases after failure occurs. Under these conditions the response varies from 3.6% to 17.5% as compared to the base case, which has the steepest load-deflection curve.

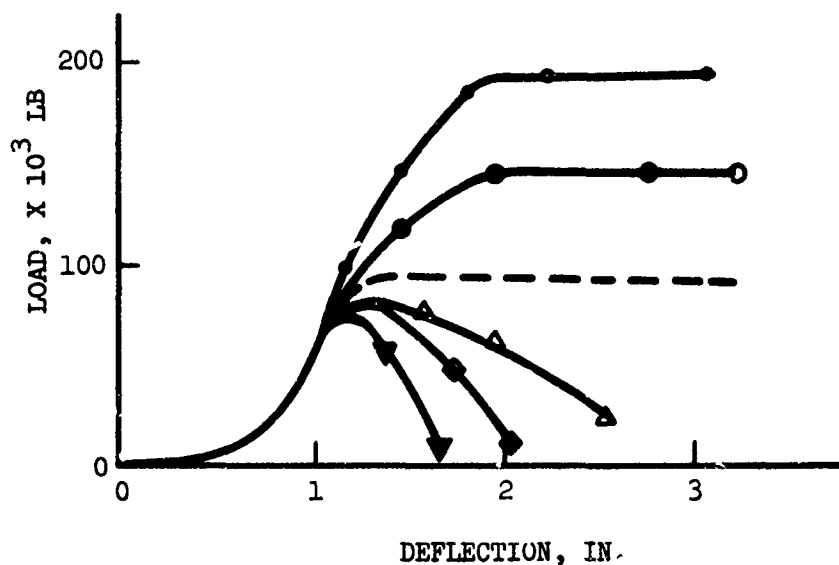
Landing Gear

The results of the landing gear bending load-sensitivity studies are shown in Figure 17 and Table XIV. The engine and transmission mounts are insensitive to these changes because failure of the struts occurs approximately 30 milliseconds after ground contact while the engine and transmission loads occur between 60 and 70 milliseconds after impact. The DRI peak values which occur between 80 and 90 milliseconds after impact show a slight sensitivity (~10%) to changes in landing gear load-stroke values within the constraints of this type of gear.

Fuselage

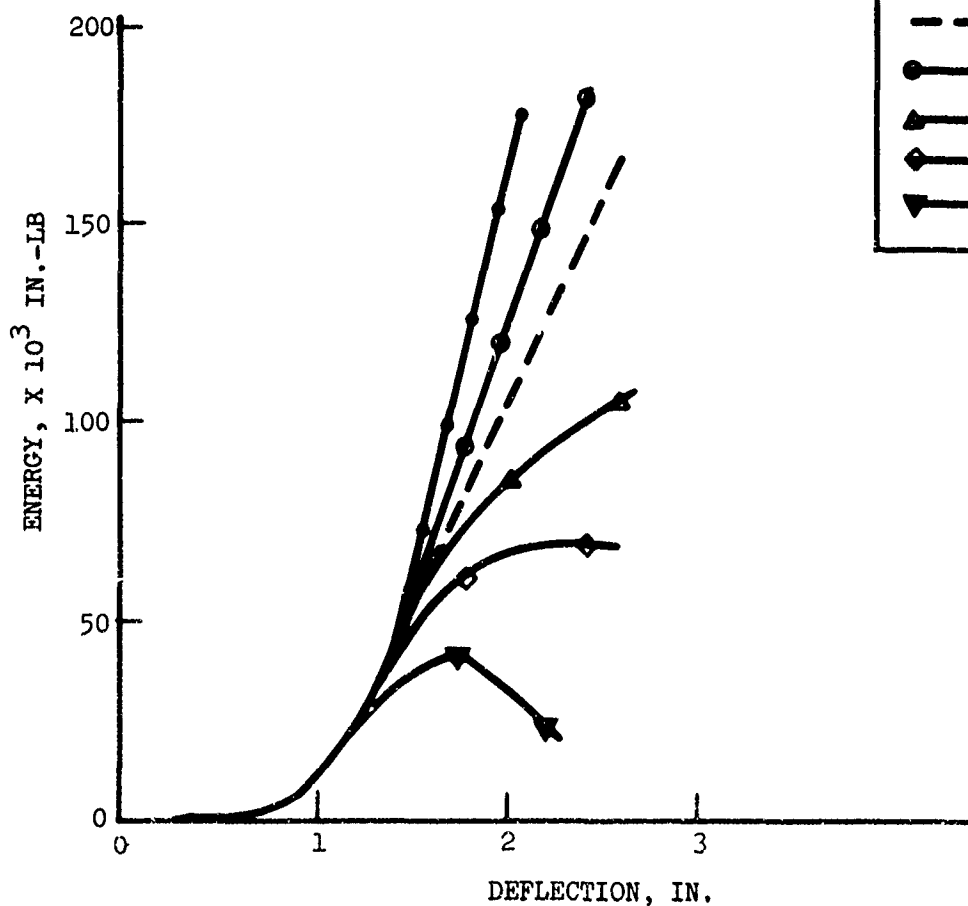
The results of the fuselage load-sensitivity studies are shown in Table XV. Increasing the load stroke from 3.5 inches to 7 inches affects the response of the transmission and DRI's by approximately 10%. (The DRI model is described in Reference 1. Basically the DRI is a quantitative measurement of the occupant response which is related to the probability of a spinal compression injury. A DRI value of 19, for example, would relate to a 10% probability of spinal compression injury.) Increasing the load level by a factor of two during the flat portion of the stroke has the further effect of reducing peak responses of the transmission (~5%) and DRI (~5%). The most significant factor affecting the response in the UH-1H model is the bottoming spring. The engine response is increased 23%, and the transmission response is changed 27% when the bottoming spring is doubled (case F5). When the bottoming spring is halved (case F6), the engine response is reduced by 20% and the transmission response by 30%. The DRI's responses in the UH-1H model are more sensitive to changes in load level and stroke. The DRI peak responses occur later after impact compared to the engine and transmission responses and, consequently, are affected by the amount of energy that is absorbed by the crushing of the fuselage.

Conversely, the engine and transmission responses are affected by the rate of load change due to the stiffness of the fuselage. The external fuselage springs bottom (reach peak deflection) at between 60 and 70 milliseconds after impact, which coincides with the time at which peak engine and transmission responses occur.



(a) LOAD VERSUS DEFLECTION

SYMBOL	CASE
—●—	BASE
- - -	T
—○—	T1
—△—	T2
—◇—	T3
—▽—	T4



(b) ENERGY ABSORBED VERSUS DEFLECTION

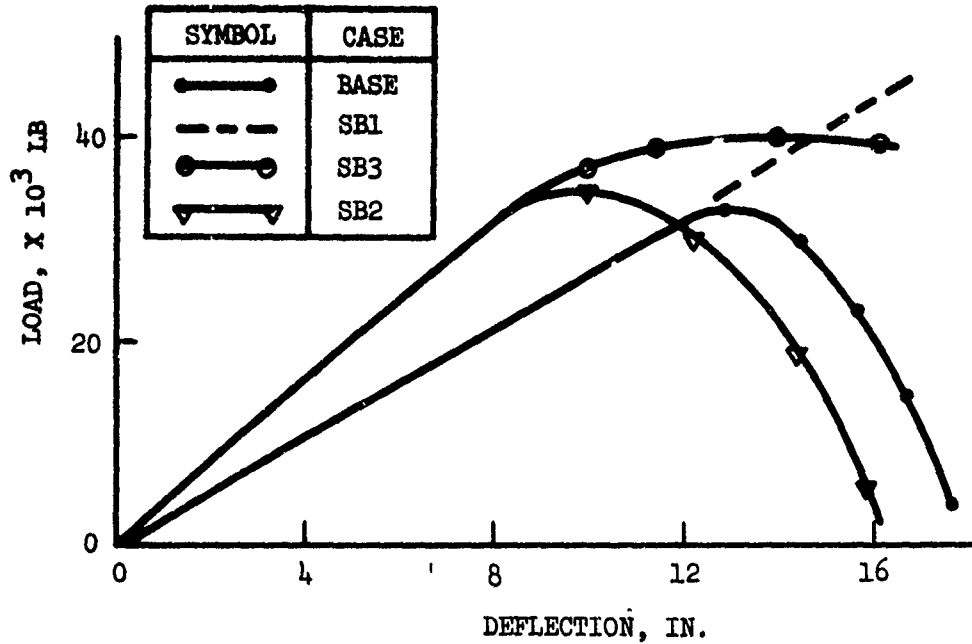
Figure 16. Transmission-Mount Axial Load and Energy Absorbed Versus Deflection Curves.

TABLE XIII. TRANSMISSION-MOUNT AXIAL LOAD SENSITIVITY STUDY RESULTS				
Condition	Peak Load (lb) @ Time $\leq \Delta$ max.	Peak Response (G's) @ Time $\leq \Delta$ max	Percent Change	
			Load	Response
Base	150,000	86	-	-
T1	120,000	83	20.	3.6
T	95,000	71	36.7	17.4
T2	85,000	64.5	43.3	25.
T3	75,000	60	50.	30.2
T4	70,000	54.6	53.	36.5

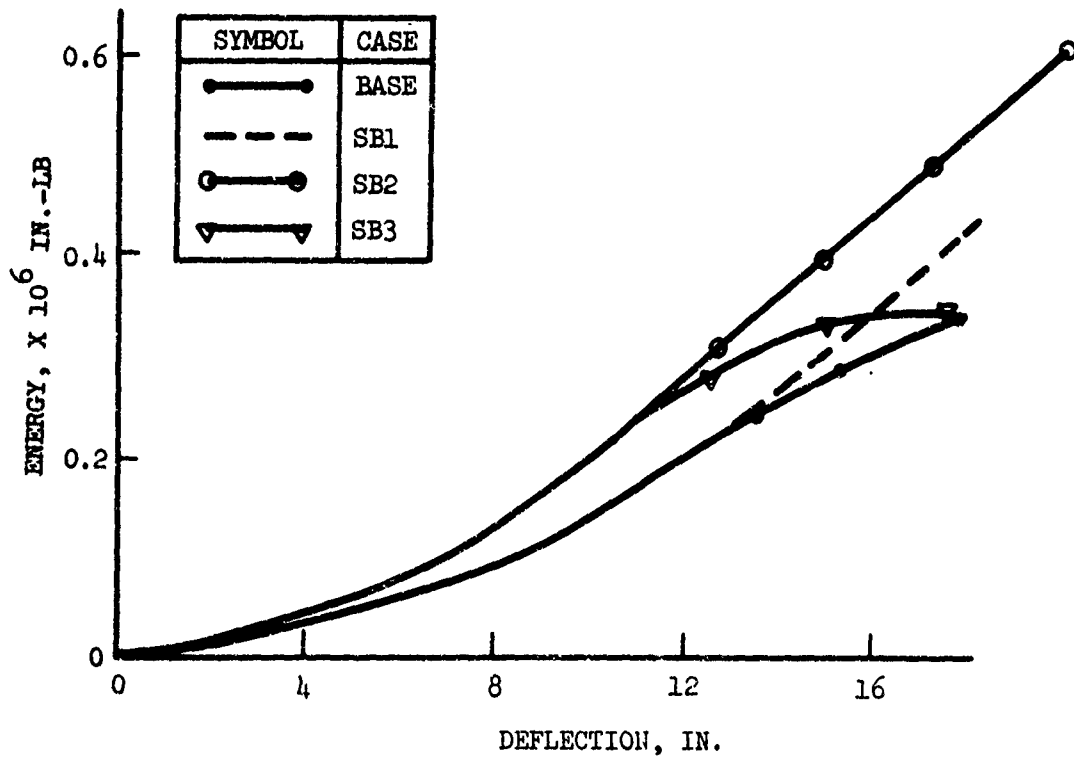
TABLE XIV. LANDING GEAR LOAD SENSITIVITY STUDY RESULTS						
Condition	Relative Energy Absorption to Failure	Peak Load (lb) (@ Deflection)*	Max. Response (G's)		Max DRI	
			Engine	Transm.	Aft	Fwd
Base	4	33,000 (13)	53	86	63	60
SB1	3	40,000 (15)	53	87	63	60
SB2	2	35,000 (10)	52	84	59	55
SB3	1	40,000 (12)	51	86	58	54

NOTE:

* Deflection in Inches



(a) LOAD VERSUS DEFLECTION



(b) ENERGY ABSORBED VERSUS DEFLECTION

Figure 17. Landing Gear Load and Energy Absorbed Versus Deflection Curves.

TABLE XV. FUSELAGE LOAD SENSITIVITY STUDY RESULTS

Case	Engine Peak Acceleration G's @ Time *	Trans. Peak Acceleration G's @ Time *	Forward Max. DRI @ Time *	Aft Max. DRI @ Time *	Load Level (Lb)	Crushing Stroke (In.)	Bottoming Stiffness (Lb/In.)
Base	52 @ 065	84 @ 062	59 @ 080	63 @ 088	16500	3.5	33000
F1	50 @ 072	78 @ 066	53 @ 090	60 @ 095	16500	7	33000
F2	49 @ 074	73 @ 066	47 @ 086	52 @ 095	33000	7	33000
F3	49 @ 074	73 @ 066	48 @ 086	58 @ 095	16500/33000	7	33000
F4	51 @ 066	73 @ 060	57 @ 078	62 @ 087	16500	3.5	33000
F5	64 @ 062	82 @ 048 114 @ 058	58 @ 072	63.3 @ 082	16500	3.5	66000
F6	42 @ 065	57 @ 063	55 @ 088	57 @ 100	16500	3.5	16500
F7	58 @ 070	102 @ 065	48 @ 080	59 @ 090	33000	7	66000
F8	41 @ 075	51 @ 066	42 @ 092	50 @ 100	33000	7	16500

* Time in Milliseconds

SUBSTRUCTURE ANALYSIS

OBJECTIVE

The purposes of the analysis are to:

- Develop simplified techniques to obtain approximate load-deflection characteristics of failure and post-failure regions of typical aircraft substructure.
- Develop ways of incorporating empirical and analytical procedures to correlate with experimental data.
- Extend the procedures to apply the analytical techniques to structures which have a different geometrical configuration.
- Predict the crashworthiness capability of substructure segments to be used in vehicle crashworthiness design by the use of the techniques and design procedures to be developed in this study.

METHODS OF ANALYSIS

The model specimen used (Figure 18), which represents the lower fuselage, is a composite built-up substructure made of stiffened panels with longitudinal reinforcement by main beams along the sides. The specimen dimensions are 46 x 18 x 6.125 inches. The drawing for specimens 1 and 2 is presented in Figure 19. Complete details are given in the SUBSTRUCTURE TEST PROGRAM section which follows. Drawings for all 12 specimens, which are analyzed and tested during the study described herein, are presented in Volume II. The specimen is approximately half size except that the skin, web and angle stiffeners are actual thicknesses. Under vertical impact conditions the loads are transmitted from the fuselage segment to the transmission housing via the supports at the four edges noted in Figure 20.

In this study, identifying dominant failure mechanisms and post-failure behavior is of primary concern. Emphasis is placed on examining the applicability of various existing analytical and semiempirical approaches.

The structural elements selected in this program are stiffened panels, which are subject to crushing deformation modes (or end shortening), starting with the initial buckling of the webbed structure, followed by post-buckling behavior, which is characterized by geometrical nonlinearity as well as material nonlinearity due to plastic deformation. As the loads are further increased, an ultimate point is reached, and beyond this point, as the displacement is further increased, the load reduces drastically.

For most plates and stiffened panels under in-plane compressive loads, failure is characterized by one of the following:

- For long plates and long panels, the structure fails mainly due to column instability behavior.

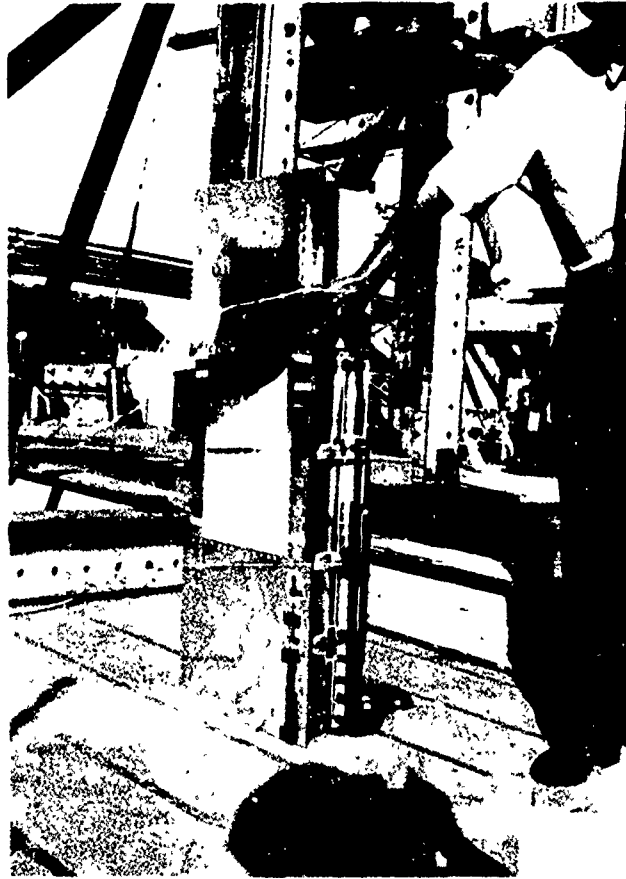


Figure 18. Model Specimen of Lower Fuselage Substructure.

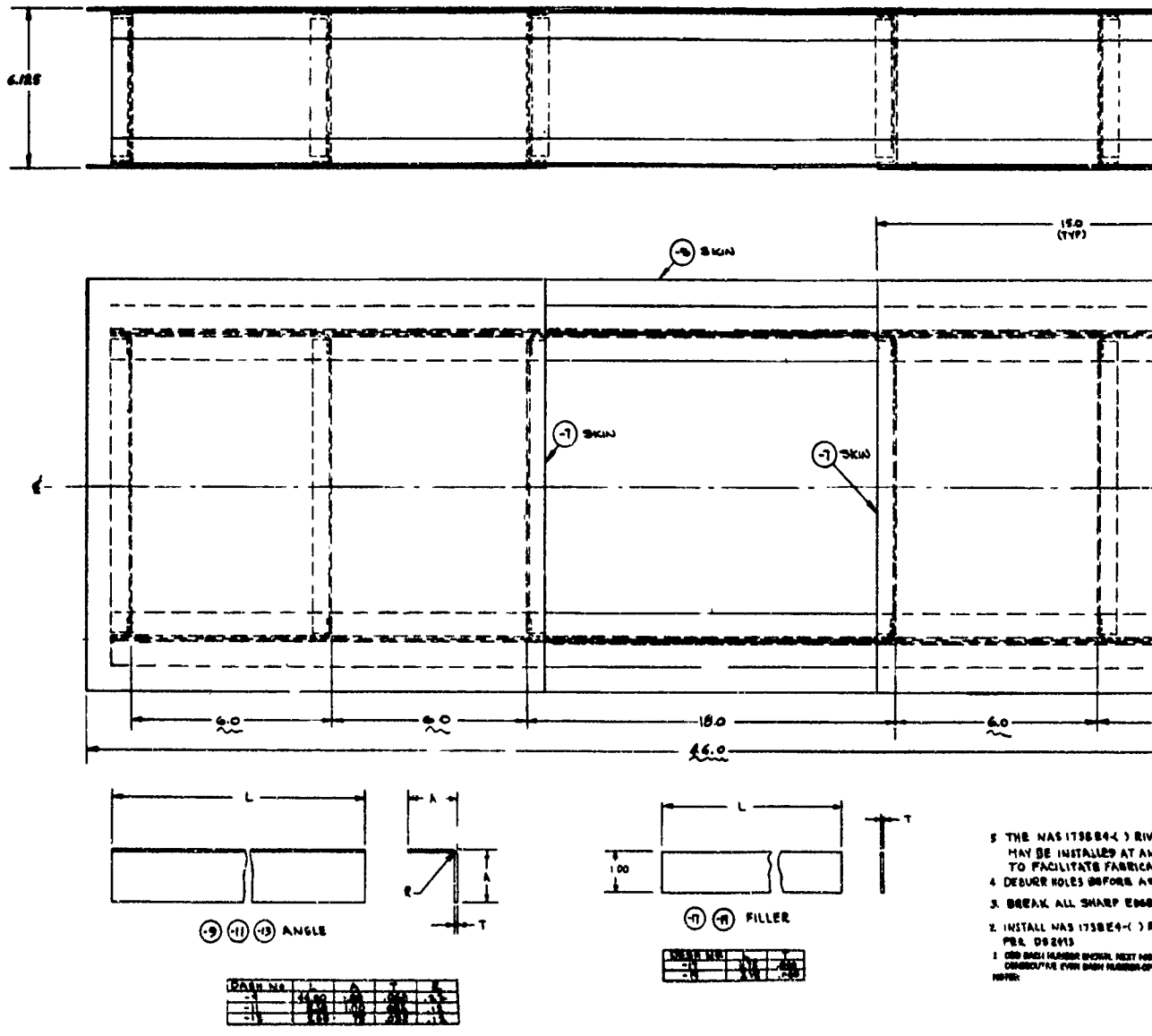
- For short panels, crippling is the dominant failure mechanism.
- For intermediate length, failure is a result of combined crippling and column behavior with possible torsional effects added.

On the other hand, the longitudinal beams (top and bottom skins) are subject to bending and possibly stretching if the ends are constrained. These beams and skins, with stiffened panels and bulkheads placed between them, are expected to give rise to very complicated interactive response.

In conjunction with the analysis described in this section, available methods were explored and evaluated. The applicability as well as complexities of these methods is discussed. In addition, simplified methods for the present study are proposed and applied to the model specimen structures.

Accurate large-deflection failure and post-failure analyses of a general stiffened panel require complex mathematical formulations including the incorporation of plasticity theory. The behavior of the flat plates within the initial.

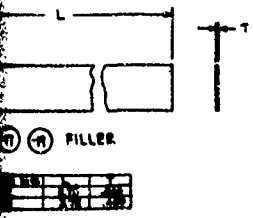
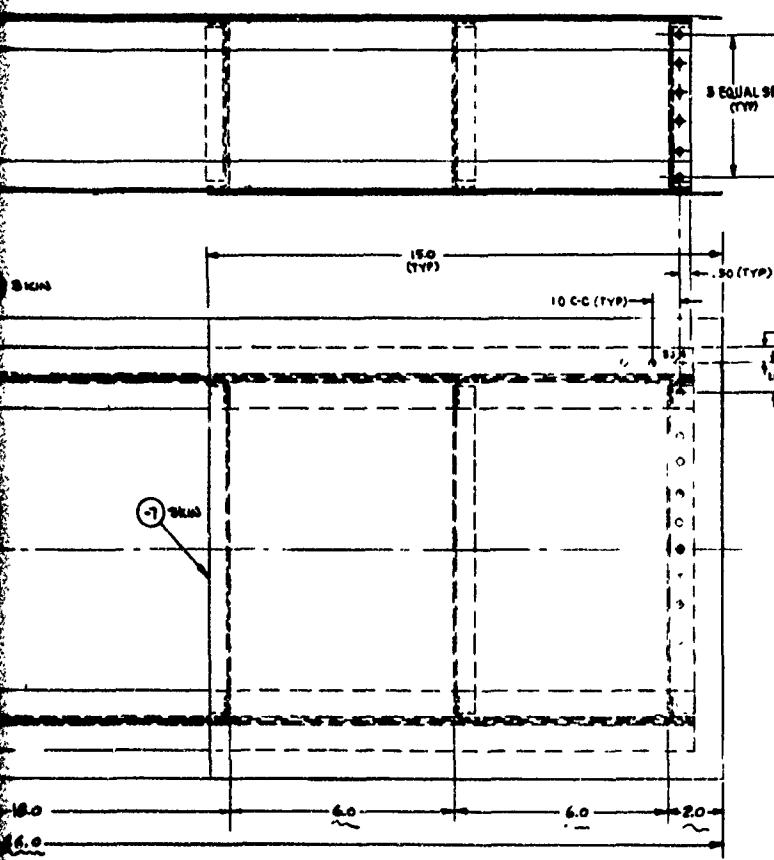
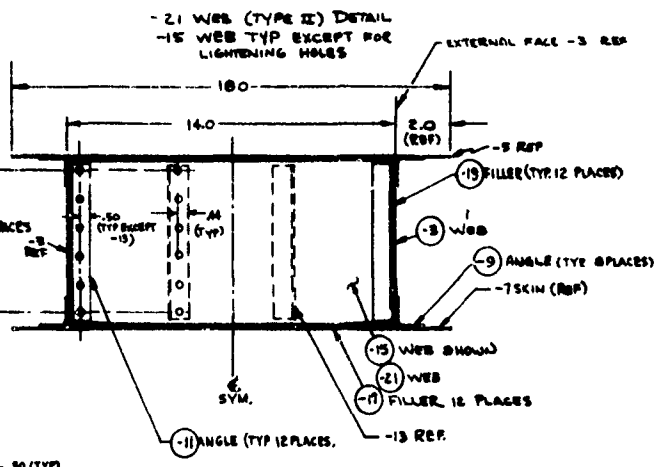
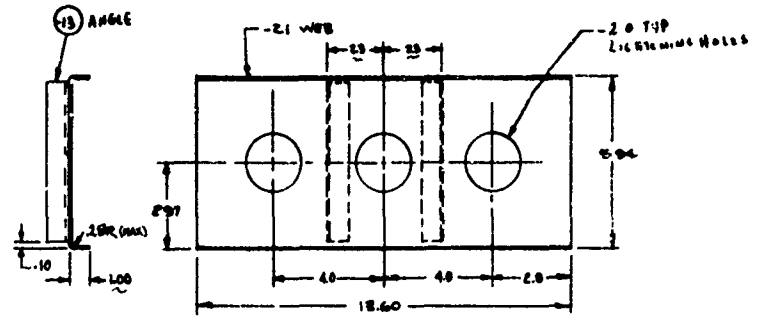
A



- 5 THE WAS 1738E4C) RIV MAY BE INSTALLED AT AN TO FACILITATE FABRICA
- 4 DEBUR HOLES BEFORE A4
- 3 BREAK ALL SHARP EDGES
- 2 INSTALL WAS 1738E4C) R P&A 082913
- 1 USE DASH NUMBER ON WORK NEXT FOR CORRECTION/EVEN DASH NUMBER ON NOTES

Figure 19. Drawing for Specimens 1 and 2.

B



5. THE HAS 175B4(-) RIVETS MAY BE INSTALLED AT ANY LOCATION TO FACILITATE FABRICATION.
4. DEBURR HOLES BEFORE APPLY.
3. BREAK ALL SHARP EDGES.
2. INSTALL HAS 175B4(-) RIVETS PER DB243.
1. USE BUSH PLUGS ON ALL NEXT INNER CONDUCTIVE CYCLE BUSH PLUGS OPPOSITE HOLES.

QTY	AV	AV	REMARKS	MS20500ADA OR	NAS175B4(-)											
			WEB	-21	CLAD	7071-76	2226 B 254									
	12	12	FILLER	-19		7071-76	460 X 10275									
	12	12	FILLER	-17		7071-76	460 X 10275									
		6	WEB	-15		7071-76	460 X 10275									
	12	12	ANGLE	-3		2026-72	412X 176 X 1/8									
	12	12	ANGLE	-11		2026-72	412X 176 X 1/8									
	8	8	ANGLE	-9		2026-72	460 X 10275									
	2	2	SKIN	-7		2026-72	412X 176 X 1/8									
	1	1	SKIN	-5		2026-72	412X 176 X 1/8									
	2	2	WEB	-3	CLAD	7071-76	412 X 5372 44									
			SKIN													
	-3	-1														

LIST OF MATERIALS OR PARTS LIST

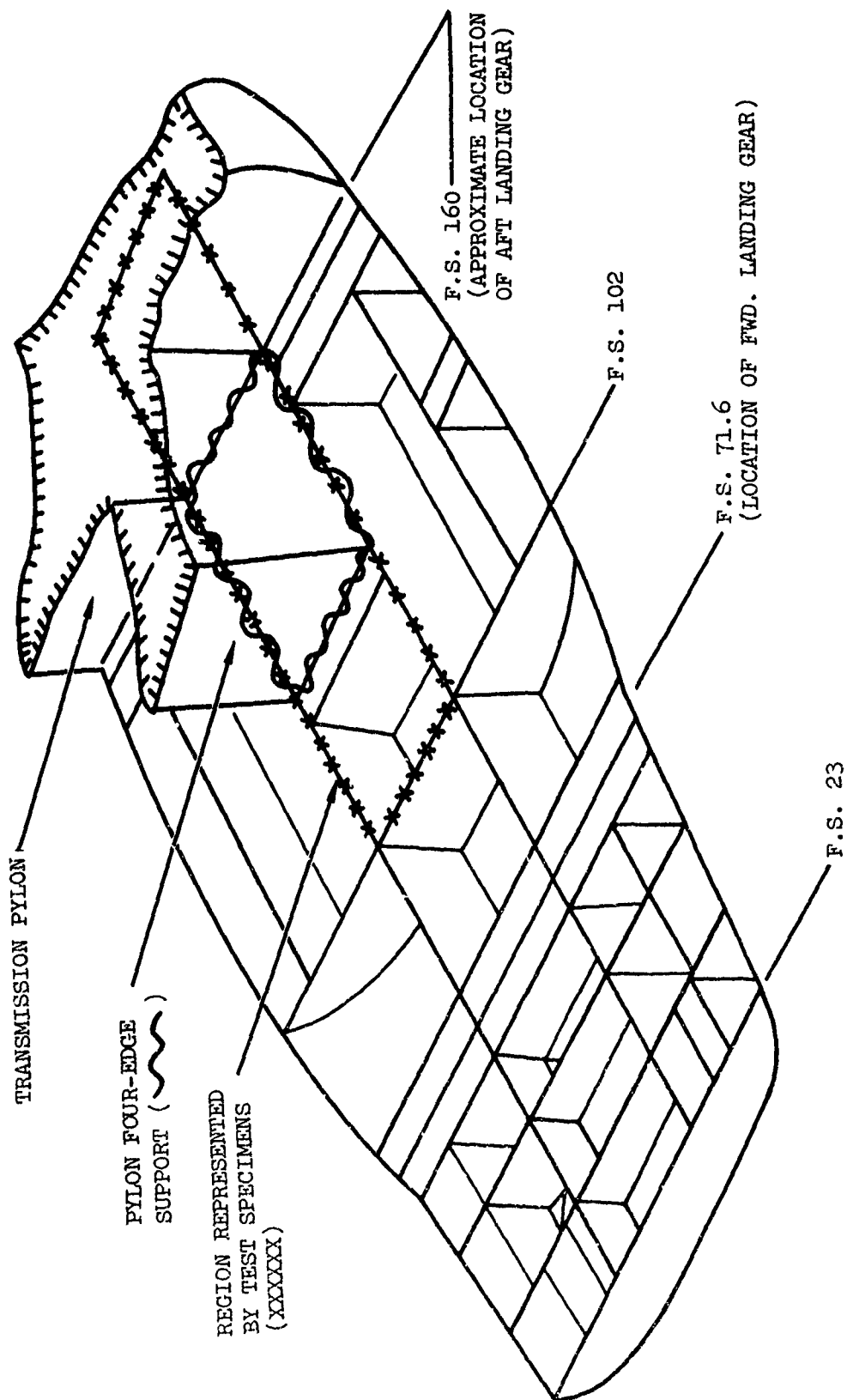


Figure 20. UH-1H Lower Fuselage Bulkhead and Stiffener Arrangement.

post-failure range is generally available. However, the methods of estimating maximum strength from the post-buckling analysis, References 87 through 90, are limited in that there appears to be a lack of adequate correlation between analytical procedures and experimental work. In addition, the influence of parameters such as material and fabrication-induced imperfections, boundary condition influence, and geometry changes has not been thoroughly examined. Compared to analysis and testing to determine failure points of structure designs, failure beyond the ultimate strength point appears to have received very little attention. Yet, it is this region, from the crashworthy design point of view, that is vital in terms of energy-absorbing capability and in determining whether this portion of substructure would maintain structural integrity throughout the crash sequence.

Except for the cases of simple geometry and boundary conditions, available methods generally require a fairly sophisticated level of computer coding. Unless the use of sophisticated programming leads to reasonably simple design charts, the effort would not meet the primary objective of the study, namely, designer-oriented tools. Therefore, the development of such computer programs, which not only account for the elastic stability behavior but also include plasticity phenomena for carrying out failure and post-failure analysis is potentially desirable. However, it will undoubtedly take some time before such techniques are verified as reliable. Therefore, it is important to develop simplified methods which fully utilize both empirical and analytical approaches for predicting large deflection behavior in an approximate sense. They would provide not only some insight as to how one can get load-deflection behavior for similar structures without going through costly test and computer runs, but also some perspective as to which way to pursue this relatively unexplored area.

The use of test data combined with analysis has resulted in the development of semiempirical approaches, particularly for structure subject to buckling. Buckling, post-buckling and compression strength of flat plates, composite elements and stiffened panels received great attention during the last four decades. Although substantial theoretical development has been achieved in recent years via the general stability theory as described in References 64 and 65, the literature does not indicate that there has been any additional extensive experimental investigation since the comprehensive undertaking by NACA, described in Reference 12, in the late 1950's.

Although the literature contains comprehensive information regarding buckling of plates (via design charts) obtained by the classical analysis, and an estimate of ultimate strength based on the empirical correlations with experimental test data, this data excludes the use of end-shortening characteristics and post-failure behavior. Furthermore, structural imperfections dealing with rivet strength and associated failure modes (rivet pitch, offset, rivet spacing) as well as geometrical imperfections were rarely considered in modern analytical approaches to nonlinear structural analysis.

References 87 and 89 describe the attempts that have been made to predict collapse loads by their analyses for flat plates under in-plane compression.

Recently, in Reference 90 it was suggested that by extending Koiter's theory (Reference 64) and combining the elastic-perfectly plastic theory, a method to estimate the collapse loads for the lateral buckling of a rectangular beam can be achieved. Although some of these approaches must prove to be feasible, the literature indicates that the current state of the art is such that no post-failure analysis of composite structures, made of stiffened panels and beams, exists for typical fuselage substructure.

Therefore, in the following sections the emphasis has been placed on using semiempirical/analytical methods to develop simplified procedures for predicting crashworthy (or post-failure) load-deflection characteristics of typical built-up structure used in fuselage design.

PROCEDURE

The general procedure for determining the total load-deflection characteristics, including failure and post-failure behavior, for the composite structure selected for the test program is described in the following sections. Included in the procedure is a step-by-step process with the following sequence:

- Prediction of failure loads for stiffened panels
- Post-failure analysis of stiffened panel
- Main beam and bottom skin analysis
- Total load-deflection curve

Prediction of Failure Loads for Stiffened Panels

The various failure modes of general stiffened (riveted) panels are shown in Figure 21 (Reference 12). Depending upon the rivet pitch, spacing, and strength, a given structure may fail either by interrivet failure, wrinkling failure, or monolithic behavior.

Using the semiempirical/analytical methods described in References 12, 76, and 83 for stiffened short panel elements, the failure loads are estimated. In addition, the analysis outlined is based on the following assumptions:

- At the threshold of failure loads, full plastic hinges are developed at constrained supports and mid cross section of the panels.
- The free warping energy of the flange of the stiffening angles is neglected.
- The effect of strain hardening is neglected.
- The influence of the axial force on the plastic hinge mechanisms of the stiffened panels is neglected.

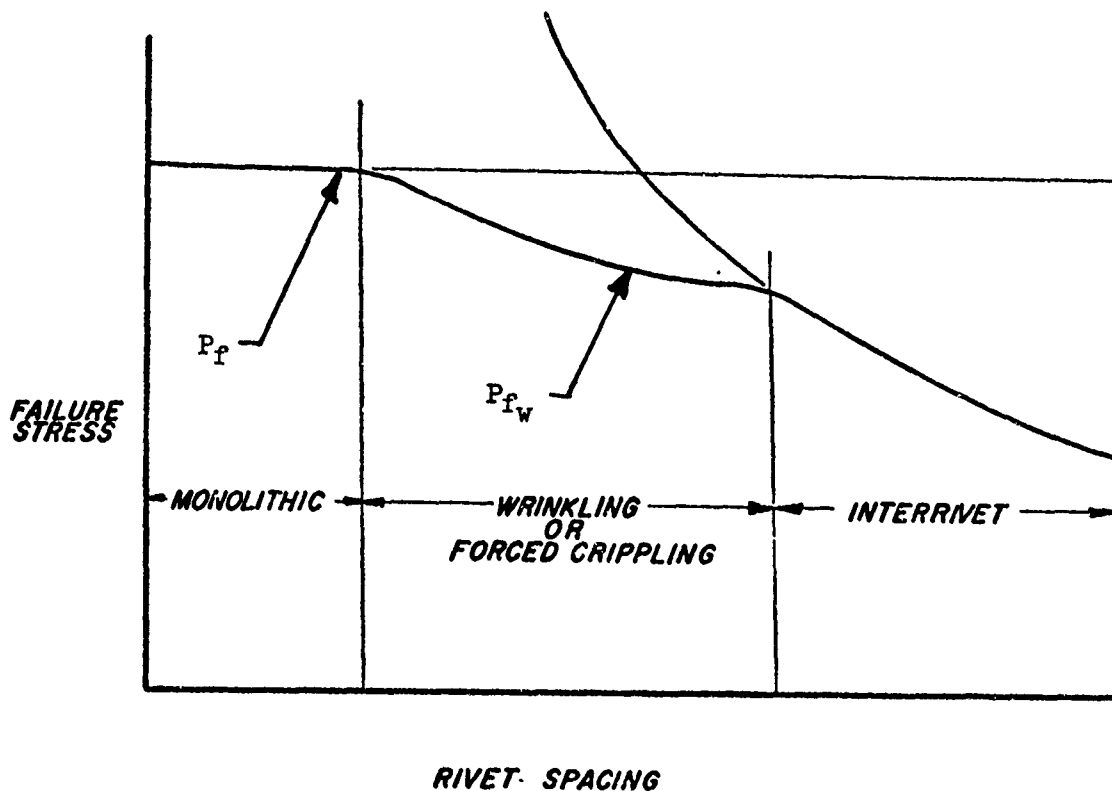


Figure 21. Various Failure Modes of Short Riveted Panels (Reference 12).

- The local failure pattern changes during the post-failure stages are neglected.
- The effect of geometrical imperfection sensitivity is neglected.

Since the present stiffeners are of one-corner angles, the suggested failure stress formula by Gerard in Reference 12 is:

$$\sigma_f = \beta_f \left[\frac{f \bar{t}_w t_s}{A} \left(\frac{\bar{\eta} E}{\bar{\sigma}_{cy}} \right)^{1/2} \right]^m \left[\bar{\sigma}_{cy} \right] \quad (1)$$

Correlating test data from Reference 92 and casting them into the Schuette's method (Reference 93), the constants β_f and m for equal angles are given in Reference 12 to be:

$$\beta_f = 0.665 \quad (2)$$

$$m = 0.85 \quad (3)$$

Wrinkling failure is expressed in Reference 94 as shown below in equation (4):

$$\sigma_w = \frac{K_w \cdot \pi^2 \cdot \eta \cdot \bar{\eta} \cdot E}{12 (1 - \nu^2)} \left(\frac{t_s}{b_s} \right)^2 \quad (4)$$

where $\bar{\eta}$ and η can be estimated, respectively, from References 93 and 94.

The empirical criterion for at least wrinkling failure rather than inter-rivet failure given in Reference 12 is shown to be

$$\frac{P}{b_s} < 1.27 K_w^{1/2} \quad (5)$$

Instead of using Equation (4), which requires K_w to determine σ_w , a simplified approximation is given in Reference 92 as

$$\bar{\sigma}_w = .48 \eta \bar{\eta} E \left(\frac{\bar{t}_w}{f} \right)^{4/3} \left(\frac{t_w}{b_w} \right)^{1/6} \left(\frac{t_s}{b_s} \right)^{1/2} \quad (6)$$

Another approach to determine the effects of rivet fastening on the failure stress based on the monolithic structural configuration is shown empirically in References 96 and 97. The empirical data is reproduced from Reference 12 in Figures 22 and 23.

When the sheet material is different from the stiffener material, the effective yield stress can be approximated as

$$\bar{\sigma}_{cy} = \frac{\sigma_{cy_s} + \sigma_{cy_w} (\bar{t}_w/t_s - 1)}{\bar{t}_w/t_s} \quad (7)$$

where

$$\bar{t}_w = \Sigma \frac{b_i t_i}{\Sigma b_i} \quad (8)$$

The method of determining the number of flanges to be used in Equation (1) is shown in Figure 24.

Equations (1) through (6) provide sufficient information for the present study to determine the failure stress for a given stiffened panel segment under inplane compressive loads.

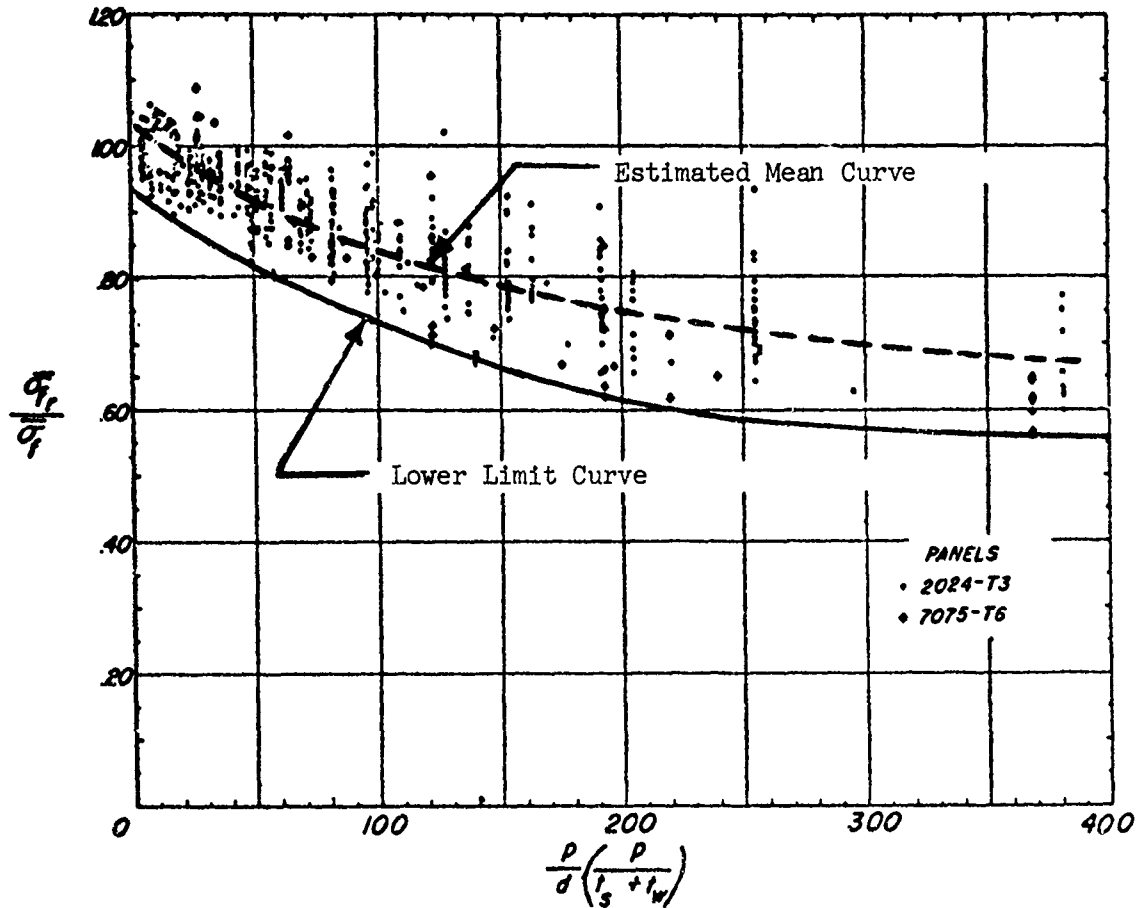


Figure 22. Effect of Rivet Tensile Strength, Pitch, and Diameter Upon Compressive Strength of Short, Riveted, Aluminum-Alloy Z-Panels, 2117-T4 Rivets (Reference 12).

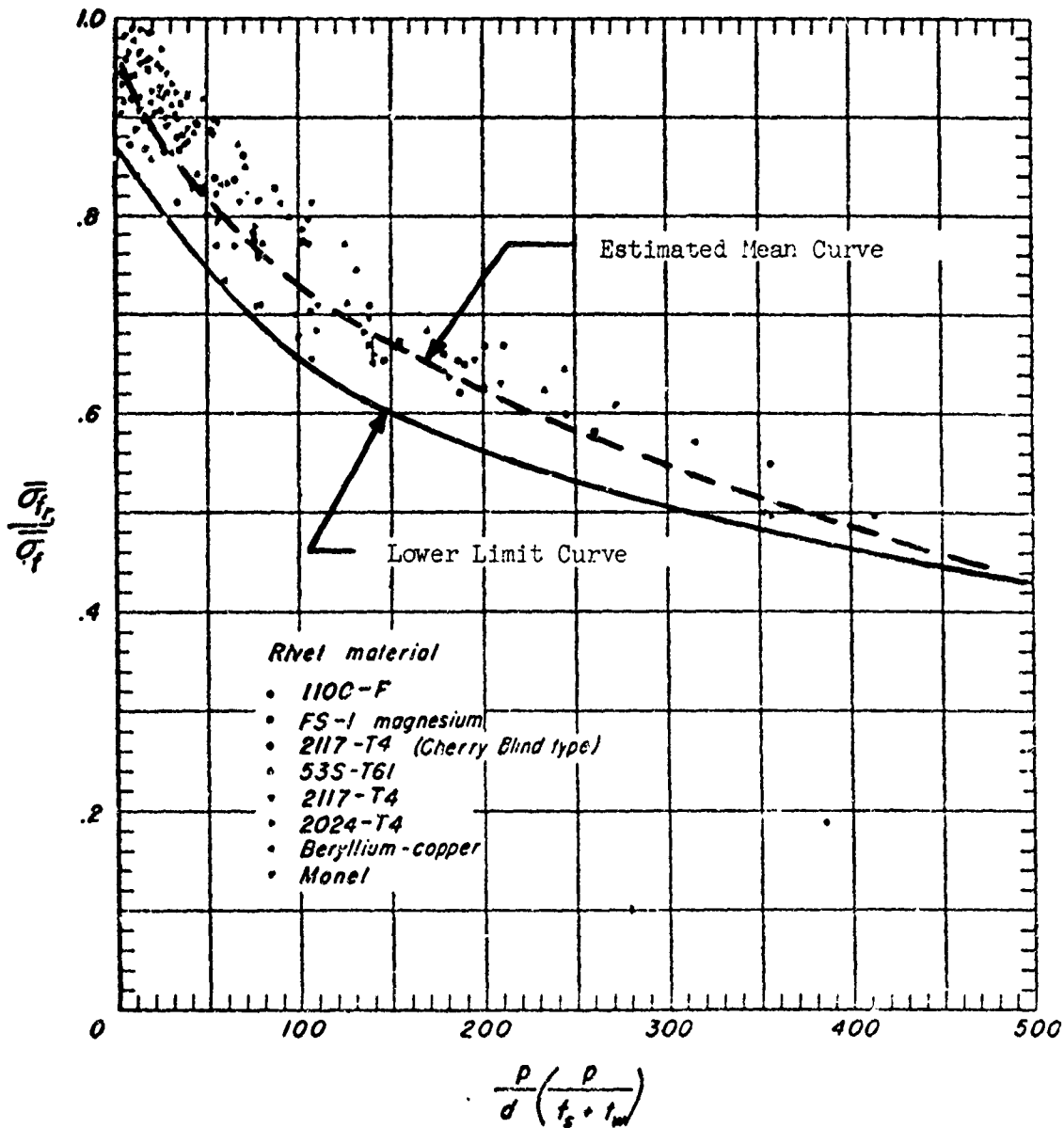
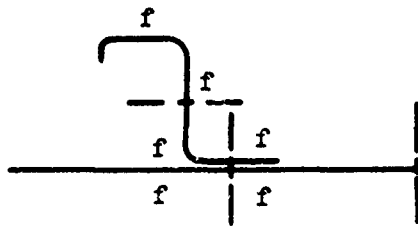
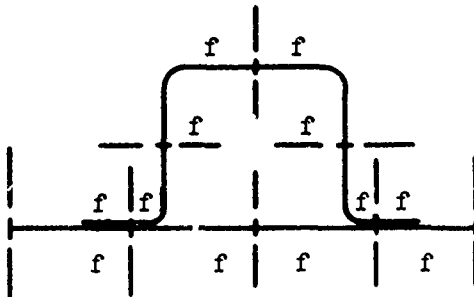


Figure 23. Effect of Rivet Tensile Strength, Pitch, and Diameter Upon Compressive Strength of Short, Riveted, Aluminum-Alloy Z-Panel, Various Rivet Materials (Reference 12).



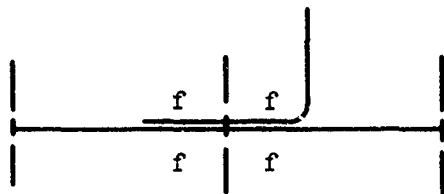
$f = 6 = \text{NUMBER OF FLANGES}$

(a) z STIFFENED PANEL



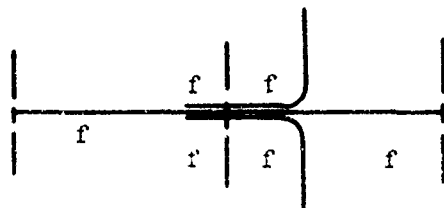
$f = 12$

(b) HAT STIFFENED PANEL



$f = 4$

(c) ONE-ANGLE STIFFENED PANEL



$f = 6$

(d) TWO-ANGLE STIFFENED PANEL

Figure 24. Method of Determining Number of Flanges.

In order to determine the corresponding failure load from the failure stress, the so-called "effective width concept" is introduced. Based on the work described in References 98 and 99, an extensive test made by C.I.T. during the early 1930's suggested the following formula which is obtained from Reference 83:

$$\frac{w_e}{b} = .25 \left(1 - \frac{\sigma_{cr}}{\sigma_f} \right) \left(\frac{\sigma_{cr}}{\sigma_f} \right)^n \quad (9)$$

where $n = 0.37 \left(\frac{\sigma_f}{\sigma_{cy}} \right)$ for the sheet effective width. (10)

The method of determining the effective width for various configurations is shown in Figure 25, adopted from Reference 83.

Once σ_{cr} from the classical buckling theory is determined as described in Reference 100, the effective area of the sheet can be calculated. Then the failure load can be obtained by

$$P_f = (\Sigma A_{se} + \Sigma A_w) \sigma_f \quad (11)$$

Post-Failure Analysis of Stiffened Panels

A representative schematic sketch of a typical segment of stiffened panels during the post-failure deformation is shown in Figure 26.

From the energy consideration,

$$\int P \cdot \delta u = 2 \left[\int M_{P_1} \cdot \delta \theta + \int M_{P_2} \cdot \delta \theta \right] \quad (12)$$

From the geometry,

$$\theta = \tan^{-1} Z \quad (13)$$

where

$$Z = \frac{\sqrt{2u - u^2/4}}{l - u/2} \quad (14)$$

$$\delta \theta = \frac{\partial \theta}{\partial Z} \cdot \frac{\partial Z}{\partial u} \cdot \delta u \quad (15)$$

Substituting Equation (15) into Equation (12) and applying the variational method, Equation (12) can be shown as

$$\int \left[P - 2M_P \cdot \frac{\partial \theta}{\partial Z} \cdot \frac{\partial Z}{\partial u} \right] \cdot \delta u = 0 \quad (16)$$

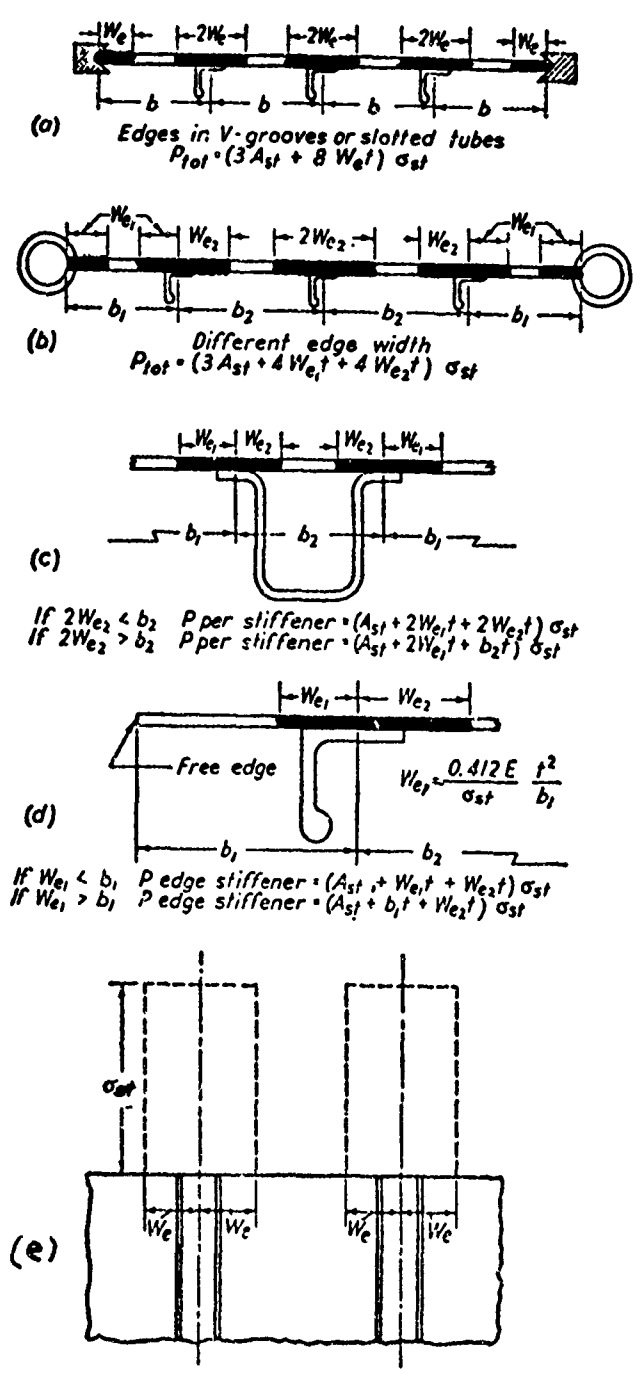
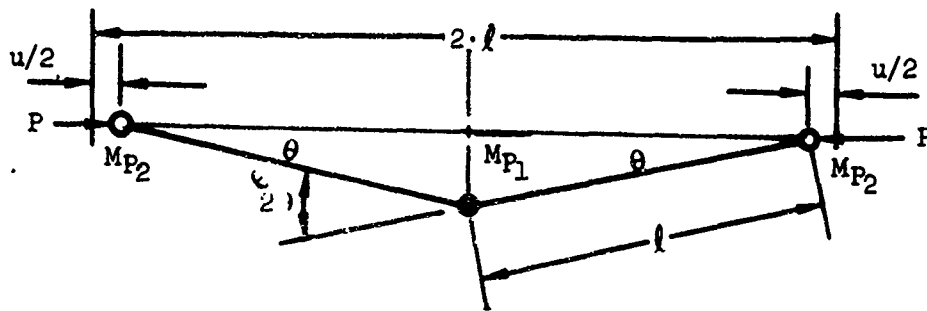
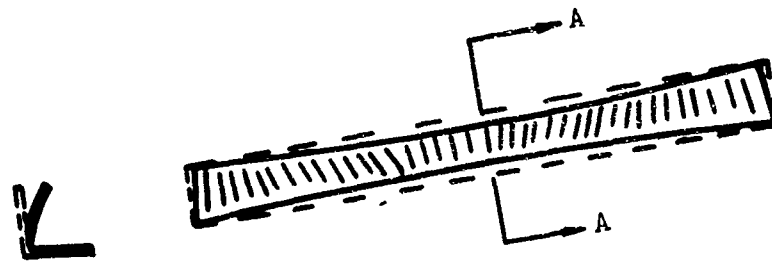


Figure 25. Method of Determining Effective Width.

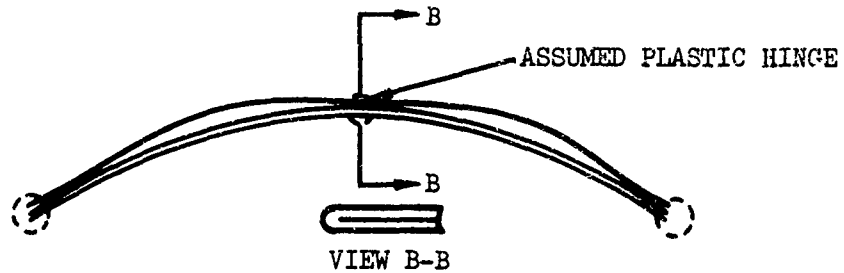


(a) HINGE MECHANISM OF POST-FAILURE PATTERN OF A STIFFENED PANEL.

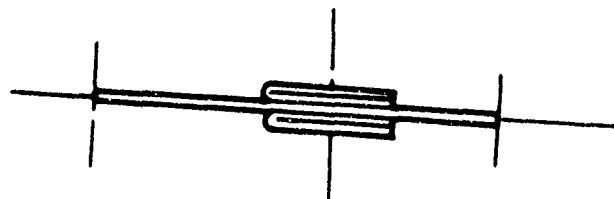


VIEW A-A

(b) INTERMEDIATE WARPING OF FLANGE DUE TO FORCED BENDING OF WEB.



(c) LIMITING CASE OF FLANGE FOLDING DUE TO FREE WARPING.



(d) LIMITED CONSERVATIVE CROSS SECTION FOR OBTAINING PLASTIC BENDING MOMENT.

Figure 26. Plastic Hinge Mechanisms and Effective Cross Section To Determine Plastic Moment.

From Equation (16), after some mathematical manipulation,

$$P = \frac{M_P}{\sqrt{lu - u^2/4}} \quad (17)$$

where

$$M_P = M_{P_1} + M_{P_2} \quad (18)$$

Calculation of Plastic Hinge Moment (M_p)

It has been shown in Reference 75 that, after buckling, the bending stress in the plate increases in proportion to $[\sigma_{cr} \cdot (\sigma - \sigma_{cr})]^{1/2}$, whereas the direct compressive stress decreases in proportion to $(\sigma - \sigma_{cr})$. The proportionality factor depends on the boundary conditions, aspect ratio of the plate, and buckled wavelength.

In particular, for an aspect ratio of $a/b = 1$, and with the plate under uniaxial compression and free to expand laterally, the bending stress can be shown as

$$\frac{\sigma_b}{\sigma_f} = \pm 2.36 \left[\frac{\sigma_{cr}}{\sigma_f} \left(1 - \frac{\sigma_{cr}}{\sigma_f} \right) \right]^{1/2} \quad (19)$$

Therefore if

$$\sigma_f / \sigma_{cr} = 6$$

then the bending stress at the outermost fiber of the sheet skin becomes

$$\sigma_b = \pm 0.88 \sigma_f \quad (19a)$$

and if

$$\frac{\sigma_f}{\sigma_{cy}} = 0.25$$

then

$$\sigma_b = \pm 0.22 \sigma_{cy} \quad (20)$$

Under this circumstance, assuming linear bending distribution across the cross section, the yielding will set in on the stiffener at the location approximately 2.3 times the sheet skin thickness from the neutral axis of the sheet skin.

Although it is premature to assume that at collapse loads the plastic hinges have formed as shown in Figure 26, from the foregoing assessment it can be argued that this assumption is not too unreasonable.

The effect of axial force on the plastic hinge mechanism can be obtained by applying the interaction mechanism described in Reference 101 and shown in Figure 27.

Then

$$\left| \frac{M}{M_P} \right| + \left(\frac{N}{N_P} \right)^2 = 1 \quad (21)$$

It can be shown that at the failure load

$$\frac{N}{N_P} = \frac{\sigma_f}{\sigma_{cy}} \quad (22)$$

Therefore, for the same σ_f/σ_{cy} value of 0.25,

$$\left| \frac{M}{M_P} \right| = 0.9375 \quad (23)$$

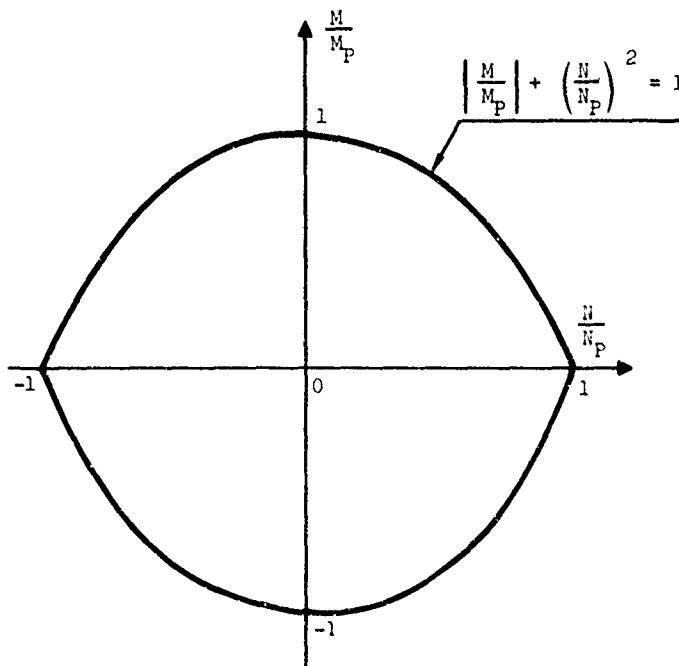


Figure 27. Approximate Yield Function for Combined Bending and Axial Force (Reference 101).

Equation (23) implies that the neglect of axial force would give about a 6-percent overestimate of the plastic moment at the highest direct compressive stress state.

As will be discussed below, the neglect of axial force and the assumption of full plastic hinge formation at the threshold of maximum load are critical when compared with how the M_p value is obtained due to the free warping flange portions of the stiffened panels.

An assessment of the effect of free flange warping instability is made qualitatively in Reference 102 using Vlasov's theory. It is concluded from the assessment that the effect of warping on the simplified plastic failure mechanism can be neglected without degrading the accuracy of the post-failure analysis.

Therefore, the conservative full plastic moment of the stiffened panel may be when the flange portion is assumed to have folded completely against the web, so the effective conservative cross section thickness of the stiffener would be twice the web thickness as shown in Figure 26. However, an accurate assessment of the upper bound plastic moment is difficult due to the complex behavior of the free warping flange during the post-failure stage.

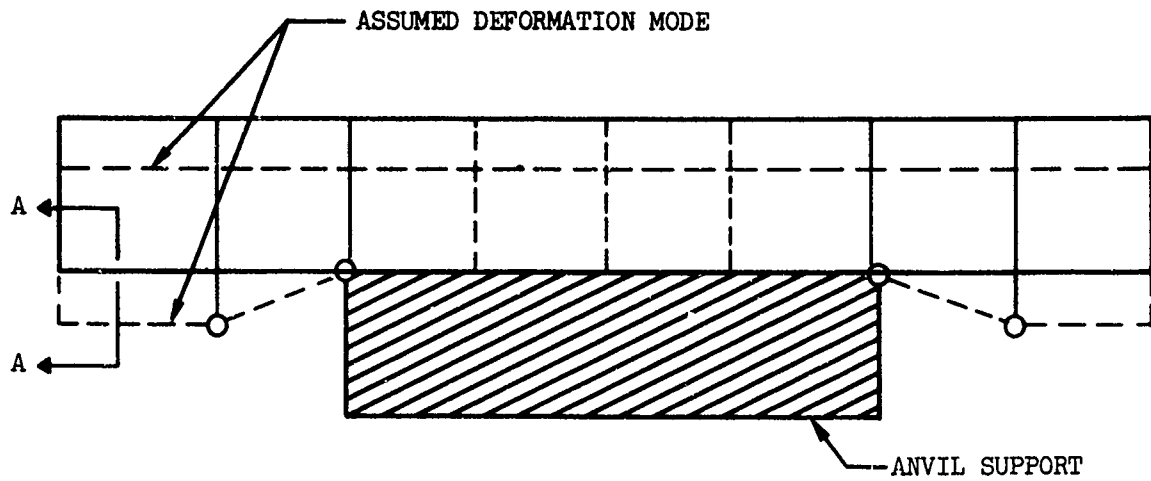
Main Beam and Bottom Skin Analysis

The subelement of bottom main beams and skin is shown in Figure 28(a). In order to simplify the subsequent analysis, the following assumptions are introduced:

- The subelement is modeled as a single beam with simple supports at bulkhead stations A, B, E, and F, respectively, as shown in Figure 28(b).
- In view of the solid support system between stations C and D, it is assumed that the bending rigidity for this portion of beam has an infinite value, i.e., $I_1/I_2 = 0$.
- Although top beams at station A and F are expected to undergo a certain bending, and some shear flow for the corresponding side stiffeners, it is assumed that this bending is not too influential. Therefore, the surface of the top skin and beams throughout the entire deformation is assumed flat.

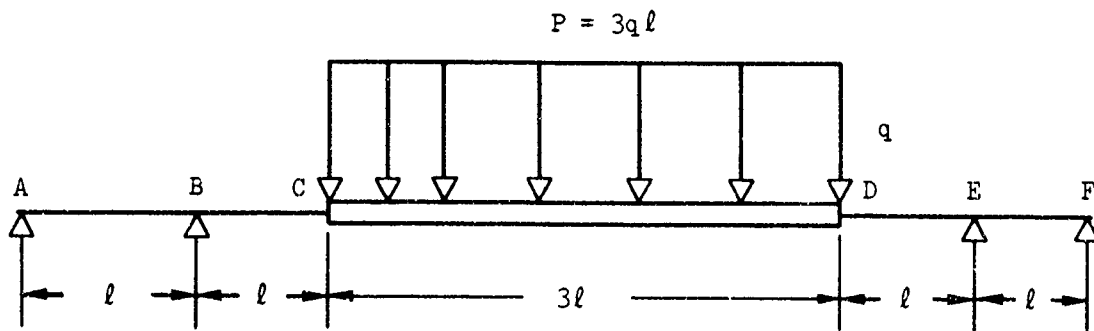
If the above assumptions are introduced, the beam deflection of Figure 28(b) at C and D will be the same as the shortening distance of the panels between stations C and D.

Following the procedures described in References 103 and 104, it is found that the plastic hinge forms at stations C and D simultaneously, and the corresponding applied force and deflection are



SIMPLIFIED VIEW A-A

(a) SIMPLIFIED DEFORMATION MODE



(b) IDEALIZED BEAM MODEL

Figure 28. Lumped Model of Bottom Skin and Main Beams.

$$P_1 = \frac{16 M_p}{5l} \quad (24)$$

$$\delta_1 = \frac{13}{30E I_1} \cdot M_p \cdot l^2 \quad (25)$$

As load is further increased the bending moments at B and E reach the plastic moment and the corresponding force and deflection are

$$P_{\max} = \frac{4 \cdot M_p}{l} \quad (26)$$

$$\delta_2 = \frac{M_p \cdot l^2}{2EI_1} \quad (27)$$

Beyond this stage, the load does not increase, and the deflection increases until the hinge rotation reaches complete failure at the location.

The foregoing analysis has some theoretical drawbacks when the displacement becomes large, due to the introduction of the simply supported assumption.

For example, when the crushing distance becomes about 3.0 in., assuming that the axial strain is uniformly spread throughout the beam, the average axial strain is about 0.03 in./in. This is certainly more than failure strain. However, if roller guide supports rather than simple supports are remodeled for the main beam, then the axial influence can be eliminated. The assumption would compensate for bending of the cantilevered portion of the specimen. This arbitrary drawback seems to be contradictory in a strict theoretical sense; however, the approximate load-deflection curve obtained by this assumption is believed to represent the dominating deformation mode.

Total Load Deflection

In the present model substructure, the stiffened panels are assembled to form rectangular cross sections. At each edge, at least one or more stiffeners join the panels by rivets, together with sheet skins.

In order to obtain a load deflection curve of this typical cellular cross section, two factors must be considered:

- The effect of the jointed edge constraint on the initial local buckling of the composite cellular cross sections.
- The effect of the constraint of the joining stiffening members at the corners during the failure and post-failure stages.

Neglect of the first effect can be alleviated by the fact that the so-called "four moment equations", for buckling of rectangular tube sections, would render no more reliable results than the separate buckling estimate of the individual panels when the tube itself has stiffening members as in the present case.

The effect of corner constraint on the failure load presents greater complications, and this will require indeed a fairly involved analysis. If a conservative failure load is emphasized, it is assumed that the connecting corner stiffener belongs either to the side stiffener or the bulkhead; and neglecting the interaction between two neighboring stiffened panels, the approximate failure load can be estimated from the individual failure load of stiffened panels.

Another complication arises for the nonuniformly compressed portion of the side skin between stations B and C, and D and E. These plates may be approximated as subjected to a linearly varying edge compressive load as described in Reference 88.

While the involved analysis to determine the failure load for this portion is desirable, in view of the effective width and average maximum stress concept shown in Figure 25 plus the assumption that the bulkhead stationed at B and E would remain within the elastic range, another approximation is introduced which assumes that only one-half of the skin width participates in failure load and post-failure deformation. It is noted, however, that no quantitative assessment was sought to evaluate this approximation. Nevertheless, preliminary analysis vs. experimental observation tends to justify this approximation.

Column Effect on the Failure Strength of Stiffened Panels

In the preceding section, the crushing stress (or failure stress) formulas are based on the value of $L'/\rho = 20$. For a sufficiently larger value of L'/ρ the panels behave as columns, and the ultimate stress may be calculated by the well-known Euler's formula

$$\sigma_e = \pi^2 E / (L'/\rho)^2 \quad (28)$$

However, for the transition range as shown in Figure 29, the parabolic approximation based on the value of σ_f at $L'/\rho = 20$ can be obtained from the following equation derived and presented in Reference 12.

$$\frac{\sigma_{co}}{\sigma_f} = 1 - \left(1 - \frac{\sigma_{cr}}{\sigma_f}\right) \frac{\sigma_{cr}}{\sigma_e} \left(\frac{\sigma_{20}^{1/2} - \sigma_e^{1/2}}{\sigma_{20}^{1/2} - \sigma_{cr}^{1/2}} \right)^2 \quad (29)$$

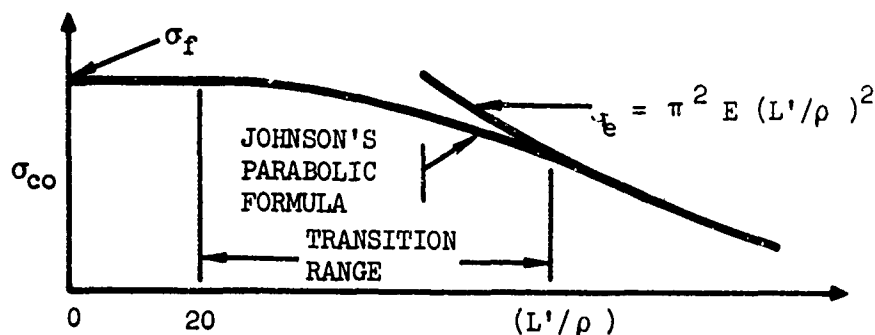


Figure 29. Critical Stress Versus L'/ρ Ratio.

For aluminum material, the stress at $L'/\rho = 20$ is

$$\sigma_{20} = \pi^2 E / (20)^2 = 246,740 \text{ lb/in.}^2 \quad (30)$$

To determine (L'/ρ) , first σ_{co} must be obtained from Equation (29). In calculating σ_e , first ρ and L' must be determined. These values are obtained following procedures similar to those described in Reference 83.

Figure 30 shows the scatter values of end fixity obtained from testing flat-ended panels. It is observed in Reference 83, from the test data, that about 75 percent of the test points lie within ± 5 percent of the curve for $C = 3.0$. Therefore, it is suggested that a value of $C = 3.0$ be used as a good average value of the panel end fixity. The same value will be adopted in this study since there is limited data available. Using $C = 3.0$, the following expression for L' is obtained:

$$L' = L / \sqrt{C} = .57735L \quad (31)$$

In order to determine ρ , the necessary steps are:

- 1) Calculate b_e as shown in Figure 31 based on the failure stress σ_f .
- 2) Calculate ρ_w for stiffeners alone.
- 3) Calculate the distance, S , from the mid cross section of the skin to neutral axis of the stiffener as shown in Figure 31.
- 4) Use Figure 32 or obtain from Equation (32):

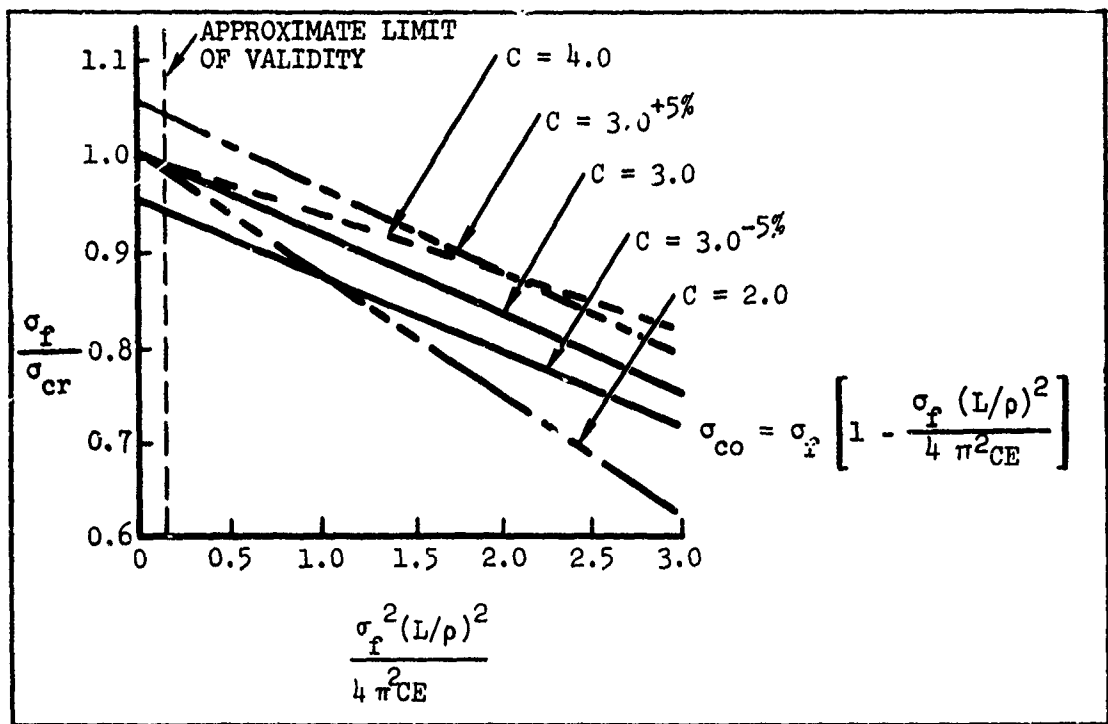


Figure 30. Failure Stress Versus Slenderness Ratio of Stiffened Panels.

$$\left(\frac{\rho}{\rho_w}\right)^2 = \frac{1 + \left[1 + \left(\frac{S}{\rho_w}\right)\right]^2 \frac{b_e t_s}{A_w}}{\left(1 + \frac{b_e t_s}{A_w}\right)^2} \quad (32)$$

This completes all the necessary information to obtain a new σ_{co} . The next steps to obtain the ultimate load are:

- Calculate new w_e/b_s based on a new σ_{co} (see Equation 9 and Figure 25).
- Calculate ΣA_{se} based on the new value of b_e .

Then the ultimate load is calculated as previously by Equation (11).

$$P_f = \sigma_{co} (\Sigma A_{se} + \Sigma A_w) \quad (33)$$

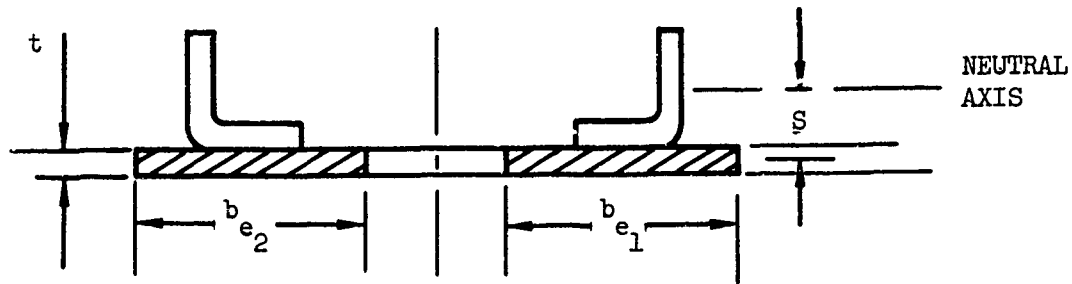


Figure 31. Effective Skin Width.

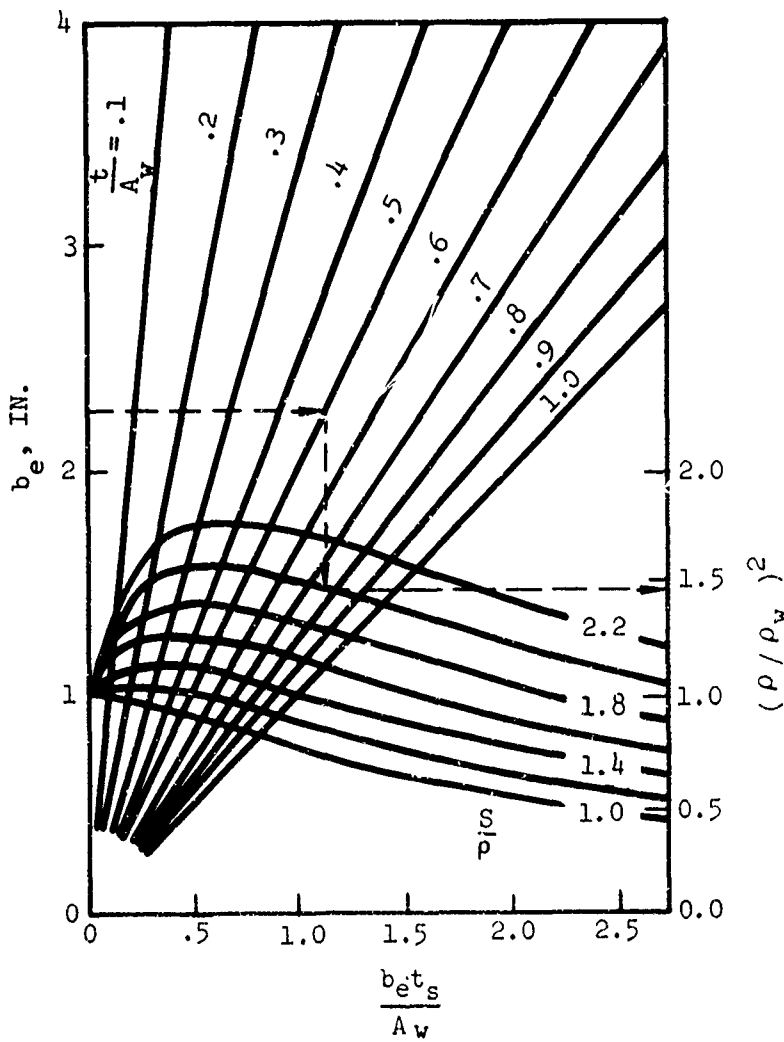


Figure 32. Chart for Determining $(\rho/\rho_w)^2$.

General Application of the Procedure

The procedure presented in the previous sections to determine the failure stress for the angle-type stiffened panel is also applicable to a variety of other types of panels, if the parameters such as β , n and m (in Equation 34) are adjusted to the experimentally evaluated data.

In general, according to the data in Reference 12, the failure strength can be generalized by the following form

$$\frac{\sigma_f}{\sigma_{cy}} = \beta_g \left[\frac{g \cdot t_w \cdot t_s}{A} \left(\frac{E}{\sigma_{cy}} \right)^n \right]^m \quad (34)$$

where

g = the number of flanges + the number of cuts

$$\beta_g = \beta_c \left(\frac{c}{g} \right)^m \quad \text{for multi-corner elements} \quad (35)$$

$$\beta_g = \beta_f \left(\frac{f}{g} \right)^m \quad \text{for one-corner elements} \quad (36)$$

$$\beta_g = \beta \left(\frac{1}{g} \right)^m \quad \text{for two-corner elements or plates} \quad (37)$$

In Figure 33, representative types of stiffeners with from one to six corners are shown. In Figure 34 and Table XVI, values of β_g , g , n and m , obtained from Reference 12, for different configurations^g are listed. A detailed illustrative sample problem using the analytical procedure is presented in the Design Procedure section. The following subsection presents analytically predicted subelement and total load-deflection curves and discusses the manner in which the curves are obtained.

Predicted Subelement and Total Load-Deflection Curves

Following the procedure outlined in the preceding portion of the Substructure Analysis section, the failure load for the stiffened panels (and stiffener and bulkhead) are determined. Next, the post-failure load-deflection curve shape is obtained for each of the stiffened panels. The failure deflection is then derived from the intersection of the ultimate failure load (failure analysis) and a coinciding load from the post-failure analysis. The assumptions regarding the plastic hinge formation at the threshold of failure implies that the yield strain (ϵ_y) has been reached which can be considered as the upper bound strain at the failure load. Thus, the derivation of the deflection from the failure point, although approximate, is in effect based on the upperbound value of the yield strain. The

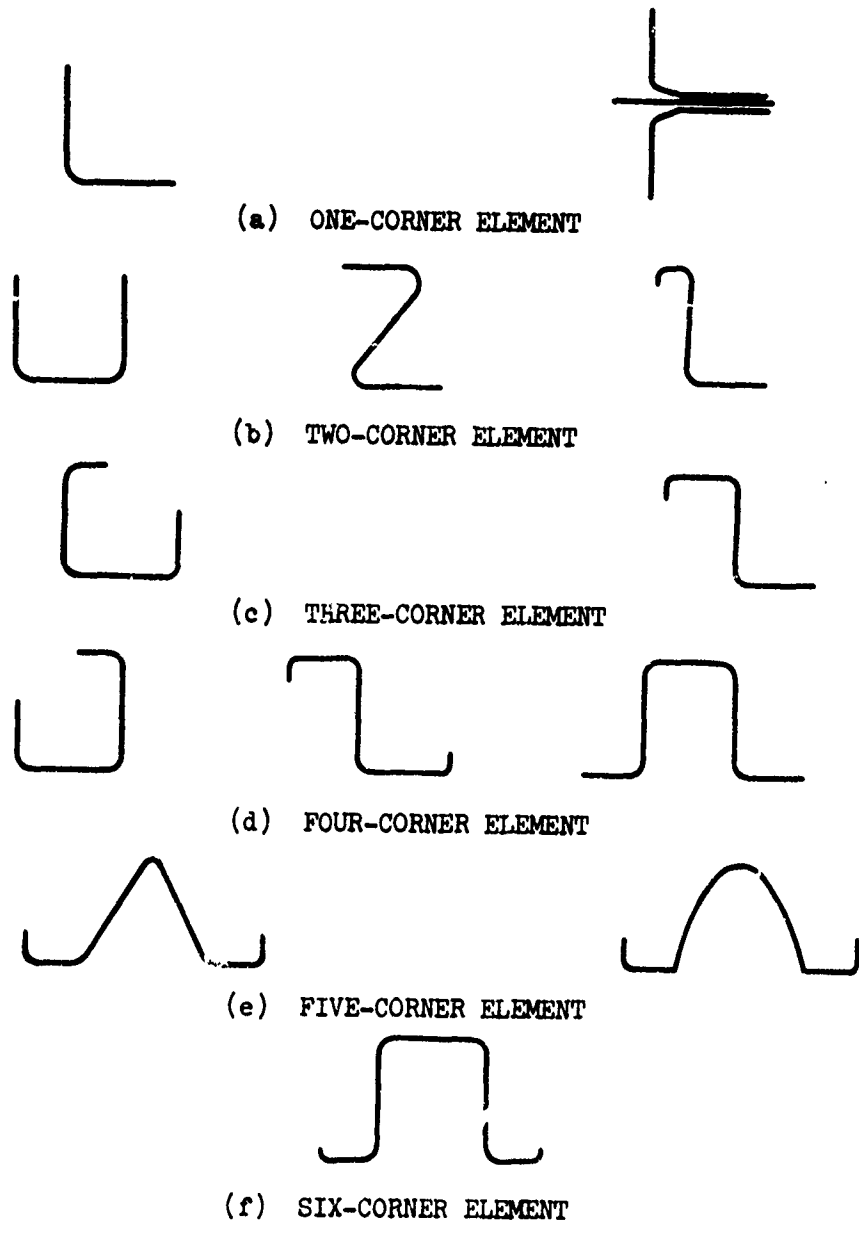
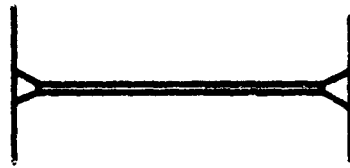


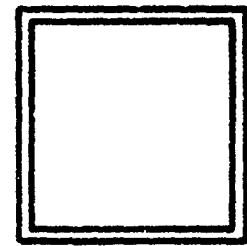
Figure 33. Stiffeners With Various Corners.



ANGLE

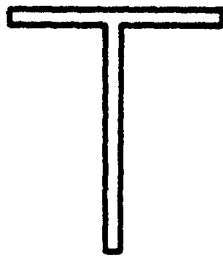


PLATE

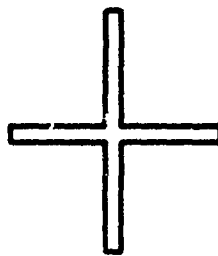


TUBE

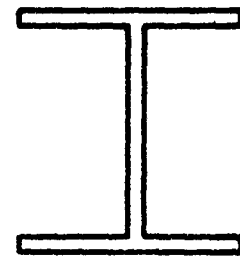
(a) EXTRUDED ANGLE TYPE



T-SECTION

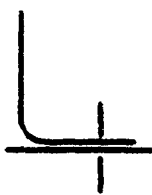


CRUCIFORM

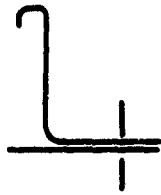


H-SECTION

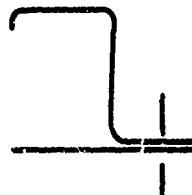
(b) EXTRUDED T-TYPE



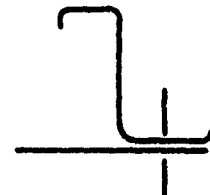
ONE-CORNER
ELEMENT



TWO-CORNER
ELEMENT

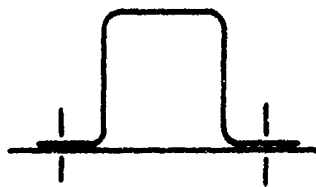


THREE-CORNER
ELEMENT

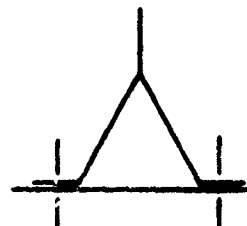


FOUR-CORNER
ELEMENT

(c) FORMED ANGLE STIFFENERS



(d) FORMED HAT STIFFENED PANEL



(e) FORMED Y STIFFENED PANEL

Figure 34. Various Stiffener Configurations.

Table XVI. VALUES OF n , m , g , β_g AS FUNCTION OF STIFFENED PANEL CONFIGURATION (REFERENCE 12)

	Value of			
	n	m	g	β_g
Extruded Angle Type				
Angle	.5	.85	2	.558
Plate	.5	.85	3	.558
Tube	.5	.85	12	.558
Extruded T Type				
T-Section	.5	.4	3	.67
Cruciform	.5	.4	4	.67
H-Section	.5	.4	7	.67
Formal Angle-Stiffened Panel				
Single Angle	.5	.85	5	.55
Double Angle	.5	.85	7	.583
Formed Two-Corner Stiffened Panels	.333	.75	5	.917
Formed Three-Corner Stiffened Panels	.5	.35	8	.558
Formed Multi-Corner Stiffened Panels	.5	.85	11	.55
Formed Hat Section	.5	.85	17	*
Extruded Y Stiffened Panels	.5	.85	19	**

*	t_w/t_s	1.25	1.0	.63	.39
	β_g	.591	.561	.499	.483

**	t_w/t_s	1.16	.732	.464
	β_g	.562	.505	.478

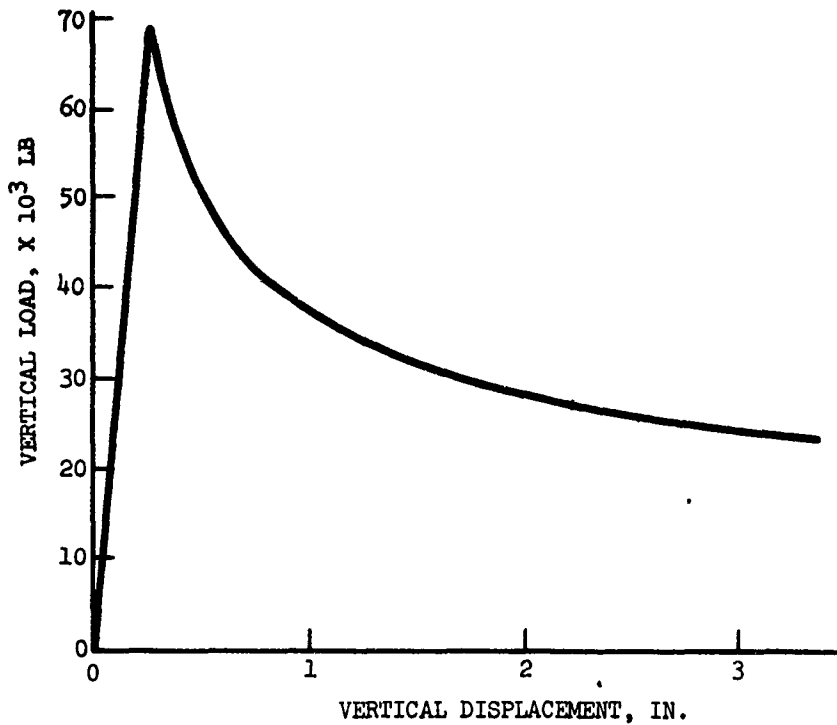


Figure 41. Predicted Total Load-Deflection Curve for Specimens 5 and 6.

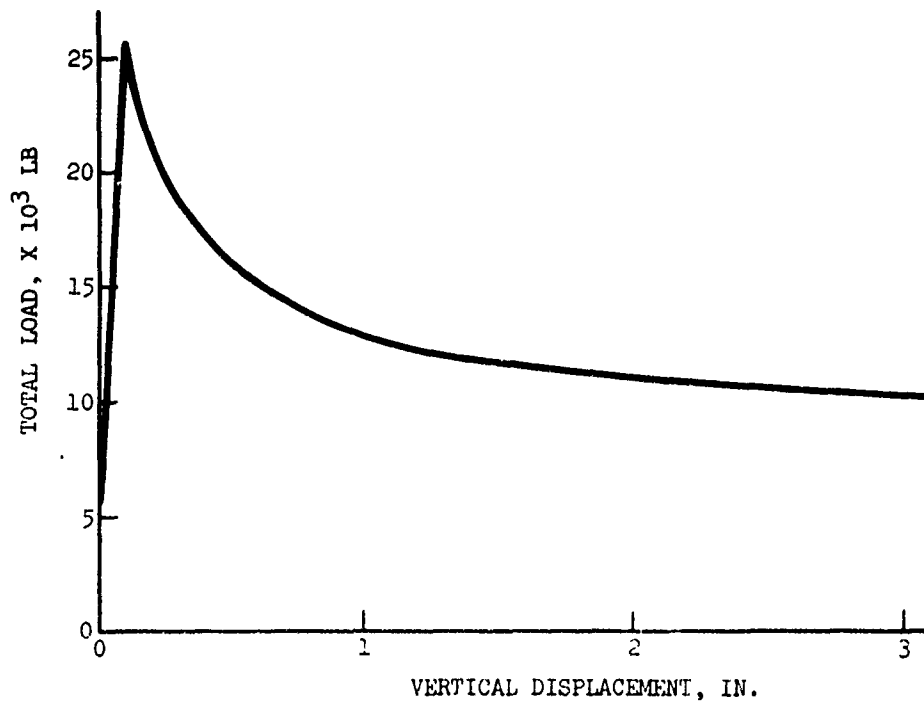


Figure 42. Predicted Total Load-Deflection Curve for Specimens 2, 3 and 4.

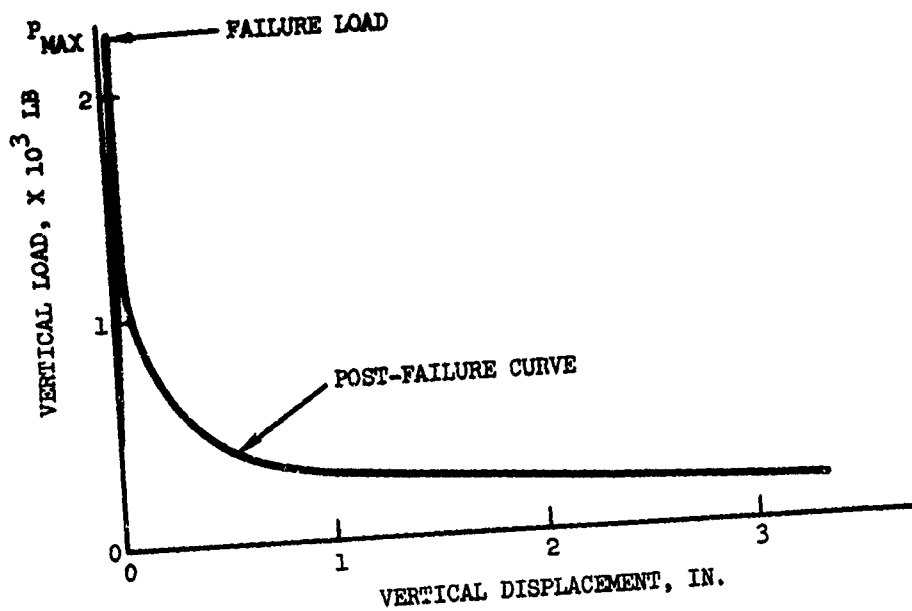


Figure 35. Bulkhead Load-Deflection Curve for Specimens 1 through 6.

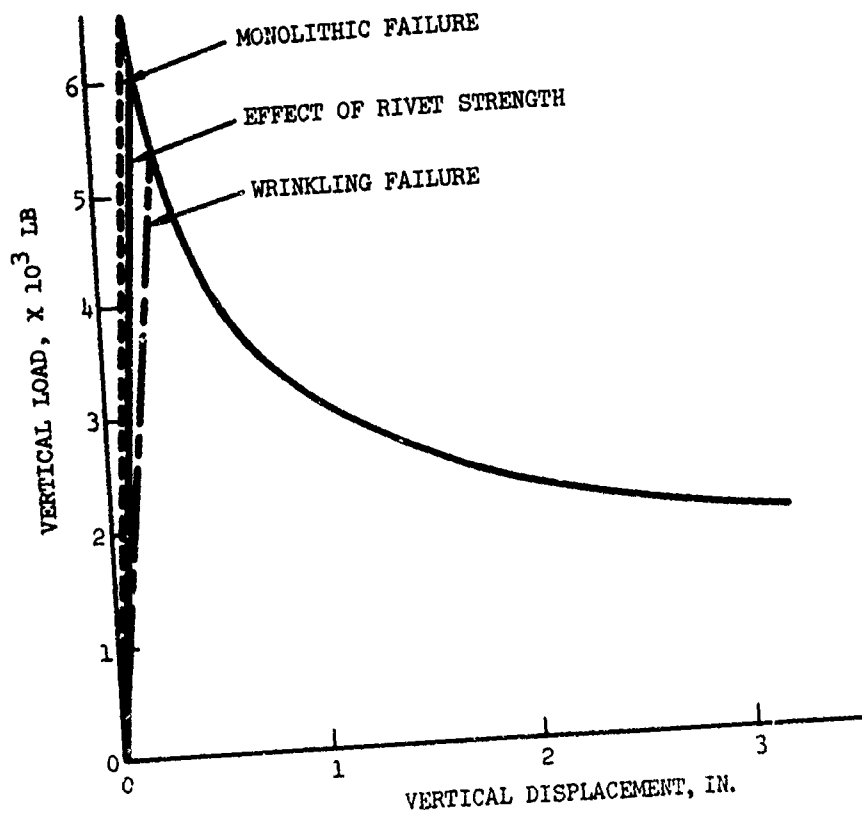


Figure 36. Side Skin Load-Deflection Curves for Specimen 1.

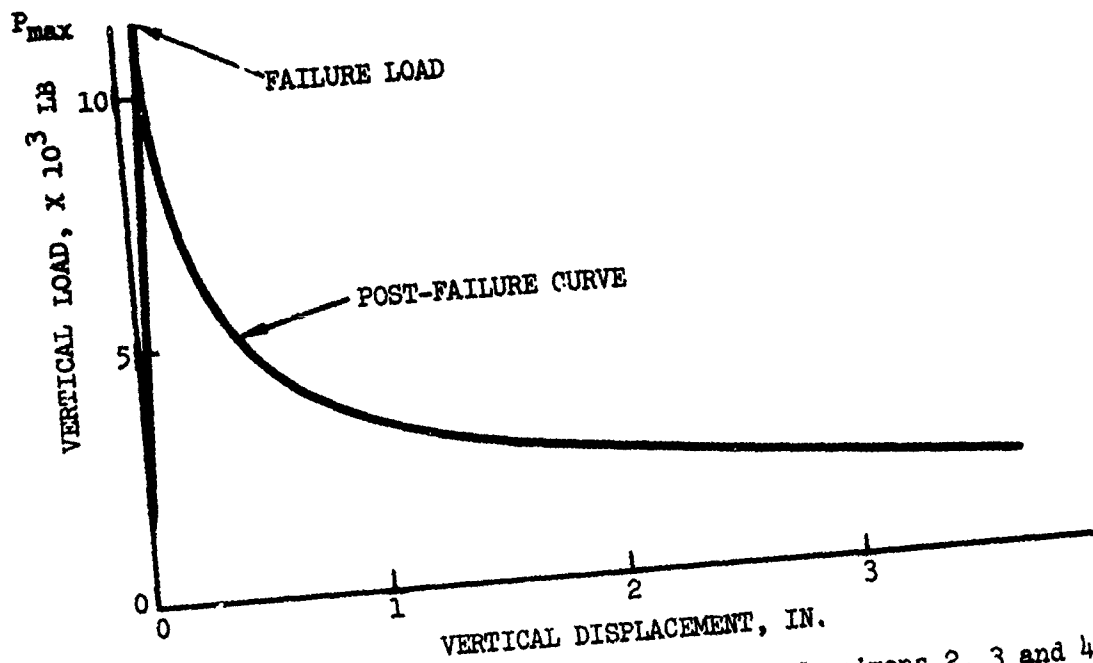


Figure 37. Side Skin Load-Deflection Curve for Specimens 2, 3 and 4.

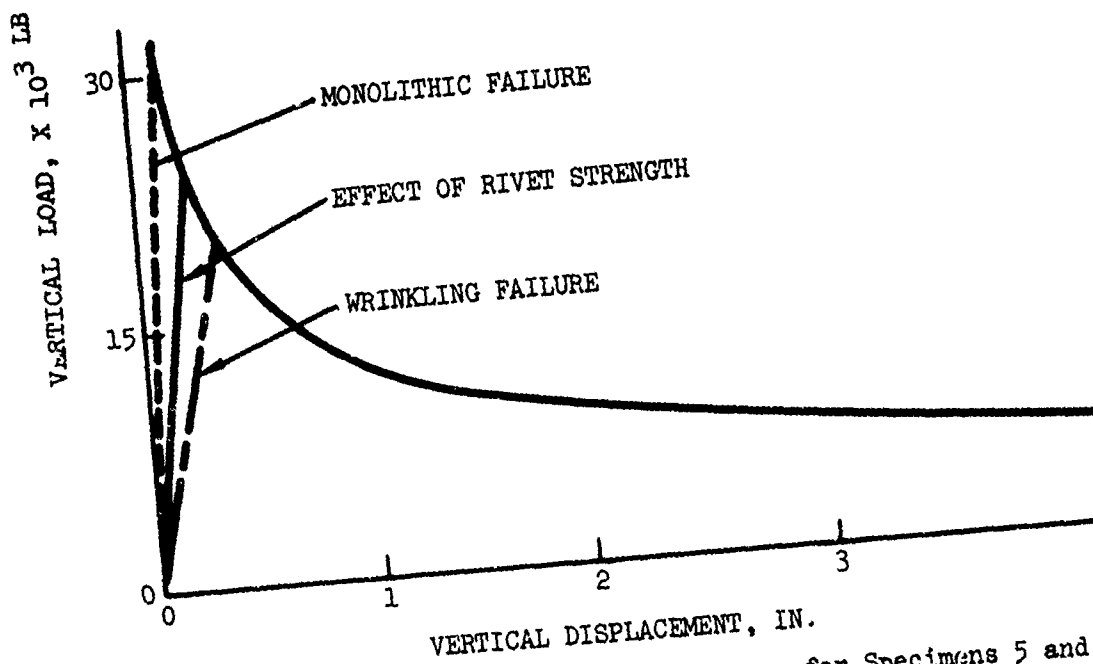


Figure 38. Side Skin Load-Deflection Curve for Specimens 5 and 6.

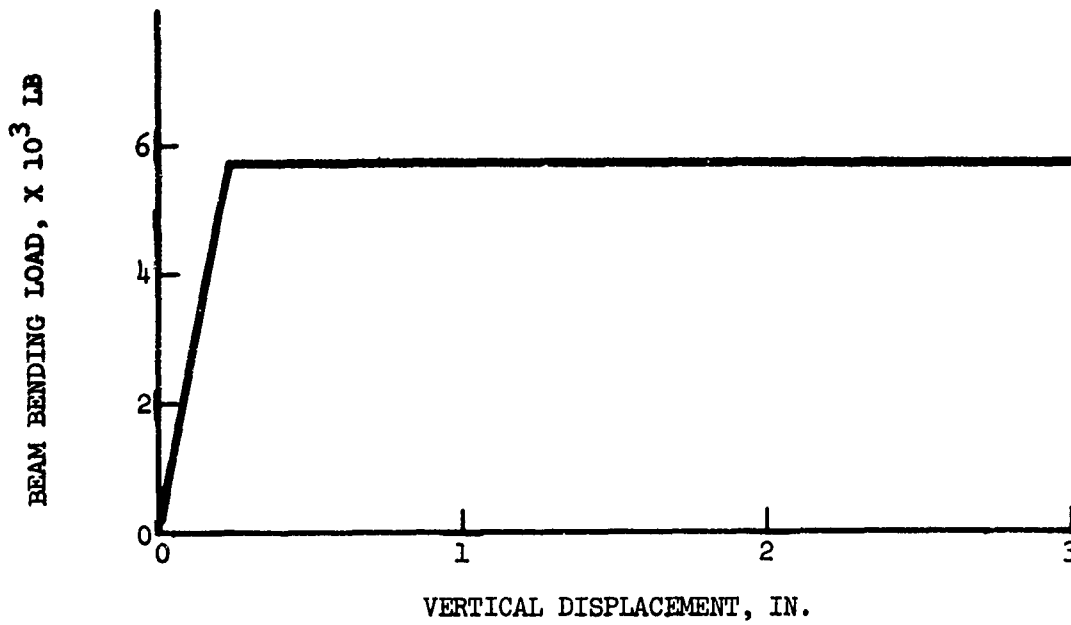


Figure 39. Main Beam and Bottom Skin Load-Deflection Curve for Specimens 1 and 6.

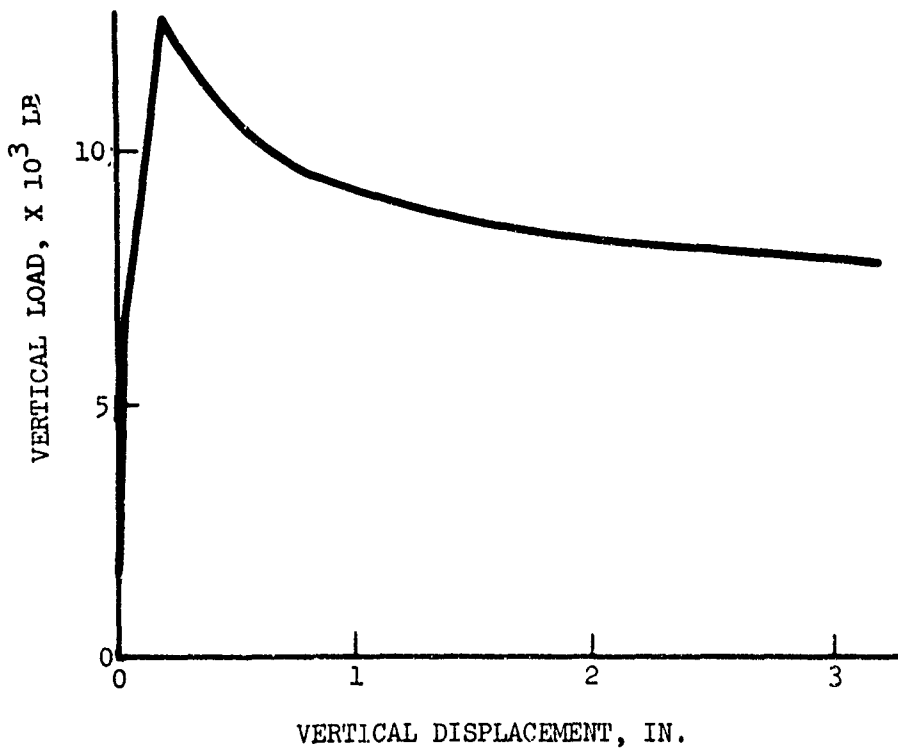


Figure 40. Predicted Total Load-Deflection Curve for Specimen 1.

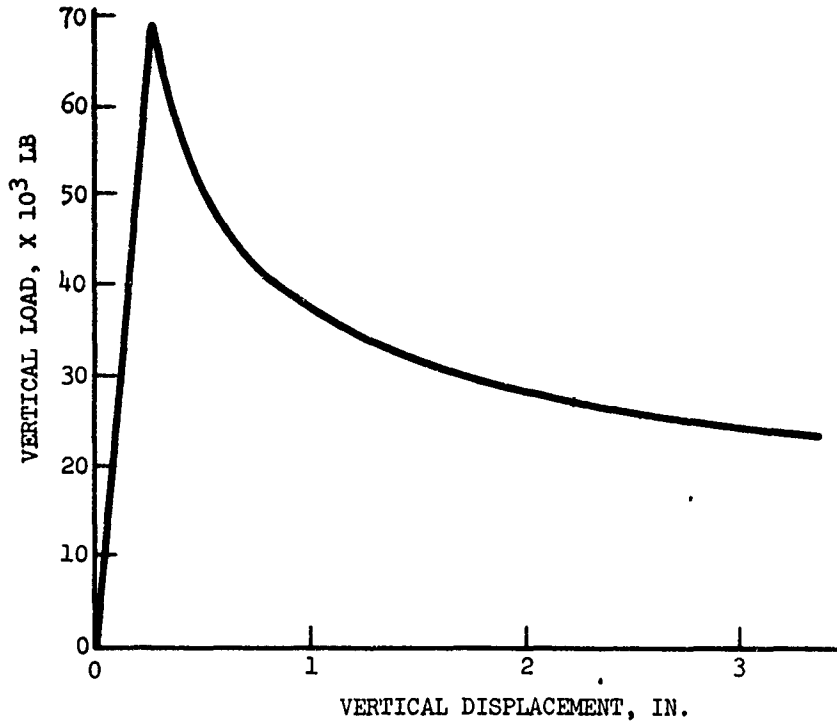


Figure 41. Predicted Total Load-Deflection Curve for Specimens 5 and 6.

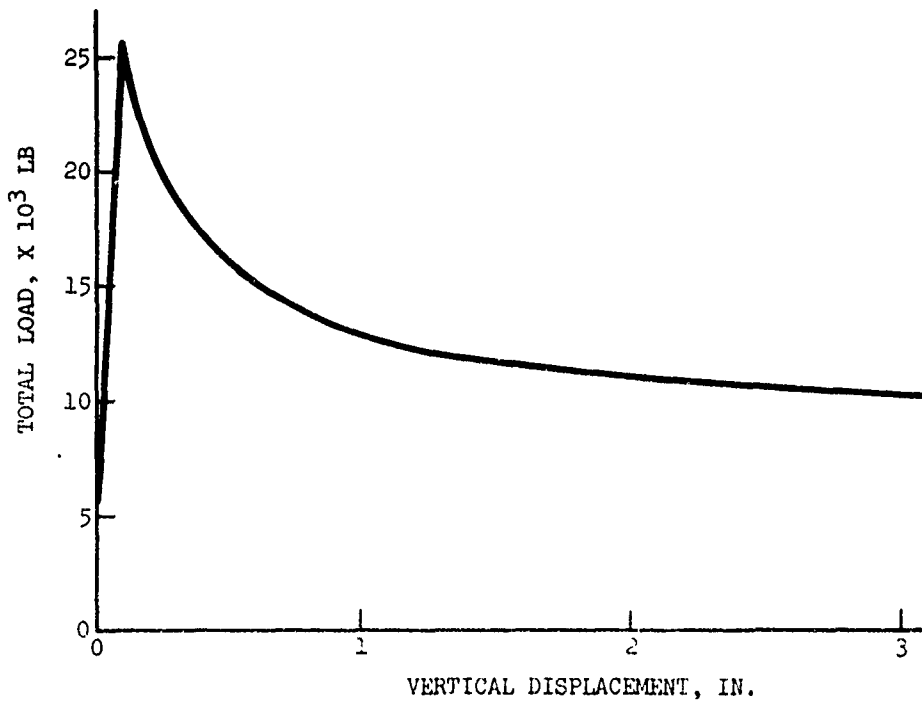


Figure 42. Predicted Total Load-Deflection Curve for Specimens 2, 3 and 4.

SUBSTRUCTURE TEST PROGRAM

TEST PROGRAM OBJECTIVES

The objectives of the test program are to:

- (1) Develop testing techniques for determining load-deflection characteristics of structural elements subjected to loads involving crash-oriented large deformations.
- (2) Establish the validity of simplified analytical techniques for use in predicting load-deflection characteristics for crashworthiness analysis.
- (3) Verify the application of simplified analytical techniques for different types of structural elements used in aircraft design.
- (4) Obtain information which can be used in future studies for improving crashworthiness analytical capabilities.
- (5) Determine limitations associated with simplified analytical techniques in the prediction of crashworthiness capability.

GENERAL

It is important, in the establishment of the test program, that consideration be given to:

- representing typical structural designs
- ascertaining the effects of detail design differences on load-deflection characteristics
- representing a crash loading condition
- relating the test data to procedures for predicting load-deflection characteristics
- relating the test data to analytical modeling data requirements.

Twelve tests were performed to aid in evaluating whether or not simplified analytical techniques and experimental tests provide data of sufficient accuracy, when applied in a crashworthy analysis of helicopters, to yield reliable results.

In examining the type of structure used in helicopter design, the most critical area from the standpoint of energy absorption and habitable volume is the fuselage. In addition, this area, because of its built-up

construction, is most difficult to analyze for large deformation. Structural elements representative of other regions of the aircraft, i.e., landing gear, engine mount, and tail boom, are of lesser complexity than the fuselage structure, and in many instances they are not primary energy absorbers. In addition, there is more test and analytical data available for these types of structural elements than for multi-web construction.

Testing of several different types of representative fuselage substructure provides the opportunity to obtain data which produces meaningful load-deflection characteristics such as failure modes due to the design changes associated with the various elements within the substructure.

The tests are to: (1) ascertain if the analytical techniques to be developed in this study for determining approximation of large deformation response characteristics are valid, and (2) obtain experimental load-deflection data.

Inasmuch as an infinite number of combinations of loading conditions and edge restraints are available, care is exercised to select only those combinations that will provide the necessary data to fulfill these requirements. Once analytical techniques are compared with experiments and verified regarding their limitations, they can be applied to variations in design, geometry, and constraints with a greater degree of confidence.

TEST SPECIMENS

A representative pylon support structure is selected as a basic test specimen from which normal types of detail design variations are made to alter its load-deflection characteristics under large deflection loading conditions. The pylon support structure consists of an inner and an outer skin, representative of the basic floor and the helicopter lower fuselage skin respectively, tied together by a series of beams running fore and aft and bulkheads. This structure, during helicopter accidents, is the means by which the vertical ground impact is transmitted to the transmission. Accordingly, its modes of failure, the amount of energy absorbed, and the pulse shape produced are of interest in assessing the crashworthiness capabilities of a helicopter.

Figures 43 and 44 show specimens of the two different depths that are represented. The specimen shown in Figure 43 is 6.125 inches deep and is applicable to specimens 1 through 9, Table XVII. The specimen shown in Figure 44 is 12.125 inches deep and represents specimens 10 through 12. The specimen configurations and test conditions include:

- static load
- dynamic impact (14 ft/sec \leq velocity \leq 30 ft/sec)
- four-edge support
- two-line support
- skin web thickness from .025 in. to .064 in.
- angle stiffener thickness from .032 in. to .072 in.
- specimen weight from 13.6 lb to 31.25 lb

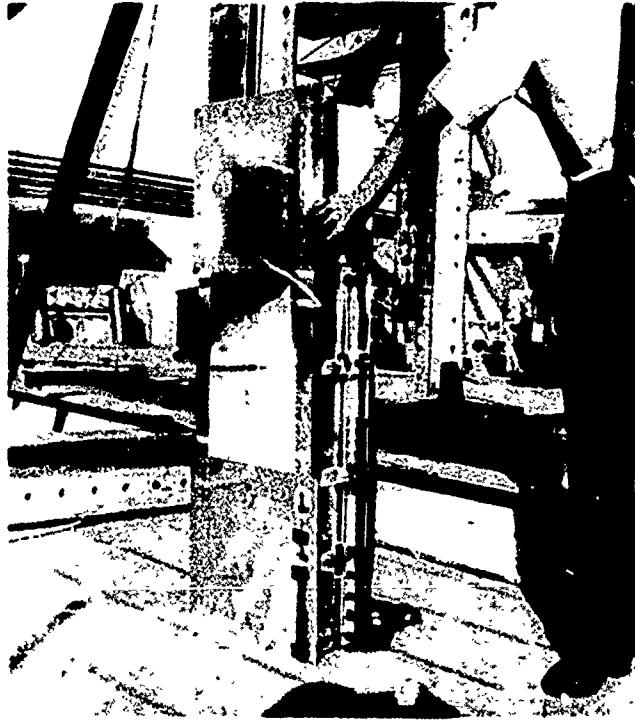


Figure 43. Typical 6.125-Inch-Deep Test Specimen (Specimens 1-9).

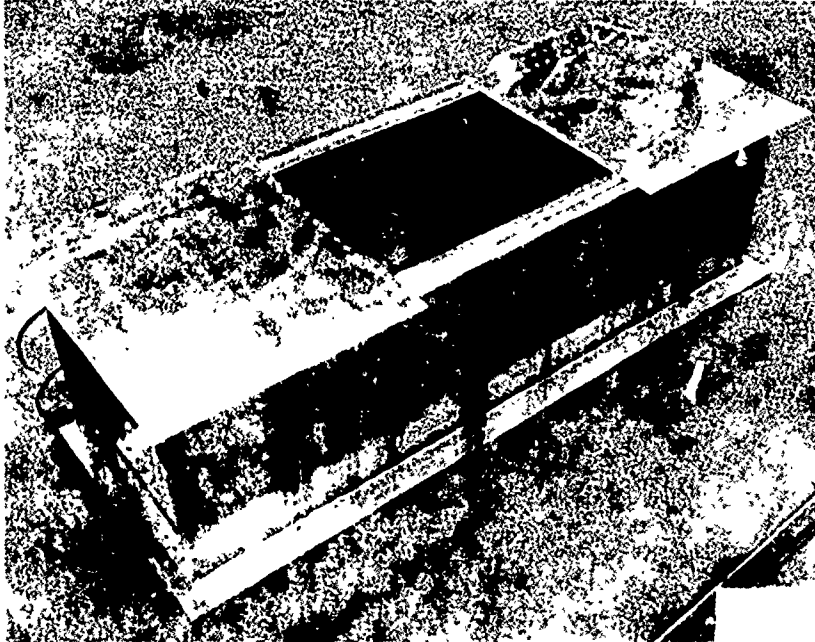


Figure 44. Typical 12.125-Inch-Deep Test Specimen (Specimens 10-12).

TABLE XVII. SPECIMEN DESIGN CONFIGURATION, DIMENSIONS AND TYPES OF TESTS PERFORMED*

Specimen No.	Basic Dimensions (In.)			Web Thickness (In.)		Angle Member	Stiffeners, Thickness (In.)	Blind Web Lightening Holes	Nominal Weight (lb)	Test Type **, *** ****
	Length	Width	Depth	End Item						
				Bulkhead	End Item					
1	46	18	6.125	.025	.032	12	.032	Yes	13.6	Static
2	46	18	6.125	.025	.032	20	.032	Yes	14.3	Static
3	46	18	6.125	.025	.032	20	.032	No	14.3	Static
4	46	18	6.125	.025	.032	20	.032	No	14.3	Dynamic @ 17 ft/sec
5	46	18	6.125	.025	.032	32	(12).032 (20).072	Yes	16.0	Dynamic @ 30 ft/sec
6	46	18	6.125	.025	.032	32	(12).032 (20).072	No	16.0	Dynamic @ 14 ft/sec
7	46	18	6.125	.064	.064	32	.064	Yes	19.5	Dynamic @ 14 ft/sec ****
8	46	18	6.125	.064	.064	32	.064	Yes	19.5	Dynamic @ 27 ft/sec ****
9	46	18	6.125	.064	.064	32	.064	Yes	21.0	Static
10	46	18	12.125	.025	.032	32	.032	Yes	21.4	Static
11	46	18	12.125	.064	.064	32	.064	Yes	31.3	Static
12	46	18	12.125	.025	.032	32	.032	Yes	21.4	Static *****

* See Volume II Figures 2 through 6 for detail drawings of Specimens

** Impact head and carriage weight = 840 lb (Test 5), = 1085 lb (Test 8)

*** Impact head and carriage weight = 3550 lb (Tests 4, 6), = 3585 lb (Test 7)

**** Six load cells were installed below the specimen support

***** Lines supported, all other tests were with four-edge supports

number of angle stiffeners from 12 to 32
specimen depth from 6.125 in. to 12.125 in.

Each test specimen is 46 inches long, including five bays, and is 18 inches wide with a side panel on each side to represent the main bulkhead. The test specimen basic overall dimensions and bulkhead and stiffener spacing are approximately half size.

The typical lower fuselage bulkhead and stiffener arrangement shown previously in the Substructure Analysis section (Figure 20) is presented again in Figure 45. Illustrated in this figure is the location of the test specimens relative to the entire lower fuselage, the landing gears, the transmission pylon and the pylon support. The drawing for Specimens 1 and 2 is presented in Figure 46. Drawings for all 12 specimens fabricated and tested during the program are provided in Volume II. Table XVII shows the dimensions, thickness, number of angles, number of stiffeners, nominal weight, design configuration, and type of test performed for each of the 12 specimens.

INSTALLATION

The planned test program required that both static and dynamic tests be performed. The static tests are performed using a Baldwin Universal testing machine (Figure 47). The static setup with a specimen installed is shown in Figure 48. The impact head is used throughout all the tests --static and dynamic. A quasi-static loading procedure is followed in which a controlled constant deflection rate is applied. Initially, the rate is 0.05 inch/minute. After the initial failure load is reached, the loading rate is increased to at least 2 inches/minute. The dynamic tests are performed using the frame structure test tower and carriage shown in Figure 49. The minimum carriage weight and aluminum impact head is 840 pounds. The drop test facility has sufficient clearance to perform 30-ft/sec impact tests; however, the weight of the carriage and impact head and the energy-absorbing capacity of the structure are the determining factors in the final impact velocity selected for a particular test. The initial drop tests (test specimens 4, 5 and 6) employed a four-edge wooden support between the specimen and the ground. The load was obtained from accelerometers mounted on the impact head. The second set of dynamic tests (specimens 7 and 8) was performed with a set of six load cells installed between the specimen and the ground. This setup is shown in Figure 50 for the 14-ft/sec and 27-ft/sec impact test conditions. In the lower velocity test, mass was added to the impact head to provide comparable energy levels as would be experienced at higher impact velocity level. The five 500-pound weights used can be seen on top of the impact head in Figure 50a.

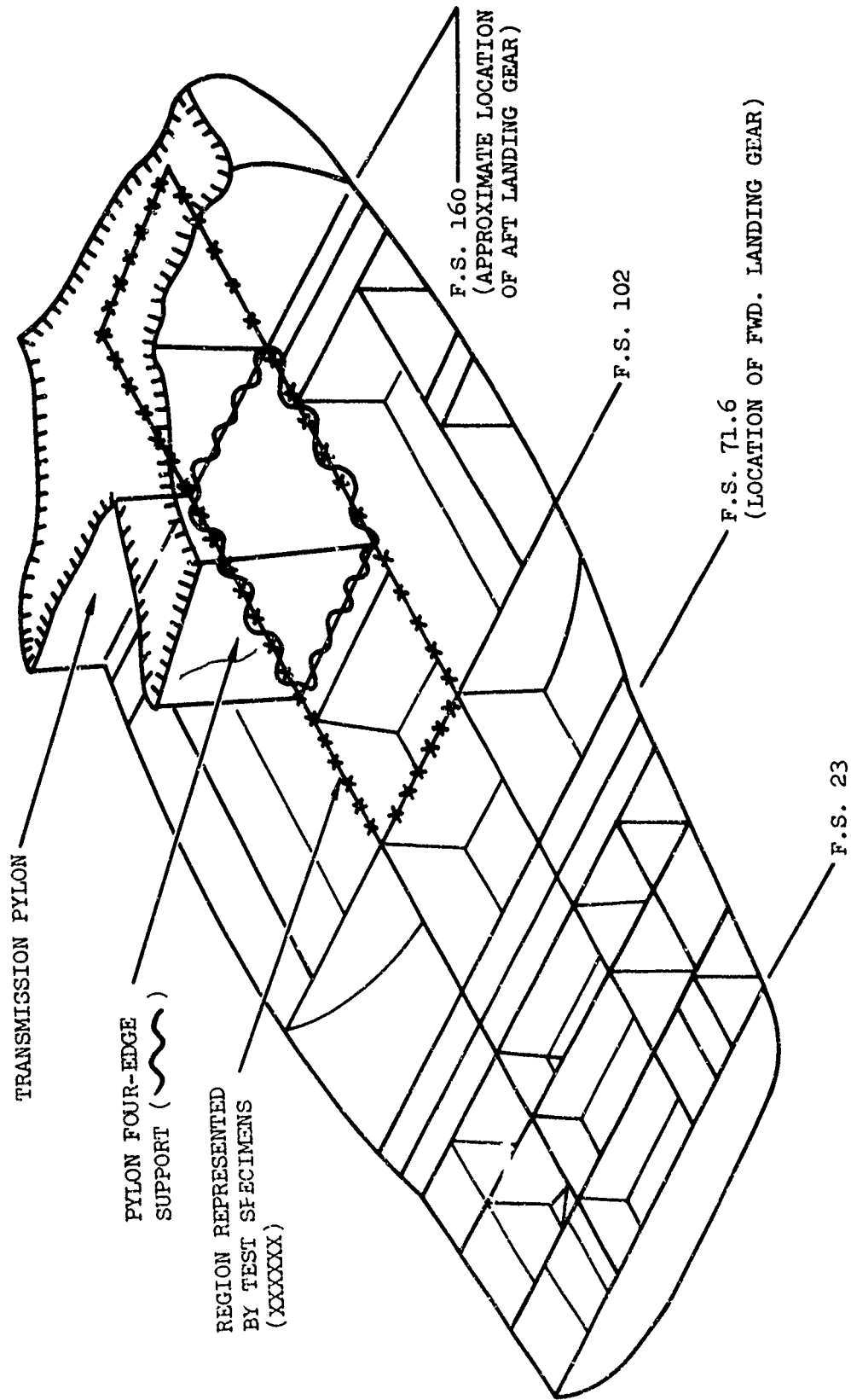


Figure 45. UH-1H Lower Fuselage Bulkhead and Stiffener Arrangement.

A

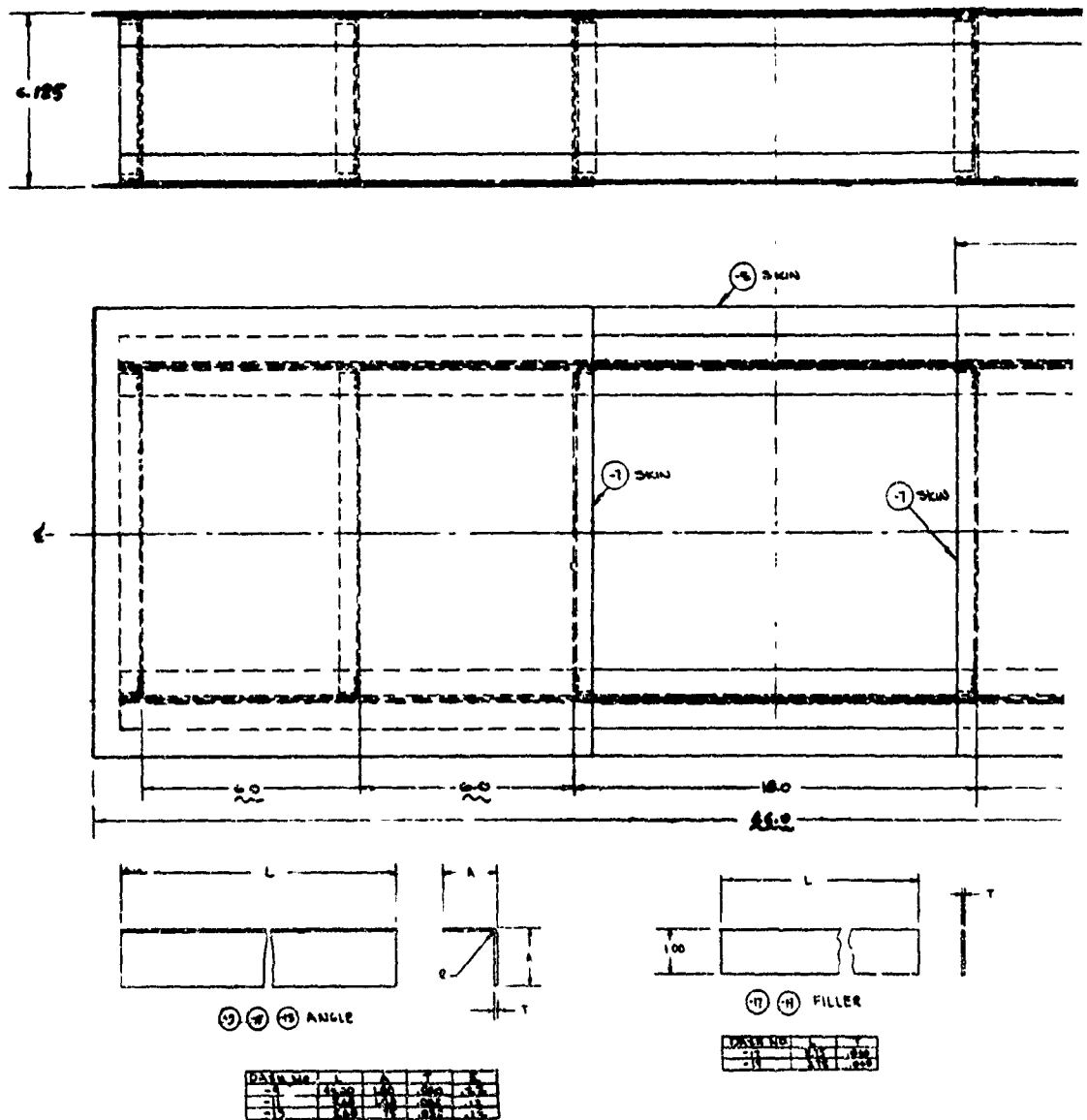
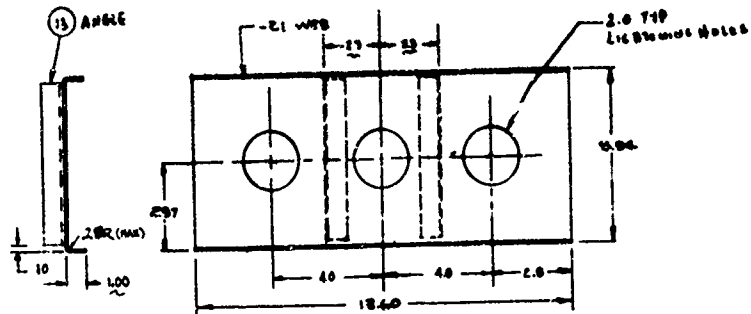
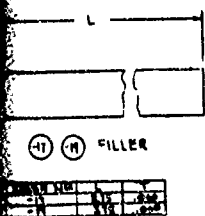
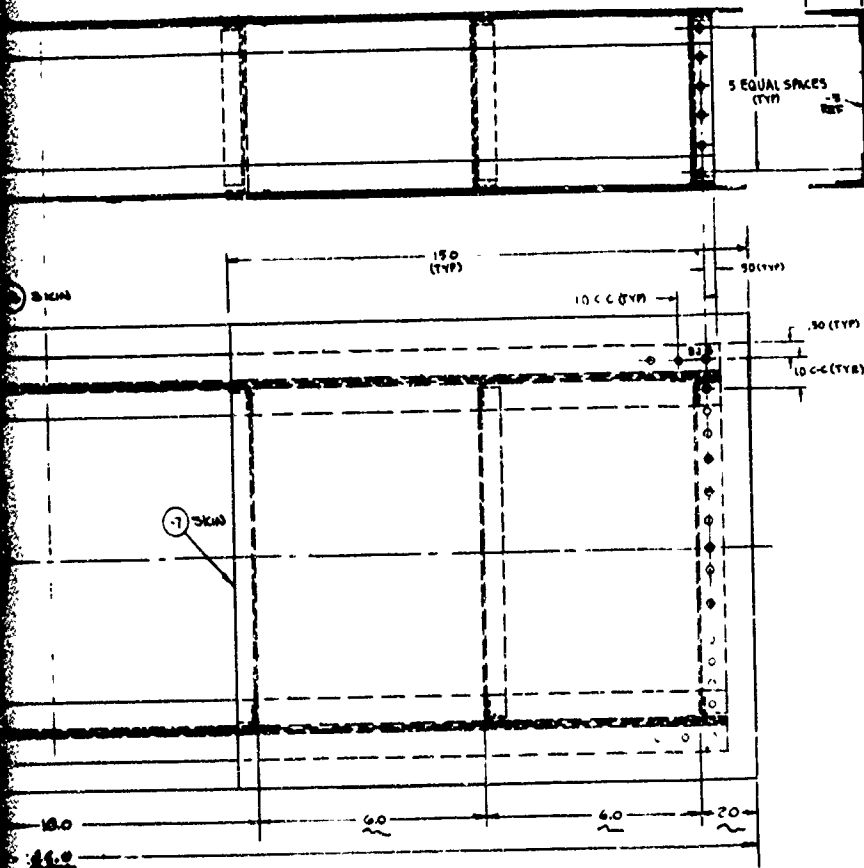
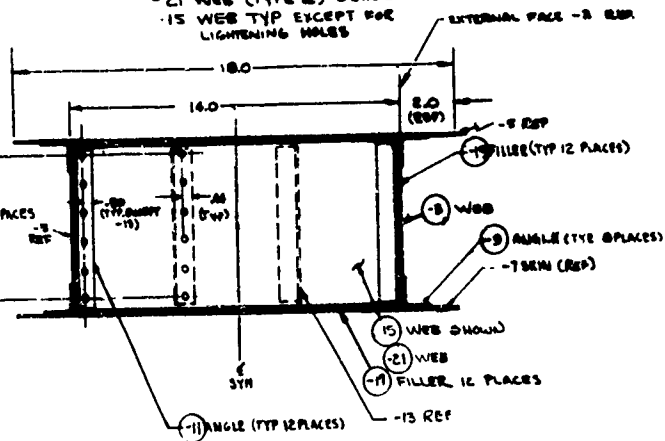


Figure 46. Drawing for Specimens 1 and 2 (All Dimensions in Inches)

B



- 21 WEB (TYPE B) DETAIL
 - 15 WEB TYP EXCEPT FOR LIGHTENING HOLES



5. THE HAS 1758E4-L 3 RIVETS MAY BE INSTALLED AT ANY LOCATION TO FACILITATE FABRICATION
4. DEBURR HOLES BEFORE ASSY.
3. BREAK ALL SHARP EDGES
2. INSTALL HAS 1758E4-L 3 RIVETS PER DRAWING

QTY	REV	DESCRIPTION	REV	DESCRIPTION	REV	DESCRIPTION	REV	DESCRIPTION
6	6	WEB	- 21	CLAD	7071-76	0.218 X 1.50		
12	12	FILLER	- 19		7075-76	0.031 X 0.125		
12	12	FILLER	- 17		7071-76	0.031 X 0.125		
6	6	WEB	- 15		7075-76	0.031 X 0.125		
12	12	ANGLE	- 13		2028-73	0.125 X 1.50 X 0.031		
12	12	ANGLE	- 11		2028-73	0.125 X 1.50 X 0.031		
8	8	ANGLE	- 9		2028-73	0.031 X 1.50 X 0.125		
2	2	SKIN	- 7		2028-73	0.125 X 1.50 X 0.031		
1	1	SKIN	- 5		2028-73	0.125 X 1.50 X 0.031		
2	2	WEB	- 3	CLAD	7071-76	0.218 X 0.875 X 0.031		
		ASSY						

(All Dimensions in Inches).

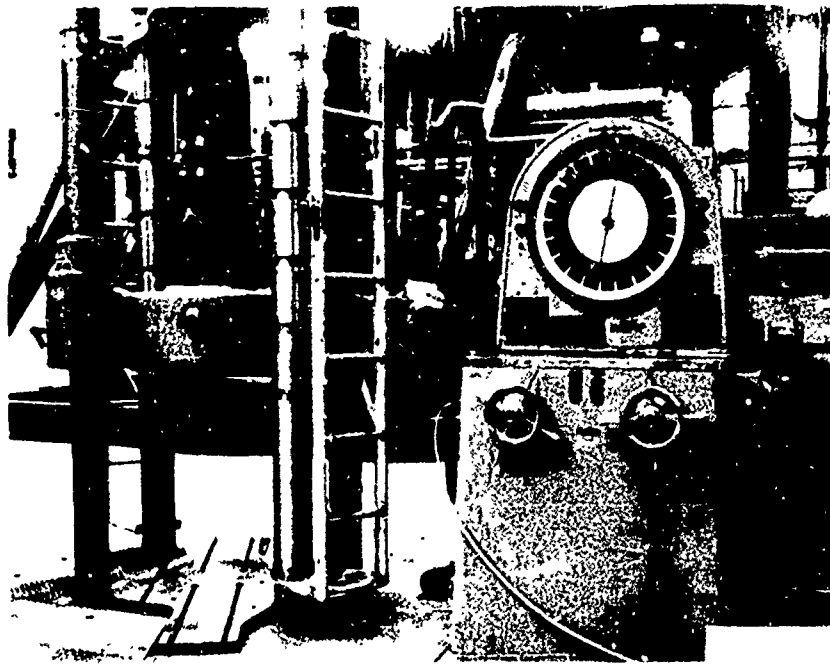


Figure 47. Baldwin Universal Static Testing Machine.

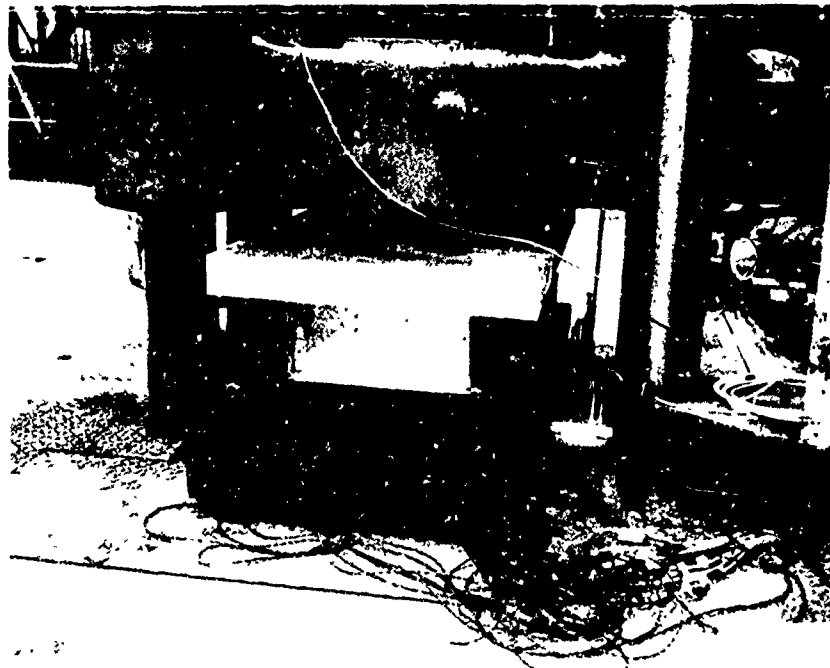


Figure 48. Static Test Setup.

Preceding page blank

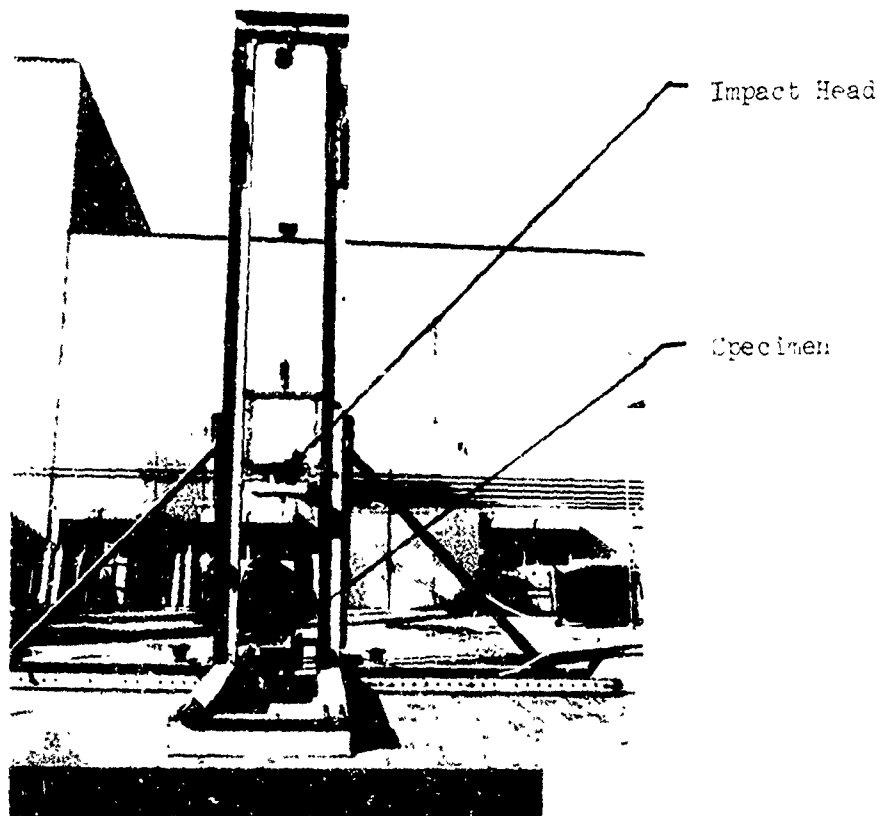


Figure 49. Frame Structure Test Tower for Dynamic Tests.

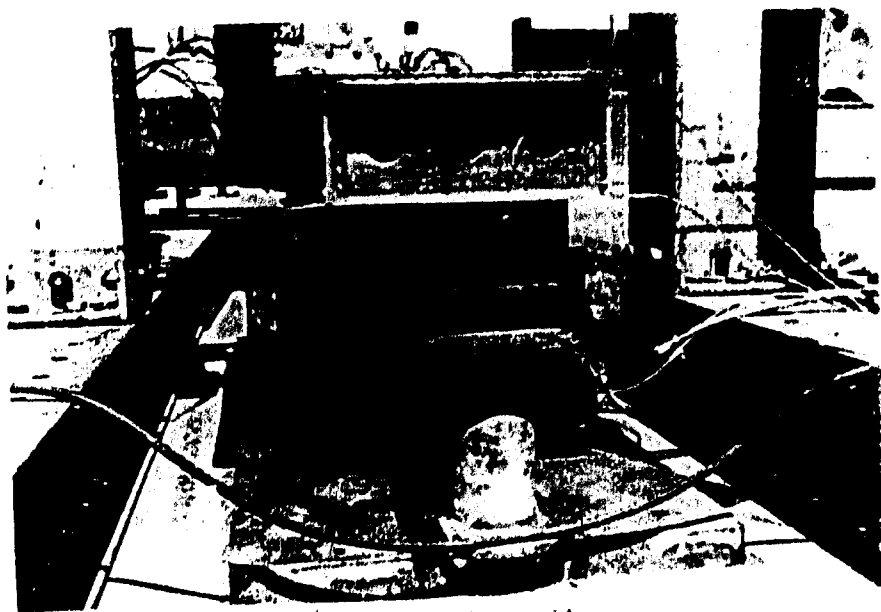
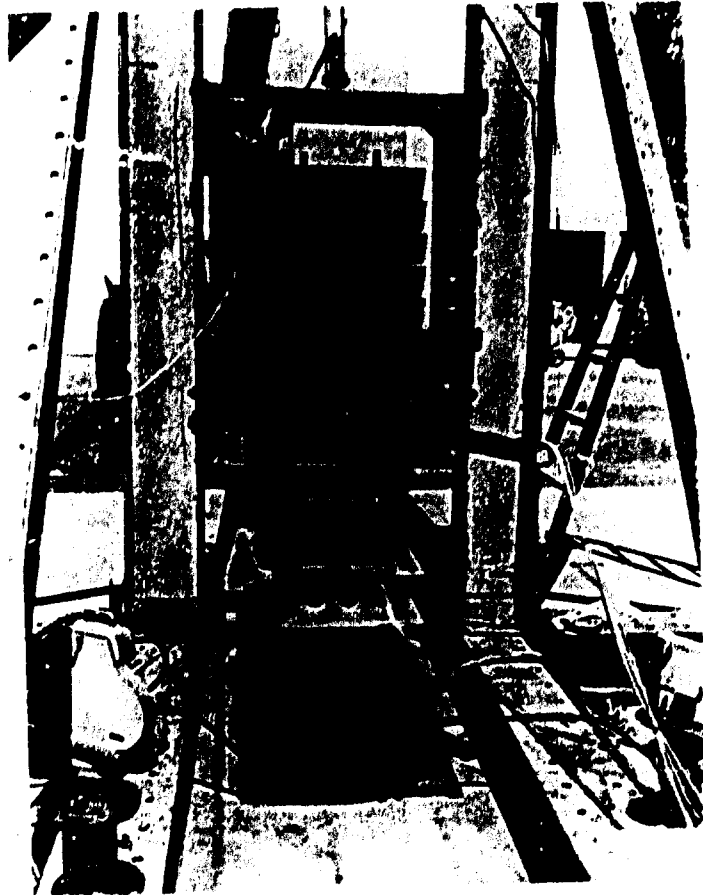


Fig. 10 - 20/1000 impact condition

Figure 10. Impact condition. With the impact condition, the impact condition is shown in the figure.

INSTRUMENTATION

For the initial series of tests, seven strain gages were installed to measure compression and/or bending. The locations of the strain gages are described in Figure 51 and Table XVIII. For the static tests, the load is measured directly with a force transducer, and the deflection is obtained using a linear variable differential transducer (LVDT). All data is recorded directly on the Lockheed Central Data System (CDS), from which response time history and force acceleration versus deflection plots are obtained.

In the dynamic tests, in addition to the strain gage and displacement measurements, three vertically oriented accelerometers (> 100 g range and with frequency response ≈ 800 Hz) are used.

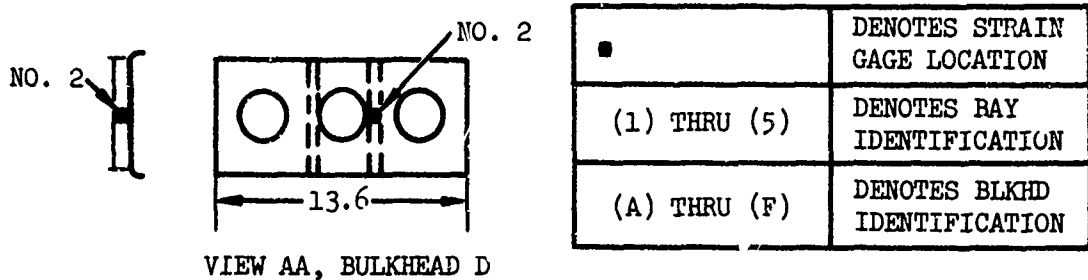
For the first set of dynamic tests (4, 5 and 6), accelerometers are placed on the impact head and acceleration data (mass x g's) is used to determine the load. In the second set of dynamic tests (7 and 8), in addition to the accelerometers mounted on the impact head, load cells are installed between the test specimen support and the ground.

TEST SEQUENCE

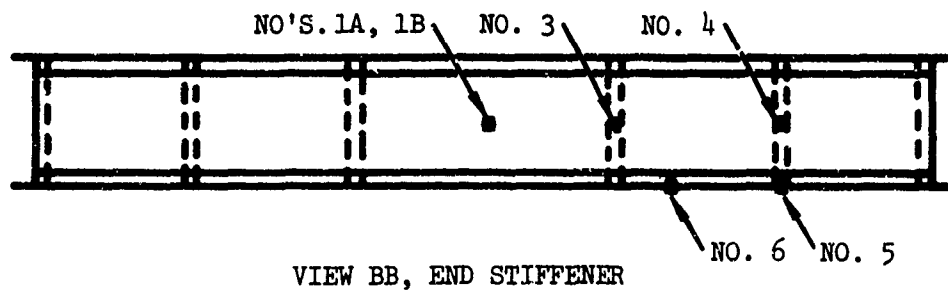
The purpose of the initial tests is to verify the significance of inertia effects and design configurations (i.e., lightening holes, modified stiffener arrangement) on the load-deflection characteristics of typical fuselage structure. Prior to the actual tests, preliminary tests were performed to check out the test setup, motion of the carriage, and instrumentation. The preliminary tests were run with a rubber pad in place of the test specimen and performed for a drop height of 2.5 feet. The results of the preliminary tests indicated that the drop tower and data reduction systems were satisfactory for performing the dynamic tests.

The testing sequence used is as follows:

1. Static test (specimen with reduced number of angle stiffeners)
2. Static test (specimen with representative number of angle stiffeners)
3. Static test (same as specimen 2 except for lightening holes)
4. Dynamic test (same as specimen 3, impact velocity 17 ft/sec)
5. Dynamic test (specimen 2 stiffened for 30 - ft/sec impact velocity)
6. Dynamic test at 14 ft/sec (same as specimen 5)
7. Dynamic test at 14 ft/sec (load cells installed)
8. Dynamic test at 27 ft/sec (load cells installed - same as specimen 7)
9. Static test (same as specimens 7 and 8)
10. Static test (12.125-inch depth)
11. Static test (12.125-inch depth; skin and angles thicker than specimen 10)



VIEW AA, BULKHEAD D



VIEW BB, END STIFFENER

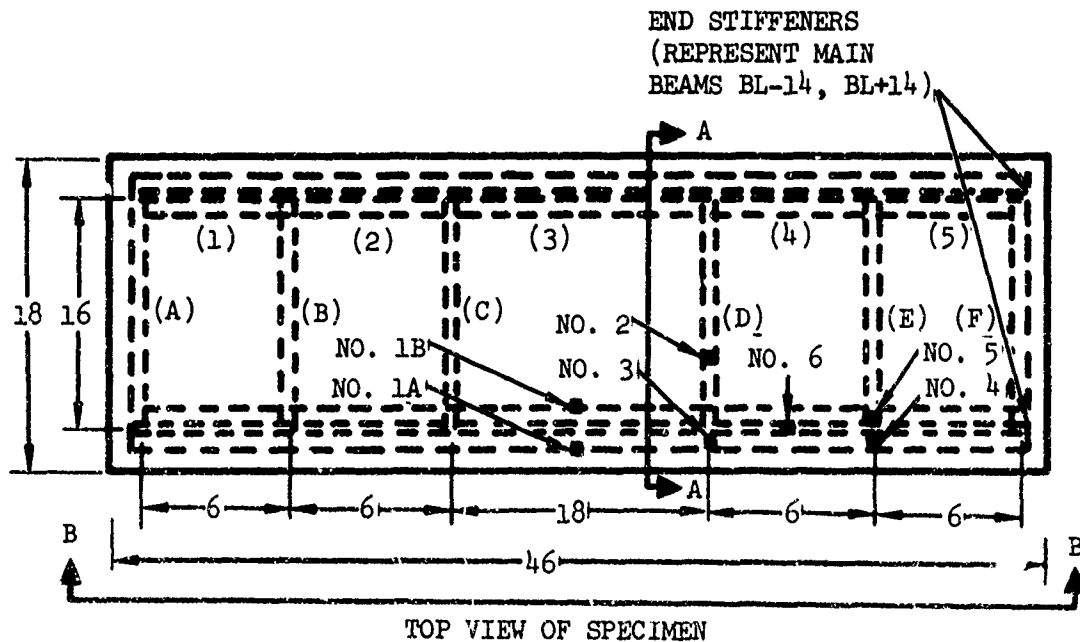


Figure 51. Strain Gage Locations (All Dimensions in Inches).

TABLE XVIII. STRAIN GAGE LOCATIONS

Strain Gage No.	Location **	Direction Of Measurement	Strain Gage Mounted On Test Specimens
1A	Web of center bay, end beam inside	Compression and/or bending of end beam	1 thru 12 *
1B	Web of center bay, end beam outside	Compression and/or bending of end beam	1 thru 12
2	Web of bulkhead "c"		1 thru 9
3	Web end beam at junction of bulkhead "c"	Axial compression of end beam	1 thru 3
4	Web of end beam at junction of bulkhead "d"	Axial compression of end beam	1 thru 3
5	Bottom of beam flange 1-1/2 inches from junction of bulkhead "d"	Axial strain for bending of beam	1 thru 3
6	Bottom of flange 2 inches from junction of bulkhead "e"	Axial strain for bending of beam	1 thru 9

* On specimen 9, strain gage 1A is placed on the free flange of the outside angle stiffener in the center of the middle bay, since this specimen is closed on the bottom.

** Strain gage locations are shown in Figure 51.

12. Static test (12.125-inch depth; same as specimen 10 except for line supports)

PHOTOGRAPHY

During the static tests, time lapse (2 frames/sec and 6 frames/sec) photographic coverage and 35 mm slides were taken during the application of load. In addition, still photographs of test setup, test specimen and post-test failure modes were obtained.

During the dynamic tests, high-speed motion-picture (500 frames/sec and 1000 frames/sec) coverage was employed in synchronization with the tape-recorded data. The location of the cameras was such that two different angles were covered on each test.

RESULTS

The results of the tests are shown in Table XIX. The load-deflection curves for each of the test specimens are shown in Figures 52 through 63. Because the initial dynamic tests were performed with accelerometers mounted on the impact head, the acceleration time histories have oscillations from which it is difficult to accurately interpret the proper loads. Since the accelerometer response is influenced by the impact tower vibration, impact head and carriage, the load-deflection curves for specimens 4, 5 and 6 (Figures 55, 56 and 57, respectively) have oscillations which are believed to fluctuate about a mean value.

Because of the difficulty in interpreting accelerometer data, tests 7, 8 and 9 were designed to test the same configurations (with the exception of a lower skin on specimen 9) under the following three equal energy input conditions:

- 27 ft/sec impact velocity
- 14 ft/sec impact velocity
- static load

The results of these three tests are shown in Figures 58, 59 and 60. Specimens 10, 11 and 12 were designed to be approximately twice as deep (12.25 inches) as the other specimens (6.125 inches). Specimens 10 and 12 were identical. Specimen 11 was designed with skin and angle gage thickness twice that of specimens 10 and 12.

Specimens 10 and 11 were tested using the same four-edge metal support chat was used for specimens 7, 8 and 9. Previously a four-edge wooden block support was used, but when load cells were added to the dynamic test setup, the stiffer support was considered to be more desirable. The load-deflection curves are shown in Figures 61, 62 and 63. Specimen 12 was tested using line supports beneath the side panels (Figure 64). Specimen 11 (138,000 lb) was considerably stiffer than specimen 10 (39,000 lb), and this is easily observed in the failure loads for each specimen.

TABLE XIX. TEST RESULTS

Specimen No.	Test Type	No. of Beam Angle Stiffeners	***** Lightening Holes	Failure Load (Lb)	Failure Point Deflection (In.)	*** Energy Absorbed (In.-Lb)	Deflection (In.)	
							Maximum	Perma ent
1	Static	12	Yes	14200	.30 - .40	25850.	3.1	2.32
2	Static	20	Yes	26400	.24	41800	3.65	2.35
3	Static	20	No	26100	.24	41400	3.3	2.32
4	Dynamic (17 ft/sec)	20	No	26840**	.16	40360	3.65	2.54
5	Dynamic (30 ft/sec)	32	Yes	84840**	.25	102900	3.8	2.58*
6	Dynamic (14 ft/sec)	32	No	90000**	.29	117860	4.25	3.75*
7	Dynamic (14 ft/sec)	32	Yes	133000***	.31	136000	3.25	2.5*
8	Dynamic (27 ft/sec)	32	Yes	144000***	.38	142750	2.45	1.5*
9	Static	32	Yes	132000	.29	130000	3.92	2.5
10	Static	32	Yes	39000	.20	51750	3.20	2.5
11	Static	32	Yes	69200	.30	83600	3.11	2.0
12	Static	32	Yes	65330	.27	70000	2.8	2.0

* Immediately after the dynamic test, the specimen was noted to have sprung back from the maximum deflection. The specimens that were statically tested required several days to relax to the final deformed position.

** Estimated from acceleration data.

*** Obtained directly from load-cell data.

**** Energy absorbed calculations are for 3 inch deflection or less.

***** Where applicable there are three lightening holes in each bulkhead; see Volume II, Figures 2 through 6 for size and spacing and location data.

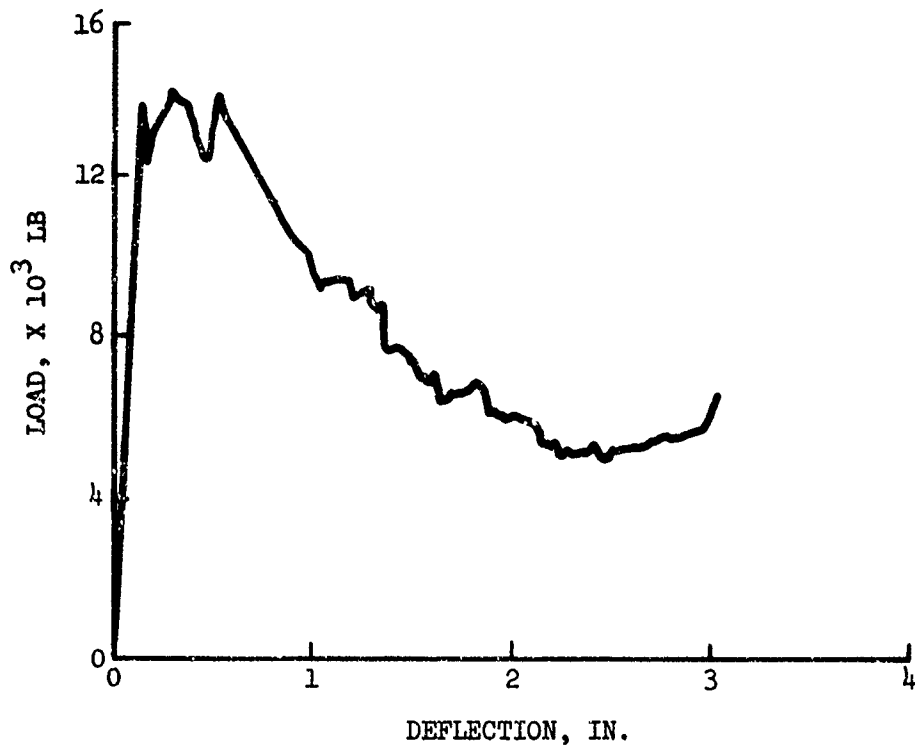


Figure 52. Load Versus Deflection, Test 1.

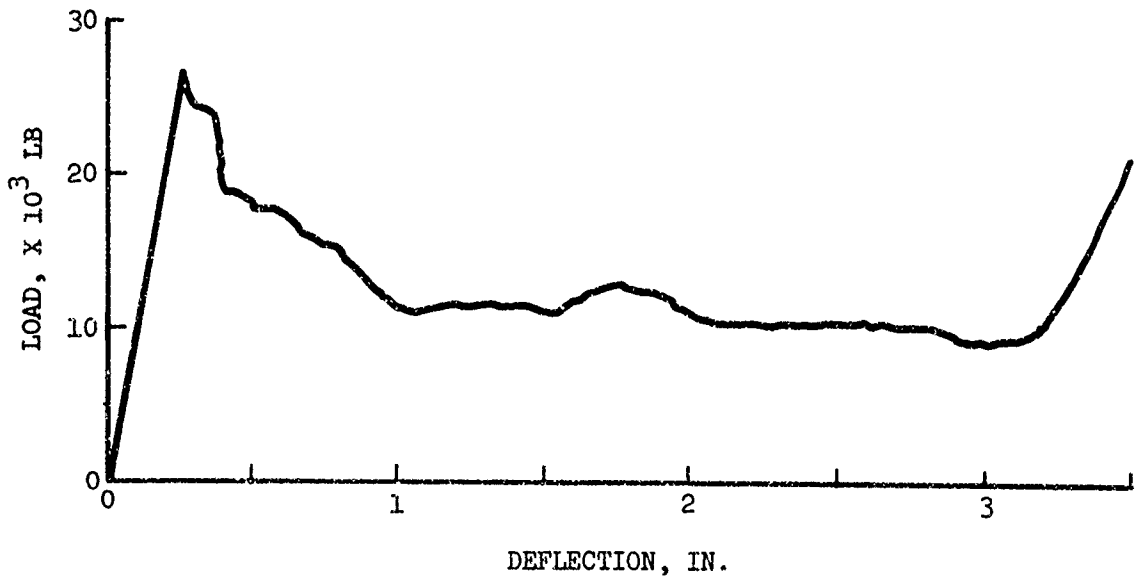


Figure 53. Load Versus Deflection, Test 2.

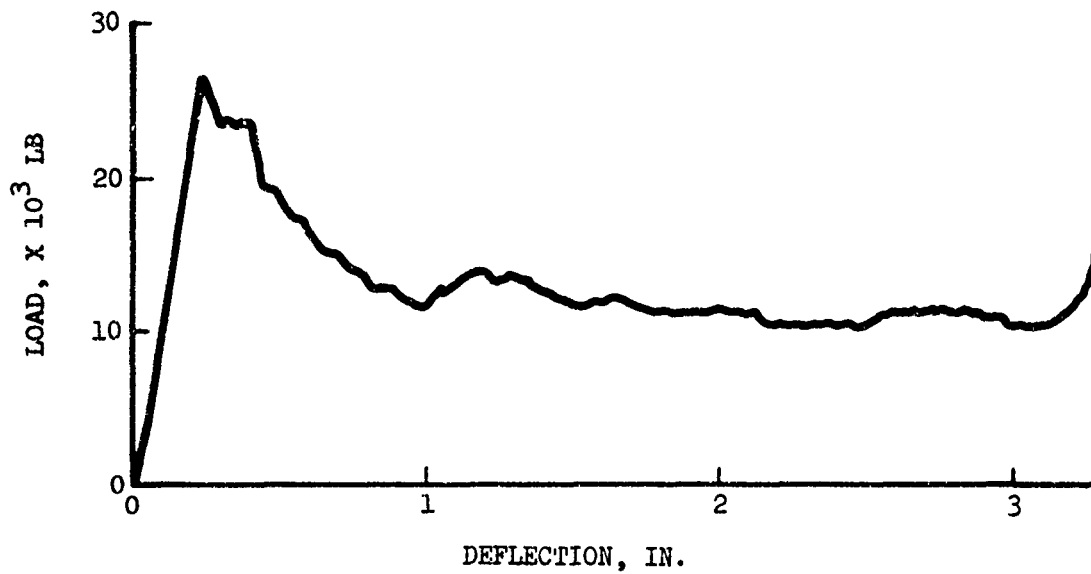


Figure 54. Load Versus Deflection, Test 3.

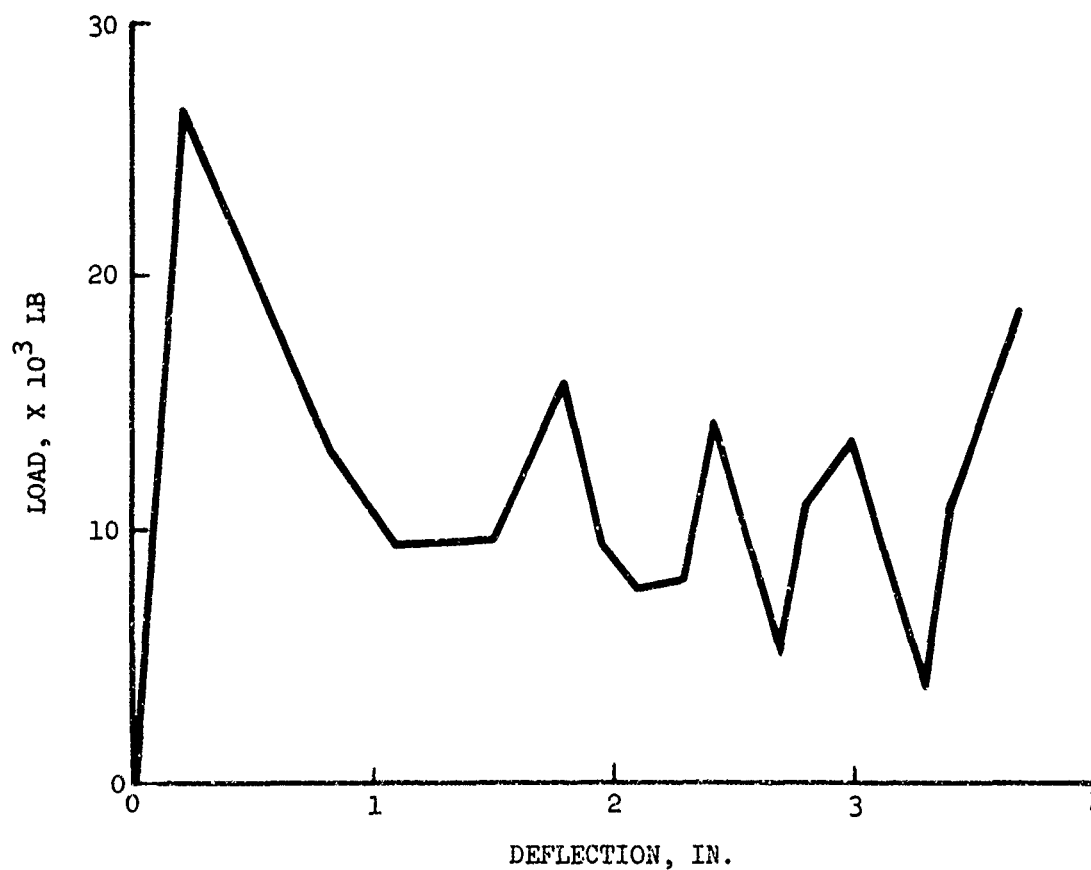


Figure 55. Load Versus Deflection, Test 4.

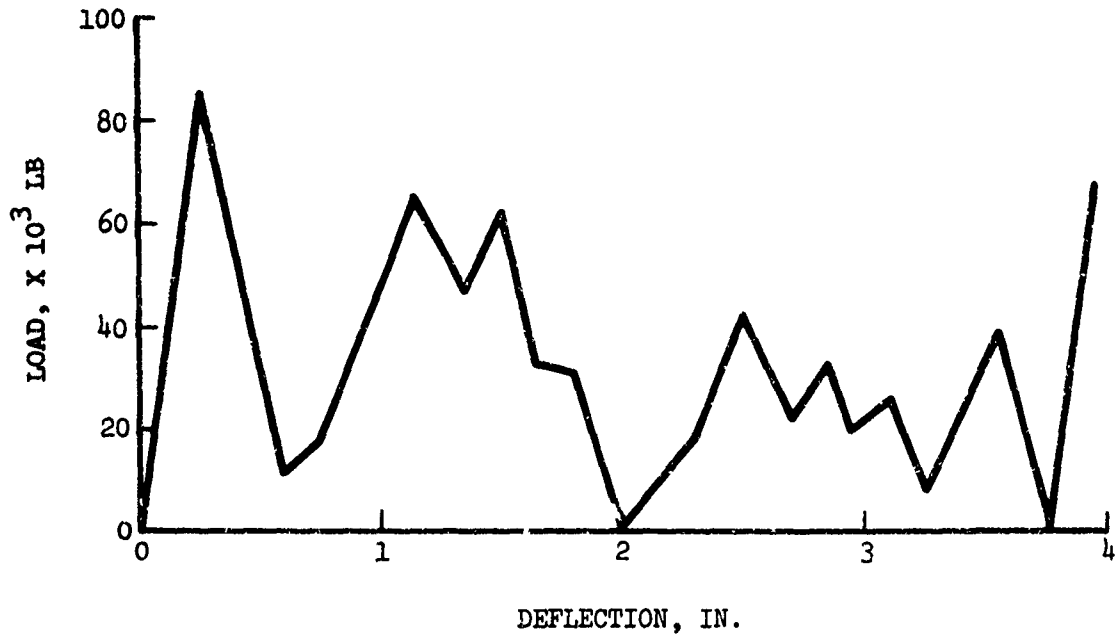


Figure 56. Load Versus Deflection, Test 5.

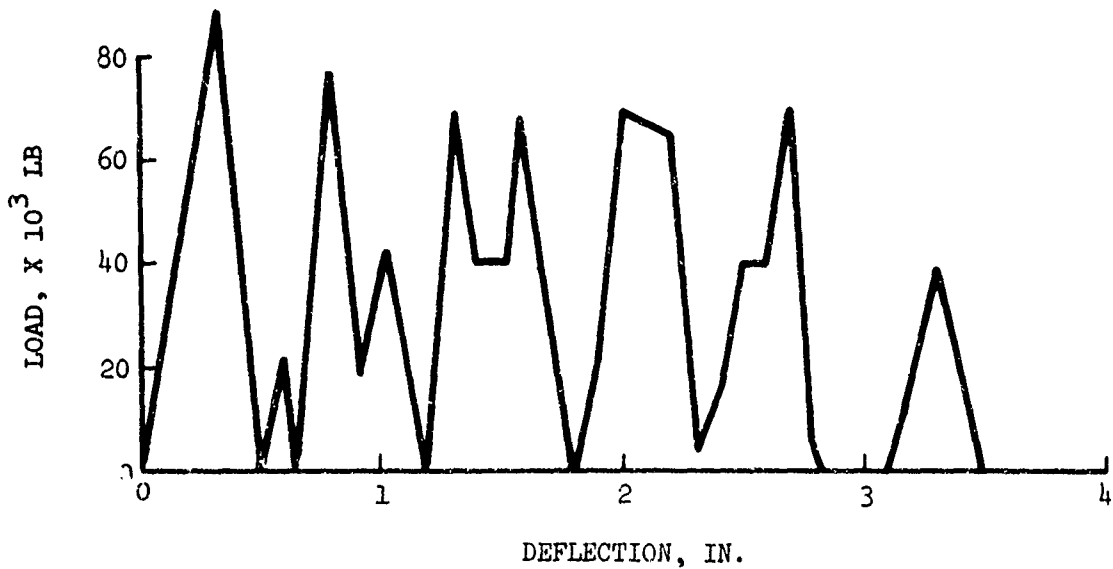


Figure 57. Load Versus Deflection, Test 6.

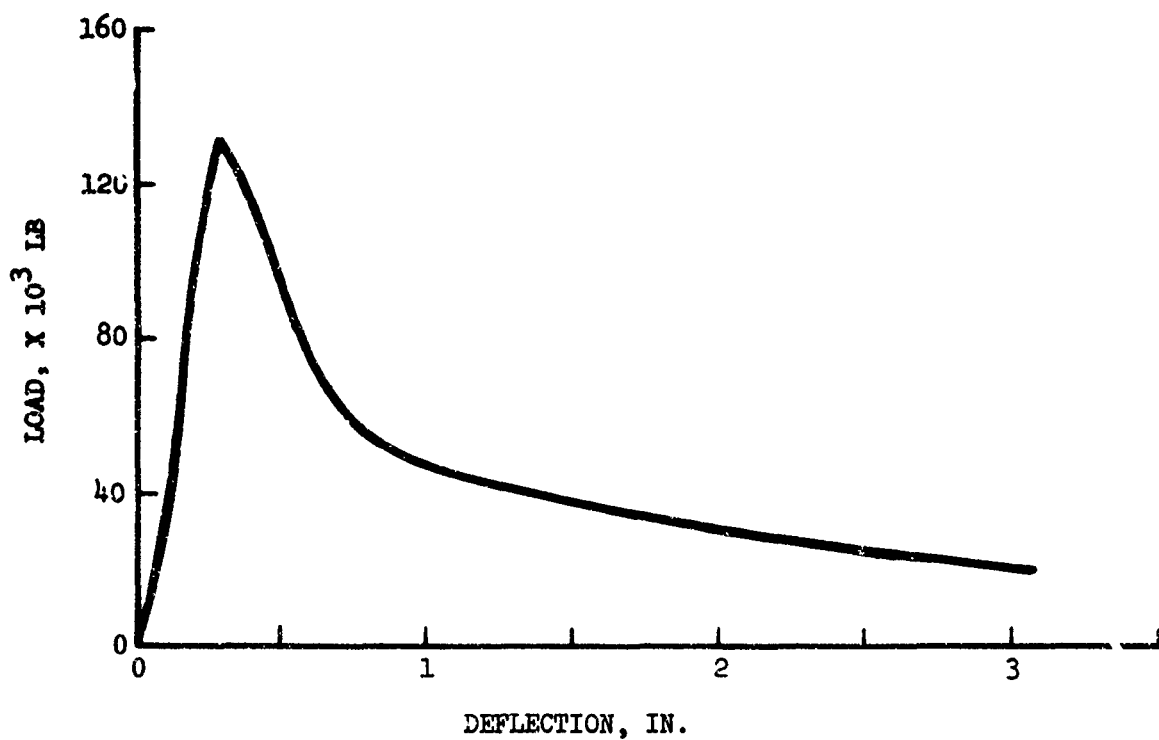


Figure 58. Load Versus Deflection, Test 7.

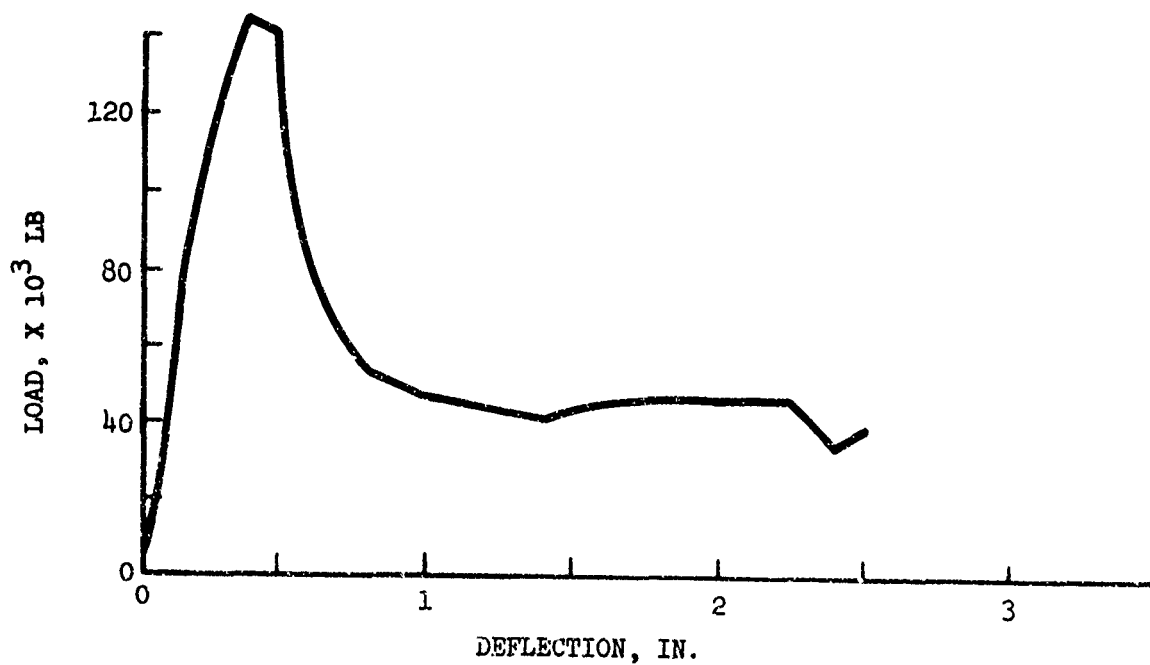


Figure 59. Load Versus Deflection, Test 8.

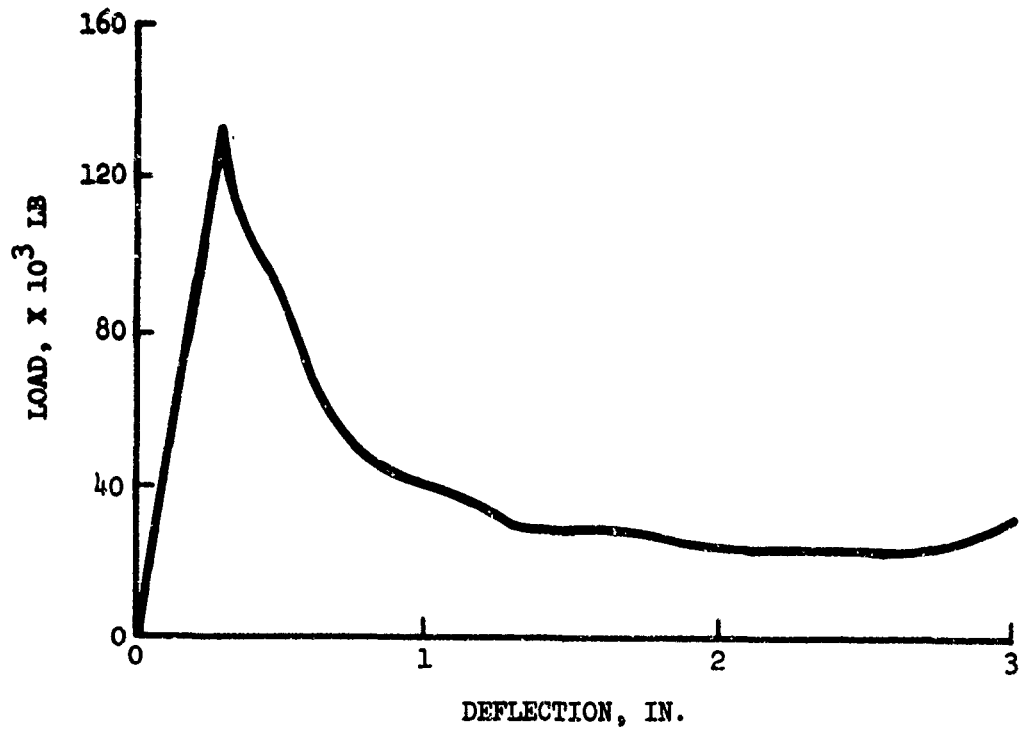


Figure 60. Load Versus Deflection, Test 9.

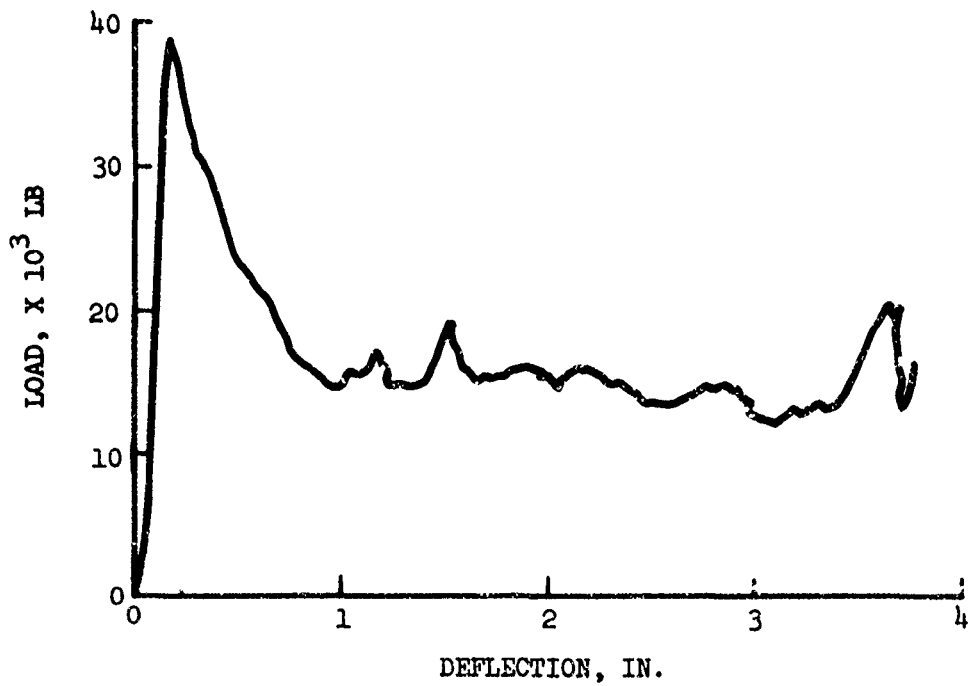


Figure 61. Load Versus Deflection, Test 10.

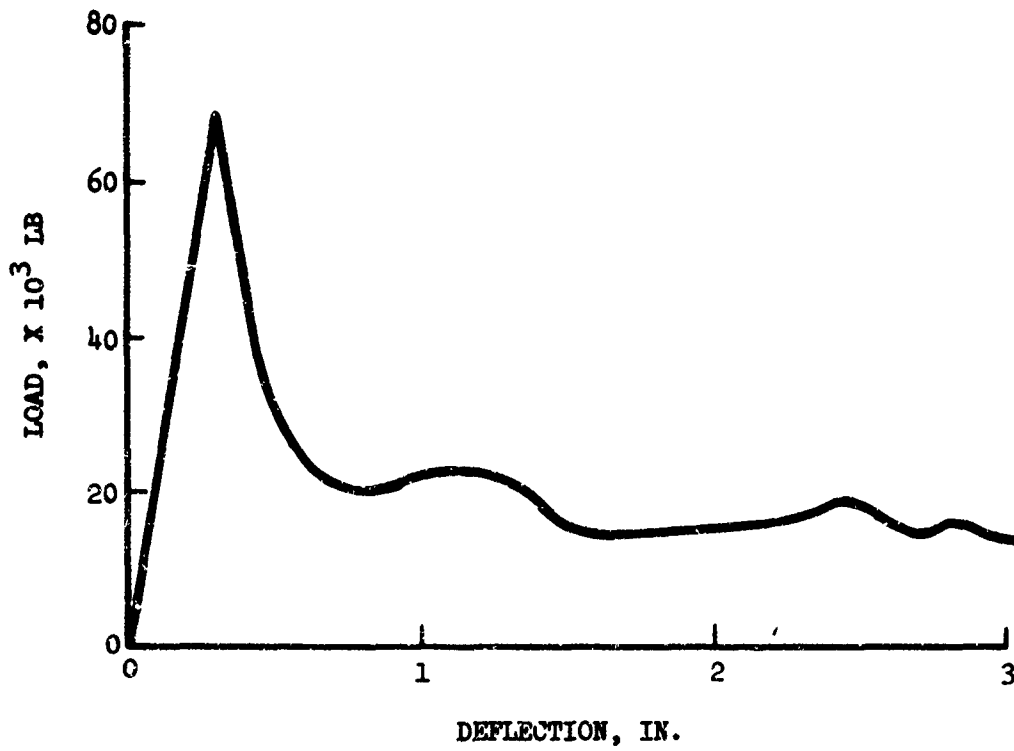


Figure 62. Load Versus Deflection, Test 11.

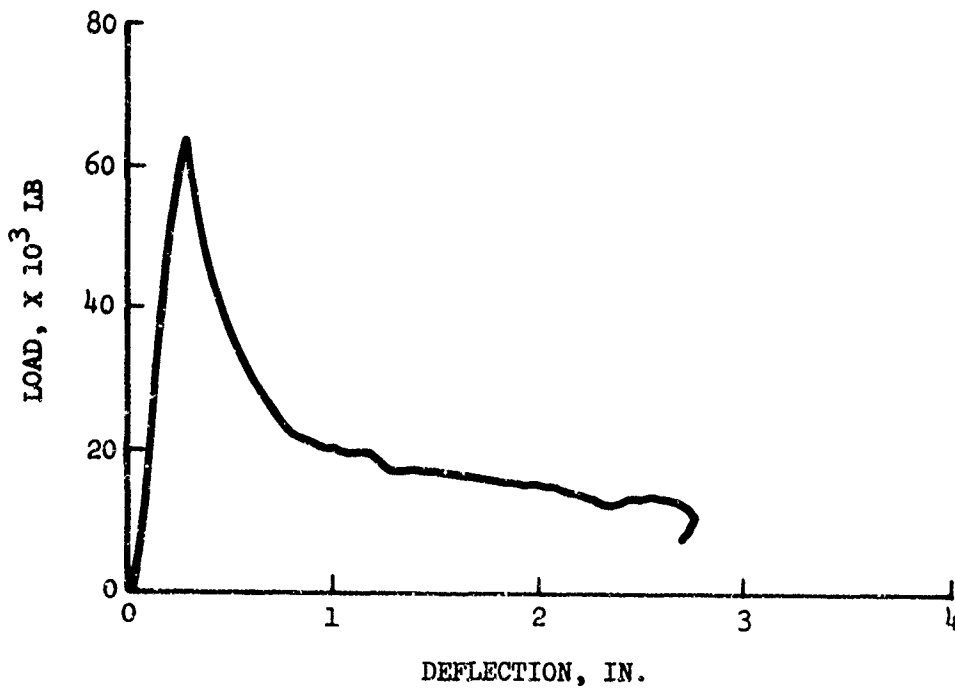


Figure 63. Load Versus Deflection, Test 12.

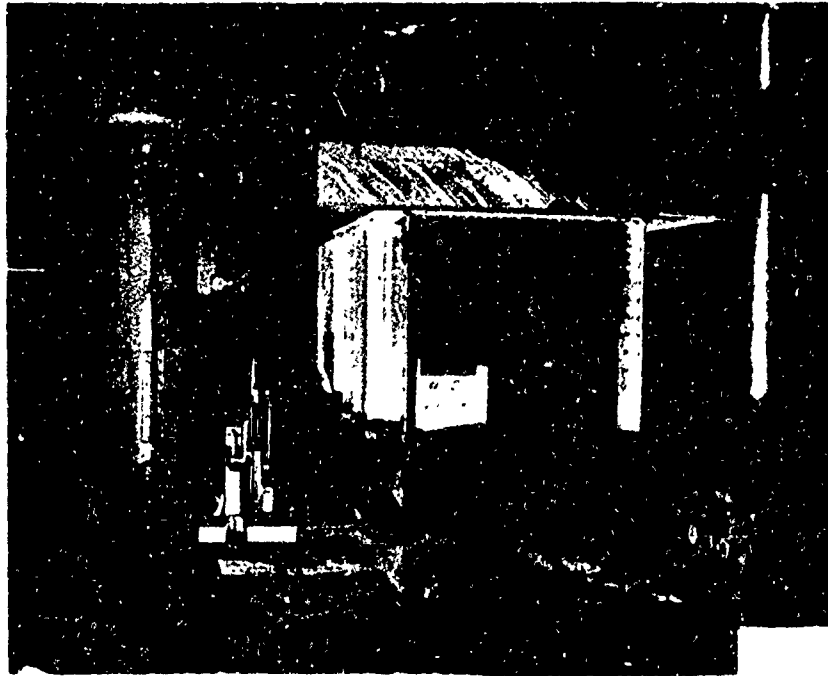


Figure 64. Setup for Specimen 12.

As anticipated, the failure load of Specimen 12 was higher than that experienced by specimen 10 (68,000 lb vs. 39,000 lb).

Figures 65 through 70 show the post-test condition for specimen 1 through 6, respectively. Figures 71 and 72 shows a side-by-side comparison of specimens 5 and 6 after equal energy dynamic impact tests at 30 ft/sec and 14 ft/sec, respectively. The post-test condition is very similar for the two specimens. Figures 73 through 77 show the post-test condition of specimens 7, 8 and 9 individually and side-by-side. The test of these specimens provides data regarding the comparative effects of dynamic versus static testing on load-deflection characteristics. The test results indicate that the lower the impact velocity, the more severely the specimen is deflected, the most extreme deflection occurring under static load. In addition, the lower the impact velocity, the less springback* is evident immediately after the load is released from the specimen. From Table XIX, the springback effect is shown to be as high as 40% of the maximum deflection for a 27-ft/sec impact velocity (specimen 8) but is reduced to 25% at a 14-ft/sec impact velocity (specimen 7). For specimens 5 (30 ft/sec) and 6 (14 ft/sec), the springback effect is 31% and 12%, respectively.

*Springback is defined here as $\frac{\text{Maximum deflection} - \text{permanent deflection}}{\text{Maximum Deflection}}$

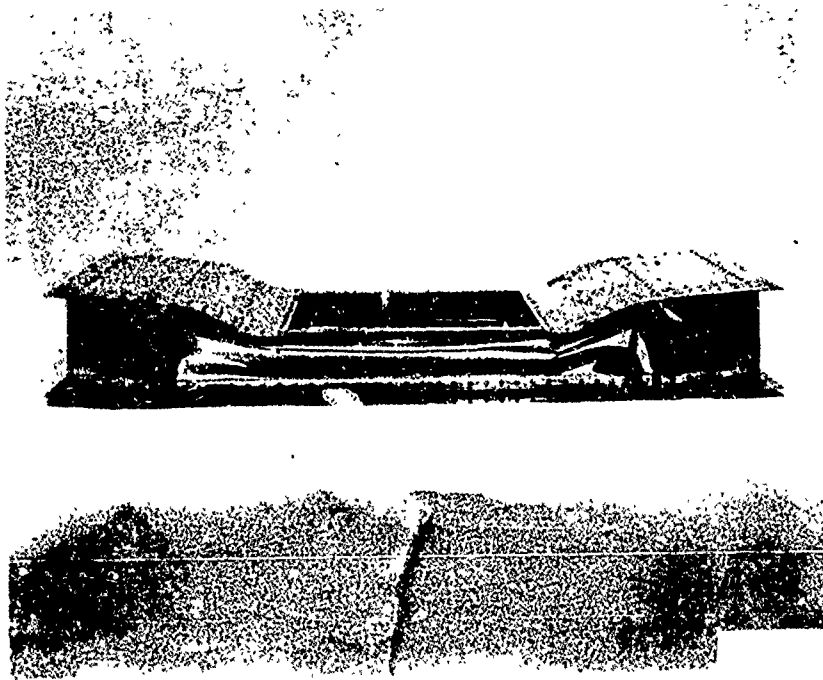


Figure 65. Post-Test Condition of Specimen 1.

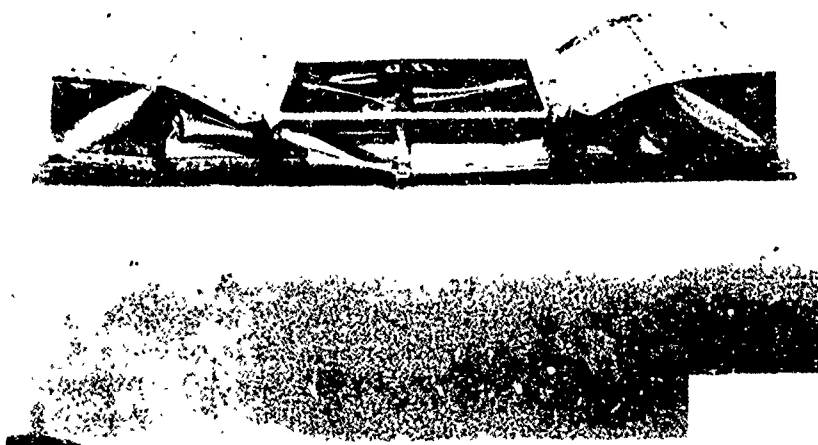


Figure 66. Post-Test Condition of Specimen 2.

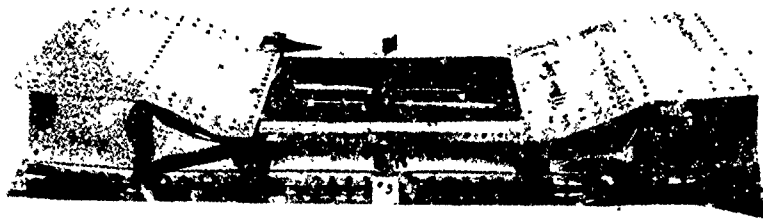


Figure 67. Post-Test Condition of Specimen 3.

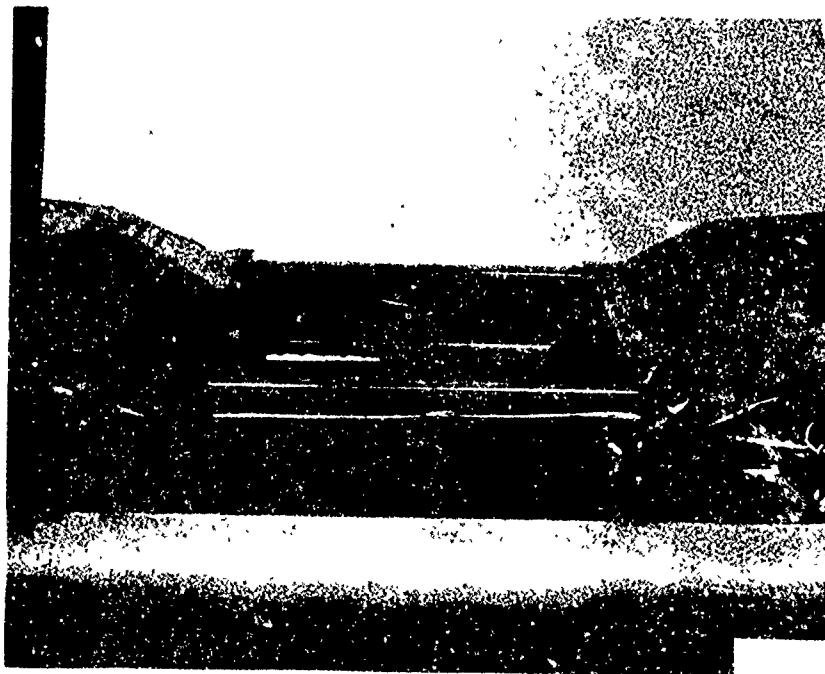


Figure 68. Post-Test Condition of Specimen 4.



Figure 69. Post-Test Condition of Specimen 5.



Figure 70. Post-Test Condition of Specimen 6.

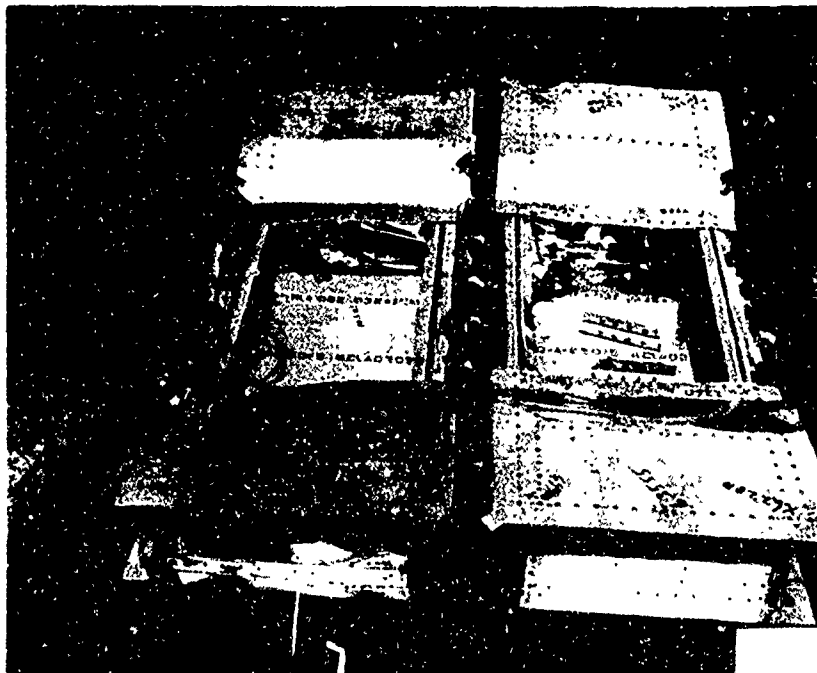


Figure 71. Comparison of Post-Test Damage for Specimens 5 and 6 (End View).

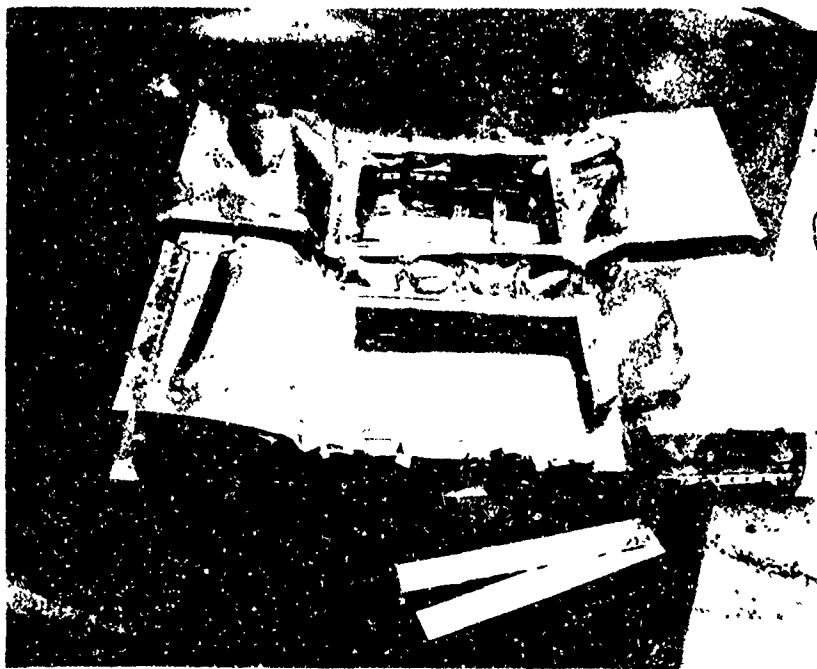


Figure 72. Comparison of Post-Test Damage for Specimens 5 and 6 (Top View).

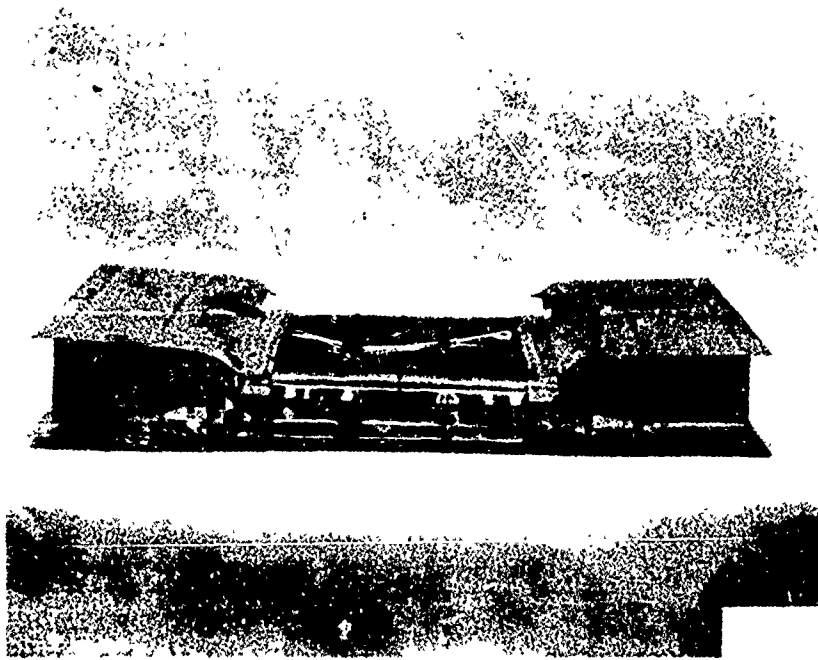


Figure 73. Post-Test Condition of Specimen 7.



Figure 74. Post-Test Condition of Specimen 8.

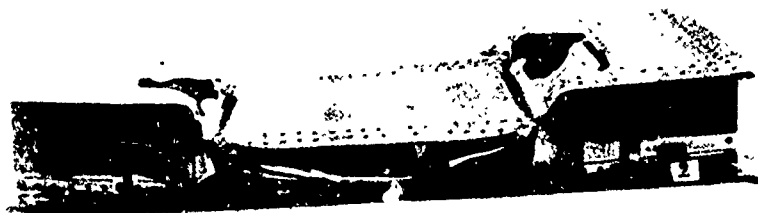


Figure 75. Post-Test Condition of Specimen 9.

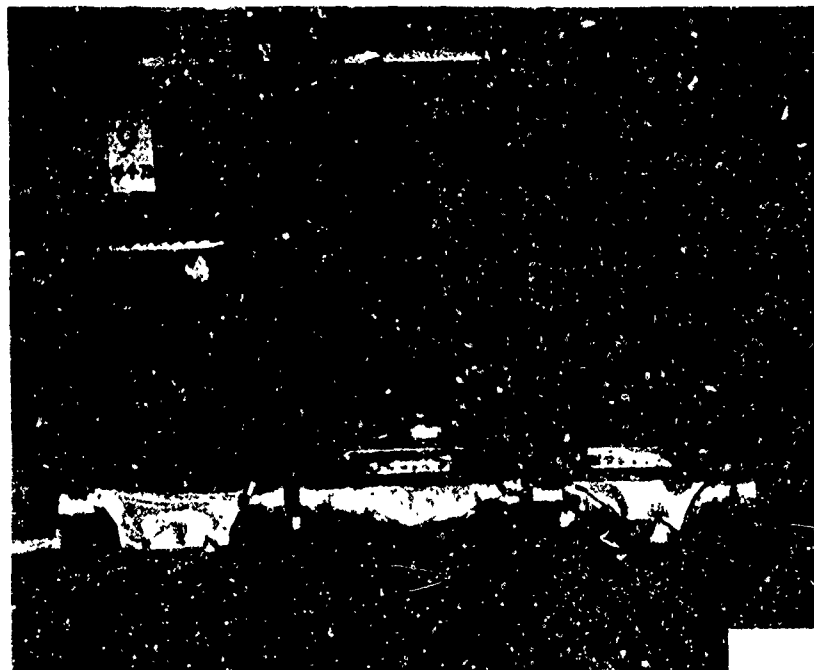


Figure 76. Comparison of Post-Test Damage to Specimens 7, 8 and 9 (Top View).

Figures 78 through 82 show the post-test condition for specimens 10, 11 and 12 (12.125-inch-deep specimens). Unlike all the other tests, specimen No. 12 was tested with two line supports. The post-test condition differs considerably from specimen 10 with which specimen 12 was identical except for the load restraint system (four-edge versus two-line support). There is more of a beam bending mode of failure present in specimen 12. Specimen 11 is similar, in general configuration, to specimen 10 except with thicker angles and skins and as anticipated withstands a considerably higher failure load (69,200 lb versus 39,000 lb) and absorbs more energy (73,800 in.-lb versus 51,750 in.-lb). Figure 81, in which a comparison of specimens 10 and 11 is shown, indicates a similar type of failure for both specimens.

A review of post-test damage photographs (Figures 65 through 80) indicates that the assumptions regarding the formation of a plastic hinge at the threshold of failure, the cross-section of the structure participating in forming a plastic hinge (flange warping), and the symmetry associated with the mode of failure for the stiffened panels are generally valid. However, the failure patterns for the stiffened panels are irregular from one test to another test and for each stiffener location. While plastic hinges do form at many locations they do not always form at every constraint support or necessarily at each midpoint of all the stiffened panels. There appears to be evidence of hinge formation in varying degrees for specimens 2 through 11. In nearly all the cases the angle stiffener flanges warp. An exception to this is specimen 1 which had the least number of angle stiffeners and failure was initiated by rivet pull-out. However, in about half the test results there is noticeable warping of the main beam flange. For several of the specimens (Figures 69-74) warping of the main beam flange is quite noticeable. The failure pattern of the stiffened panels indicates symmetrical failure modes for nearly half the specimens (1, 3, 7, 8, 11) and an equal number clearly unsymmetrical.

The effect of each of the above-mentioned analytical assumptions on the comparison between the analysis and test results is discussed, in detail, in the following section entitled Correlation. Where applicable, potential modifications to the analyses, which utilize empirical data, that will enhance prediction capability, are discussed.

The most significant implication of the above observations is that the overall failure modes of the specimens are predictable although the exact failure mode of each individual element is difficult to predict.

Although the individual stiffeners and panels deform under different modes (due to differences in design and imperfections) the overall deformation modes indicate a consistent trend. For example, although specimens 2 and

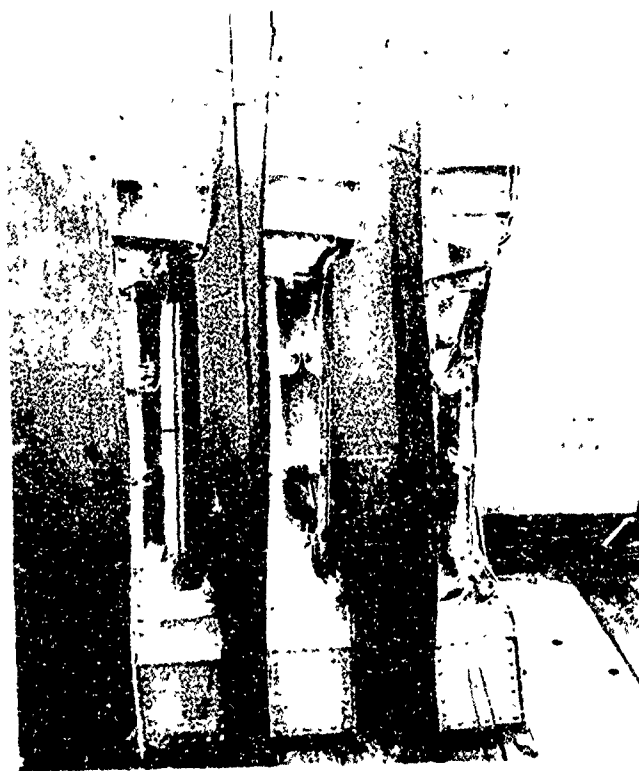


Figure 77. Comparison of Post-Test Damage for Specimens 7, 8 and 9 (Side View).



Figure 78. Post-Test Condition of Specimen 10.

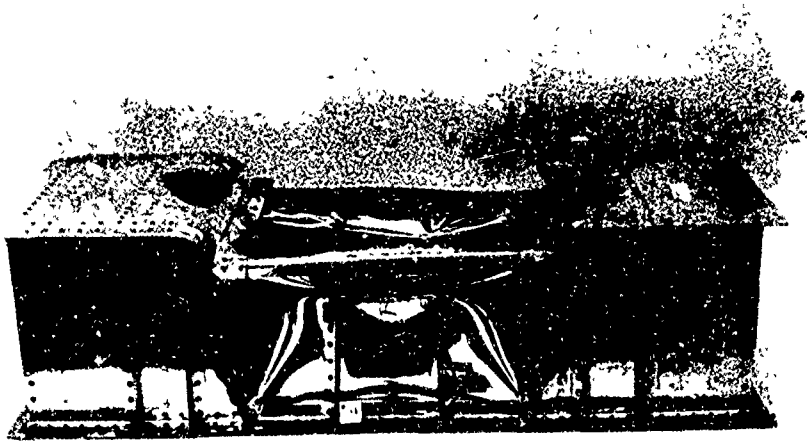


Figure 79. Post-Test Condition of Specimen 11.

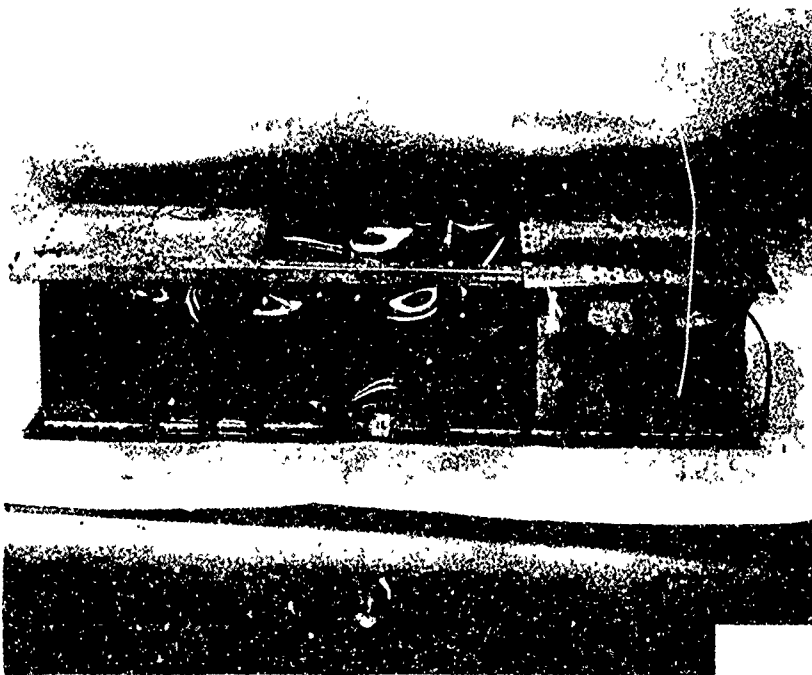


Figure 80. Post-Test Condition of Specimen 12.

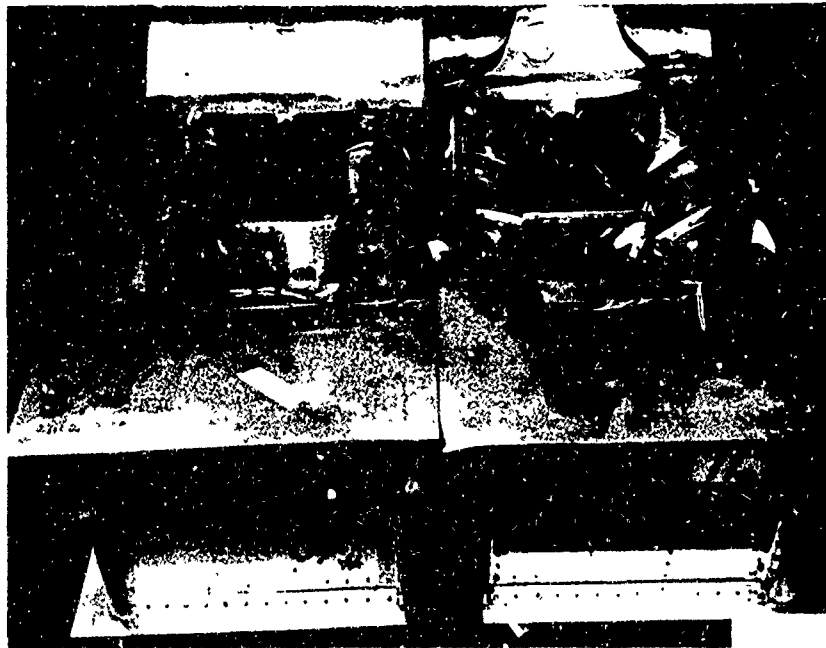


Figure 81. Comparison of Post-Test Damage for Specimens 10 and 11 (Top View).



Figure 82. Comparison of Post-Test Damage for Specimens 10 and 12 (Side View).

3 are supposedly identical in design and energy-absorption capability, the post-test configurations show entirely different deformation modes for individual elements, but the load-deflection curves are nearly identical (Figures 53 and 54). This aspect of the validity of the analytical assumptions relative to the overall results is discussed in more detail in the Correlation section under the Remarks on the Initial Analytical Assumptions subsection.

All the strain gage data that was obtained during the test program is presented in Volume II under the section entitled Test Data.

CORRELATION

GENERAL

A comparison of test and analytical data for the 12 test specimens is presented in Table XX. The predicted versus test load-deflection curves are presented in Figures 83 through 94. The comparison of test and analytical data shows reasonable agreement for the crushing characteristics of the model specimens selected in this program as representative of a segment of the UH-1H fuselage.

Test specimens 1 and 2 afford the opportunity to assess changes in design configuration (difference in the number of angle stiffeners) under an identical loading condition. Test specimens 2 and 3 provide an opportunity to compare analysis and test for specimens with and without bulkhead lightening holes, under identical loading conditions.

A comparison of load-deflection characteristics under static and dynamic loading conditions is obtained from the analysis and test of specimens 3 and 4 and for specimens 7, 8 and 9. The effect of the impact mass on the response of the structure can be obtained from the analytical and experimental results between specimens 5 and 6, and between specimens 7 and 8.

Finally, specimens 10, 11 and 12 provide the opportunity to exercise the analytical approach for deeper (12.125 inches versus 6.125 inches) specimens and compare the effect of line supports in lieu of four-edged supports.

COMPARISON OF TEST AND ANALYSIS LOAD-DEFLECTION CURVES

Results of the analysis and tests for specimens 1 and 2 are shown in Figures 83 and 84, respectively. The analysis predicts the peak failure load within 15%. The deflection at peak failure, from the analysis, is a lower value (0.10 to 0.20 inch) than that obtained experimentally (0.25 to 0.40 inch). The deflection at the analytically predicted peak failure value is the point at which the post-failure load-deflection curve intersects the computed peak-failure load value. This matching process is described, in detail, in the sections entitled Substructure Analysis and Design Procedures.

The lower initial slope in the test load-deflection curves (Figures 83 and 84) is attributed to the indentation of the bottom skin rivet heads into the wood support used to distribute the loads. The wooden support was used for tests 1 through 6. Thereafter, an aluminum support was used when load cells were installed for the second series of dynamic tests. The wooden support is not considered to have significantly influenced the overall results.

TABLE XX SUMMARY OF COMPARISON BETWEEN TEST RESULTS AND PREDICTED VALUES

Specimen No.	Type of Test	Peak Loads (Lb)		Energy Absorbed (In.-Lb)		Percent Error Between Predicted and Test Results	
		Test	Predicted	**** Test	Predicted	Peak Load	Energy Absorbed
1	Static	14200	12700	28850	26375	-10.6	-8.6
2	Static	26400	28500	45400/41800	39975	+ 8	-4.3
3	Static	26100	28500	45150/41400	39975	+ 8.0	-3.4
4	Dynamic (17 Ft./Sec)	26880	28500	44900/40360	39975	+ 6.8	-1.0
5	Dynamic (30 Ft./Sec)	84840	68500	111130/102900	129800	+22.5	+26.3
6	Dynamic (14 Ft./Sec)	90000	68500	124250/117860	129800	+24.	+10.2
7	Dynamic (14 Ft./Sec)	133000	138000	136000	128000	+ 3.7	- 5.9
8	Dynamic (27 Ft./Sec)	144000	138000	134750**	113000**	- 3.9	-17.8
9	Static	132000	138000	130000	128000	+ 4.5	- 1.54
10	Static	39000	40000	51750	45000	+ 2.5	-13.0
11	Static	69200	63700	83600	70100	-8.0	-16.1
12	Static	65330	66100	70000***	51000	+ 1.3	-27.1

* ENERGY Calculated for 3.5 inches deflection; all other calculations for 3.0 inches deflection unless otherwise noted

** Energy based on 2.45 inches of deflection

*** Energy based on 2.8 inches of deflection

**** Test value for peak loads and energy absorbed for specimens 4, 5 and 6 are based on accelerometer data. Test values for specimens 7 and 8 are based on load cell data.

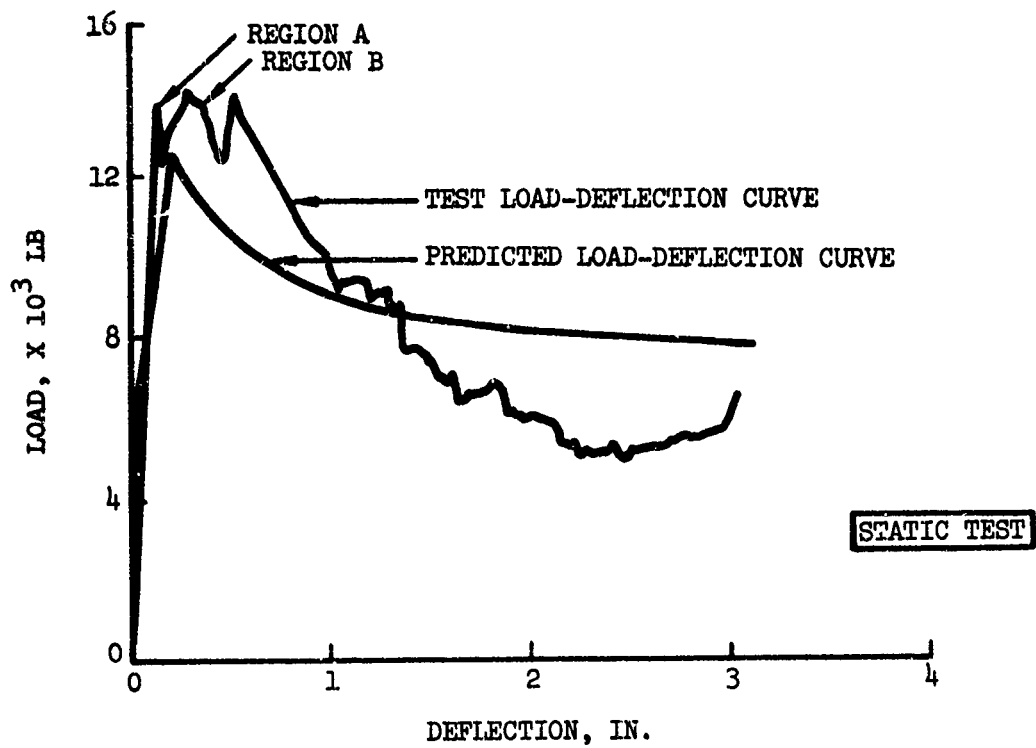


Figure 83. Predicted Versus Test Load-Deflection Curves for Specimen 1.

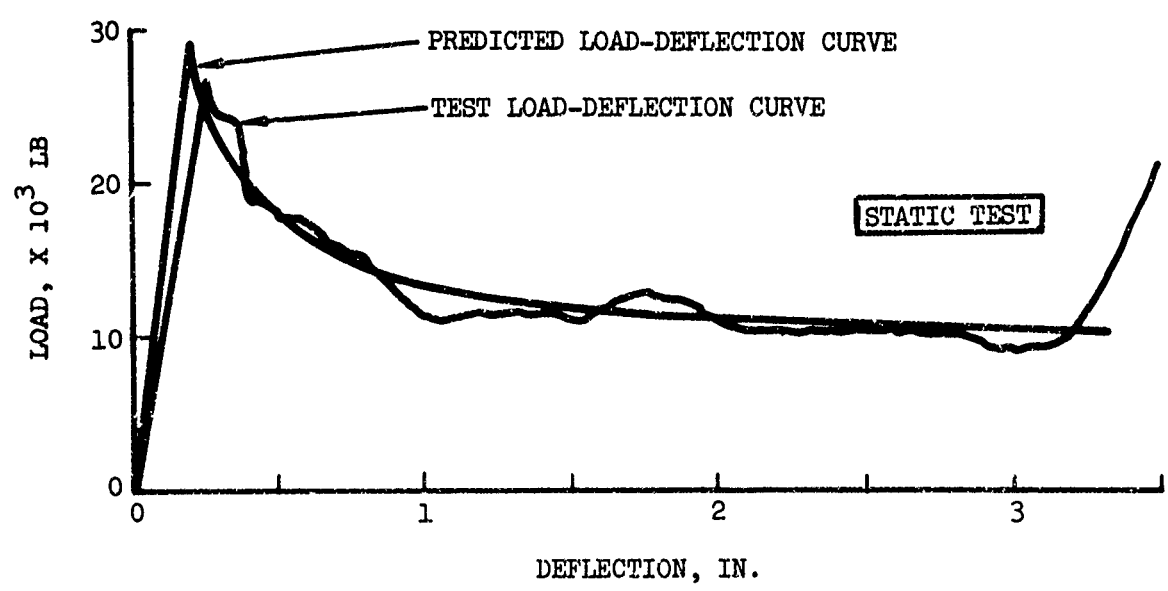


Figure 84. Predicted Versus Test Load-Deflection Curves for Specimen 2.

For specimen 1 the deformation mode started with the buckling of the central bay (Bay (3), Figure 47), side skin, and the two transverse bulkheads (C and D, Figure 47). The center bay spacing is 18 inches and the distance between the end stiffeners is also 18 inches. As the deformation increased, the skin tore out from the stiffeners at the rivet locations. At this point, the load suddenly increased by approximately 2000 pounds (Region A, Figure 83). After this initial tearing incident, the load increased until additional skin tore out from other rivet locations. The load decreased again, as is noted by Region B in Figure 83. The third peak load point in Figure 83 is believed to have occurred after tearing had been experienced at several rivet locations. The maximum crushing strength appears to have been encountered in the second or third peak load value. After crushing, the load gradually decreases to approximately 5000 pounds. Beyond a deflection of 3 inches, which corresponds to approximately half of the specimen height (6.125 inches), the load started to increase rapidly. This increase is attributed to increased stiffness developed from the trapped material as the specimen is crushed.

The predicted value shown in Figure 83 is based on procedures similar to the one given in the example of specimen 2. First, the monolithic failure stress is calculated; then, by taking into account rivet strength/geometry effect, a modified failure stress can be obtained. From the latter stress, the failure (or peak) load is estimated. It is felt that the failure load by this approach falls somewhere between the monolithic failure load and the complete wrinkling failure load.

The discrepancies between the test result and the prediction are: (1) for the deflection in the range between 0.2 to 1.0 inch, the successive (three times) abrupt failure mode changes from monolithic to rivet tearing failure, observed during the test, are believed to be responsible for the experimental load being higher than that obtained from the analyses; and (2) after a deflection of 1.5 inches complete tear-out of the angle stiffener occurred, drastically reducing the post-failure plastic bending moment, and in turn reducing the experimental load substantially below the predicted load.

For specimen 2, additional angles were added over that shown in the basic drawing (specimen 1); 1 inch x 1 inch x 0.032 inch angles were added outside of bulkhead stations C and D. In the middle of Bay (3) (see Figure 51), the skin is stiffened by two angles, one on each side of the web (inside and outside). Eight angles were added to the specimen along the side skins. The comparison of predicted and test load-deflection curves is given in Figure 84.

Because the side skins are reinforced by angle webs at both sides, the rivet tearing did not occur prior to failure load. As the crushing deformation increased, however, the specimen failed at various locations (i.e., skin was torn from the stiffener web). Free warping of the stiffener flanges, assumed in the post-failure analysis and noted in Figure 66, justifies the conservative estimate of rigid-plastic hinge moment used in

the analysis. In Figure 84, it is seen that, in general, close agreement is achieved between test and analysis except for the difference between the time of occurrence of the peak loads. This discrepancy in analysis is believed to be caused by two factors: (1) the neglect of stiffness changes during the post-buckling stage up to the failure point, and (2) the assumption of rigid-plastic hinge mechanisms while ignoring interactions of the complicated stress state.

Specimen 3 is identical with specimen 2 except for the bulkhead skins which are solid (no lightening holes). Even though the initial buckling load might be different, it was anticipated that the ultimate load would not be noticeably different from the one with lightening holes, since the effective width of the skin varies very little at the failure stress level. The comparison of the experimental load-deflection curves of specimen 2 versus Specimen 3 (Figures 84 and 85) shows that this assumption is accurate. Figures 66 and 67, which show the post-test condition of specimens 2 and 3, also indicate similar failure modes for the two specimens.

Specimen 4, which is identical to specimen 3, was tested under dynamic loading conditions using the same four-edge boundary condition as the first three static tests. An 840 pound mass was dropped with a maximum impact velocity of 17 ft/sec. The calibrated load-deflection curve, based on the accelerometer level located near the center of the impact head, is given in Figure 86 together with the predicted curve. For specimen 4, the maximum deflection is about 3.75 inches at a time of 40 msec. The maximum g-level is estimated to be approximately 31 g's, which is equivalent to a peak dynamic load of about 26,880 pounds. The final deflection was recorded to be 2.54 inches. The data sampling rate used during this test was 750 samples/second. It is slightly lower than desired and, consequently, may have resulted in a lower peak load. For all the subsequent dynamic tests, a data sampling rate of 1500 samples/second was used to ensure obtaining peak values within the desired frequency range (≤ 300 Hz). Figure 86 shows that the predicted peak failure load is approximately 6.8% higher than the test value using faired accelerometer data. The failure deflection point, as in previous comparisons, is lower for the analysis as compared to the test.

Specimens 5 and 6 are the same as specimen 4, except for the added thicker gage angles between the bulkhead stations (C) and (D), Figure 47, and for the replacement fasteners that attach the angle to the main beam (stiffener) web which are 0.25-inch-diameter screws. The screws are installed to prevent a separation of the angles from the side stiffeners due to tearing or tension failure at the higher impact velocity of 30 ft/sec (specimen 5). Specimen 6 was tested at 14 ft/sec, so the impact head weight had to be increased to 3550 pounds to ensure that both specimens, 5 and 6, were tested at the same energy level. Figures 87 and 88 show a comparison of the load-deflection curves for specimens 5 and 6, respectively. As in the test of specimen 4, the load values were obtained from faired accelerometer data. As can be noted in Figures 86, 87 and 88, the oscillations in the accelerometer readings make it difficult to define the continuous load-stroke curve. At best, it can be ascertained that the accelerometer

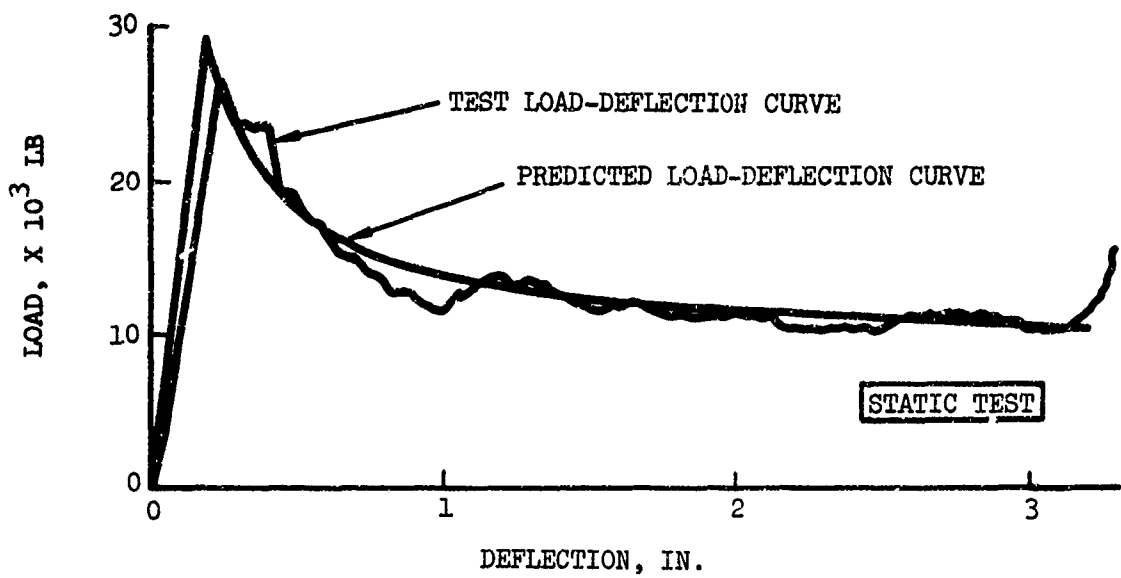


Figure 85. Predicted Versus Test Load-Deflection Curves for Specimen 3.

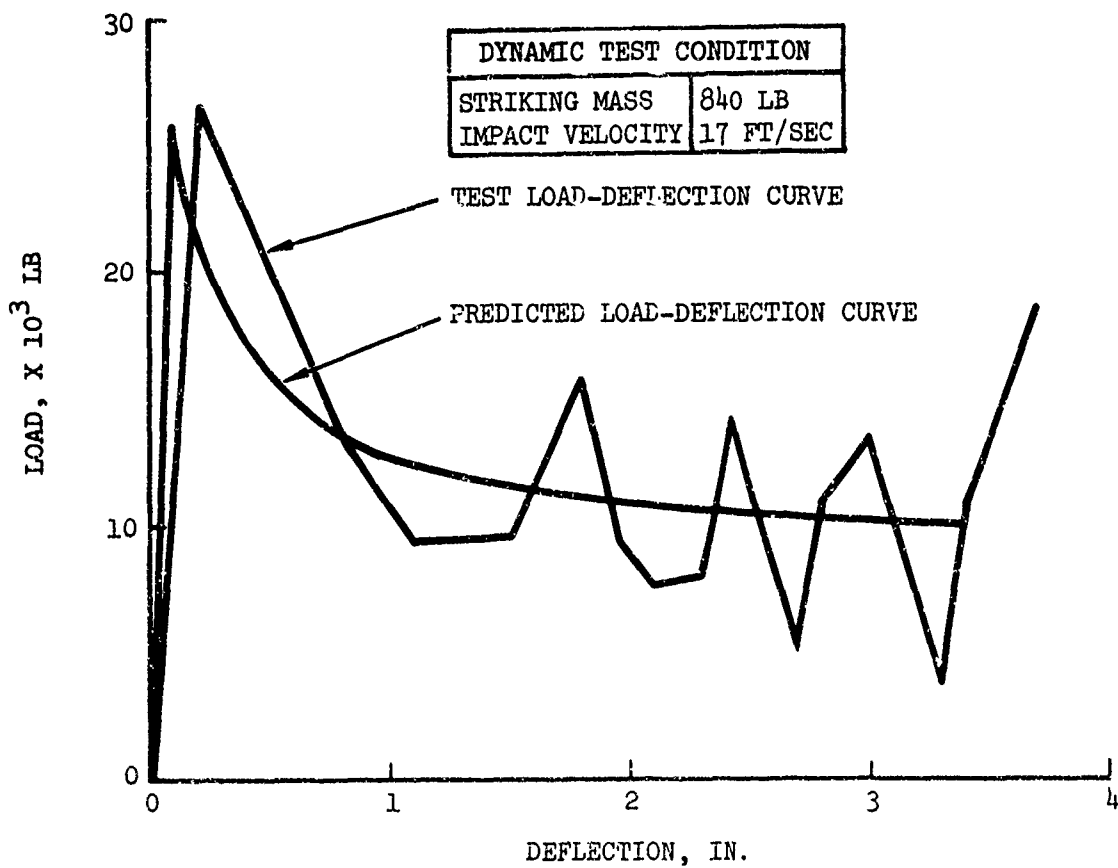


Figure 86. Predicted Versus Test Load-Deflection Curves for Specimen 4.

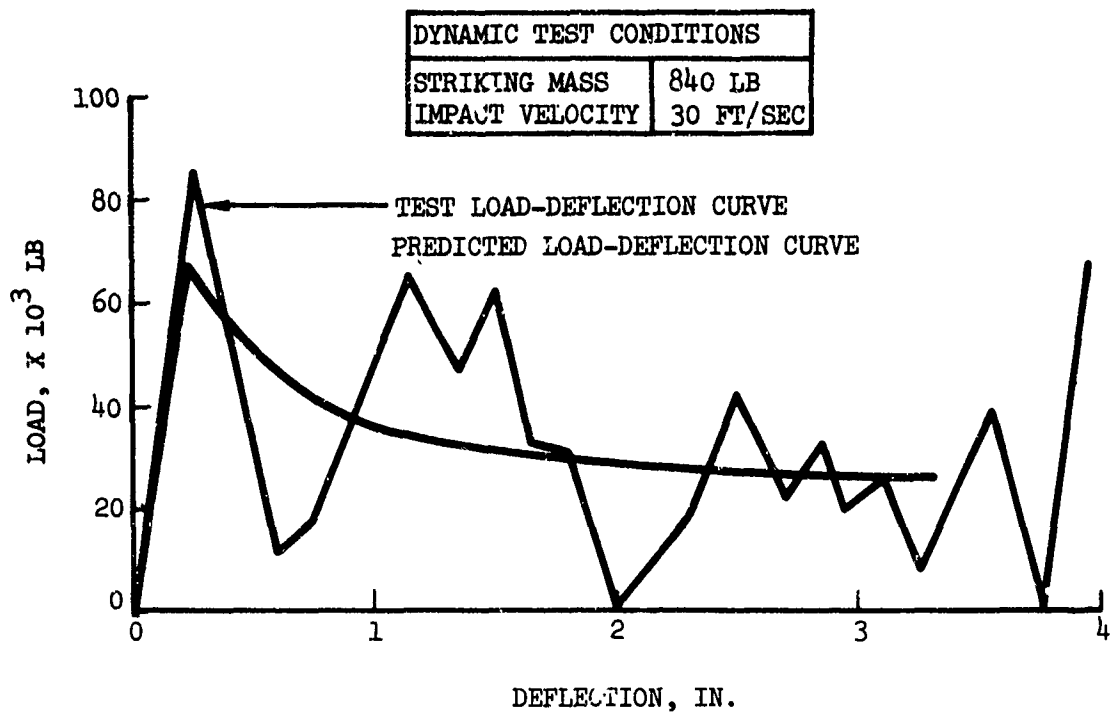


Figure 87. Predicted Versus Test Load-Deflection Curves for Specimen 5.

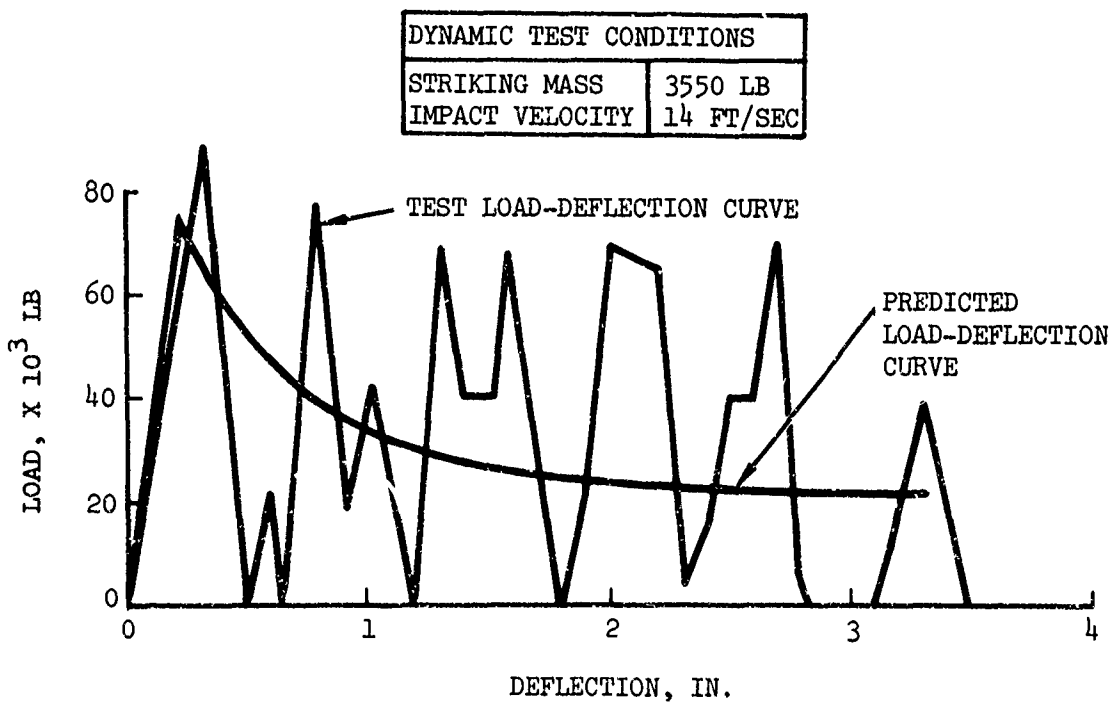


Figure 88. Predicted Versus Test Load-Deflection Curve for Specimen 6.

response level is faired about a mean curve. All subsequent dynamic tests (7 and 8) were performed with load cells installed between the support and the ground. This setup was described earlier in the section entitled Sub-structure Test Program. The mode of failure for specimens 5 and 6 is very similar, as can be noted in Figure 71. Using faired accelerometer data, the difference between experimental and predicted peak values for specimens 5 and 6 is between 22.5% and 24%.

Tests 7, 8 and 9 were designed to test the same configuration of specimens (except for lower skin for specimen 9) under three conditions: 27 ft/sec impact velocity, 14 ft/sec impact velocity, and statically. In these tests, load cells were installed beneath the four-edge support and the ground surface. The results of these tests are shown in Figures 89, 90, and 91. The load cells appear to provide a better definition of the load than is obtained from accelerometer readings, which are influenced by the frequencies of the total system, including impact head, carriage, tower, and specimen. The results of these three tests also show that for this type of structure, static tests are sufficiently accurate to determine load-deflection characteristic shape, peak load and post-failure load. However, in dynamic tests the springback effect is immediate, and the structure will experience slightly lower deflection values than when tested statically. The predicted load-stroke curve for the static load condition was used for all three cases, and the peak failure load varied from -3.9% to 4.5% from the peak load obtained from the load cell data. The maximum load obtained during the 27-ft/sec dynamic impact test is 144,000 pounds, and the failure load experienced in the static test is 132,000 pounds. The difference between peak static and dynamic (27 ft/sec) failure load for this type of specimen is approximately 9%.

The comparisons of predicted and test load-deflection curves for specimens 10, 11 and 12 are shown in Figures 92, 93 and 94. The discrepancy between predicted and test failure loads obtained for specimens 10, 11 and 12 is between +1.3% and -8%. A slight slippage of one of the supports, which was noted at the conclusion of the test, may account for the "diagonal" like buckling failure mode indicated in Figures 80 and 82.

COMPARISON OF TEST AND ANALYSIS ENERGY ABSORPTION

Table XX summarizes the comparative values of energy absorption and the percentage of difference between test and analysis. The analysis ranges from -27.1% (specimen 12) to 26.3% (specimen 5) of the measured data. For specimens 1 through 4 the analysis is between -1% and -8.6%. For specimens 6, 7, 8, 9 and 10, the predicted energy absorbed is +10%, -6%, -1.8%, -1.5% and -13%, respectively. The shape of the post-failure load-deflection curve will greatly influence the amount of energy that is absorbed. The analysis, with its assumed plastic hinge moment, presents a lower bound post-failure curve and thus, in general, is expected to underestimate the structural energy absorption capability. This occurs in 10 of the 12 specimens tested.

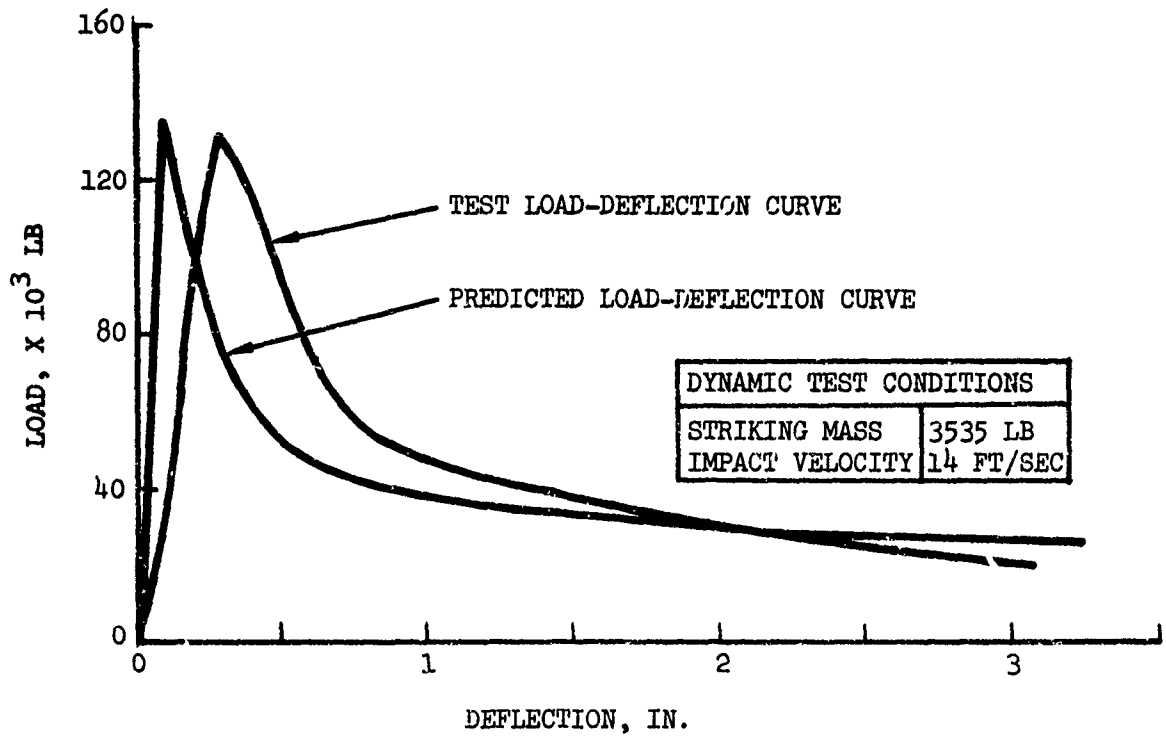


Figure 89. Predicted Versus Test Load-Deflection Curves for Specimen 7.

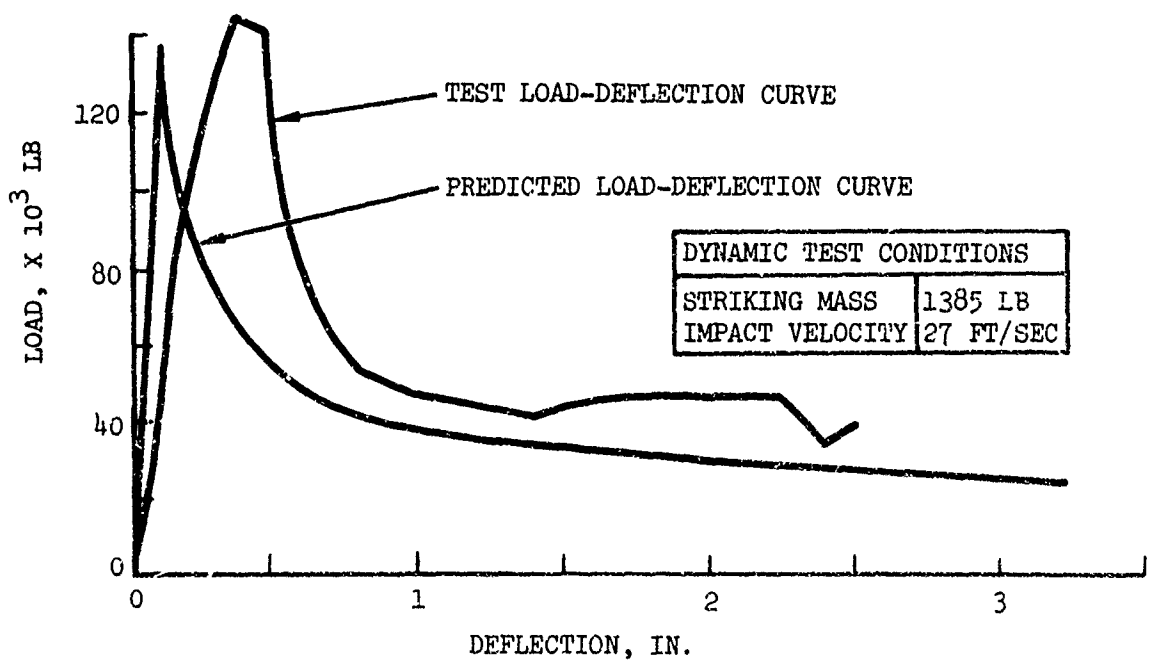


Figure 90. Predicted Versus Test Load-Deflection Curves for Specimen 8.

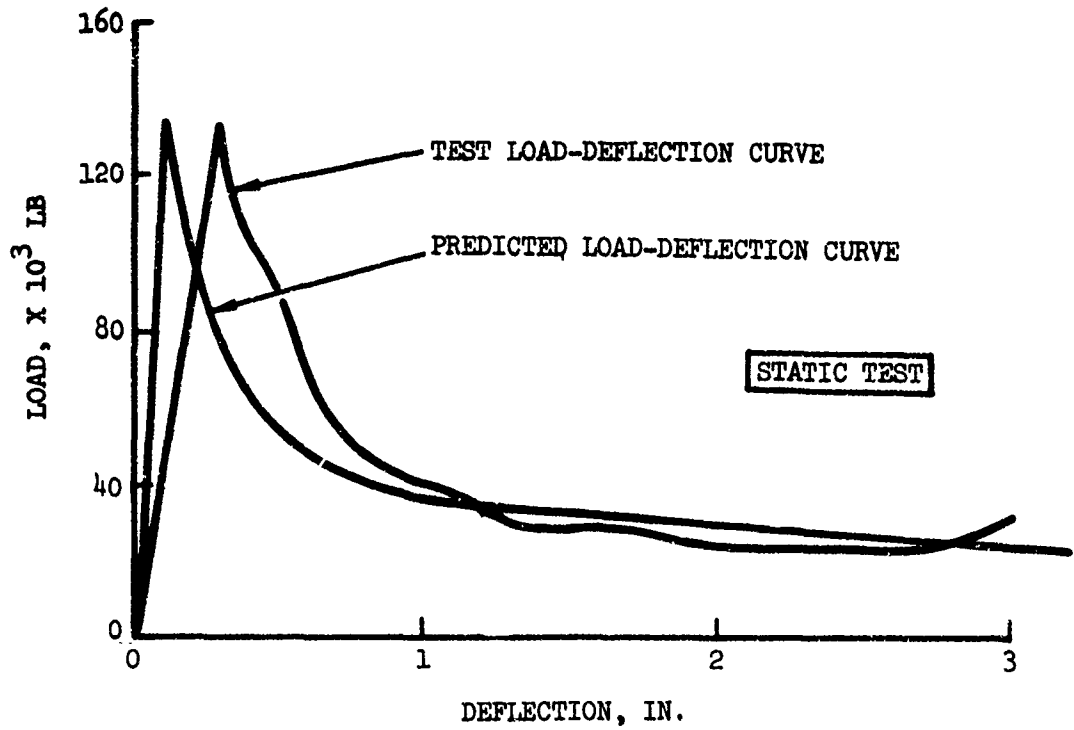


Figure 91. Predicted Versus Test Load-Deflection Curves for Specimen 9.

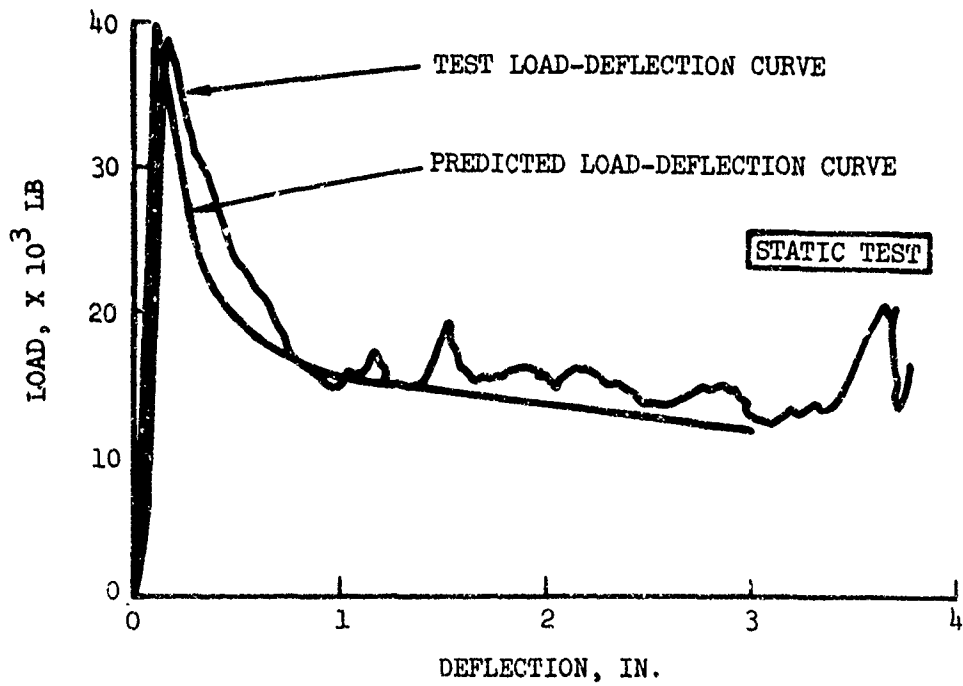


Figure 92. Predicted Versus Test Load-Deflection Curves for Specimen 10.

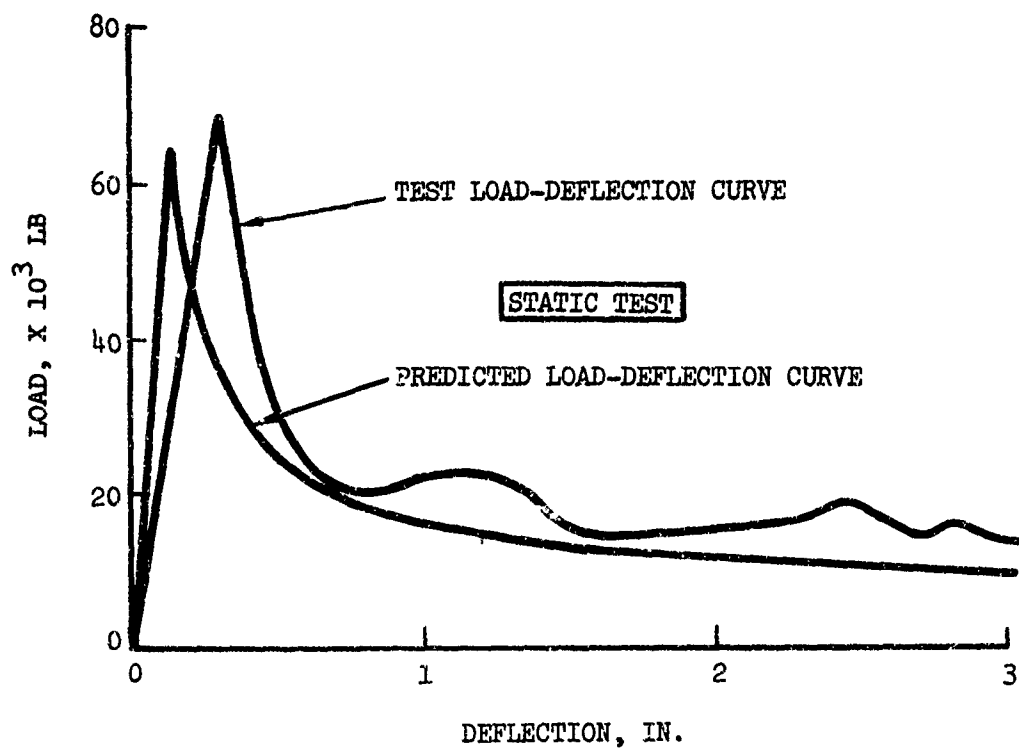


Figure 93. Predicted Versus Test Load-Deflection Curve for Specimen 11.

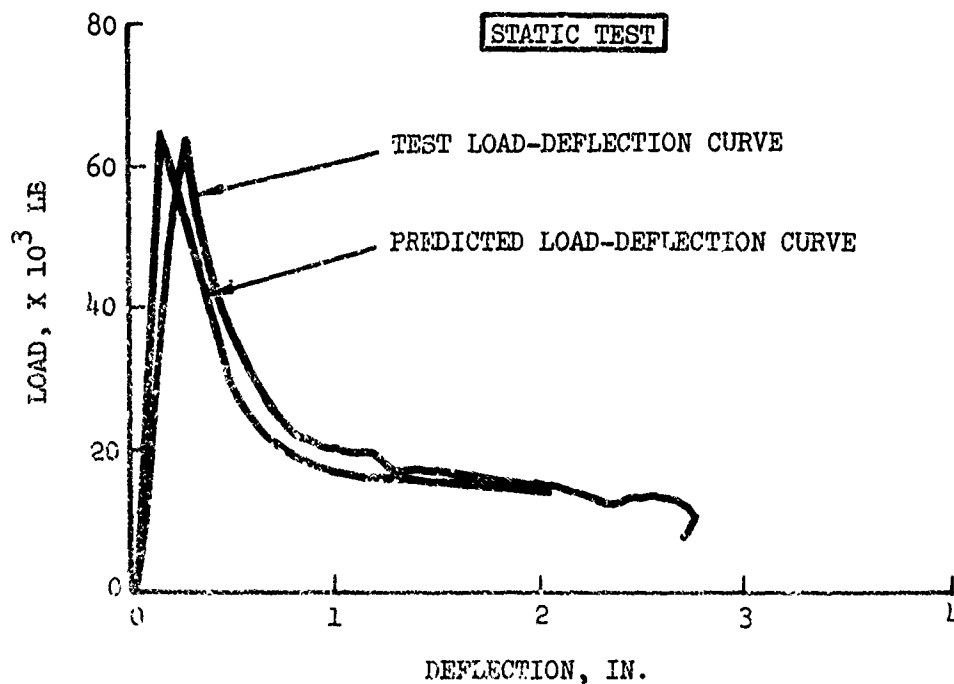


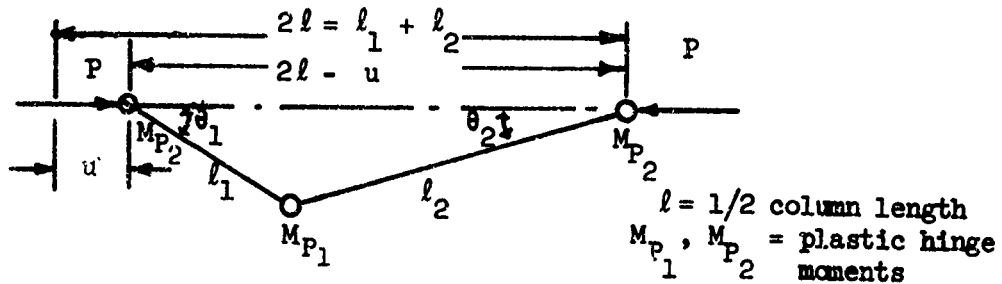
Figure 94. Predicted Versus Test Load-Deflection Curves for Specimen 12.

The following sub-sections discuss the effect of the initial assumptions on the comparison between analysis and test results previously described. In addition, empirically based correction factors, which are designed to improve predictions of failure and the post-failure load-deflection curve, are presented, where applicable.

REMARKS ON THE INITIAL ANALYTICAL ASSUMPTIONS

Plastic Hinge Formation

The post-failure analysis is based on the plastic hinge forming in a symmetrical manner as is shown in Figure 26a. While the analytical prediction based on such a mode yields reasonable results, it has been observed from the tests performed, during the study described herein, that an asymmetric plastic hinge mode occurred in some of the panels. An asymmetric plastic hinge mode, as shown in the sketch below, may result from structural imperfections.



The energy expression for the above asymmetric mode system is as shown below:

$$\int P. du = \int (M_{P1} + M_{P2}) \cdot \delta (\theta_1 + \theta_2) \quad (38)$$

From geometry

$$l_1 \cos \theta_1 + l_2 \cos \theta_2 = 2l - u \quad (39)$$

$$l_1 \sin \theta_1 - l_2 \sin \theta_2 = u \quad (40)$$

By squaring both sides of Equations (39) and (40)

$$l_1^2 \cos^2 \theta_1 + l_2^2 \cos^2 \theta_2 + 2 l_1 l_2 \cos \theta_1 \cdot \cos \theta_2 = (2l - u)^2 \quad (41)$$

$$l_1^2 \sin^2 \theta_1 + l_2^2 \sin^2 \theta_2 - 2 l_1 l_2 \sin \theta_1 \sin \theta_2 = 0 \quad (42)$$

By adding Equations (41) and (42) and using trigonometric identities, Equation (43) is obtained.

$$2l_1 l_2 \cos (\theta_1 + \theta_2) = (2l - u)^2 - (l_1^2 + l_2^2) \quad (43)$$

Equation (43) can be rearranged as shown:

$$\delta (\theta_1 + \theta_2) = - dz / (1-z)^{1/2} \quad (44)$$

where

$$z = \left[(2l - u)^2 - (l_1^2 + l_2^2) \right] / 2l_1 l_2 \quad (45)$$

Therefore

$$\delta (\theta_1 + \theta_2) = \frac{(2l - u)}{\sqrt{4l_1 l_2 - 4l u + u^2}} \cdot \frac{\delta u}{\sqrt{u(l - u/4)}} \quad (46)$$

Equation (47) is obtained by substituting Equation (46) into Equation (38).

$$\int \left(P - Q(u) \cdot \frac{M_P}{\sqrt{u(l - u/4)}} \right) \cdot \delta u = 0 \quad (47)$$

where

$$Q(u) = \frac{(2l - u)}{\sqrt{4l_1 l_2 - 4l u + u^2}} \quad (48)$$

From Equation (47)

$$P = Q(u) \left[\frac{M_P}{\sqrt{ul - \frac{u^2}{4}}} \right] \quad (49)$$

Equation (49) has the identical form as Equation (17) except for the weighting term $Q(u)$. It is concluded that for asymmetric cases the post-failure load can be estimated by multiplying the expression shown in Equation (17) by the sensitivity factor $Q(u)$ described by Equation (48).

Figure 95 shows the sensitivity factor versus deflection (crushing deformation) for panel depths of 6 inches and 12 inches.

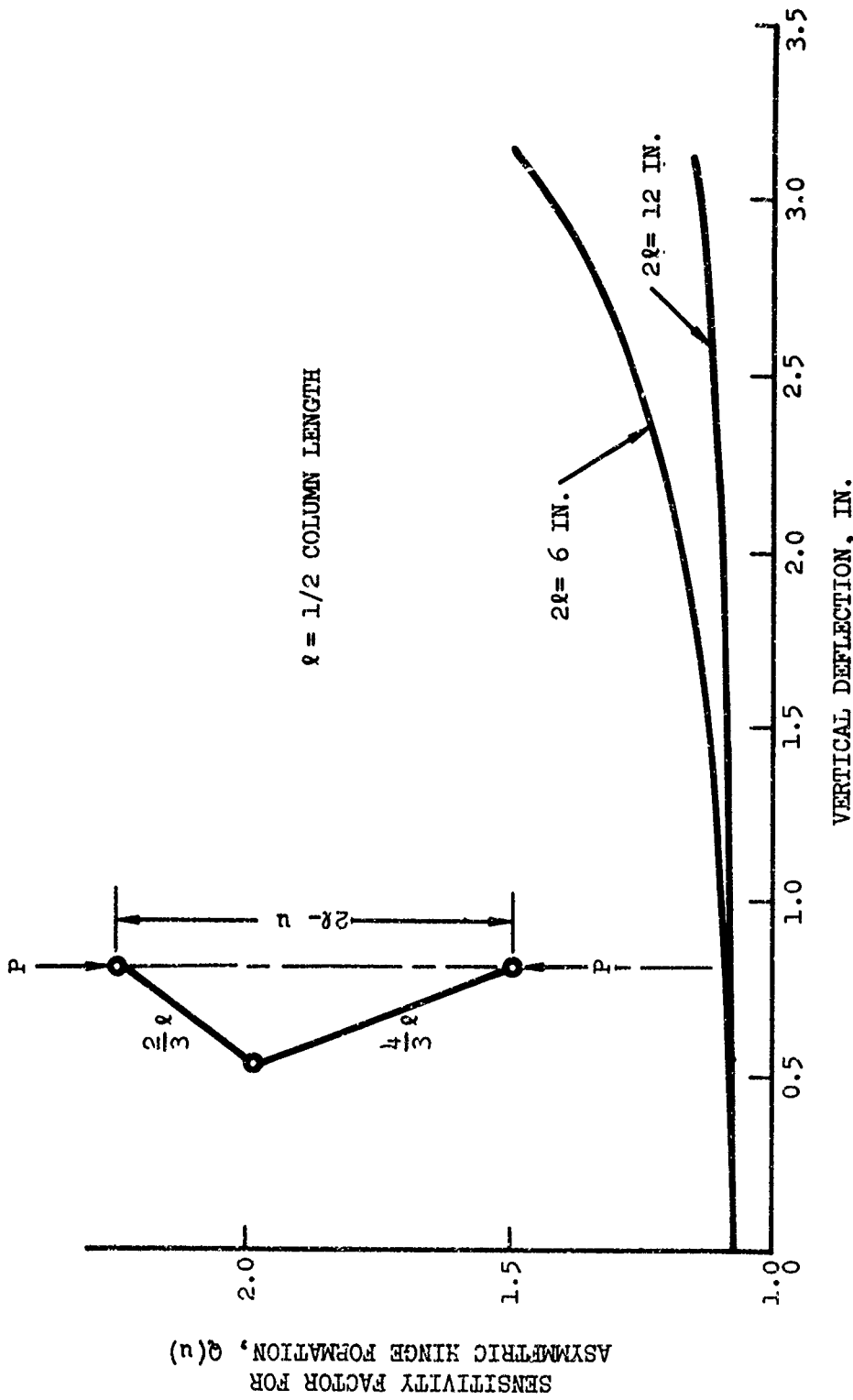


Figure 95. Sensitivity Factor for Asymmetric Hinge Formation Versus Deflection as a Function of Column Length.

It can be seen that as either the panel depth increases, or the ratio of l_1/l_2 decreases, the sensitivity factor converges to the symmetric case ($l_1 = l_2$). In general, the asymmetric modes cause higher post-failure loads from 10% to 35%, for column lengths of 12 inches and 6 inches, respectively, at about three inches of deflection. If for example, the sensitivity factor shown in Figure 95 is applied to the analysis of specimen 10 (Figure 92) in which asymmetric failure modes are noted, the post-failure curve load level at three inches of deflection would show improved agreement with the test data with regard to energy absorption. However, the energy absorption correlation, without the application of the sensitivity factor, is within 13% of agreement. The sensitivity factor would be applicable, as shown, only if all the observed failures are asymmetrical modes. Since the test results indicate the presence of both symmetric and asymmetric failure modes, the basic assumption of a symmetrical failure mode, while slightly underestimating energy absorption, is adequate.

Empirical Corrections to the Post-Failure Load-Deflection Curve

The post-failure load-deflection curve derived in Equation (17), subsection entitled Post-Failure Analysis of Stiffened Panels, has the general shape shown in Figure 96 as a function of panel depth and the value of the plastic hinge moment that is formed.

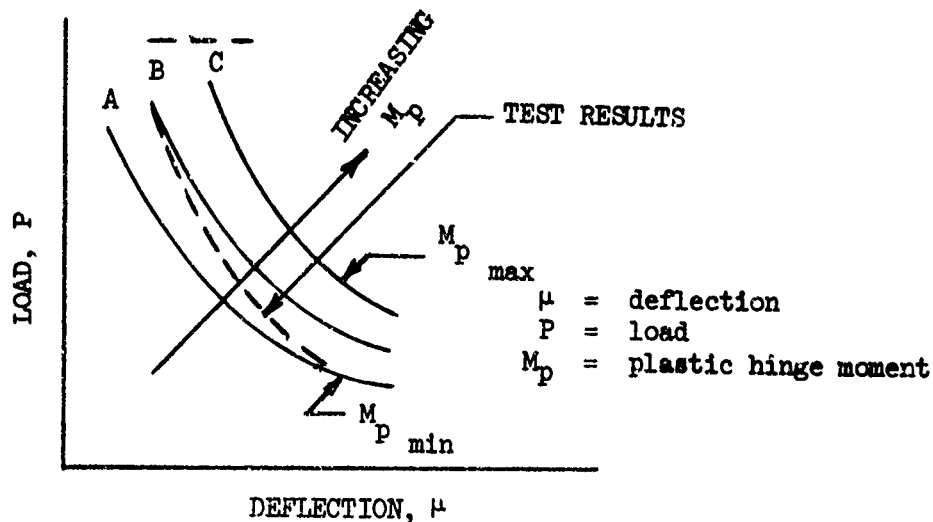


Figure 96. Post-Failure Load-Deflection Curves .

In the Substructure Analysis section the plastic hinge moment (M_p) given in Equation (17) is based on the most conservative geometry shape, or minimum value, which corresponds to the condition in which the stiffener flange folds completely over due to warping. This condition results in a much lower bending stiffness than would be obtained if the flange is extended. Although the correlation of analysis and test shows good agreement with regard to load-deflection characteristics, the analysis yields a consistently lower deflection value at failure when compared to test data. In part this discrepancy may be due to the formation of asymmetric hinge modes

as opposed to the formation of symmetric hinge modes, as initially assumed. It is estimated that the formation of an asymmetric failure mode in lieu of a symmetric failure mode will influence the failure load predicted by analysis with a shift in the failure deflection point.

Thus, the primary difference between the failure deflection obtained by analysis and test is attributed to the fact that the original analysis (Equation 17) assumes an overly conservative hinge moment. This, for example, would be reflected in post-failure curve A of Figure 96. The less conservative the hinge moment, the more the post-failure curve shifts to the right (B and C). The test results indicate that the plastic hinge moment could be higher for the transitional range (at and immediately after failure).

The same phenomenon is noted in Reference 41, which based the post-failure analysis on pure bending. The following simple idealization of such behavior in view of the experimental data is suggested in Reference 41.

$$M_p = M_{\min} + (M_{\max} - M_{\min}) e^{-K\theta} \quad (50)$$

where K is constant and

θ is a plastic hinge rotation in radians

M_{\min} is the most conservative plastic hinge moment

M_{\max} is the moment for the undeformed cross-section

However, no attempt is made to determine K in Reference 41. In the following discussion, the parameters which influence the value of K are assessed. In the rigid perfectly plastic hinge moment, the only variables which govern the value of K in Equation (50) are the section modulus and the column length. Thus, the exponential function of $e^{-K\theta}$ should have a decreased section modulus value. For the typical angle-type stiffener arrangement, as shown in Figures 24(c) and 24(d), the following simple form of constant K is proposed.

$$K = \alpha \left(\frac{y_o}{y} \right)^2 \left(\frac{t_o}{t_w} \right) \quad (51)$$

where

$$y = \frac{l}{\sqrt{C \cdot \rho}}$$

$$\rho = \sqrt{\frac{I}{A}}$$

$$\left. \begin{array}{l} C = 3.0 \\ t_o = .032 \text{ in.} \\ y_o = 20 \\ \alpha = 5 \end{array} \right\} \begin{array}{l} \text{constants} \\ \text{for typical} \\ \text{angle-type} \\ \text{stiffeners} \end{array}$$

Correlation with the test data obtained in this study suggests K as

$$K = 5 \left(\frac{20}{\gamma} \right)^2 \cdot \left(\frac{.032}{t_w} \right) = \frac{64}{\gamma^2 t_w} \quad (52)$$

Although the expression for K given in Equation (51) has been limited to application to angle type stiffened panels, it may be applicable to other types of stiffeners. Until additional crushing test data is evaluated, however, the expression for K noted above should be limited to angle stiffeners.

The use of Equation (51) is extended to zee stringer stiffened panels by using a value of $\alpha = 10$ in Equation (51) based on post-failure load-deflection data deduced from test data presented in Reference 4. Figure 97 shows the experimental load-deflection curve of a stiffened panel with zee stringers versus the predicted curve using the analytical method, modified by Equation (51). The comparison between test and analysis matches reasonably well up to a vertical crushing deflection of 0.2 inches. However, beyond this deflection, especially above 1.0 inch, the predicted load increases to approximately twice the load obtained from testing. This discrepancy in load is attributed to the relaxation of the end constraints of the test setup in the large post-failure range, thereby approaching a simply supported end condition. Photographs of the test specimens in the post-test condition, presented in Reference 4, show evidence of end restraint relaxation.

If the end restraints remained fixed it is anticipated that the test load at a deflection ≥ 1 inch would be approximately twice the load level shown in Figure 97 due to additional hinge formations at the supports. Therefore, the analytically predicted values shown in Figure 97 are expected to show good correlation with Reference 4 test data, assuming the end restraints are held fixed.

Failure Deflection

Determination of the Deflection Value at Failure

Although extensive use of semi-empirical approaches has been made in this study to predict the buckling and failure load, the literature evaluation indicates that information regarding failure deflection and pre-failure stiffness is very limited with the exception of simple configurations such as flat plates. Figure 98, obtained from Reference 107, shows a typical curve of changes in stiffness versus applied load for a square plate. The relationship between the structural imperfection parameter, α , and plate thickness (t_s), initial lateral deflection (W_0), critical stress (σ_{cr}), and yield stress (σ_{cy}) is given in Reference 107 by the following expression:

$$\left(\frac{W_0}{t_s} \right)^2 = \alpha^2 \cdot \left(\frac{\sigma_{cy}}{\sigma_{cr}} \right) \quad (53)$$

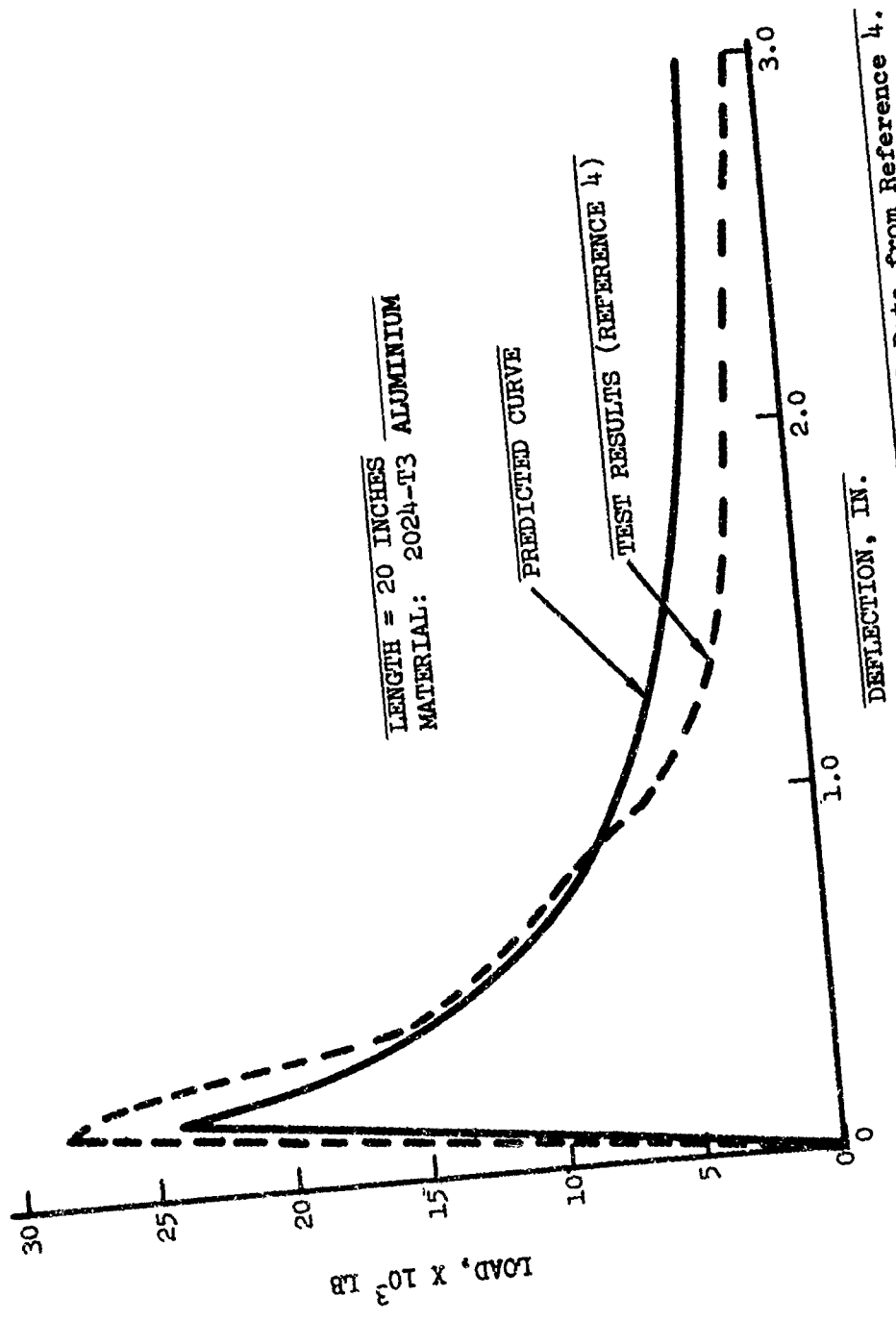


Figure 97. Comparison of Analysis with Experimental Data from Reference 4.

$$\frac{\sigma_{cr}}{\sigma_{cy}} = 0.25 \quad \alpha = .3$$

IMPERFECTION PARAMETER, $\alpha = 0.3$

SQUARE PLATE:

SIMPLY SUPPORTED WITH
FREE EDGES

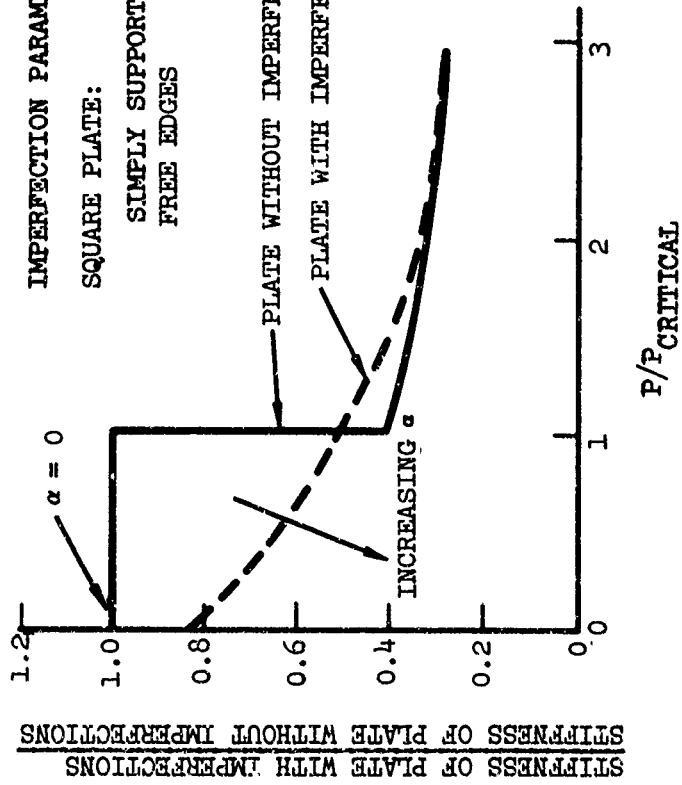


Figure 98. Variation of Stiffness with Load (Reference 107).

For example, from Figure 98 it can be seen that as the initial structural imperfection become greater (increasing α) the prebuckling stiffness ($P/P_{crit} \leq 1$) is more strongly affected than the post-buckled stiffness ($P/P_{crit} \geq 1$). Figure 98 shows changes in stiffness versus P/P_{crit} for a flat square plate in which $\sigma_{cr}/\sigma_{cr} = 0.25$ and $\alpha = 0.3$, and is simply supported with no edge restraint. As α increases it is expected that in the limit, the stiffness in the pre-buckled region will nearly equal the stiffness in the post-buckled region. Thus, the greater the initial imperfection the more it would be expected that a constant stiffness will be maintained up to the failure point. However, the prediction of the stiffness for complex structures up to failure is difficult to ascertain accurately by simple techniques due to the sensitivity of the stiffness of these structures to initial imperfections and their nonlinear response.

The test data for the specimens tested during this study indicate that there may be significant imperfections in the structure, in that the initial slope of the load-deflection curve in the pre-buckled region is not markedly different from that in the post-buckled region up to the failure load.

For the analytical method developed during this study and described in the Substructure Analysis section, the prefailure stiffness is obtained from the intersection of the predicted failure load and the post-failure analysis curve. This point determines the failure point deflection. The correlation between analysis and test shows that the analysis consistently underestimates the failure deflection (Figures 83 through 94) although predicted energy absorption and failure load values show reasonable agreement with test data. In general the test results show failure deflections of .20 to .35 inches whereas the analytically predicted failure deflection values vary from .12 to .25 inch. Table XXI is a comparison of the deflection at failure obtained by test and analysis for each set of test specimens.

TABLE XXI. COMPARISON OF TEST AND ANALYTICALLY OBTAINED FAILURE DEFLECTIONS		
Specimen	Deflection (In.)	
	Analysis	Test
1	.25	.35
2,3,4	.16	.21 *
5,6	.25	.27 *
7,8,9	.12	.32 *
10	.14	.20
11	.12	.30
12	.16	.27

* Average Value

Unless an extensive analysis, perhaps requiring involved computer coding, is performed it is expected a semi-empirical approach using simplified analytical techniques would not ensure significantly better agreement in determining failure deflection than is obtained using the approach adopted in this study. Implicit in this approach is a presumption that yield strain is reached at the point of failure. The failure criterion which most investigators adopt for collapse analysis is in fact an upperbound solution for failure. This can be shown by the following simplistic approach to an analysis of a flat plate using von Karman's plate equations.

$$U = \int_0^l \left[e_x - 1/2 \left(\frac{\partial w}{\partial x} \right)^2 \right] dx \quad (55)$$

However, since $\left(\frac{\partial w}{\partial x} \right)^2 > 0$, the upper bound value of u can be given as

$$U_{\text{upper bound}} = \int_0^l e_x dx \quad (56)$$

where

u = total end shortening

w = lateral deflection

e_x = axial strain

l = length of web

$\frac{\partial w}{\partial x}$ = partial derivative of w with respect to the coordinate x

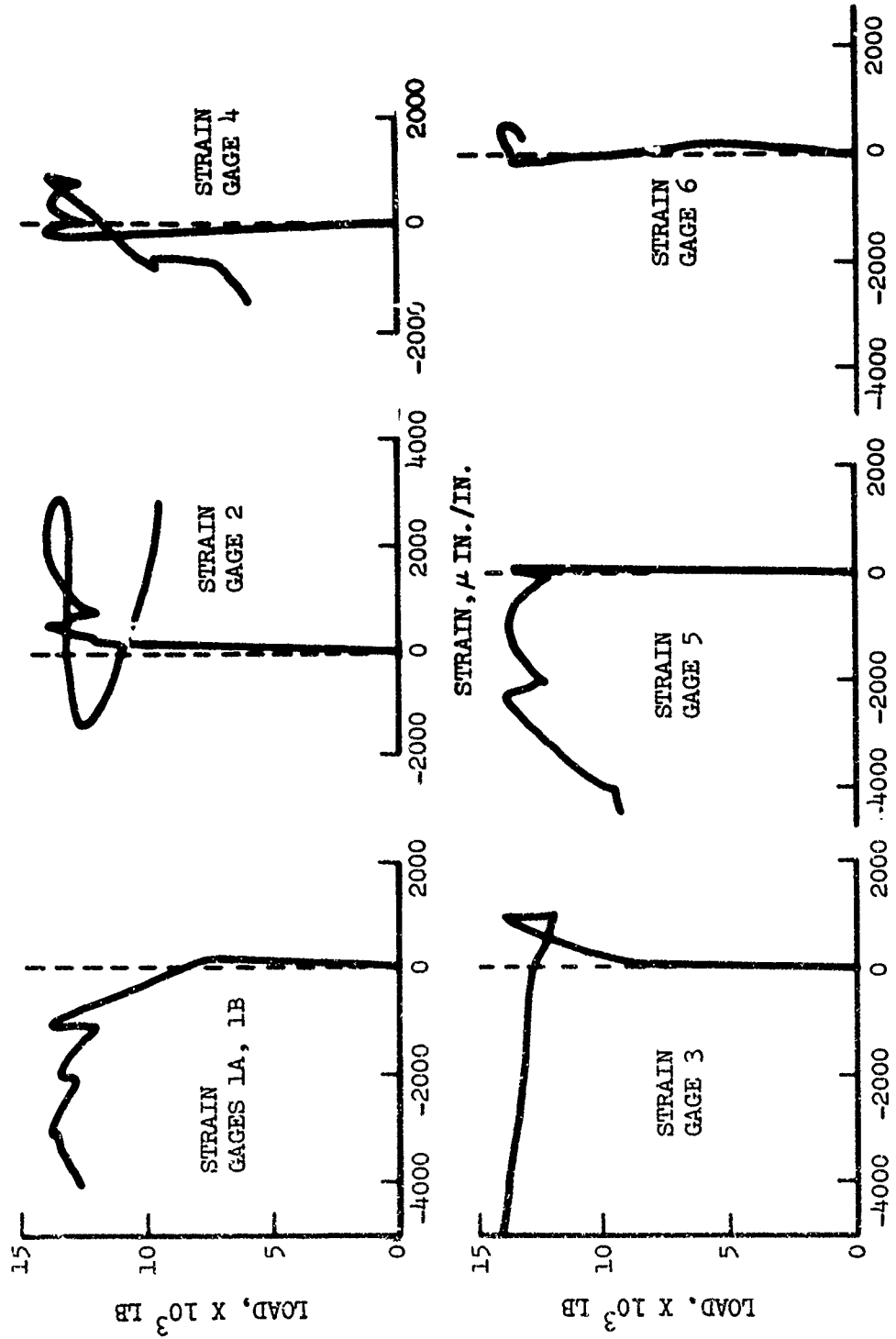
In view of the fact that the failure stress can, at most, be expected to reach the yield stress it follows that the upper bound value of e_x can be considered to equal the yield strain (e_{yp}) and, therefore, the maximum probable value of e_x can be approximated as equal to $e_{yp} \cdot l$

The analysis described in this study is based on the assumption that full plastic hinge moments are developed at the threshold of failure which implicitly suggests that the yield strain (e_{yp}) has been reached. In principle this assumption is equivalent to determining the upper bound end-shortening using the general collapse criteria which assumes the stress at the supports has reached yield. For all practical purposes of obtaining approximate energy absorption capability and characteristic load-deflection shapes for crashworthiness analysis, the approach adopted in this study is reasonable, especially when it is realized that the pre-failure deflection region accounts for only a very small fraction of the total crushing deformation.

The present method adopts a modified conservative plastic hinge moment in line with a similar observation made in a study described in Reference 108 in which it is stated "if the stiffener is riveted to the web, - - - - the bending stiffness that comes into play is more nearly that of the attached leg alone, rather than that of the entire stiffener - - -". Therefore, the end-shortening at the failure load, determined by the present method, will in fact be an intermediate value somewhere between the maximum and minimum possible plastic hinge moments that can be developed. If the maximum possible plastic hinge moment is to be used in the analysis it would result in obtaining an upperbound failure point deflection which would show better agreement with failure deflection values obtained from specimen testing. However, the use of the maximum hinge moment would then result in an overestimation of the post-failure load and energy absorption. Therefore, the present approach, although simplifying the complex structural behavior involved with regard to the prediction of the failure deflection, does account for the dominating crushing modes observed from the test performed during this study.

Strain Data and Failure Modes

The strain gages are installed to detect the modes of failure and to verify the assumptions introduced in the analysis. Strain gage data has limitations when seeking quantitative measurements of large deflection failures. In addition, wrinkling and inter-rivet tearout make it difficult to accurately interpret strain values. On the first series of tests, seven strain gages were used. The number of strain gages was reduced to two for the last six tests after a review of the initial strain data showed that the failure modes assumed in the analysis are valid. For example, Figure 99 shows load versus strain for the strain gages installed on specimen 1. Gages 1A and 1B mounted on the outer and inner sides of the side skin responded to strain in the same direction as a result of rivet-tearout. In subsequent tests these two gages responded to both compression and bending. In this particular test the strain exceeds 0.0048 in./in. which is the yield point for 2024-T3 material. The curve for strain gage 2 shows that up to the failure load (14,000 lb) there is an increasing compressive stress to approximately 30,000 psi (0.003 in./in.) at the stiffener flange surface. After the failure load is reached there is an apparent change in failure pattern. Strain gage 3 was located at a point where the side skin tore out from the rivets, and no meaningful interpretation is given to the data beyond the failure load. The readings from strain gage 4 indicate that the strain at that particular location remained within the elastic range ($\epsilon_{\max} = 0.0015$ in./in.) during the deformation of the stiffener. This response tends to support the contention resulting from analyses of the main beam and bottom skin, that a built-in support exists at the location of this strain gage. Strain gage 4, installed for the purpose of detecting a plastic hinge formation at its location, recorded low strain levels (≈ 0.0021 in./in.) at the time of initial failure. As bending increased the plastic hinge zone increased, as is noted by the increase in tensile strain as the load decreases. Observations of the specimen during the test and the post-test



STRAIN, μ IN./IN.

Figure 99. Load Versus Strain for Specimen No. 1.

inspection indicated that a plastic hinge formed approximately six inches from strain gage location 5. Strain gage 6 underwent very little strain throughout the deformation of the stiffener. The maximum strain recorded is 0.0004 in./in. ($\approx 4000 \text{ lb/in.}^2$). The low strain reading at this location supports the assumption of a double plastic hinge model in the bottom beam and skin analysis.

The following discussion provides some insight into the potential modes of failure and the difficulty associated with accurately interpreting strain gage data. In the subsequent specimen tests (2 through 11), in which additional angle stiffeners are added to the side panels, strain gages 1A and 1B are located on the outer and inner surfaces, respectively, of the angle stiffener legs. Figure 100 shows exaggerated local deformation modes exhibited by the side panel, for small and large post-failure deflections. Deformation Mode A is shown by the solid lines while deformation Mode B is shown by the dashed lines. In the case of Mode A the stiffeners move together, which places strain gage 1A in tension and strain gage 1B in compression. On the other hand, Mode B is formed by the two stiffeners moving in opposite directions. In this case both strain gages will be placed in tension. The direction in which the stiffeners move under the compression load is a function of the residual strains incorporated during manufacture; for example, in the installation of the fasteners at x and y in Figure 100. A change in mode shape could also take place depending on the influence of the global modes on the initial local modes.

Table XXII presents a summary of the stiffener response of some of the specimens employed in the tests. The data used to develop the table are contained in figures presented in Volume II in the section entitled Test Data.

Behavior of the stiffeners during pre-failure and post-failure application of the load is random. That is, the fact that the stiffeners may move together prior to failure does not mean that they will move together after failure or vice-versa.

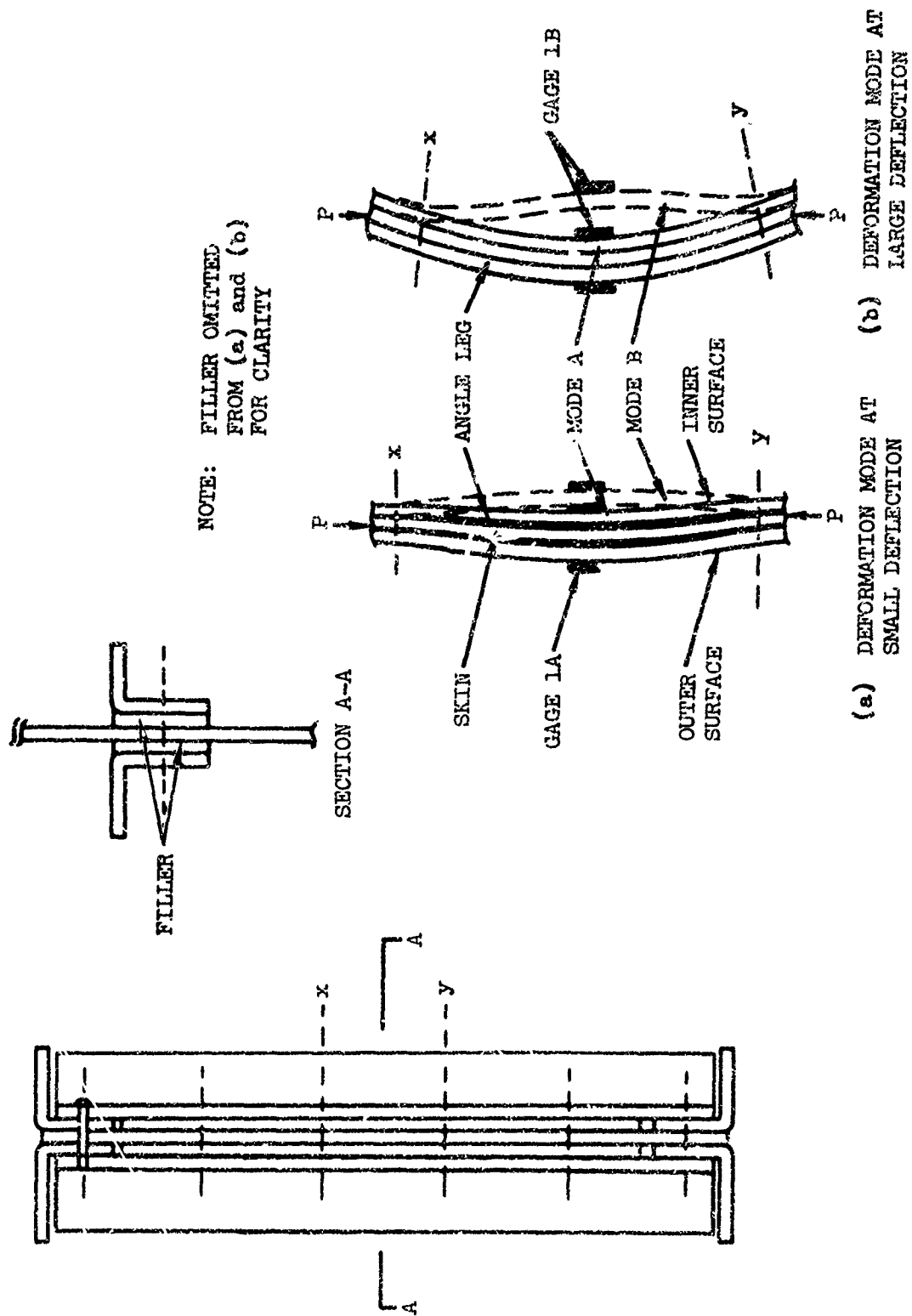


Figure 100. Observed Deformation Modes of Stiffened Panels.

TABLE XXII. SUMMARY OF TEST SPECIMEN STIFFENER RESPONSE

Specimen	Pre-Failure				Post-Failure				Remarks
	#Strain Gage		Stiffener Movement	#Strain Gage		Stiffener Movement			
	LA	LB		LA	LB				
1									
2	+	+	Apart	+	-	Together			Mode A failure
3	-	+	Together	-	+	Together			Mode A failure
4									Strain gage LB did not operate properly
5	-	-	Together	+	-	Together			
6									Strain gage LB out
7									Both strain gages out
8	-	-	Together	+	+	Apart			Mode B failure
9	-	-	Together	-	-	Together			After failure LB twice LA compression indicates failure elsewhere
10	-	+	Together	0	0				Failure unloaded stiffener
11	+	+	Apart	+	-	Together			Mode A failure
12	+	+	Apart	+	+	Apart			LA stiffener failed in tension and unloaded Failure Mode B
* - = Compression, + = tension, 0 = No appreciable strains									

PROGRAM "KRASH" REFINEMENT

GENERAL

Program KRASH was developed as an analytical tool to be used during preliminary phases of design. In Reference 1 the results of a parametric study are integrated into an iterative design procedure by which a trade-off between potential incremental cost and/or weight versus incremental improvements in crashworthiness capability could be accomplished. The results of that study and a subsequent study for the U.S. Army (Reference 106) showed the potential benefits that could be achieved for designers using a comprehensive but unsophisticated analytical approach. As is the situation with newly developed advances in the state-of-the-art, there are generally areas in which the analytical techniques can be simplified for the user.

In an effort to facilitate a designer's usage of program KRASH and to incorporate the results of the literature survey, load sensitivity study, substructure analysis, and tests, the program is revised. In particular, the input data format is changed for ease of data input and subsequent data changes, as would be required during parameter tradeoff studies. In addition, flexibility is added in the manner by which the stiffness reduction factors (KR's) are input. The revised program was run for the following conditions:

- Correlation case 31-52 from Reference 1 (to demonstrate that the revised program format is compatible with previous results: 23 ft/sec vertical velocity combined with a 18.5 ft/sec lateral velocity),
- Three-dimensional velocity (~ 40 ft/sec combined velocity impact - 27.5 ft/sec longitudinal, 23 ft/sec vertical, 18.5 ft/sec lateral).
- Upper mass penetration into a specified occupiable volume.
- Simplified blade contact.
- Utilization of load-deflection data obtained from the 12 substructure tests, performed during the study, and related to actual fuselage structure size.

Volume II contains a revised input-output format description as well as two sample problems. One sample problem represents the updated correlation run, Case 31-52, and the second sample problem corresponds to the three-dimensional velocity impact condition. Also included in Volume II is a write-up of the energy balance equations and a sample of the format in which energy results are provided. The energy balance data is currently in the program as an option since only limited checkout of the equations has been performed.

PROGRAM "KRASH" INPUT FORMAT REVISIONS

The input format changes are divided into three categories:

- Reordered data
- Standardization of certain inputs
- Allowance for more general KR curves

First, the input data is rearranged so that all mass associated data (subscript i) is in one block, followed by all external spring data (subscript ik) and then all internal beam data (subscript ij). Next, standard values are assigned to certain input data items unless otherwise specified. Thus, much repetitive data input is eliminated. The following quantities are given standard values unless otherwise specified:

QUANTITY	SYMBOL	STANDARD VALUE
Angular Momenta	He_i	0
Euler Angles	$\phi_i'', \theta_i'', \psi_i''$	0
Aerodynamic Lift	lc_i	0
Stiffness Reduction Factors	KR_{ij}	1
Failure Deflection	$v_{max_{ijl}}$	100

Thus, the angular momenta of the masses (He_i) and the aerodynamic lift (lc_i) are normally zero, as are the Euler angles $\phi_i'', \theta_i'', \psi_i''$, relating mass body-fixed axes to airplane c.g. axes. For linear internal beam elements, $KR = 1$ for the entire run, so only nonlinear KR data need be input. Similarly, v_{max} 's need only be input for those elements where rupture is expected to occur; for elements not specified, a failure deflection of 100 inches and rotation of 100 radians are assumed. Thus, the nonspecified beams will not rupture during the run.

The input has also been revised to allow more general KR (stiffness reduction factor) curves. Previously, each KR curve could have only six data points, equally spaced. Now each curve can have up to 15 data points, with any desired spacing. This greatly facilitates modeling more complex load-deflection relationships. However, the load-sensitivity study results indicate that for many structural elements a very simple KR representation is adequate. The KR representation for the various load-deflection categories is discussed, in detail, in the Design Procedures section.

As a result of the program refinement and rearrangement of coding, the program capacity has been expanded to treat at least 80 lumped masses and 100 internal beam elements simultaneously. Previous capacity was 40 and 80, respectively.

THREE-DIMENSIONAL IMPACT AND MASS PENETRATION

Case Description

After program KRASH was refined, as described previously, correlation run 31-52 from the preceding study (Reference 1) was performed, and the results indicate that the program conversion is successful. Case 31-52, run with the refined program, is presented as a sample problem in Volume II.

The basic 31 mass model described in Reference 1 is modified by adding a mass 32 to represent a lumped mass on the rotor blade, with the blade in the fore-aft position, as shown in Figure 101. In order to obtain a mass penetration of mass 32 into the cabin area within a reasonable run time, the rotor is lowered and tilted so that mass 32 starts out just above the helicopter cabin. Figure 101 is a left-hand side view of the model; the dashed lines represent the mass penetration control volume, which is referenced to mass 9. Mass 32 is located just above the control volume since the purpose of the computer run is to demonstrate mass penetration capability and not to correlate with any particular accident condition. The top surface of the control volume, which mass 32 penetrates, is properly located.

The initial c.g. velocity is chosen as 40 ft/sec, vectored as follows:

$$V_x = 27 \text{ ft/sec}$$

$$V_y = 18.6 \text{ ft/sec}$$

$$V_z = 23 \text{ ft/sec}$$

Thus, a three-dimensional impact with a horizontal surface is simulated. The initial vehicle attitude is flat (zero roll, pitch and yaw angles), and the initial angular velocities are zero.

Results

Mass 32 penetrates the control volume at .086 second after initial impact. The aft skids fail at .056 and the forward skids at .062. The fuselage first contacts the ground just after skid failure, the aft fuselage contacting just slightly before the forward fuselage. After fuselage contact, the engine and transmission accelerations build up to their peaks as follows:

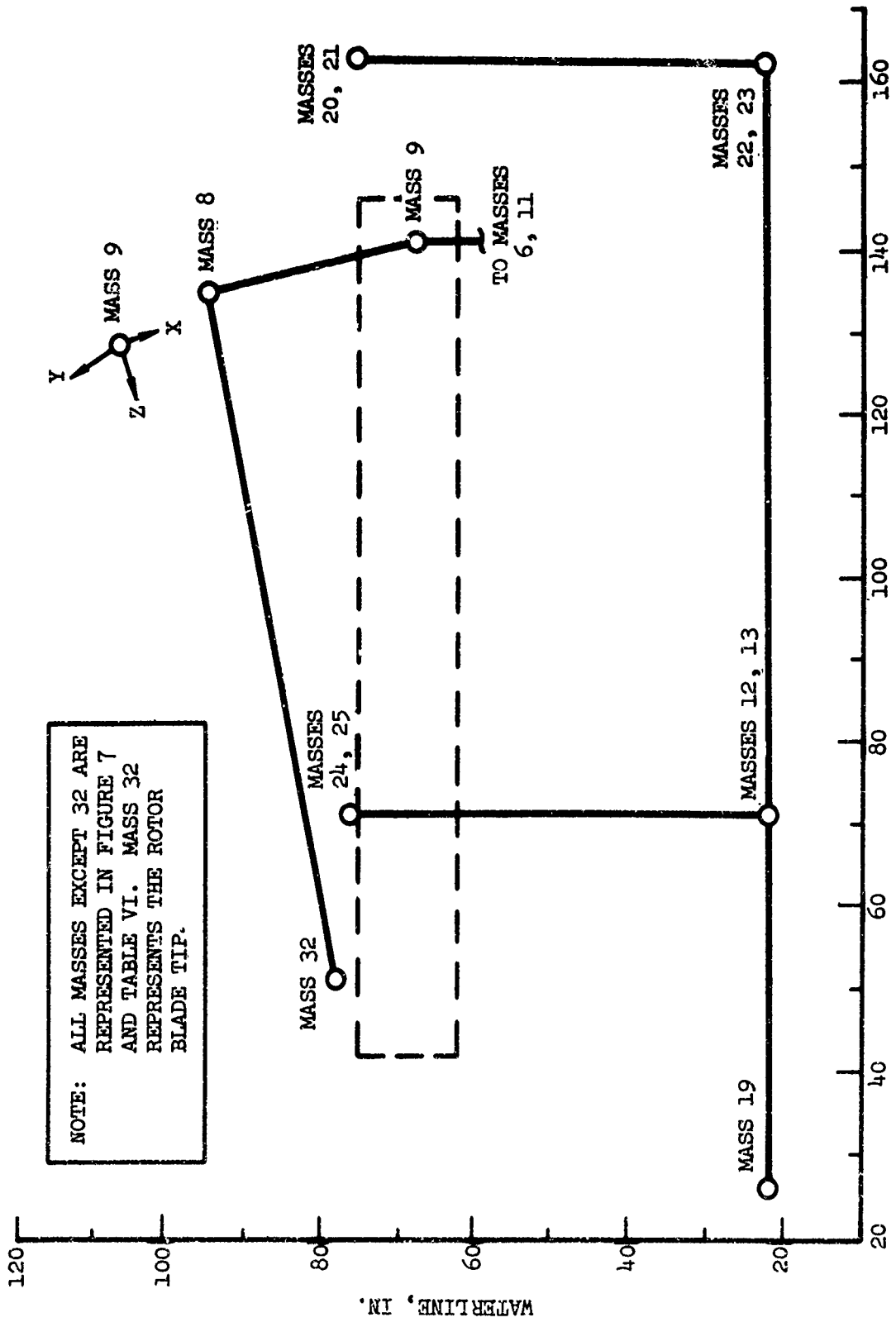


Figure 101. Three-Dimensional Impact and Mass Penetration Model.

Item	Vertical Accel. (g's)	Lateral Accel. (g's)	Longitudinal Accel. (g's)
Engine	31.3 @ .097	7.3 @ .087	5.2 @ .086
Transmission	30.0 @ .089	3.5 @ .096	2.3 @ .088

The engine mounts deform nonlinearly vertically; the transmission mount goes nonlinear longitudinally. Lateral deformations remain linear.

ROTOR BLADE CONTACT

Case Description

A rotor blade is added to the basic 31 mass, 38 beam model shown in Reference 1, resulting in a 36 mass model with 43 internal beams. Figure 102 shows the revised configuration. Masses 32 through 36 were added to represent the rotor hub and blade, with the blade stationary and perpendicular to the plane of the longitudinal axis of the helicopter. Figure 102 shows a rear view of the right side of the vehicle. The rotor blade is represented with masses lumped at 33 and 34. External springs in the y and z direction are placed at masses 34 (rotor tip), 14 (skid end), and 12 and 22 (lower right corners of fuselage).

The vehicle is initially rolled 35 degrees to the right, so the right rotor tip and landing skid contact the ground simultaneously. The initial c.g. velocity vector is 30 ft/sec perpendicular to the ground.

Results

The only beam elements which fail are the right-hand landing skids, elements 10-14 and 16-17. These fail at .055 and .076 second, respectively. After their failure, the fuselage contacts the ground at mass 12 (aft end) at .086. Within the run time analyzed (.1 second), the rotor blade did not fail. The maximum vertical deflection of the rotor blade is about 38 inches at the tip. The stiffness and strength of the rotor blade are only modeled approximately. The intent of the case is to illustrate that rotor blade contact can be modeled, not to determine precisely what happens to the vehicle in this situation.

TEST DATA LOAD-DEFLECTION CURVE

Case Description

A computer run was made to utilize load-deflection information obtained from the specimen testing performed during the earlier stages of the program.

A modified load-deflection curve is shown in Figure 103. The load-deflection characteristics indicate a rapid load buildup until failure load is reached.

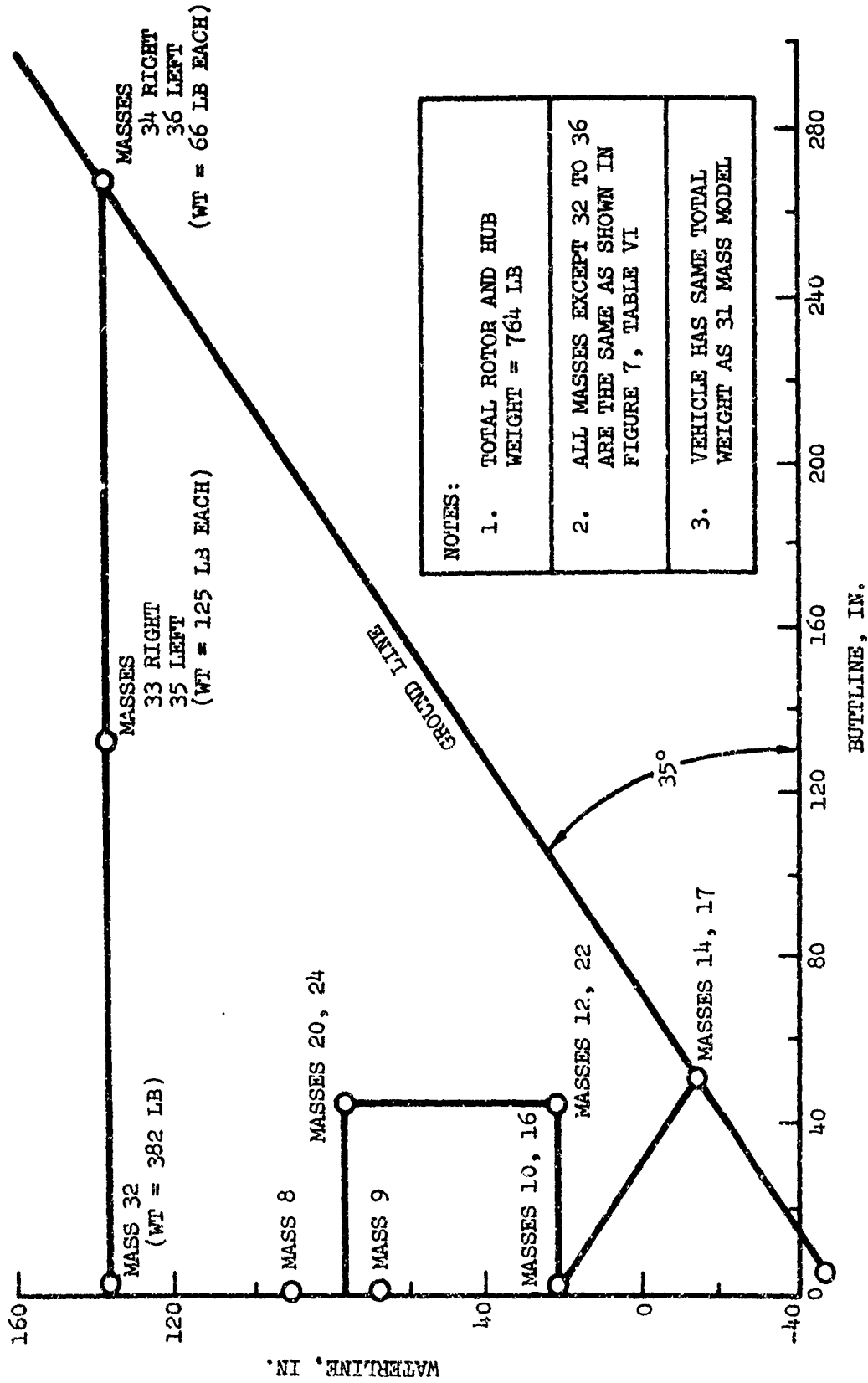


Figure 102. Rotor Blade Contact Model.

Thereafter, the load decreases until a near-constant level is reached. Finally, bottoming occurs as the structure crushes. This curve compares favorably with the analytical load-deflection curves used in Reference 1 except for the sharp peak at the failure load.

The test data is related to actual fuselage structure design (size, thickness, spacing, number of angles) and is incorporated into the UH-1H lumped mass model (Figure 7) for fuselage masses 10 (aft), 11 (midsection), and 16 (forward).

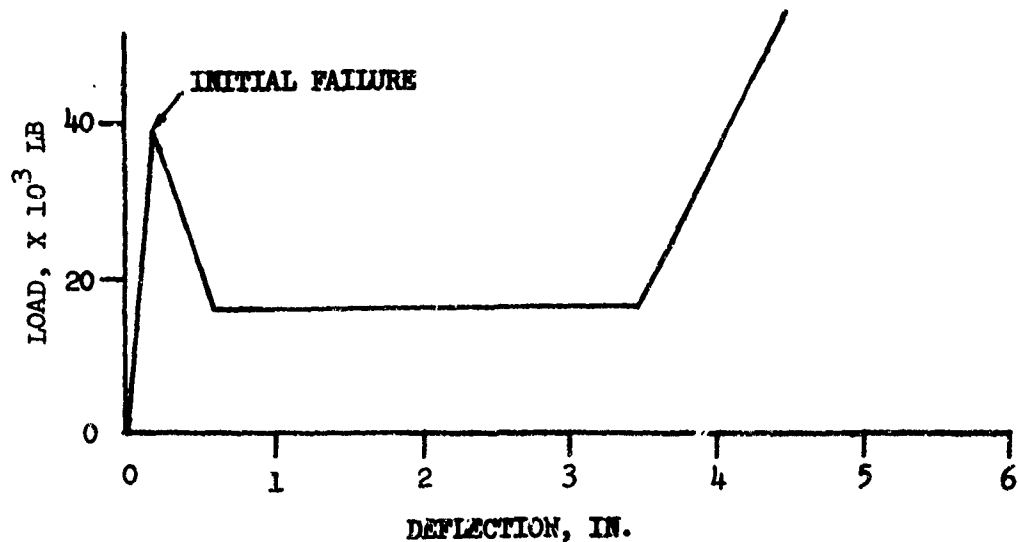


Figure 103. Test Specimen Data Load-Deflection Curve.

Results

The responses for the engine, transmission and occupants (DRI's) using the test specimen related load-deflection data are compared to the corresponding parameter response for the correlation results from Reference 1 and test data from Reference 1. These results are given in Table XXIII.

**Table XXIII. COMPARISON OF RESULTS USING TEST SPECIMEN DATA WITH
PREVIOUS CORRELATION ANALYSIS AND TEST RESULTS**

	Test Specimen Data Results		Reference 1 Correlation Analysis Results		Reference 1 Test Data Results	
	Accel.*	Time**	Accel.*	Time**	Accel.*	Time**
Engine Vertical	23.8	138	26	129	26	120
Transmission Vertical	26.0	113	30	117	27	110
DRI-Forward	20.0	140	22	142	-	-
DRI-Aft	24.5	145	27	148	30	120

*Acceleration in g's **Time in milliseconds after initial impact

The comparison of results shows that compared to previously presented analytical results, the responses change less, 8.5% to 13.6%, as far as response accelerations are concerned and that there is a shift of 2 to 9 milliseconds in the time of occurrence of events. For brevity, only several prime comparisons are made. The deflections, deformations, lateral forces, etc., are changed less than those parameters noted. The largest change (13.6%) is for the transmission, and this actually improves the comparison with test data. The engine vertical response is still within 8.5% of the test data.

DESIGN PROCEDURES

SPECIFICATION OF CRASHWORTHINESS CAPABILITY

New helicopter designs are currently required to provide occupant survivability and structural integrity to specified crash environment levels and peak acceleration forces. However, to verify a design capability would literally require that crashworthiness capability be demonstrated by a number of representative tests. The cost of testing a number of vehicles is prohibitively high and, at best, provides one data point per test. On the other hand, compliance by showing crashworthiness capability with a few simple calculations for a vertical impact condition using unverified transmissibility factors through complex structure from ground to occupant or structure is also not a satisfactory solution. Therefore, there is a need for a compromise in the manner in which compliance is shown.

Crashworthiness capability can be specified by the responsible agencies by defining impact velocity envelopes and/or peak accelerations for which airframe manufacturers would then be required to design their vehicle. Since these levels would presumably be related to percentile accident levels based on existing crash data, they would reflect a certain acceptable crash condition. This approach has the advantage of at least providing a design goal. However, it has the potential to create a situation in which the manufacturer will overdesign, underdesign, or both, depending on the location of the occupants relative to major mass items. The data from which the design criteria are obtained could very easily be adequate for one type of vehicle design while not practical for other types. For example, helicopter types vary from single powerplant lightweight utility (6000 lb) to triple powerplant heavy lift helicopters (118,000 lb) having greatly different occupant accommodations and airframe construction.

A second alternative is to allow the aircraft manufacturers to specify the level to which their vehicles are capable of providing crashworthiness capability. In so doing, the manufacturer would then have to describe, in detail, the procedures used to show that the capability can be achieved. Employing this approach, the manufacturer would then have the option to take exception to a part of the requirement, particularly if he could show that the basic objective of occupant survivability is attained. As part of the verification of crashworthiness capability, the manufacturer would be asked to provide specimen test data to substantiate structural load-deformation characteristics in critical regions.

A third approach is to specify that certain procedures be followed. For example, the iterative design process described in Reference 1 provides for a consistent crashworthiness design, in which compatibility between the essential structural elements is maintained, and takes into consideration the crash impact environment, human tolerance limits, and incremental

weight, cost and configuration penalties while treating the vehicle and its occupants as an integrated system. A procedure of this nature can be applied by the responsible agency, the manufacturer, or an impartial designated party. As in the previous approach, limited test verification could be required. Of paramount importance in this approach is the ability to specify the trade-off between penalty (weight, cost, configuration) and crashworthiness capability early in the design process. At this early stage, design changes which would not interfere with the primary operational requirement could be more economically incorporated. This approach offers the advantage of treating the aircraft, including occupants, as a total system, which would have the effect of minimizing the tendency to over-design in order to meet arbitrary design criteria.

GENERAL APPROACH

The determination of load-deflection characteristics of aircraft structures will enhance the ability of designers to predict structure and occupant response during severe yet potentially survivable accidents. However, it is important that this data be presented in a manner that will aid the designer in developing the desired level of crashworthiness capability in the airframe structure. In order to ascertain crashworthiness capability, it is necessary to define the crash environment, to understand the crushing characteristics of airframe structure and the potential structural failure modes, and to have an analytical technique which is applicable to realistic crash situations. The design procedures presented herein provide the basis for the formulation of a design manual by which designers can readily obtain pertinent data necessary to perform a crashworthiness analysis. The information presented in this section follows from earlier developments described in this study and the preceding study (Reference 1) as well as information contained in the current Crash Survival Design Guide (Reference 2). The development of design procedures, to be meaningful, must form a part of an overall process by which crashworthiness capability can be specified.

The development of a mathematical model to perform crashworthiness analysis for a particular helicopter configuration during the initial stages of the design formulation requires that consideration be given to the following.

- Identification of the overall failure modes.
- Identification of the individual element failure modes.
- Prediction of the load-deflection curve for each subelement.
- Prediction of the total load-deflection curve for each substructure.
- Simplified representation of structural element load-deflection curves while providing response values within acceptable accuracy.

By following the approach outlined above, the designer will have an opportunity to perform meaningful trade-off studies between cost and/or weight

versus crashworthiness capability. Although this approach is not necessarily rigorous, it will be consistent with the amount and quality of detailed data that is available during a preliminary design study. Furthermore, if properly evaluated, the analysis of preliminary designs will serve such useful functions as: (1) ascertaining critical design regions wherein alterations to the structural response will be most beneficial, (2) the extent to which additional energy absorption is needed, and (3) the structural element load-deflection characteristics (and, consequently, structure design and size requirements) that are needed to meet a specified or desired crashworthiness capability.

As a first step in establishing the mathematical model, it is necessary to determine the types of failure modes for the design involved. There are several potential types of failures including tension, compression, bending and shear, as well as combined failures, e.g., axial and bending. Tables II and III show some of the typical structural elements used in aircraft along with their failure modes. For example, the lower fuselage of the UH-1H is composed of a series of riveted interconnecting bulkheads and panels with top (floor) and bottom (outer contour) skins. The panels throughout the fuselage have a variety of different sized angle stiffeners attached to them. The depth of the structure and the spacing of the stiffeners vary depending on their function in the airframe of the vehicle. Although it is desirable to represent the entire fuselage with finely divided segments to accurately describe all the forces acting on each element, it is doubtful that sufficient detail to do so would be available during the preliminary design stage. Even if detailed information were provided, the task of establishing such a rigorous representation of the entire vehicle would be unwarranted from practical and economic considerations, especially since the adequate representation of the crushing behavior of the fuselage structure is the primary objective.

To establish a mathematical representation of an aircraft for crash analysis requires an awareness of the structures' behavior. Up to the point of failure, the anticipated behavior of the structure is expected to be definable since the design for normal operation will be such as to preclude reaching failure. To model for a dynamic impact such as a crash condition requires that the mass characteristics, as well as the stiffness characteristics, of the structure be represented. Regardless of the analytical methods employed in treating a complex problem, some basic assumptions are always required which compromise the actual physical system. The extent to which the physical system is compromised depends on many factors including: available detail design data, accuracy required, available computer systems, economic and time considerations. The above noted factors will influence the degree of refinement to be used in mathematically representing the structure.

Beam model representations of the major structures with lumped masses adopted in program KRASH normally result in a more coarse modeling of a structure than would be obtained using a more detailed finite element

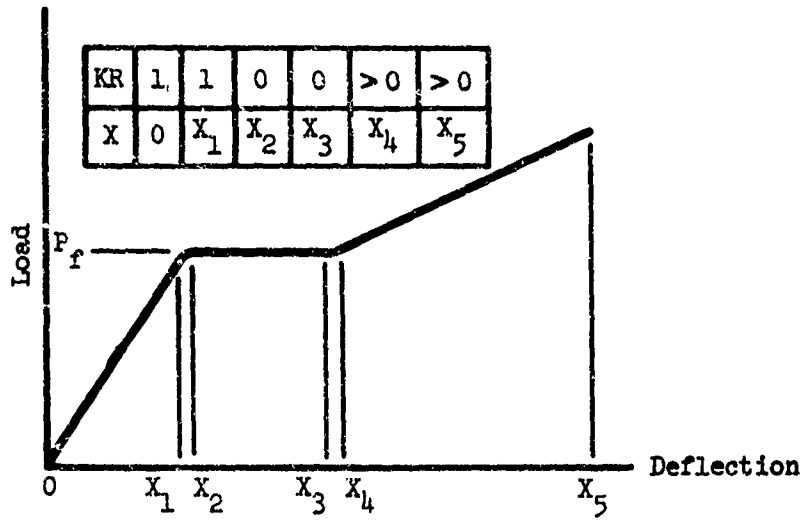
technique, although both approaches are similar. As described herein and in Reference 1 program KRASH emphasizes crashworthiness analysis during preliminary design. Thus, the application of an analytical model consisting of beam elements and lumped masses, to be of benefit to the designer, must represent the gross behavior of the structure with reasonable accuracy. The representation of the load-deflection characteristics depends on the type of structural element, its location in the structure, and the manner in which it interfaces with other structural elements. For example, in the region of the UH-1H lower fuselage, the overall crushing deformation is primarily influenced by the static structural modes and, therefore, substructure sections may be represented by their static crushing characteristics. However, as is shown by the results of the study, the total load-deflection characteristics of a large subsection can be obtained with reasonable accuracy from piecewise superposition of the individual subelement load-deflection curves.

Those mass items whose response is influenced by the energy absorbing capability of the lower fuselage, the location of the masses in the fuselage, the manner in which the mass items are attached to the fuselage along with the type and size of the attachment members, influence the load-deflection characteristics. As a consequence, the load-deflection curve may have to be obtained in a different manner than by piecewise superposition of individual subelement stiffnesses. For the mass items such as engine and transmission the subelement stiffness is, in effect, the element stiffness. Although each condition has to be reviewed and evaluated on its own merits, simplified load-deflection representations are possible without knowing the exact post-failure characteristics of the entire structure.

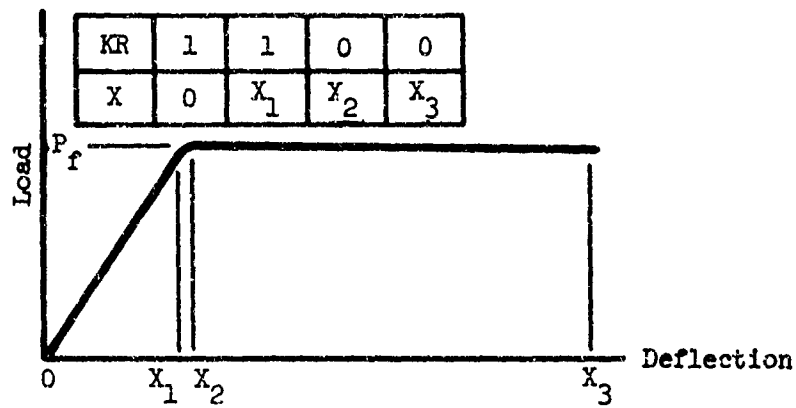
The results of the load sensitivity studies indicate that the post-failure curve can, depending on the type and location of the particular structural element, be modeled in an approximate manner. In particular, several load-deflection categories can be established which will yield response values of acceptable accuracy for preliminary design purposes. In the literature review and evaluation it was noted that structural elements can be classified into load-deflection categories. The different post-failure load-deflection categories are shown nondimensionalized in Figure 104. Included for each type of post-failure curve is the corresponding stiffness reduction factor (KR) and distance (X) terms which can be used to model the representative beam element for the respective structural elements in program KRASH.

The three categories shown in Figure 104 are described as follows.

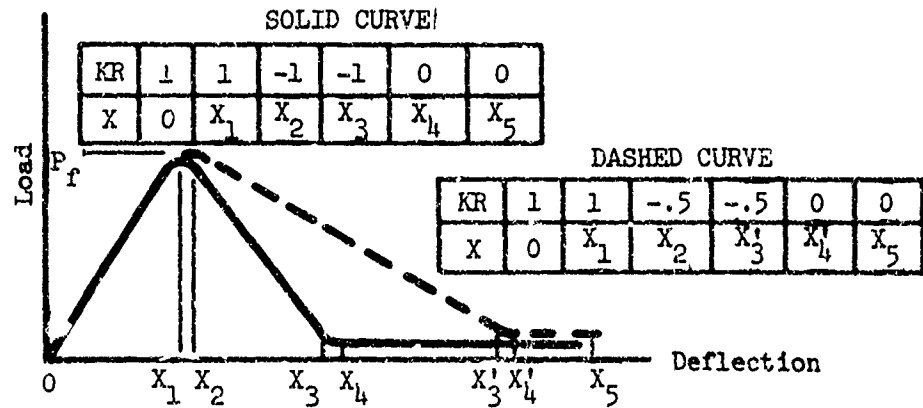
- I - The load-carrying capability increases as the deflection increases. This category is applicable to locations where secondary structure is available to carry loads after the initial structure fails; e.g., a soft transmission mount on the pylon support structure.



(a) Category I



(b) Category II



(c) Category III

Figure 104. Simplified Load-Deflection Categories.

- II - The load-carrying capability remains essentially constant as the deflection increases beyond the yield load. This category is applicable to energy absorbers like Dynasorb or honeycomb in compression; e.g., seat systems in which load limiters are used.
- III - The load-carrying capability decreases beyond the failure load. This category is applicable to support struts for some major mass elements such as an engine on pin ended column supports.

Note that in Figure 104 the X_1 terms represent the deflection at initial failure or yield and are obtained from the pre-failure mode which, in general, is elastic. A KR of 1 means that a linear stiffness applies to the structural element until deflection X_1 is reached. The program is coded with sufficient generality to handle any practical type of load-deflection curve; thus, in order to represent a transition from one stiffness to another stiffness, a small incremental change in deflection is a required input. This small incremental change is expressed as $X_2 - X_1$ for each of the categories in Figure 104. A KR value of 0 provides a zero stiffness for the associated increment of deflection which also results in a constant force. Negative KR's result in decreasing loads for the respective increments of deflection. For the category III type elements, two representations are shown. The solid line represents a failure which results in a rapid loss of load-carrying capability in the post-failure region. The dashed line is a more gradual loss of load capability. From the UH-1H engine sensitivity given in Tables XI and XII for a 42 ft/sec vertical crash condition, the difference in load between the dashed and solid lines would be approximately 12%.

DETAIL APPROACH

Detail Design Procedure and Illustrative Sample Calculations

The following procedure is a description of the step-by-step process that a designer would follow to obtain the load-deflection characteristics of a composite built-up substructure made of stiffened panels with main beam longitudinal reinforcements along the sides. The procedure is based on the simplified analytical techniques described earlier in the report and illustrates the types of curves, nomographs, tables and equations which can be used to formulate a designer-oriented procedure. At present, the simplified analytical techniques have been verified by test for four-edge and two-line supported configurations. An example is included. The analysis presented in this section is based on the representation of the actual structure in the region from Fuselage Station (FS) 102 to 180, Water line (WL) 10 to 22, Butt Line (BL) -14 to +14. The angle stiffener and bulkhead arrangement is shown in Figure 105.

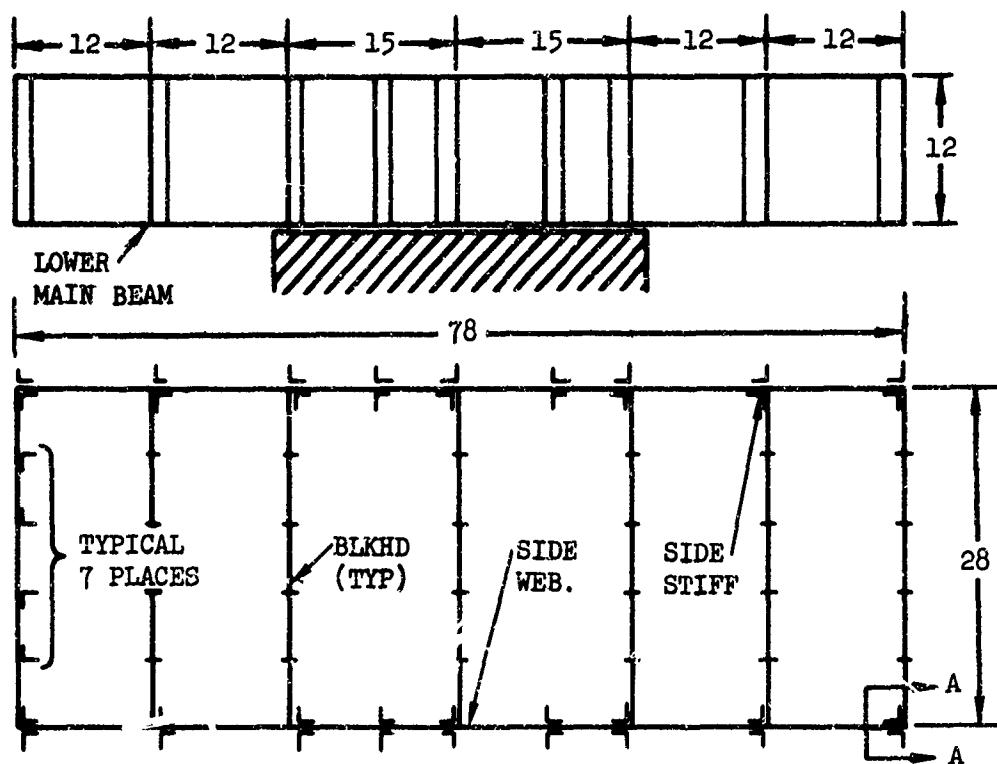


Figure 105. Structure Used in Example.

The pertinent dimensions for the structure are:

Bulkheads; $t_s = 0.032$ in.

$t_w = 0.032$ in.

angle stiffener; 0.75 in. x 0.75 in. x 0.032 in.

Main Beams; 1 in. x 0.063 in. x 78 in.

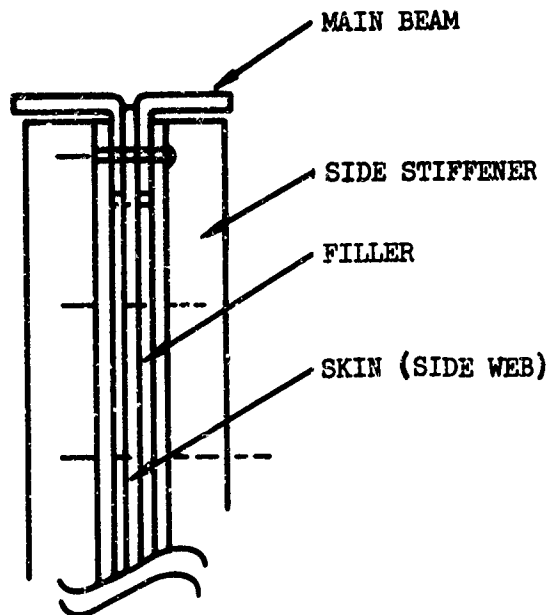
Side Webs; $t_s = 0.032$ in.

Side Stiffeners; $t_w = 0.032$ in.

Fillers; 1 in. x 0.063 in. x 8.8 in.

Material; 2024 - T3, $\sigma_{cy} = 45,000$ psi

A sketch of the main beam, stiffener web, side stiffener and filler is shown on the next page. Dimensions in figures and sketches in this section are in inches unless otherwise noted.



SECTION A-A (from Figure 105)

The assumed deformation mode, as described in the analysis, for the four-edge support condition is shown in Figure 106.

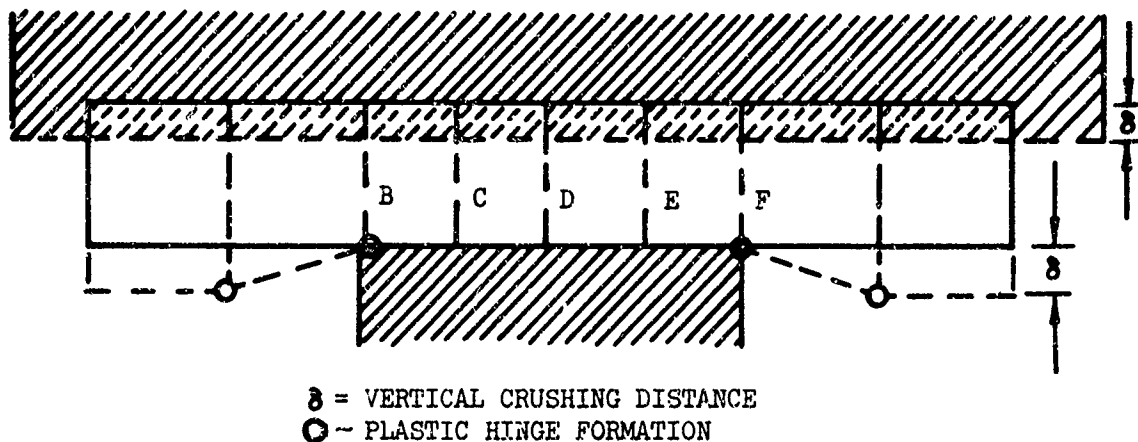


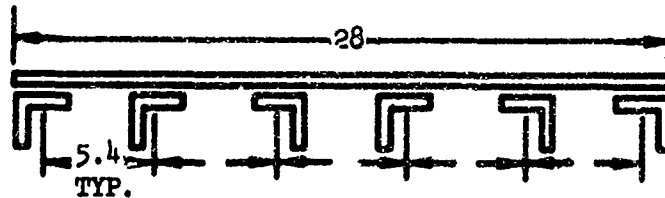
Figure 106. Assumed Deformation Mode.

The three bulkheads at stations C, D and E (Figure 106) and the side stiffener webs in this region are subjected to the in-plane compression. The side webs between B and C, and between E and F are under a varying compressive load. The main beam deformation mode is shown in Figure 106. This is the case where both beams (upper and lower beams as shown in Figure 105) behave as individual beams restrained by the web.

The step by step procedure is as follows:

A. Bulkhead Analysis

The bulkhead is represented as shown below:

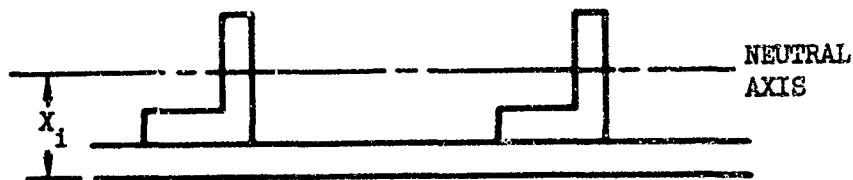


1.. Failure Load Analysis

a. Examine the column instability effect.

For stiffened panel determine the effective radius of gyration (ρ) as follows for each bulkhead and side panel.

(i) determine the effective neutral axis:



$$\text{Neutral Axis } N/A = \frac{n}{\sum_{i=1}^n} \frac{A_i X_i}{A_i} \quad (56)$$

where

A_i = area of segment i

X_i = distance to c.g. of segment i from outside face of the web

(2) determine the area moment of inertia (I)

$$I = \sum_{i=1}^n \left[\frac{b_i t_i^3}{12} + A_i d_i^2 \right] \quad (57)$$

where

b_i = width of segment i

t_i = thickness or height of segment i

d_i = distance from c.g. to N/A for segment i

Therefore:

$$I_t = I_o + 1/12 (5.4 (.032)^3) + .1728 (.0460431)^2$$

$$+ .04698 (.1994 + .032 - .0620431)^2$$

$$I_t = 4.3682 \times 10^{-3}$$

Thus,

$$\rho \sqrt{\frac{4.3682 \times 10^{-3}}{0.219776}} = .14098 \text{ in.}$$

and taking end fixity as $C = 3$

$$\frac{L'}{\rho} = \frac{L}{(\sqrt{C})(\rho)} = \frac{12}{\sqrt{3}(.14098)} = 49.14 \quad (59)$$

Therefore, for the bulkhead, correction for long column effects is required.

b. Determination of critical buckling stress (σ_{cr})

$$(1) \sigma_{cr} = \frac{K_c \pi^2 E}{12(1-\nu^2)} \left[\frac{t_s}{b_s} \right]^2 \quad (60)$$

t_s = skin thickness

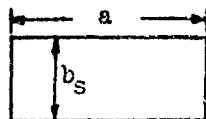
b_s = skin width between angle stiffeners

$$\sigma_{cr} = K_c K_1 \text{ where } K_1 = \frac{\pi^2 E}{12(1-\nu^2)} \left[\frac{t_s}{b_s} \right]^2 \quad (61)$$

For aluminum, K_1 can be calculated from the above expression or obtained from Figure 107 knowing $\frac{t_s}{b_s}$

K_c can be obtained from Figure 108.

For the bulkhead in the illustrative procedure the buckling load for the sheet skin of one angle stiffener spacing is obtained as follows:



$$a = 12 \text{ in.}$$

$$b_s = 5.4 \text{ in.}$$

$$a/b = \frac{12}{5.4} = 2.2$$

boundary condition A (all edges clamped)

$$E = 10 \times 10^6 \text{ LB/IN.}^2$$

$$\nu = .3$$

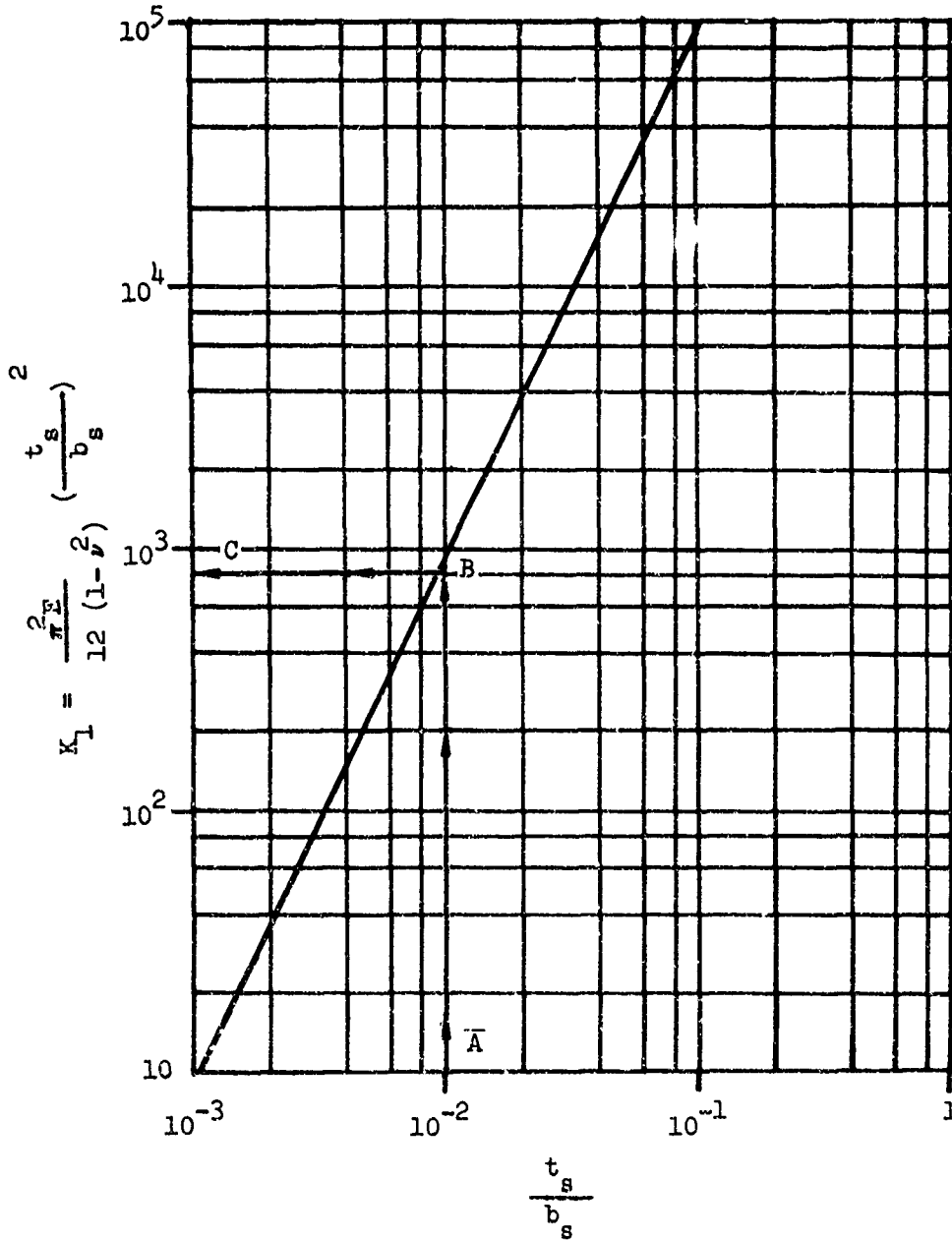


Figure 107 . Determination of K_1 .

c = clamped
 ss = simply supported
 f = free

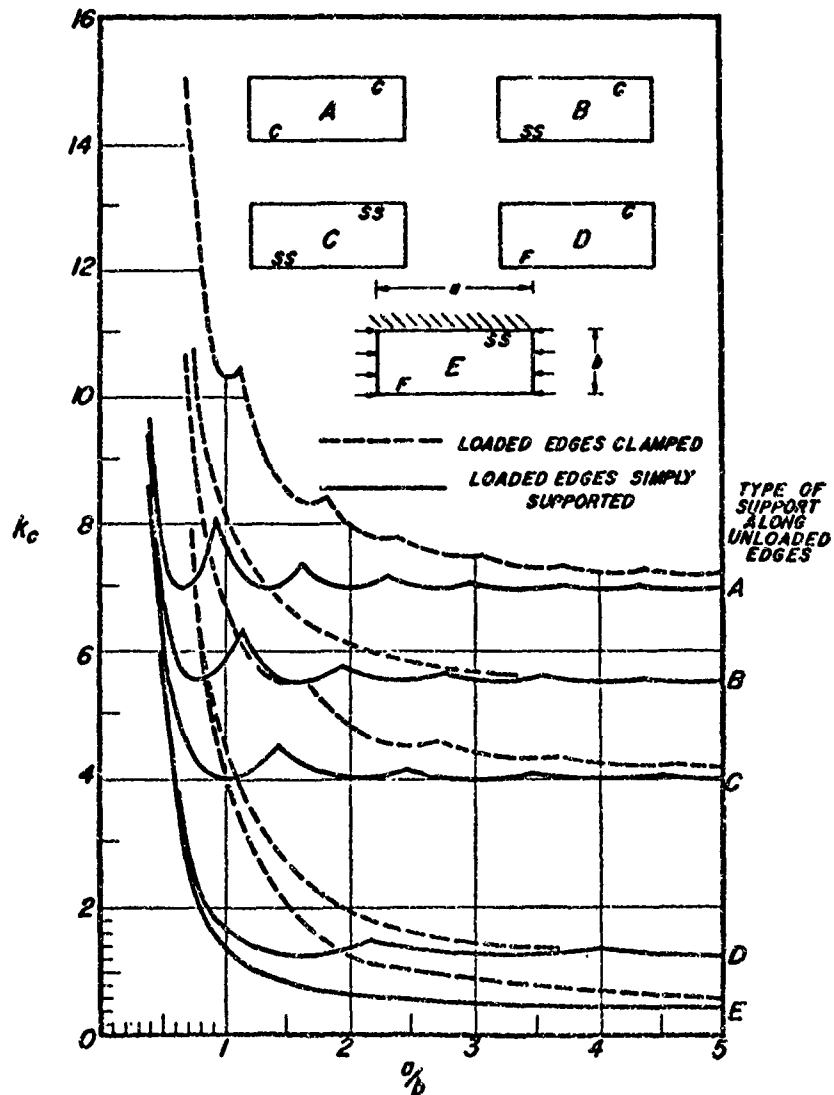


Figure 108. Compressive-Buckling Coefficient for Flat Rectangular Plates (Reference 12).

Therefore, from Figure 107 for condition A and $a/b = 2.2$

$$K_c = 7.8$$

and

$$\begin{aligned} \sigma_{cr} &= K_c \frac{\pi^2 E}{12 (1-\nu^2)} \left[\frac{t_s}{b_s} \right]^2 \\ &= 7.8 \left(\frac{\pi^2 \cdot 10^7}{12 (1-.3^2)} \right) \left(\frac{.032}{5.4} \right)^2 = 2476 \text{ psi} \end{aligned}$$

or obtain K_1 from Figure 107 and multiply by K_c

c. Determination of type of failure

- (a) Wrinkling
- (b) Interrivet

(1) Calculate wrinkling coefficient K_w

$$K_w = \sigma_w \frac{12 (1-\nu^2)}{\pi^2 \eta \bar{\eta} E} \left(\frac{b_s}{t_s} \right)^2 \quad (62)$$

where wrinkling stress can be obtained as follows:

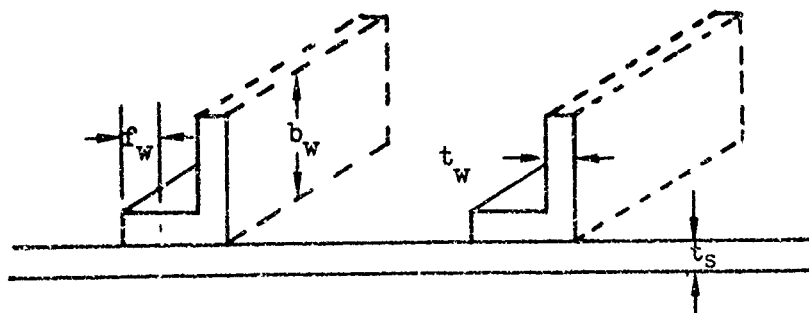
$$\sigma_w = .48 \eta \bar{\eta} E \left[\frac{t_w}{f_w} \right]^{4/3} \left[\frac{t_w}{b_w} \right]^{1/6} \left[\frac{t_s}{b_s} \right]^{1/2} \quad (63)$$

Therefore

$$K_w = .53 \left(\frac{t_w}{f_w} \right)^{4/3} \left(\frac{t_w}{b_w} \right)^{1/6} \left(\frac{b_s}{t_s} \right)^{3/2} \quad (64)$$

and

$$K_w^{1/2} = \sqrt{K_w} \quad (65)$$



For the example structure K_w is obtained either from Figure 109 or calculated as follows:

$$\sigma_w = K_w \frac{\pi^2 E \eta \bar{\eta}}{12 (1-\nu^2)} \left(\frac{t_s}{b_s}\right)^2 = .48 \eta \bar{\eta} E \left(\frac{t_w}{f_w}\right)^{4/3} \left(\frac{t_w}{b_w}\right)^{1/6} \left(\frac{t_s}{b_s}\right)^{1/2}$$

$$K_w = \frac{12 (1-\nu^2)}{\pi^2} (.48) \left(\frac{t_w}{f_w}\right)^{4/3} \left(\frac{t_w}{b_w}\right)^{1/6} \left(\frac{t_s}{b_s}\right)^{-3/2}$$

$$K_w = \frac{12 (1-.3^2)}{\pi^2} (.48) \left(\frac{.032}{.5}\right)^{4/3} \left(\frac{.032}{.75}\right)^{1/6} \left(\frac{.032}{5.4}\right)^{-3/2}$$

$$K_w = 17.577$$

therefore

$$K_w^{1/2} = 4.1925$$

Typical values are as follows:

t_w ; from .03 in. to .12 in.

t_s ; from .02 in. to .09 in.

b_s ; from 3 in. to 6 in.

b_w ; from .5 in. to 1 in.

f_w ; from .25 in. to .75 in.

The next step requires a check to see whether failure is due to wrinkling or monolithic behavior and not interrivet failure. The following expression

$$\frac{P}{b_s} < \frac{1.27}{(K_w)^{1/2}} \quad (66)$$

must be satisfied if the failure mode is due to wrinkling or monolithic behavior.

For the example the calculations are as follows:

$$p = 1 \text{ in. (rivet pitch)}$$

$$b_s = 5.4 \text{ in. (angle spacing)}$$

$$\frac{p}{b_s} = \frac{1}{5.4} = .185185$$

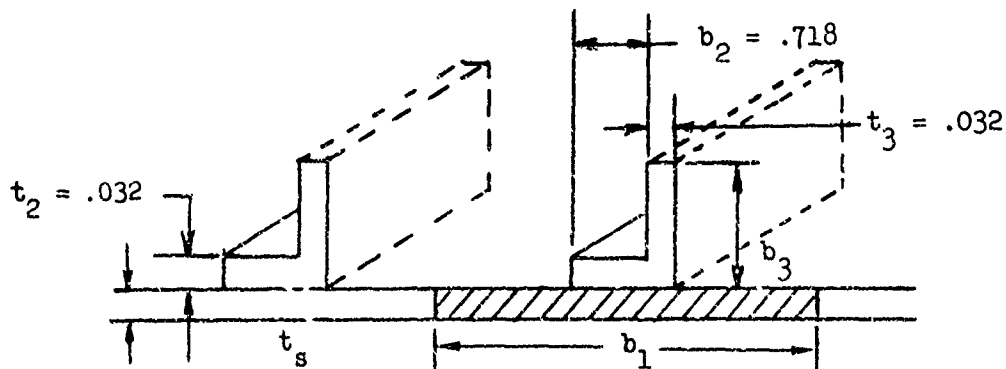
$$\frac{1.27}{(K_w)^{1/2}} = \frac{1.27}{4.1925} = .30292$$

$$\frac{p}{b_s} < \frac{1.27}{K_w^{1/2}}$$

Therefore, bulkhead fails by wrinkling or monolithic behavior and not interrivet failure.

If failure is of the interrivet type then the monolithic failure (σ_f) determined in the next step would have to be reduced to σ_{cr} .

d. Determination of yield stress



$$\bar{\sigma}_{cy} = \frac{\sigma_{cy_s} A_s + \sigma_{cy_w} A_w}{\Sigma A} \quad (67)$$

$$\bar{\sigma}_{cy} = \frac{\sigma_{cy_s} + \sigma_{cy_w} \left(\frac{\bar{t}_w}{t_s} - 1 \right)}{\bar{t}_w / t_s} \quad (68)$$

$$\text{where } \bar{t}_w = \frac{\sum_{i=1}^n b_i t_i}{\sum_{i=1}^n b_i} \quad (69)$$

From the sketch above

$$\begin{aligned} \bar{t}_w &= \frac{\Sigma b_i t_i}{\Sigma b_i} = \frac{b_1 t_1 + b_2 t_2 + b_3 t_3}{b_1 + b_2 + b_3} \\ &= \frac{5.4(.032) + .718(.032) + .75(.032)}{5.4 + .718 + .75} \end{aligned}$$

$$\bar{t}_w = .032$$

$$\text{For the same material } \sigma_{cy_s} = \sigma_{cy_w} \quad (71)$$

e. Determination of failure stress (σ_f)

- (1) For angle stiffeners failure stress can be determined as follows:

$$\sigma_f = \beta_f \left[\frac{f t_w t_s}{A} \frac{E}{\sigma_{cy}} \right]^{1/2} (\sigma_{cy}) \quad (72)$$

$\beta_f = .665$ for angle stiffeners (obtained from Table YVI and Equation (36))

- (2) According to the data in Reference 12, the failure strength can be generalized by the following form:

$$\frac{\sigma_f}{\sigma_{cy}} = \beta_g \left[\frac{g t_w t_s}{A} \left(\frac{E}{\sigma_{cy}} \right)^n \right]^m \quad (73)$$

where

g = the number of flanges + the number of cuts

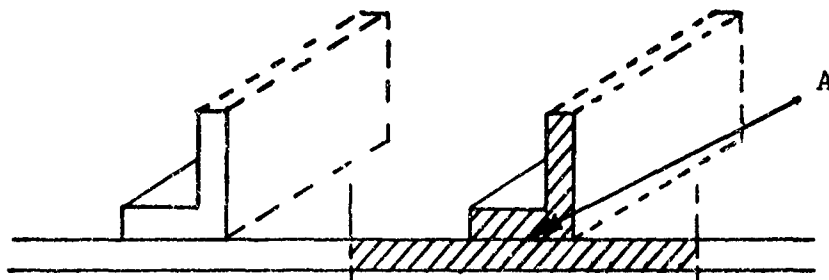
$$\beta_g = \beta_c \left(\frac{c}{g} \right)^m \quad \text{for multi-corner elements} \quad (74)$$

$$\beta_g = \beta_f \left(\frac{f}{g} \right)^m \quad \text{for one-corner elements} \quad (75)$$

$$\beta_g = \beta \left(\frac{1}{g} \right)^m \quad \text{for two-corner elements or plates} \quad (76)$$

In Figure 33 representative types of stiffeners with from one to six corners are shown. In Figure 34 and Table XVI values of β_g , g , n and m , obtained from Reference 12, for different configurations are listed.

A is the cross-sectional area indicated in the sketch below.



Determine number of flanges, f , from Figure 24.

Use cladding factor = 1 (fully cladded); Reference 12 notes other cladding factors.

- (3) Correct σ_f for rivet effect (Figure 22 or 23)

$$\bar{\sigma}_{fr} = \sigma_f \text{ times the value obtained from Figure 22 or Figure 23}$$

For the example structure the monolithic failure stress for the bulkhead is determined as follows:

$$\frac{\sigma_f}{\sigma_{cy}} = \beta_g \cdot \left[\frac{g \cdot t_w \cdot t_s}{A} \left(\frac{\bar{\eta} E}{\sigma_{cy}} \right)^{1/2} \right]^{0.85}$$

From Table XVI, $g = 5$, $\beta_g = 0.55$

$$A = A_s + A_w = 5.4 (0.032) + 1.468 (0.032) = 0.219776$$

$$t_s = 0.032, t_w = 0.032, \sigma_{cy} = 45,000 \text{ psi}, \bar{\eta} = 1$$

$$\begin{aligned} \frac{\sigma_f}{\sigma_{cy}} &= 0.55 \cdot \left[\frac{5 \times 0.032^2}{0.219776} \left(\frac{1000}{4.5} \right)^{1/2} \right]^{0.85} \\ &= 0.223843 \end{aligned}$$

To include rivet strength effect,

$$\left(\frac{p}{d} \right) = \left(\frac{p}{t_s + t_w} \right) = \left(\frac{1}{1/8} \right) \cdot \left(\frac{1}{2 \times 0.032} \right) = 125$$

From Figure 22

$$\sigma_{fr}/\sigma_f \doteq 0.8 \quad (\text{medium value})$$

Therefore:

$$\frac{\sigma_{fr}}{\sigma_{cy}} = .179 \quad \sigma_{fr} = 8058 \text{ psi}$$

The failure stress (σ_{fr}) is corrected for the long column effect from Equation (29) using the following values:

$$\begin{aligned} \sigma_c &= 59495 \text{ psi (Equation (28))} \\ \sigma_{20} &= 24674 \text{ psi (Equation 30)} \\ \sigma_{cr} &= 2476 \text{ psi (Equation (61))} \\ \sigma_{fr} &= 8058 \text{ psi (Equation (72) and Figure 22)} \end{aligned}$$

From Equation (29)

$$\sigma_{co} = 0.979 \sigma_{fr} = 7888 \text{ psi}$$

σ_{fr} can be used as a conservative upper value if the column effect is ignored.

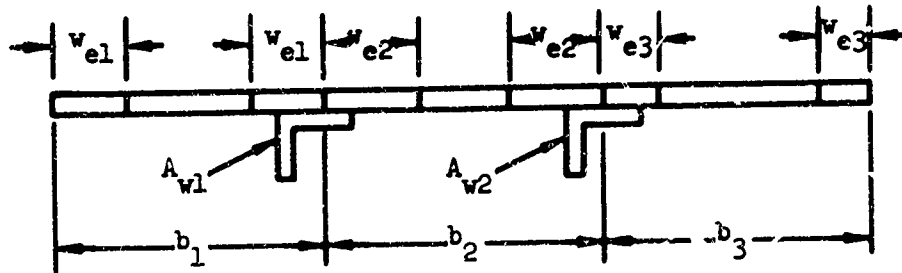
f. Determination of failure load (p_f) from failure stress ($\bar{\sigma}_{fr}$)

$$(1) \left[\frac{w_e}{b} \right]_i = .25 \left(1 + \frac{\sigma_{cr}}{\sigma_{fr}} \right) \left(\frac{\sigma_{cr}}{\sigma_{fr}} \right)^n = K \quad (77)$$

$$\text{where } n = .37 \frac{\bar{\sigma}_{fr}}{\sigma_{cy}}$$

- σ_{cr} is obtained in Step 2
- σ_{cy} is obtained in Step 4
- σ_{fr} is obtained in Step 5

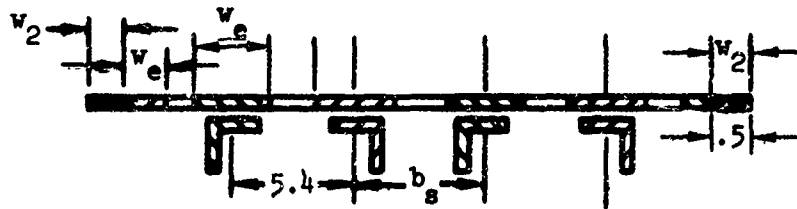
(2) From Figure 25 obtain $\left(\frac{w_e}{b_s}\right)$



- (3) Knowing b_i and K then w_{e_i} can be obtained from the expression above in which $(w_e/b)_i = K$
- (4) Sum overall effective widths $\sum_{i=1}^n w_e$
- (5) Multiply $\sum w_e \times t_s = \sum A_{s_e}$
- (6) $\sum A_w = A_{w1} + A_{w2} + \dots$
- (7) Failure load = $(\sum A_{s_e} + \sum A_w) \sigma_f$ per panel

For the example structure the effective width is given by

$$\begin{aligned} \frac{w_e}{b_s} &= .25 \left(1 + \frac{\sigma_{cr}}{\sigma_{fr}} \right) \left(\frac{\sigma_{cr}}{\sigma_{fr}} \right)^{.37} \left(\frac{\sigma_{fr}}{\sigma_{cy}} \right)^{.37} \frac{\sigma_{fr}}{\sigma_{cy}} \\ &= .25 \left(1 + \frac{2476}{8058} \right) \left(\frac{2476}{8058} \right)^{.37} (.179) = .30212 \end{aligned}$$



$$\begin{aligned}
 N_e &= \text{Number of effective widths} \\
 A_{se} &= (N_e w_e + 2 w_{e2}) t_s \quad (78) \\
 &= [10 (.30212) 5.4 + 2 (.5) .30212] .032 \\
 &= .53173 \\
 N_a &= \text{Number of Angles} \\
 A_w &= N_a A_a = 4(.75 + .718) .032 = .1879 \\
 F_f &= \sigma_{fr} (A_{se} + A_w) = 5800 \text{ lb}
 \end{aligned}$$

2. Post-Failure Analysis

a. Determination of plastic hinge moments

$$(1) \text{ obtain } N/A = \frac{\sum A_i t_i}{\sum A_i} \quad (79)$$

$$(2) \text{ obtain } M_p^* = \left(\sum_{i=1}^n A_i e_i \right) \sigma_{cy}$$

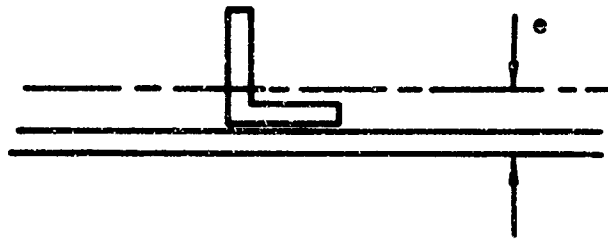
(3) calculate M as a function of deflection, M_{max} , M_{min} , plastic hinge rotation θ , and constant K.

For the sample structure the maximum and minimum plastic hinge moments for post-failure analysis are obtained as follows:



$$\begin{aligned}
 M_{2, \min} = M_{2, \max} &= 1/4 b t_s^2 \sigma_{cy} = 1/4 (28)(.032)^2 (45000) \\
 &= 322.6 \text{ in.-lb}
 \end{aligned} \quad (80)$$

$$*M_p \text{ for one solid rectangular cross-section} = \frac{1}{4} b t_s^2 \sigma_{cy}$$



The neutral axis N/A for the stiffener and skin is:

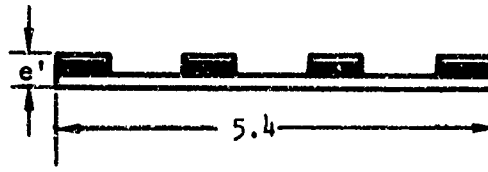
$$e = .062$$

$$M_{1, \max} = [28(.032)(.062-.016) + 4(.75)(.032)(.062 - .032 -.016) + .718 \left(\frac{.718}{2} + .032 + .032 - .062 \right) (.032) 4] \sigma_{cy} = .0757373(45000) = 3408 \text{ in.-lb}$$

To allow for the effect of brake forming on the tensile and compressive stress as noted in Reference 105 a 15% increase in the plastic hinge moment is introduced.

$$M_{\max} = 1.15 (M_{2, \max} + M_{1, \max}) = 4290 \text{ in.-lb}$$

For $M_{1, \min}$ we assume the flange of the angle has folded as



$$e' = \frac{5.4(0.32)(.016) + (.75+.718)(.032)^2}{5.4(.032) + (.75+.718).032} = .02626 \text{ in.}$$

$$M_{1, \min} = [28(.032)(.02626-.016) + 4(.75+.718)(.032)(.032+.032 - .02626)] 45000 = 733 \text{ in.-lb}$$

Therefore

$$M_{\min} = 1.15 (322 + 733) = 1213 \text{ in.-lb}$$

The post-failure plastic hinge moment is given as:

$$M = M_{\min} + (M_{\max} - M_{\min}) e^{-K\theta} \quad (81)$$

Therefore,

$$M = 1213 + 3077 e^{-K\theta} \quad (82)$$

where

$$K = 5 \left(\frac{20}{Y} \right)^2 \left(\frac{.032}{t} \right) = 4.2 \quad (83)$$

$$\theta = \tan^{-1} \left[\sqrt{\frac{u}{z}} \left(l - \frac{u}{z} / \left(\frac{l}{2} - \frac{u}{2} \right) \right) \right] \quad (84)$$

and the post-failure load-deflection curve can be obtained from the following expression:

$$P = \frac{1}{\sqrt{\frac{u}{2} (l-u)}} \left[1213 + 3077 e^{-4.2\theta} \right] \quad (85)$$

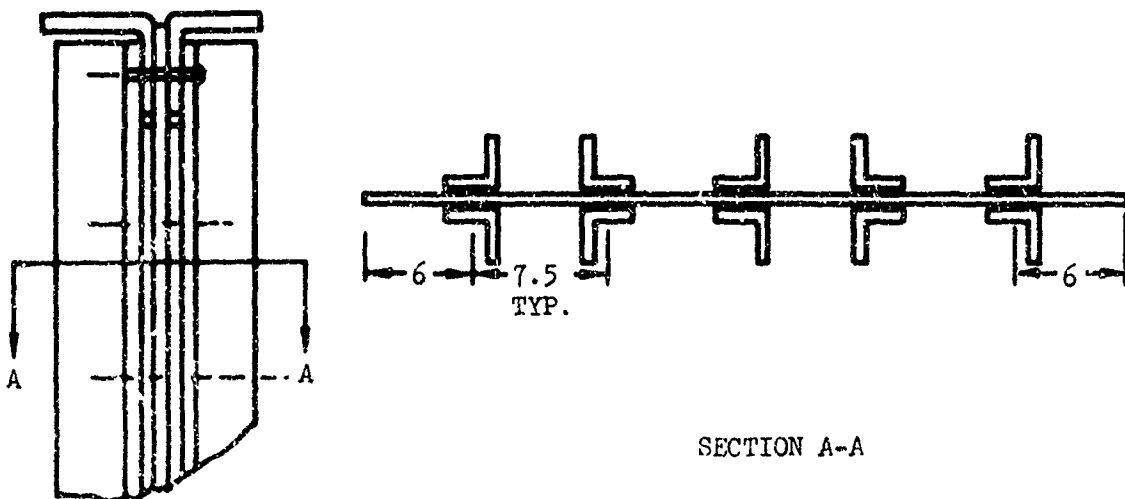
where

$$l = 12$$

u = vertical crushing distance

B. Side Stiffener Analysis

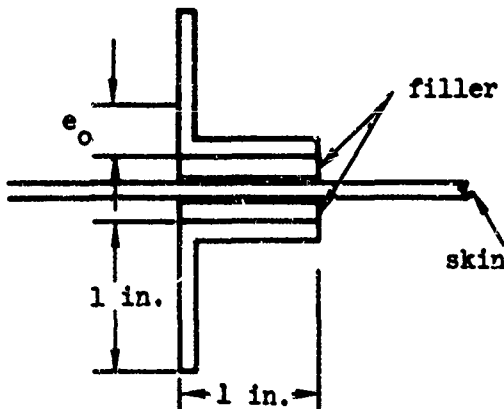
The side stiffener web is represented as shown below:



1. Failure Load Analysis

a. Examination of column instability effect.

Determine if column effect should be included in the calculation of σ_{fr}



$$I_s = \frac{7.5}{12} (.032)^3 = 2.048 \times 10^{-5}$$

$$2I_f = \frac{(.032)^3}{6} 1 = 5.46 \times 10^{-6}$$

$$e_o = \frac{1 + (1 - .032) \cdot .032}{2(2 - .032)} = .262$$

$$I_w = \frac{.032(1 - .262)^3 + 1(.262)^3 - 1(.262 - .032)^3}{3}$$

$$2I_w = 1.24532 \times 10^{-2}$$

$$I = I_s + 2I_f + .06298 (.262 + .048)^2 (2) + 2I_w + 2(1)(.032)(.032)^2 = 2.465 \times 10^{-2} \text{ in.}^4$$

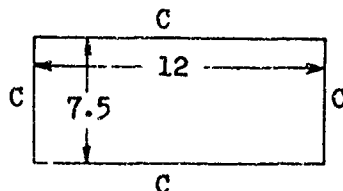
$$A = A_s + 2A_w + 2A_f = 7.5 (.032) + 2(1.968) .032 + 2(1) \times .032 = .43 \text{ in.}^2$$

$$\rho = \sqrt{\frac{I}{A}} = .2394 \text{ in.}$$

$$\delta = \sqrt{\frac{L}{C}} \rho = \sqrt{3} \left(\frac{12}{.2394} \right) = 28.9 < 30.0$$

From the flat curve range shown in Figure 29 the column instability effect is not considered significant. Therefore, any further consideration of column effect on σ_{fr} is ignored in the subsequent analysis.

b. Determination of critical buckling stress



$$a/b_s = 12/7.5 = 1.6$$

$$k_c = 8.5 \text{ from Figure 100}$$

$$\sigma_{cr} = k_c \frac{\pi^2 E}{12 (1-\nu^2)} \left[\frac{t_s}{b_s} \right]^2 \quad (86)$$

$$= 8.5 \left[\frac{\pi^2 \times 10^7}{12 (1-0.3^2)} \right] \left[\frac{0.032}{7.5} \right]^2 = 1398.5 \text{ psi}$$

c. Determination of type of failure

For this particular configuration the side stiffener panel consists of five double angle stiffeners between the supports. This is considerably stiffer than the bulkheads in the same region. Therefore, interrivet failure is ruled out in this case. However, in general, the following expression must be evaluated:

$$\frac{P}{b_s} < \frac{1.27}{K_w^{1/2}} \quad (87)$$

as previously performed for the bulkhead.

d. Determine Yield Stress

Due to same material

$$\sigma_{cy} = \sigma_{cy_s} = \sigma_{cy_w} \quad (88)$$

e. Determine the Failure Stress

The monolithic failure stress is:

$$\frac{\sigma_f}{\sigma_{cy}} = \beta_g \left[\frac{g t_w \cdot t_s}{A} \left(\frac{\eta E}{\sigma_{cy}} \right)^{1/2} \right]^{0.85} \quad (89)$$

From Table XVI,

$$\beta_g = .0583, \quad g = 7$$

$$t_w = 2 \times t_w \text{ (due to double stiffener)} \\ = 0.064$$

$$A_w = 1.968 (0.032) = 0.062976$$

$$A_s = 7.5 (0.032) = 0.24$$

$$A = A_s + 2A_w = 0.365952; \sigma_y = 45000 \text{ psi}$$

$$\frac{\sigma_f}{\sigma_{cy}} = 0.583 \left[\frac{7 (0.064) (0.032)}{0.365952} \left(\frac{1000}{4.5} \right)^{1/2} \right]^{0.85}$$

$$= 0.3690681$$

To account for the rivet strength effect

$$\left(\frac{P}{d} \right) \left(\frac{P}{t_s + t_w} \right) = \left(\frac{1}{5/32} \right) \left(\frac{1}{0.096} \right) = 67$$

From Figure 22, $\frac{\sigma_{fr}}{\sigma_f} = 0.9$

Therefore,

$$\frac{\sigma_{fr}}{\sigma_{cy}} = 0.33216 \quad \sigma_{fr} = 14,947 \text{ psi}$$

f. Determination of failure load

In calculating ρ previously the filler is included in both the A and I values. This is necessary because the fillers are assumed to participate in the bending stiffness property. However, in the calculation of crippling load (or failure load) the fillers will not carry the direct compressive load. Therefore, their contribution is neglected in determining the failure load.

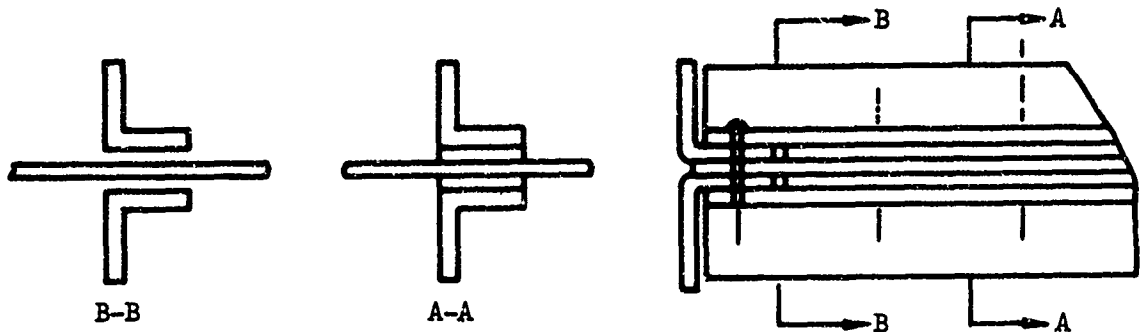
$$\Sigma A_w = 2(5) A_w = 10 (.06298) = .6298$$

$$A_{se} = 10 (7.5) \left(\frac{w_e}{b_s} \right) .032 = .49039 \quad \left(\frac{w_e}{b_s} \right) \text{ obtained from Equation (77)}$$

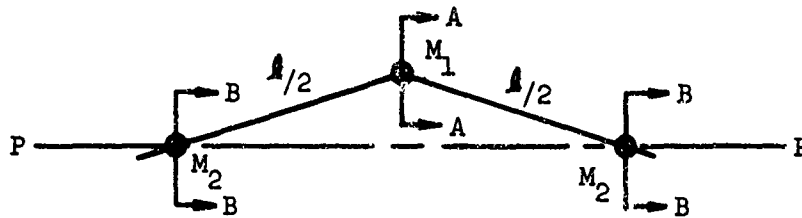
$$P_f = \sigma_{fr} (\Sigma A_w + A_{se}) = 16,743 \text{ lb.}$$

2. Post-Failure Analysis

a. Determination of maximum and minimum plastic hinge moments



The plastic hinges are assumed to occur at Sections AA and BB



The schematic model of symmetric plastic hinges is shown above.

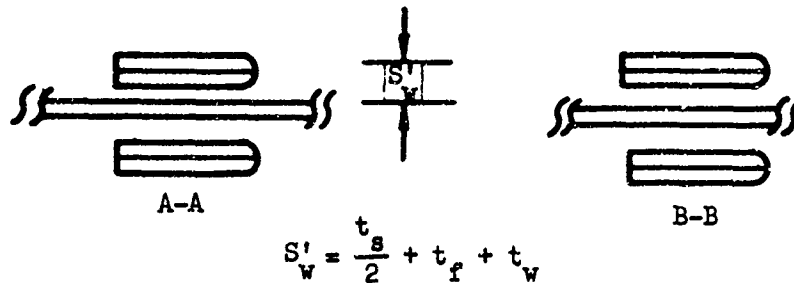
$$M_{1,\max} = \left[\frac{1}{4} b t_s^2 + 10 A_w S_w + 10 A_f S_f \right] \sigma_y \quad (90)$$

$$M_{2,\max} = \left[\frac{1}{4} b t_s^2 + 10 A_w S_w \right] \sigma_y \quad (91)$$

Therefore:

$$\begin{aligned} M_{\max} &= \left[M_{1,\max} + M_{2,\max} \right] 1.15 \quad (92) \\ &= \left[2 \left(\frac{1}{4} \right) b t_s^2 + 20 A_w S_w + 10 A_f S_f \right] \sigma_y \\ &= \left[2 \left(\frac{1}{4} \right) (42) (.032)^2 + 20 (.06298) (.262 + .032 + .016) \right. \\ &\quad \left. + 10 (.032) (.032) \right] \sigma_y (1.15) \\ &= .4222 (45000) (1.15) = 21850 \text{ in.-lb} \end{aligned}$$

For M_{\min} , the cross-section has the following geometry:



$$M_{1, \min} = \left[\frac{1}{4} b t_s^2 + 10 A_w S'_w + 10 A_f S'_f \right] (\sigma_y)$$

$$M_{2, \min} = \left[\frac{1}{4} b t_s^2 + 10 A_w S'_w \right] (\sigma_y)$$

$$\begin{aligned} M_{\min} &= \left[2 \left(\frac{1}{4} \right) (42) (0.032^2) + 20 (0.062976) (0.111) \right. \\ &\quad \left. + 10 (0.063) (0.0475) \right] (\sigma_y) \\ &= 0.19123572 (45000) = 8605.6 \text{ lb-in.} \end{aligned}$$

for modified plastic moment

$$K = 5 \left(\frac{20}{23.57} \right)^2 \left(\frac{0.032}{0.032} \right) = 3.6$$

$$M = 8605.6 + 13036 * e^{-3.6\theta}$$

$$\theta = \tan^{-1} \left[\sqrt{\frac{u}{2} \left(l - \frac{u}{2} \right) / \left(\frac{l}{2} - \frac{u}{2} \right)} \right]$$

where $l = 10$ in.

The length is based on the distance between section BB rather than the total length (12 in.) because the main-beam flanges are assumed not to bend laterally. The post-failure load/deflection curve for the side web is given:

$$P = \frac{M}{\sqrt{\frac{u}{2} (l - u/2)}} \quad (93)$$

C. Main Beam and Bottom Skin Analysis

Perform calculations for each side. The appropriate model is shown in Figure 28.

1. Load-Deflection Curve

a. Determination of neutral axis (N/A)

b. Determination of $M_p = \sum_{i=1}^n (A_i e_i) \sigma_{cy}$ for section AA (94)

c. Determination of I for Section AA

$$= \sum \frac{bt^3}{12} + \sum A_d^2 \quad (95)$$

d. Computation of P_1, P_2 from Figure 110

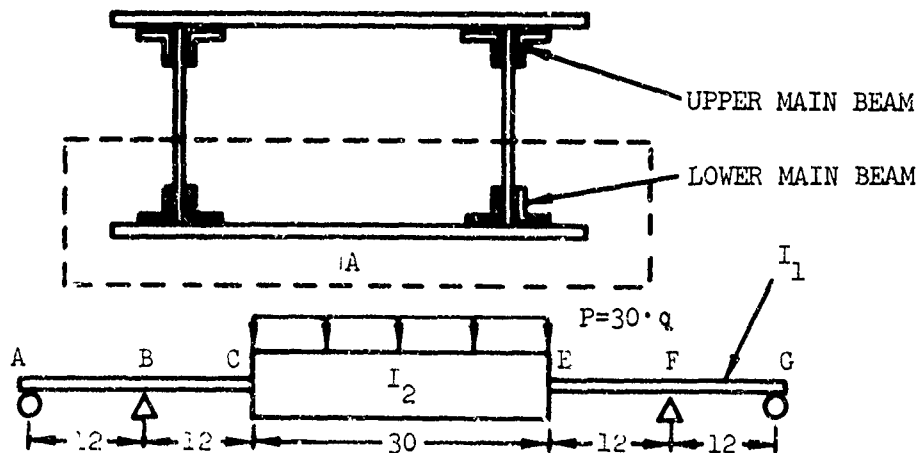
δ_1, δ_2 from Figure 111

or from expressions

$$P_1 = \frac{16}{5l} M_p \quad P_2 = \frac{4}{l} M_p \quad (96)$$

$$\delta_1 = \frac{13}{30 EI} M_p l^2 \quad \delta_2 = \frac{M_p l^2}{2 EI} \quad (97)$$

For the sample structure side stiffener web the following sketches and calculations pertain.



The lumped beam model representation of the lower main beam is given above; where due to rigid support the center section of the beam is assumed to have infinite bending rigidity, or $I_2/I_1 = \infty$.

The first stage of hinges forms at C and E

and
$$P_1 = \frac{16M_p}{5l} = \frac{16M_p}{5 \times 12} = \frac{4}{15} M_p$$

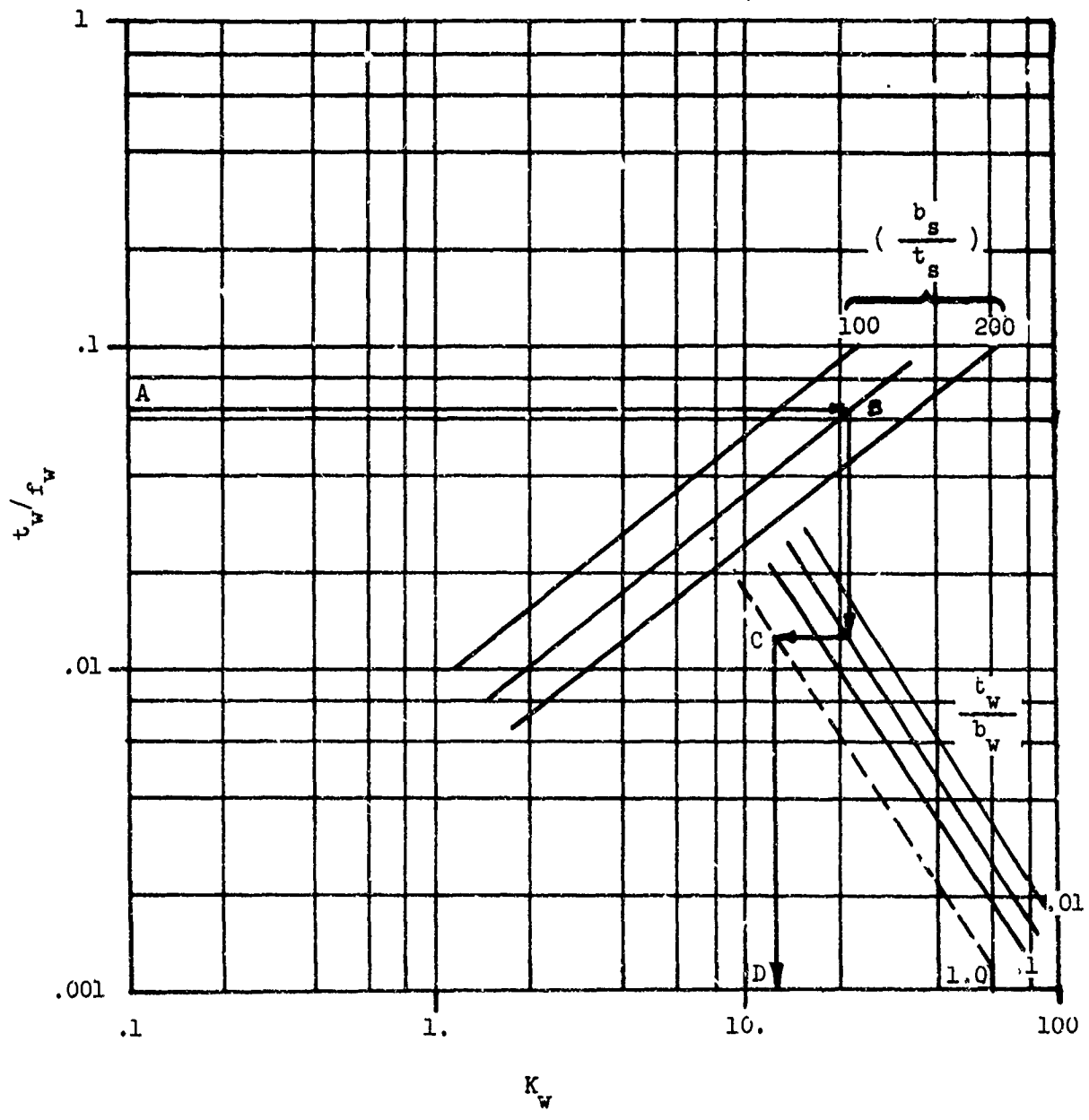


Figure 109. Determination of K_w .

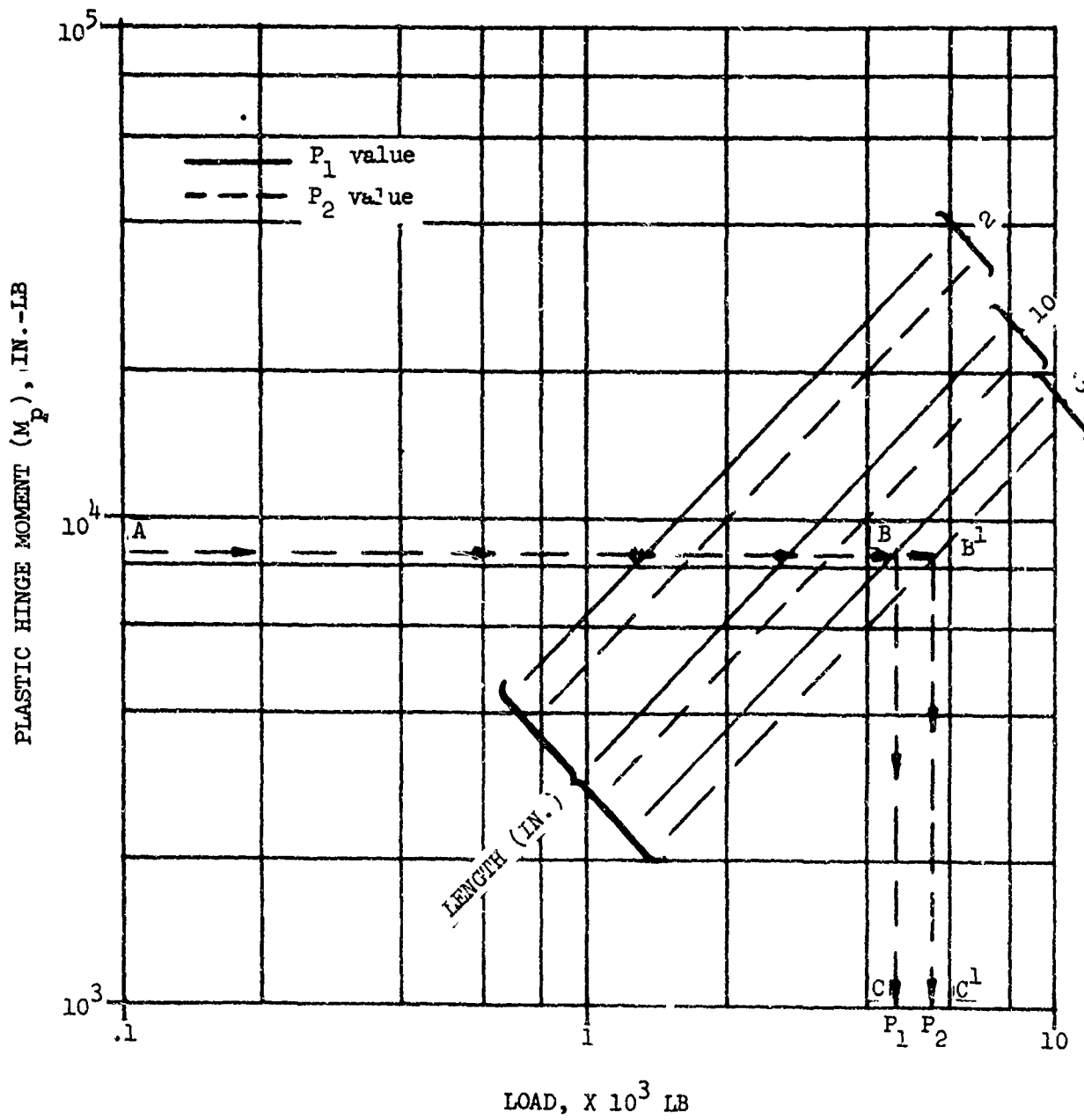


Figure 110. Nomograph To Determine Beam Bending Loads.

where $l = 12$

$$\delta_1 = \frac{13}{30 EI}, M_p l^2 = 6.24 \times 10^{-6} \frac{M_p}{I}$$

and the maximum load and the corresponding displacements are

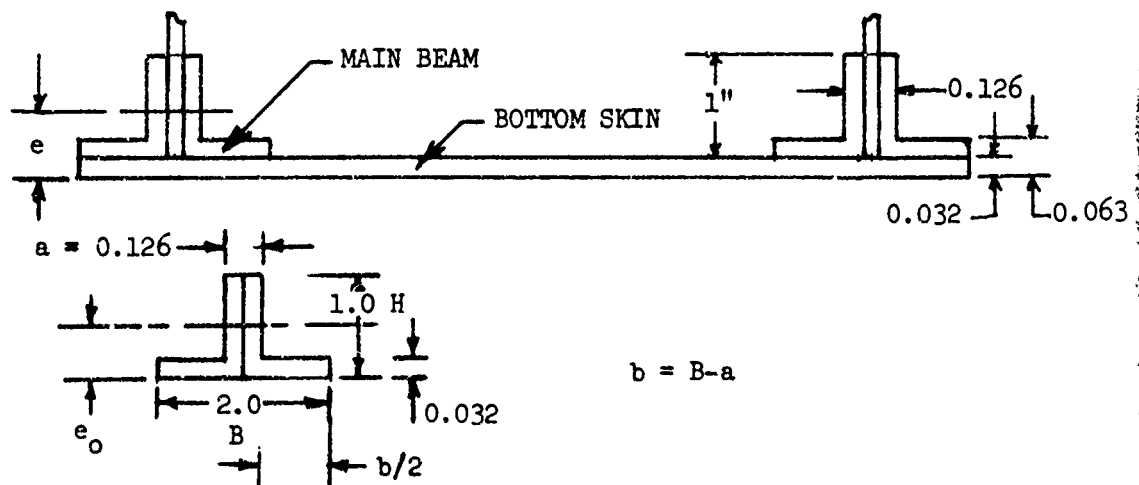
$$P_2 = \frac{4M_p}{l} = \frac{4}{12} M_p = \frac{1}{3} M_p$$

where $l = 12$

$$\delta_2 = \frac{M_p l^2}{2EI}, = 7.2 \times 10^{-6} \frac{M_p}{I_1}$$

Calculate M_p and I_1 for the beam.

Idealized beam cross-section is:



$$e_o = \frac{1}{2} \frac{aH^2 + bd^2}{aH + bd} \quad (98)$$

$$I_o = \frac{1}{3} [Be_o^3 - b(e_o - d)^3 + a(H - e_o)^3] \quad (99)$$

$$A_o = aH + bd \quad (100)$$

$$= (0.126)(1.) + (2 - 0.126)(0.032) = 0.1861 \text{ in.}^2$$

$$e_o = \frac{1}{2} \left[\frac{(0.126)1^2 + (1.874) + (0.032)^2}{0.1861} \right] = 0.343632 \text{ in.}$$

$$I_o = \frac{1}{3} \left[2(0.343632)^3 - 1.874 (0.343632 - 0.032)^3 \right. \\ \left. + 0.126 (1 - 0.343632)^3 \right] \\ = 0.059707 \text{ in.}^4$$

$$A_s = 28 \times 0.032 = 0.896 \text{ in.}^2$$

$$I_s = \frac{1}{12} \times 28 \times 0.032^3 = 7.646 \times 10^{-5} \text{ in.}^4$$

$$e = \frac{(28)(0.032)(0.016) + (2)(0.1861)(0.343632 + 0.032)}{28(0.032) + (2)(0.1861)}$$

$$= 0.10236 \text{ in.}$$

$$I_1 = I_s + 2I_o + 0.896 (0.10236 - 0.016)^2 \\ + 0.488124 (0.343632 + 0.032 - 0.10236)^2 \\ = 0.036452 \text{ in.}^4$$

$$M_p = \sigma_y \cdot \left[0.896 (0.10236 - 0.016) + \right. \\ \left. 2(2)(0.063)(0.10236 - 0.0635) + \right. \\ \left. \left(\frac{0.023^2}{2} \right) (2)(0.126) + \frac{0.914^2}{2} (2)(0.126) \right]$$

$$= 8656 \text{ in-lb.}$$

therefore

$$P_1 = \frac{4}{15} M_p = 2308.3 \text{ lb}$$

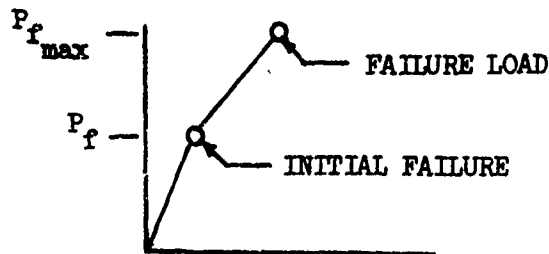
$$\delta_1 = 6.24 \times 10^{-6} \left(\frac{8656}{0.03642} \right) = 1.483 \text{ in.}$$

$$P_2 = \frac{1}{3} M_p = 2885.33 \text{ lb}$$

$$\delta_2 = 1.711 \text{ in.}$$

D. Total Load-Deflection Curve

The failure load (P_f) obtained from section for the bulkhead and side panels is depicted below:



The total load-deflection curve is obtained for the sample structure from the calculated values of the previous subsections:

- A - Bulkhead
- B - Side Stiffener Web
- C - Main Beam and Bottom Skin

If no pre-failure stiffness properties are available or easily obtainable the following procedure to superimpose individual subelement load-deflection curves into a composite load-deflection curve can be adopted.

- (1) For the stiffened panel (this pertains to bulkhead and side stiffener but excludes main beam) plot the post-failure load-deflection curve.
- (2) Asymptotically match the maximum failure load as shown in Figure 112.
- (3) The approximate total load-deflection curve is obtained by superimposing the individual bulkheads, side stiffener webs and main beam curves. For the sample problem presented this includes three bulkheads (C, D, E), two side stiffener webs and the main beam.

Figures 113 through 115 depict the load-deflection curves for the bulkheads, side stiffener webs, beam with bottom skin individually. Figure 116 depicts the total composite load-deflection curve which combines the results shown in Figures 113, 114, and 115.

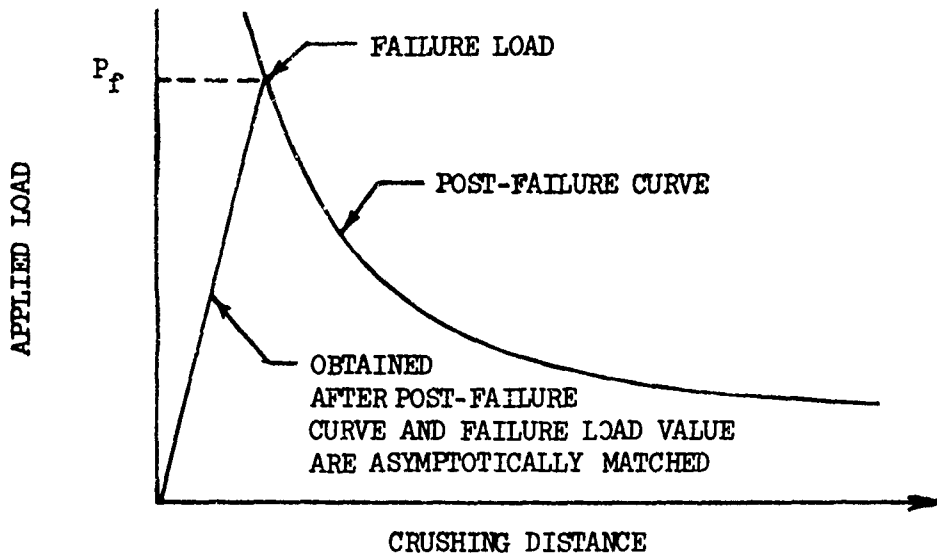


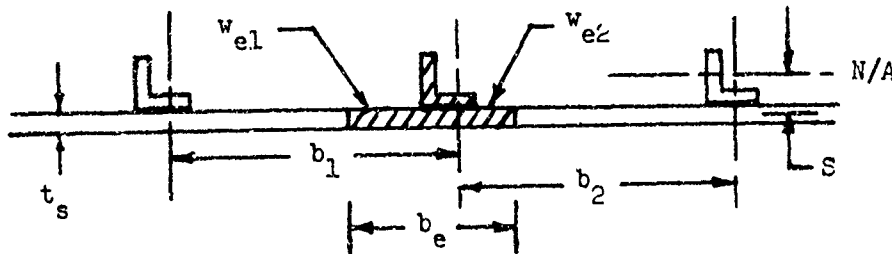
Figure 112. Load-Deflection Curve Obtained by Asymptotic Matching.

E. Long Column Effect

In the event that a L'/ρ value ≥ 30 is calculated for either the bulkheads or side stiffener webs, it is suggested that the column effect on the failure strength of stiffened panels be considered. This is done in the manner outlined below:

Determine ρ as follows:

- (1) Determine σ_{fr} (subsection A-4 of the Detail Approach)
- (2) Determine W_e/b_i (Figure 25)
- (3) Determine b_2



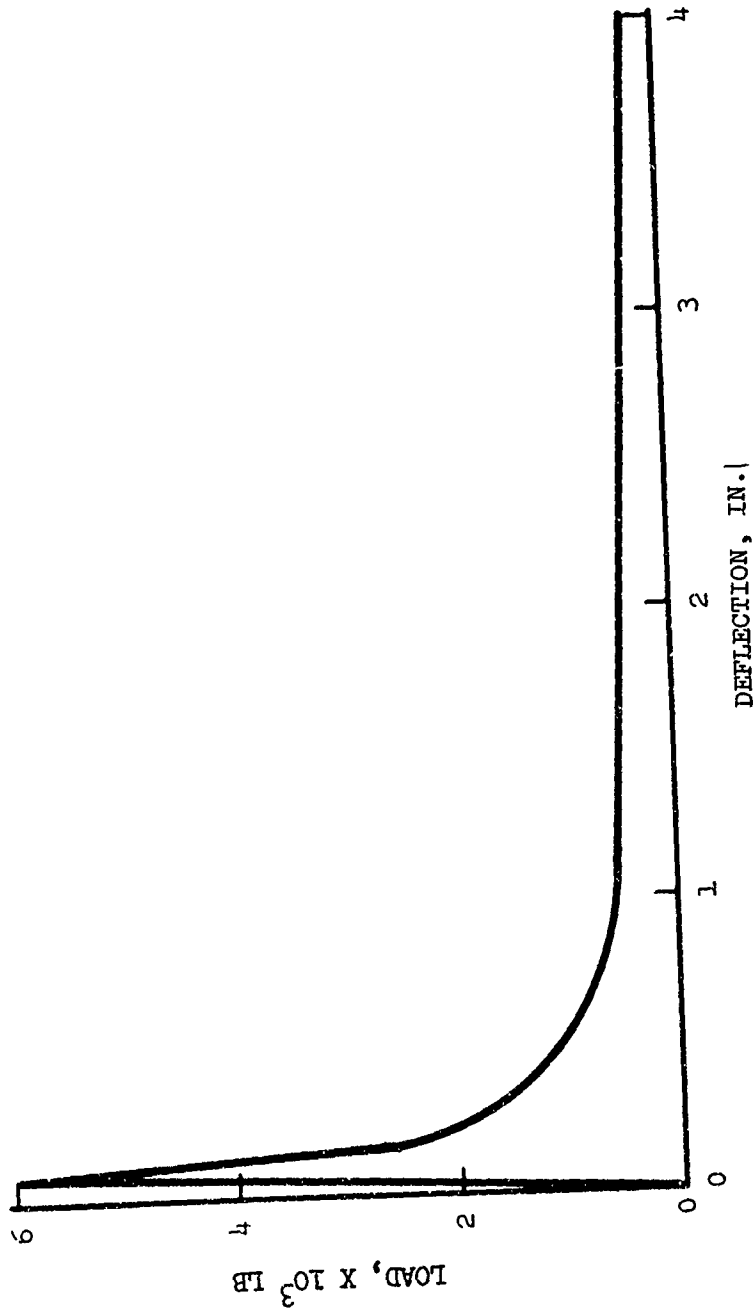


Figure 113. Load-Deflection Curve for Bulkhead, Sample Problem .

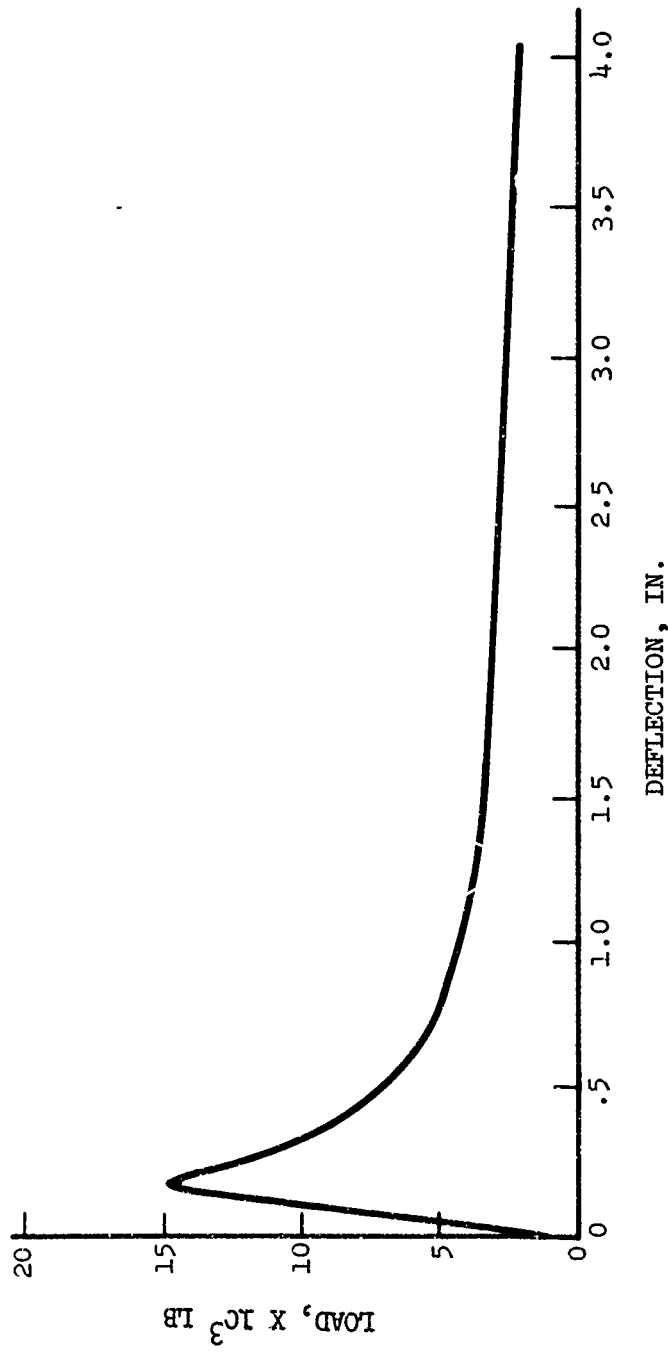


Figure 114. Load-Deflection Curve for the Side Stiffener Web, Sample Problem.

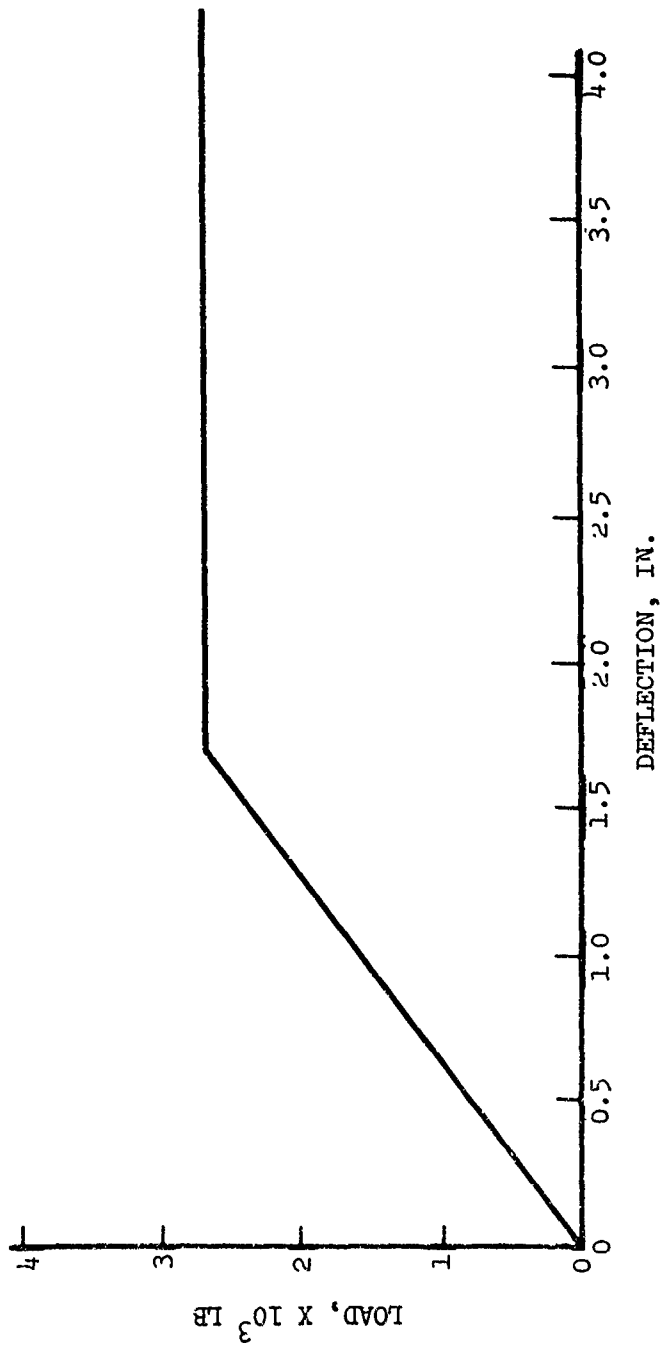


Figure 11.5. Load-Deflection Curve for the Main Beam and Bottom Skin, Sample Problem.

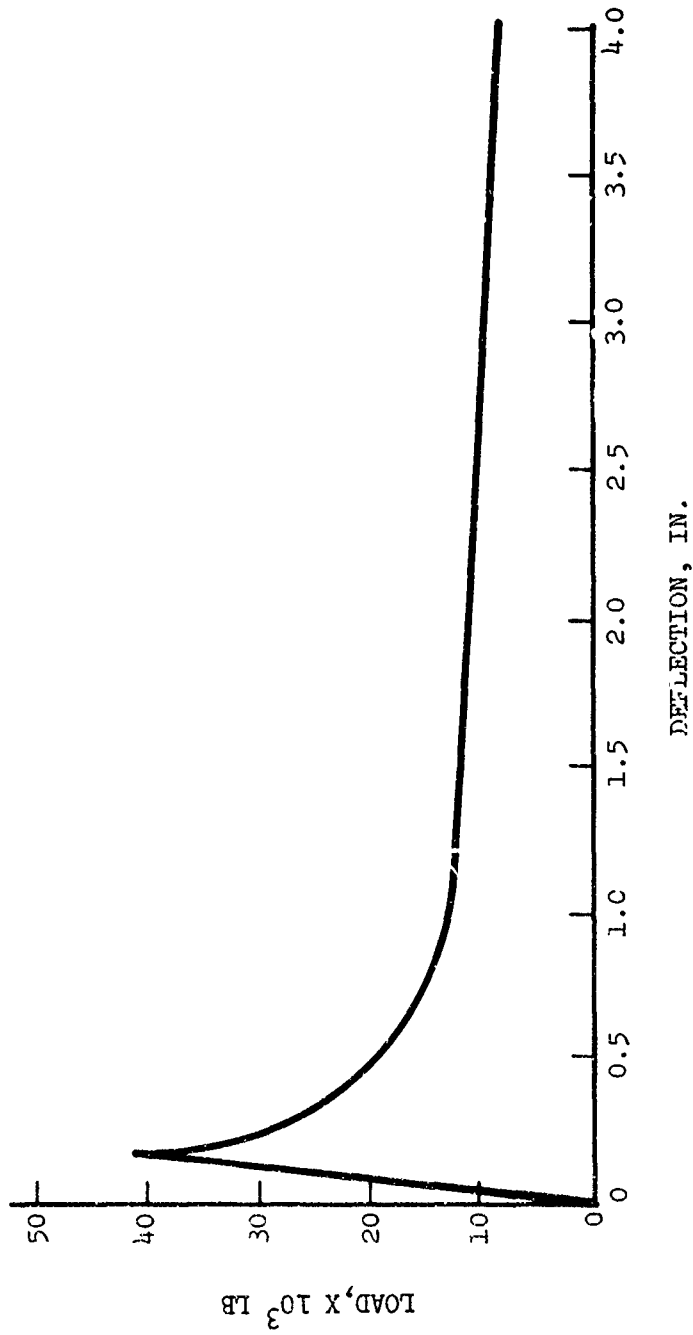


Figure 116. Composite Load-Deflection Curve, Sample Problem.

$$(4) \text{ Determine } \rho_w \text{ for stiffener} = \sqrt{\frac{I(\text{stiffener})}{A(\text{stiffener})}} \quad (101)$$

$$(5) \text{ Calculate } \frac{b_e t_s}{A_{\text{stiff}}}, \frac{t_s}{A_{\text{stiff}}}, \frac{s}{\rho_w}$$

and using Figure 32 obtain (ρ/ρ_w)

(6) Multiply value for (ρ/ρ_w) by ρ_w to obtain ρ

(7) Calculate Euler Stress σ_e

$$\text{Euler Stress} = \sigma_e = \frac{\pi^2 E}{(L/\rho)^2} \quad (102)$$

(8) Obtain stress for $L/\rho = 20$

$$\sigma_{20} = \frac{\pi^2 E}{400} = 246,740 \text{ lb/in.}^2 \quad (103)$$

(9) Obtain column stress σ_{co}

$$\sigma_{co} = 1 - \left(1 - \frac{\sigma_{cr}}{\sigma_{fr}}\right) \left(\frac{\sigma_{cr}}{\sigma_e}\right) \left(\frac{\sigma_{20}^{1/2} - \sigma_e^{1/2}}{\sigma_{20}^{1/2} - \sigma_{cr}^{1/2}}\right)^2 \quad (104)$$

(10) Obtain ultimate load (P_f) as in subsection A or B-1c

$$P_f = \sigma_{co} \left(\sum A_{se} + \sum A_w\right) \quad (105)$$

(11) Continue with post-failure analysis, main beam analysis and total load-deflection curve analysis.

Structural Element Modeling Guidelines

This subsection provides some guidelines by which designers can simplify modeling requirements and utilize approximate techniques for performing preliminary design crashworthiness studies. Although the information presented is directly applicable to the use of program KRASH, it is also general, and therefore can be used for other analytical approaches. Included in this subsection are discussions regarding the determination of stiffness and load-deflection characteristics for different types of structural elements. Design charts, curves, tables and/or equations are presented for:

- columns
- honeycomb plates
- frangible tubes

This section contains information applicable to a crashworthiness design manual in that it shows the type of information and the format in which data can be provided. The data presented in the following subsection are available in current literature.

A. Category Type III Structural Elements

Structural elements which exhibit greatly reduced load-carrying capability after failure load is reached are characterized mainly by buckling failures. As described earlier, in both the load sensitivity study and general design approach, this type of structure can be classified as a Type III load-deflection category. Typical structures which fit into this category are shown in Tables II and III of this report. To illustrate design guide procedures for obtaining approximate load-deflection curves for category III type structure, the compressively loaded column structure is used as a sample element in this subsection.

1. Solid Cross-Section Column

Column failures can be characterized as primarily flexural buckling or combined torsional-flexural buckling. Thick walled and solid cross-section columns tend to fail due to pure flexural buckling whereas thin walled columns exhibit failure as a result of a combined torsional-flexural buckling mode.

Of primary concern in column buckling and post-buckling analysis is the intermediate slenderness ratio range ($30 \leq L'/\rho \leq 120$). Using Equations (43) and (48) in Reference 61 for this range, the following expression for critical stress and lateral deflection in terms of generalized nondimensional quantities is obtained:

$$g(T,y) = y \left[3/2 \left(\frac{1}{T} - T \right) - y - K \right]^{1/2} - \alpha (2T)^{-1/2} = 0 \quad (106)$$

where

$$T = \sigma/\sigma_y$$

$$y = \delta/S$$

$$\alpha = \left[\frac{(\bar{L}'/\rho)^2 \sigma_y}{\pi^2 E} \right]$$

σ = compressive stress

δ = lateral deflection

S = core radius of the cross-section

K = eccentricity factor

L', ρ, E, σ_y have been defined earlier.

The critical stress and the corresponding deflection are obtained from the following expressions, obtained by setting $\partial T/\partial y = 0$:

$$T_{cr} \left(\frac{1}{T_{cr}} - T_{cr} - \frac{2}{3}K \right)^3 = \alpha^2 \quad (107)$$

$$y_{cr} = \left(\frac{1}{T_{cr}} - T_{cr} \right) - \frac{2}{3}K \quad (108)$$

where $T_{cr} = \frac{\sigma_{cr}}{\sigma_{cy}} = \frac{\text{critical stress}}{\text{yield stress}}$

Equation (107) is solved numerically from known values of α and an assumed value of K.

From equation (106) a (T,y)-curve is obtained by linear perturbation as follows:

(a) differentiate equation (106) with respect to y.

$$\frac{\partial g}{\partial y} = \left[\frac{3}{2} \left(\frac{1}{T} - T \right) - y - K \right]^{1/2} - \frac{y}{2} \left[\frac{3}{2} \left(\frac{1}{T} - T \right) - y - K \right]^{-1/2} \quad (109)$$

(b) differentiate equation (106) with respect to T,

$$\frac{\partial g}{\partial T} = -\frac{3}{4} \left[\frac{(T^2 + 1)}{T^2} \right] y \left[\frac{3}{2} \left(\frac{1}{T} - T \right) - y - K \right]^{-1/2} + \left(\frac{\alpha}{2\sqrt{2}} \right) (T)^{-3/2} \quad (110)$$

For $\partial g / \partial T \neq 0$

$$dT = \left(\frac{-\partial g / \partial y}{\partial g / \partial T} \right) dy \quad (111)$$

By incremental solution the approximate post-buckling (T,y)-curve for a general column can now be obtained as follows:

- (a) T_{cr} from equation (107)
- (b) y_{cr} from equation (108)
- (c) Assign increment of Δy and obtain ΔT from equation (106).

The new T vs y becomes:

$$y_{new} = y_{old} + \Delta y \quad (112)$$

$$T_{new} = T_{old} + \Delta T \quad (113)$$

- (d) Using the procedure described above a typical (T,y)-curve is obtained for a column with the following values:

$$(L'/\rho) = 78.3$$

$$\sigma_y = 10^5 \text{ lb/in.}^2$$

$$E = 3 \times 10^7 \text{ lb/in.}^2$$

$$K = 0$$

Figure 117 shows the stress ratio vs. lateral deflection, (T,y)-curve, for the column with the above noted parameter values.

To obtain axial load versus end shortening (deflection) the following procedure is to be followed:

- (a) Obtain core radius. Table XXIV shows the core radius for typical cross-sections.
- (b) Obtain actual length from the reduced length as a function of end fixity. Table XXV shows the reduced length as a function of end fixity.

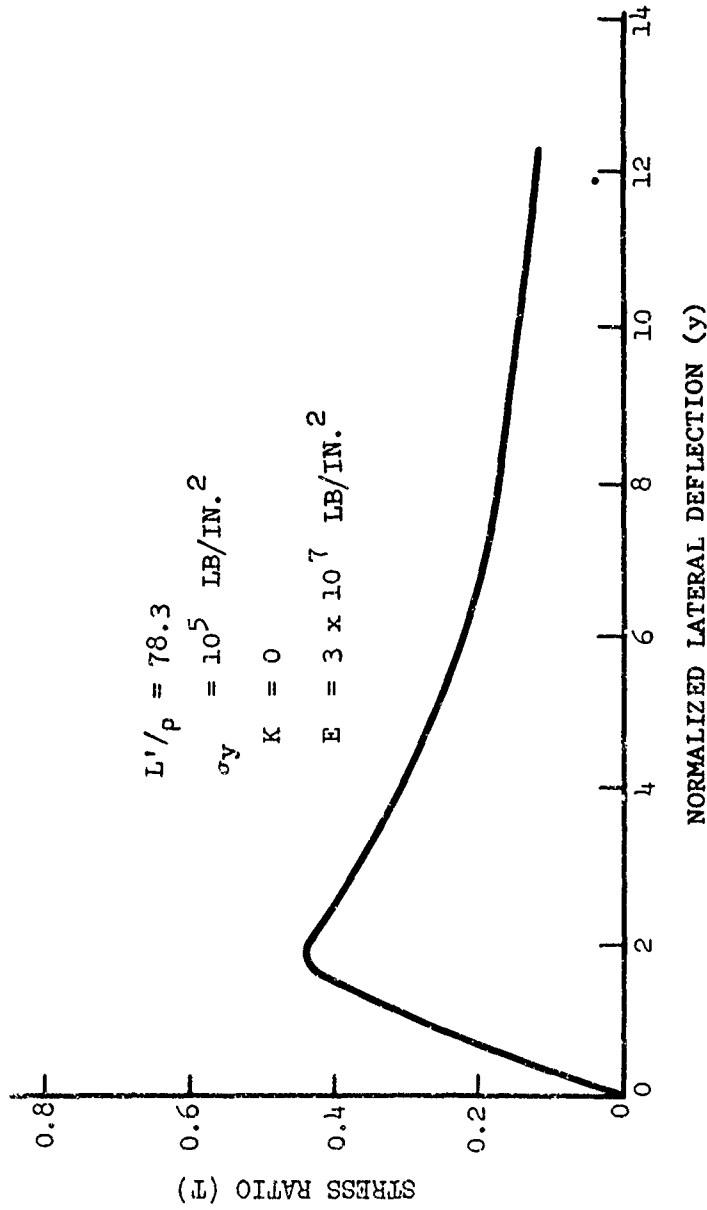


Figure 117. Stress Ratio Versus Normalized Lateral Deflection Curve for Axially Loaded Column.

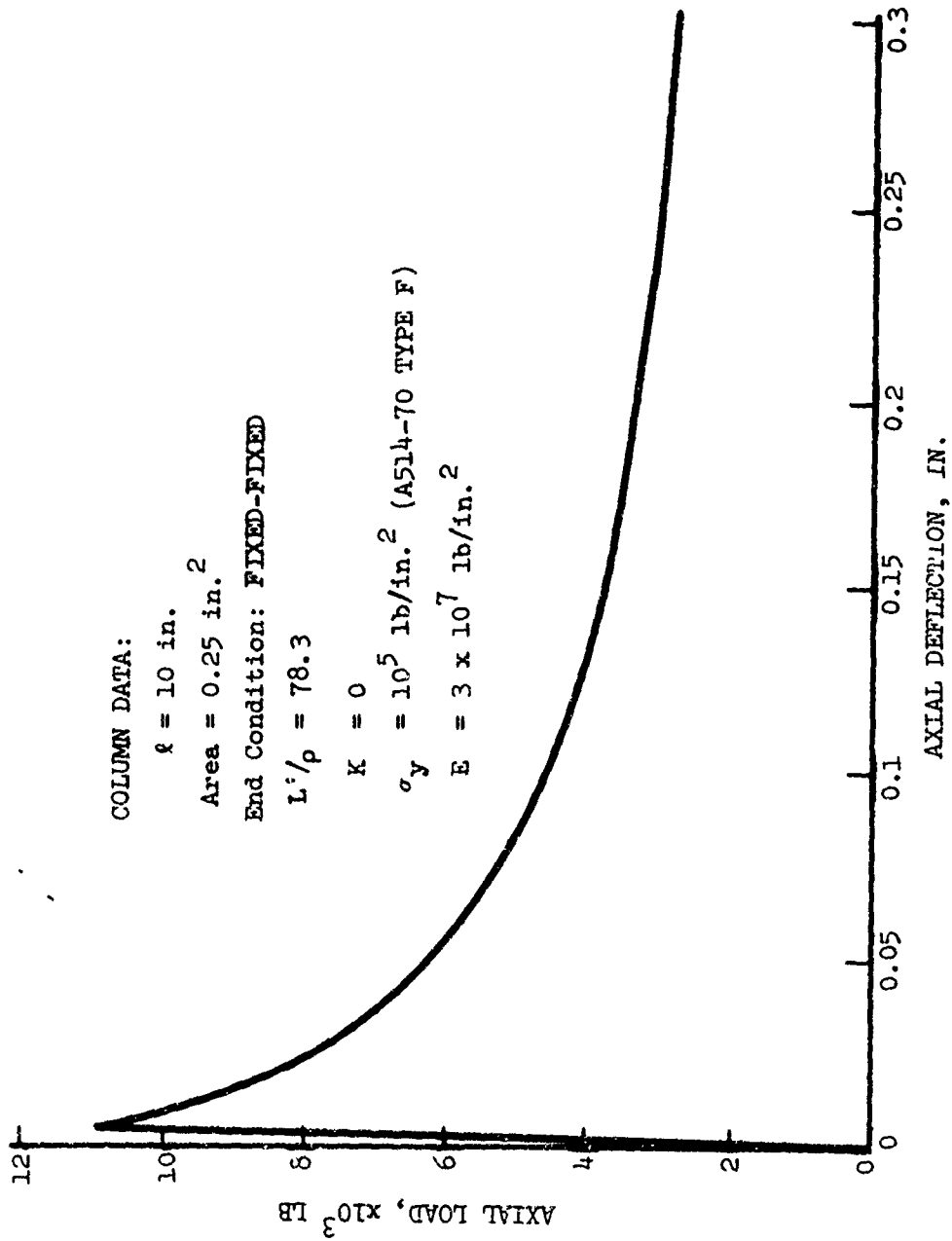


Figure 118. Load versus Deflection Curve for Axially Loaded Column.

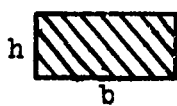
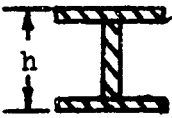
TABLE XXIV. CORE RADIUS			
			
$S = h/b$	$S = R/4$	$S = \frac{R_o^2 - R_i^2}{4 R_o}$	$S = \frac{2I}{hA}$

TABLE XXV. REDUCED COLUMN LENGTH AS A FUNCTION OF END FIXITY			
Both Ends Simply Supported	Fixed-Fixed	Fixed-Simply Supported	Fixed-Free
$L' = \ell$ $C=1$	$L' = 1/2 \ell$ $C=2$	$L' = 0.099 \ell$ $C=1/0.699$	$L' = 2 \ell$ $C=0.5$

(c) Obtain load (P) and end-shortening deflection (u) as follows:

$$P = (A)(T)(\sigma_y) \quad (114)$$

$$u = C^2 \pi^2 S^2 y^2 / 4\ell \quad (115)$$

Equation (115) is an approximate end-shortening based on the assumption that the mode shape is sinusoidal and only the fundamental mode is retained. For the same sample parameter used to obtain the (T, y)-curve (Figure 117) the corresponding load versus axial deflection (P,u)-curve is shown in Figure 118.

For Euler column range ($L'/\rho > 80$) another formula obtained from Reference 111 is:

$$g(T, y) = y \left[3 \left(\frac{1}{T} - 1 \right) - y - K \right]^2 - 4 \alpha T \left(\frac{1}{T} - 1 \right)^3 = 0 \quad (116)$$

Following the same procedure outlined previously in this subsection

$$T_{cr} = \frac{1}{\alpha} \left[\frac{3 \left(\frac{1}{T_{cr}} - 1 \right) - K}{3 \left(\frac{1}{T_{cr}} - 1 \right)} \right]^3 \quad (117)$$

if $K = 0$ Equation (117) coincides with the Euler Buckling stress

$$\sigma_e = \left(\frac{\pi^2 E}{(L'/\rho)^2} \right)$$

and

$$y_{cr} = \frac{1}{T_{cr}} - 1 - K/3 \quad (118)$$

$$\frac{\partial g}{\partial y} = \left[3 \left(\frac{1}{T} - 1 \right) - y - K \right] \left[3 \left(\frac{1}{T} - 1 \right) - 3y - K \right] \quad (119)$$

$$\frac{\partial g}{\partial T} = 4 \alpha \left(\frac{1}{T} - 1 \right)^2 \left(\frac{2}{T} + 1 \right) - \frac{3y}{T^2} \left[3 \left(\frac{1}{T} - 1 \right) - y - K \right] \quad (120)$$

To obtain load versus axial deflection the procedures described previously are to be followed.

2. Thin-Walled Column

For columns with thin-walled cross-sections, failure generally occurs as a result of a combined torsional-flexural buckling. References 100 and 102 discuss the theoretical aspects of this problem. Reference 111 presents design charts for typical cross-sections of thin-walled columns. The design charts provide preliminary design oriented data in that the torsional-buckling loads are presented in terms of Euler buckling loads, column geometry and support boundary conditions. A typical curve is shown in Figure 119 for column cross-section with unequal angle lengths. Reference 111 contains design charts for other types of cross-sections including inwardly and outwardly lipped channels, T sections and plain channels. It is assumed, for simplicity, that the (T, y) -curve for thin-walled columns follows that of solid columns by the factor α shown in Figure 119. It is suggested that Figure 119 be used in the following manner:

(a) determine Euler stress load $(A\sigma_e)$. For solid columns use Equation (28), page 63.

(b) determine τ from $\tau = \frac{Lt}{\rho b_x}$ (121)

where t = angle thickness

b_x = short angle length (see Figure 119)

- (c) determine τ/m where $2 \geq m \geq 1$ (see Figure 119)
- (d) determine α from Figure 119 using the τ/m and b_y/b_x values
- (e) determine critical load (P_{cr}) from $P_{cr} = (P_{Euler}) (\alpha)$
- (f) determine axial load versus deflection curve (P vs. u) following procedures outlined for solid cross-section columns and reduce the load curve proportional to the value of α .

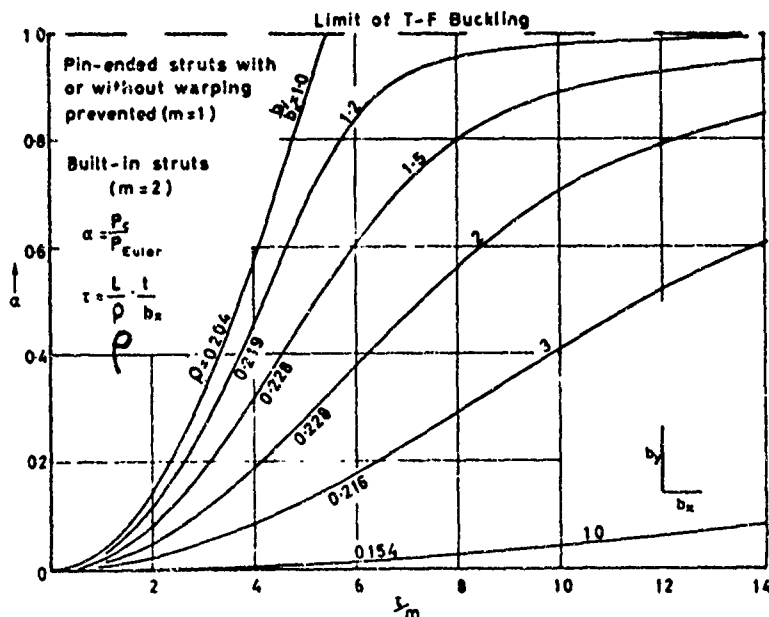
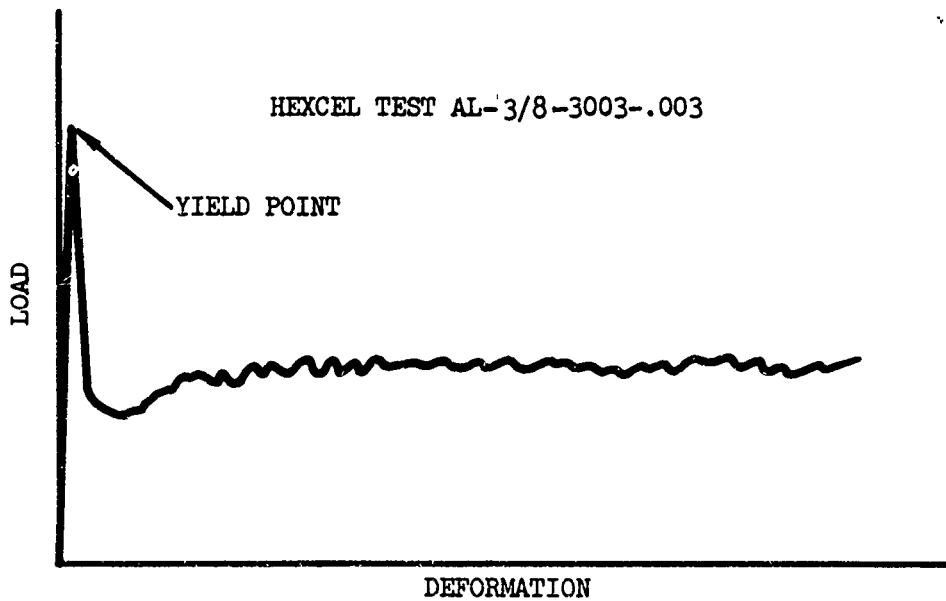


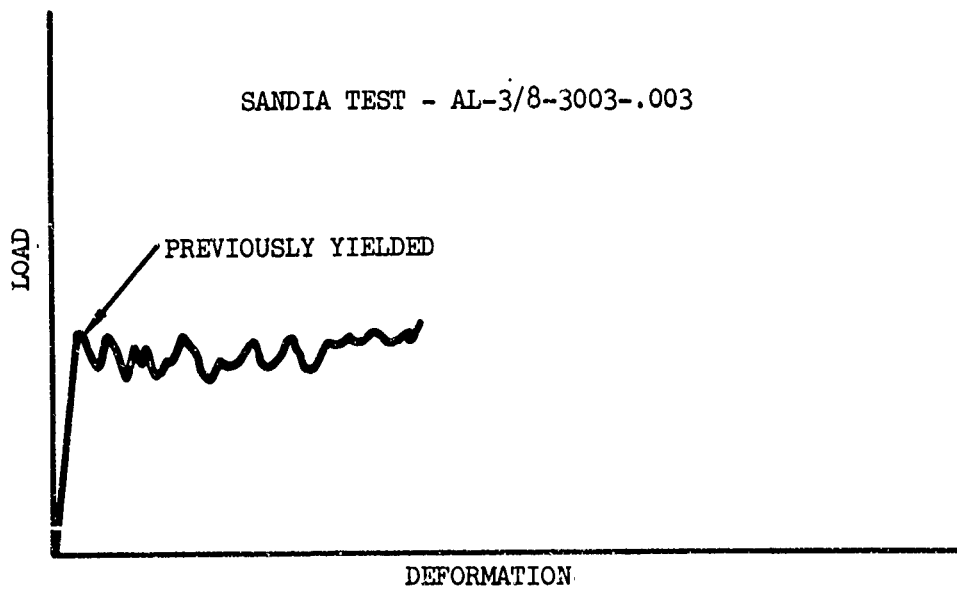
Figure 119. Critical Load Factor for Thin Walled Column with Cross-Section of Unequal Angles.

B. Category Type II

The load sensitivity study and literature evaluation presented previously in the report describe structural elements which exhibit a constant load carrying capability after the failure load is reached, as a category Type II element. Included in this category are structure types which are used as load limiters or energy absorbers such as frangible tubes, honeycomb and other multiple cell structure, stainless steel straps, inversion and telescoping tubes. Type II elements are prominently used in design regions wherein control (limit) of the load level is desired. In particular, this type of structural element is used where controlled deformation is required; e.g., seat systems



(a) STATIC LOADING (.15 IN./MIN)



(b) DYNAMIC LOADING (27.6 FT/SEC)

Figure 120. Load Deformation Characteristics for Compressively Loaded Honeycomb Panel (Reference 112).

and landing gears. Of primary concern for load and shock attenuation systems are characteristics such as:

- Energy absorption capacity
- Elastic deformation per unit load
- Peak loads to initiate crushing
- Load on-set rates
- Rebound

Another consideration in the selection of a load limiting system is the efficiency of the design with regard to absorbed energy per pound of material required. Table V (page 18) in this report presents a comparative summary of absorption efficiencies for different kinds of configurations.

To illustrate, design guide procedures for obtaining load-deflection characteristics for Type II structural element honeycomb and frangible tube design data, from the literature, are presented in the following subsections:

1. Honeycomb

Extensive testing has been performed to determine crushing load and characteristics for different sizes and configurations of honeycomb panels. Reference 23 provides test data regarding the effects which changes in specimen configuration, cell geometry, test conditions and environment have on the characteristics of crushable energy absorbing materials. Since the load-deflection characteristics of a honeycomb structure are sensitive to the tolerances for foil thickness, adhesive cell size and orientation, cross-sectional area and outer skin dimensions, test data have been generated for a wide variety of honeycomb configurations. Reference 112 is a series of technical service bulletins provided by a major manufacturer of honeycomb structure. The reference reports include comprehensive design data, design charts and procedures. The reference material also includes an excellent discussion on the general crushing characteristics of honeycomb under static and dynamic loads and the mode of honeycomb crushing. The following figures, tables and discussions obtained from information in Reference 112 are presented to illustrate the type of data that is contained in the reference.

Characteristically, honeycomb load-deflection curves will look like those shown in Figure 120(a) and 120(b) for static and dynamic loading. The average level of the load in the relatively uniform area is called the crushing stress and generally varies

between 40% and 60% of the compressive strength of the honeycomb, depending on type. The difference can be seen in the sharp peak load at yield for the static load. For design purposes, the crushing stress for the compressively loaded honeycomb panel can, as an approximation, be considered to decrease as a function of the loading angle as shown in Figure 121. Figure 122 illustrates other types of available data provided in Reference 112 which is useful to the designer for preliminary crashworthiness studies. Some basic formulas which will also aid designers are:

Stopping distance (S)

$$S = \frac{V^2}{2gG} \quad \begin{array}{l} V = \text{impact velocity} \\ G = \text{acceleration level} \\ g = 32.2 \text{ ft/sec}^2 \end{array} \quad (122)$$

minimum core thickness (t_c)

$$t_c = \frac{V^2}{.7(2gG)} \quad (123)$$

crush strength (f_{cr})

$$f_{cr} = \frac{WG}{A} \quad \begin{array}{l} W = \text{weight} \\ A = \text{area} \end{array} \quad (124)$$

kinetic energy (KE)

$$KE = f_{cr} AS \quad (125)$$

Nomographs are provided in Reference 112 for all the expressions presented above.

2. Frangible Tube

Detailed design and test data is available in References 32-35. Application areas of such energy absorbing devices include crash-worthy passenger seat systems, landing gears, and other load limiters.

The average load suggested in Reference 34 is

$$P = K_t A + 4 \pi f_c A_c \sigma_y \quad (126)$$

in which K_t is the axial tube stress caused by the resistance to ribbon bending and spitting, A is the cross-sectional tube area, f_c is the friction coefficient, A_c is the cross-sectional area of

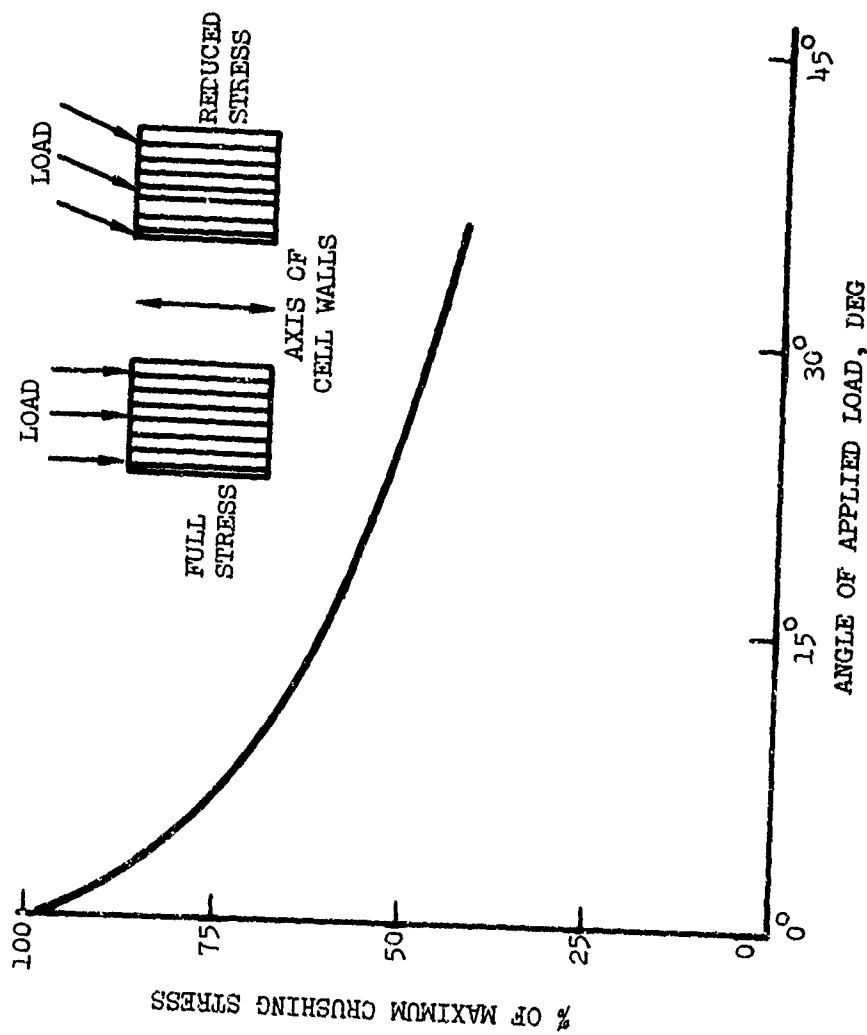


Figure 121. Variation of Stress With Angle of Applied Load (Reference 112).

TESTED BY SANDIA CORPORATION, ALBUQUERQUE

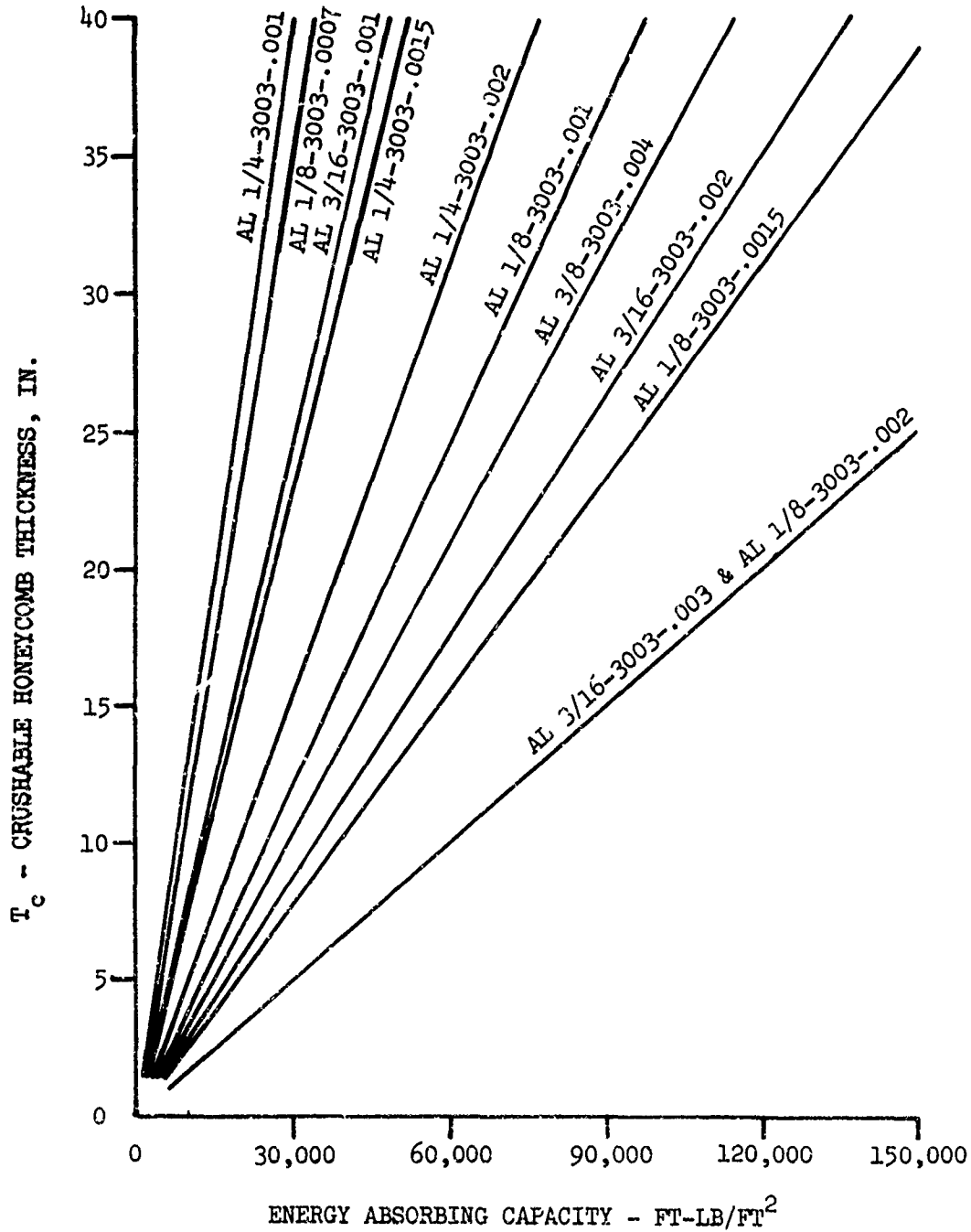


Figure 122. Thickness versus Energy Absorbing Capacity for Nonstandard Aluminum Honeycombs (Reference 112).

one side of the control ring and σ_y is the tensile yield stress of the control ring. Figure 123 shows a sketch of frangible tube energy absorber showing the tube control ring and splitter ring. For the sizes tested in References 32-35, K_t and f_c are given in Table XXVI.

TABLE XXVI. TYPICAL VALUES OF K_t AND f_c (REFERENCE 34)		
Material	K_t	f_c
2024-T3	4000	0.067
Brass	7000	0.156
Az - 31B	1750	0.110
Steel 1015	11000	0.119
Steel 4130	25000	0.104

A typical load-deflection curve for a tube made of mild steel 1015 is shown in Figure 124. From Equation (126), the average load is

$$P = (11000) (\pi) (2) (0.049) + 4\pi (0.119) (0.0764) (55000) \\ = 9670.3 \text{ (lbs)}$$

This value is about a 7.5% higher load than the test obtained load and overestimates the energy absorption for 6.2 inch travel by approximately 8%.

C. Category Type I Structural Elements

As discussed previously, Type I elements are characterized by load-deflection curves which show an increase in load-carrying capability after initial failure is experienced. Generally, structure of this nature is representative of combined responses from two or more elements with different modes of failure. For example, the fuselage bumper structure tested and analyzed during the study described in Reference 1 illustrates Type I structure. The fuselage bumper load-deflection curve is shown in Figure 1. The crushing of the spherical cap occurs within the first two inches of deflection. However, as the cap collapses, the load is transmitted to two bulkheads which exhibit a second region of increased stiffness (2 to 3 inches deflection). As the bulkhead plastically deforms, the stiffness reduces and a relatively constant load is realized. This is shown in the region in which the structure deflects 3 to 9 inches. Another example of a Type I loading situation is a transversely loaded beam on bulkhead supports at the ends. The beam will yield locally in bending and pull the bulkhead into tension. The load-deflection curve for this condition is characterized in the following sketch:

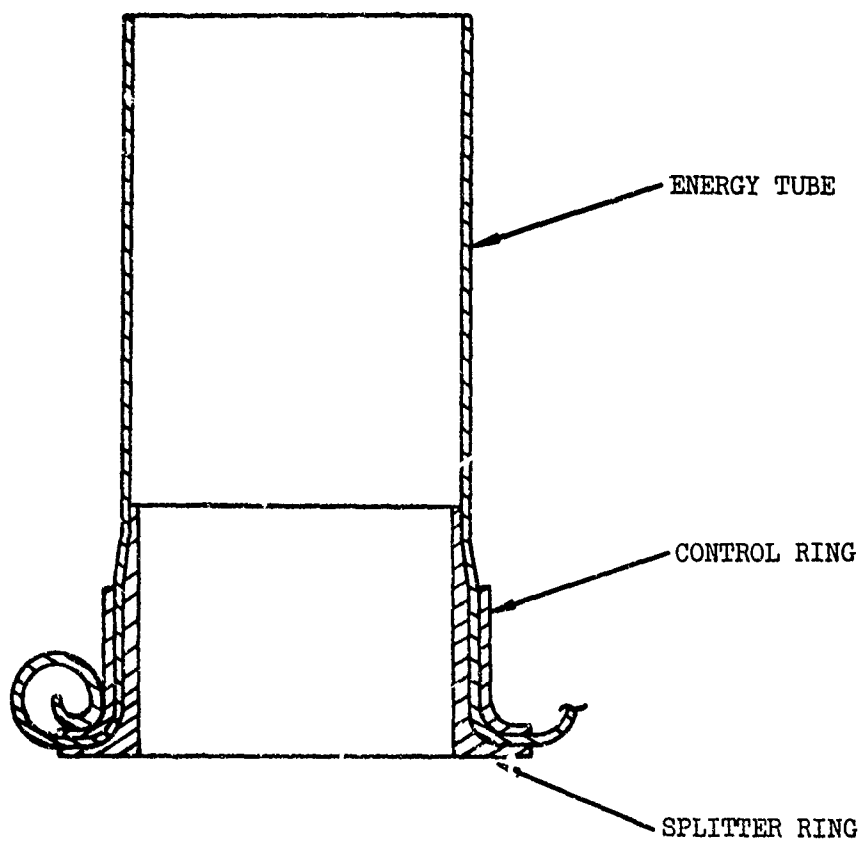


Figure 123. Cross-Section of Frangible Tube Energy Absorber (Reference 34).

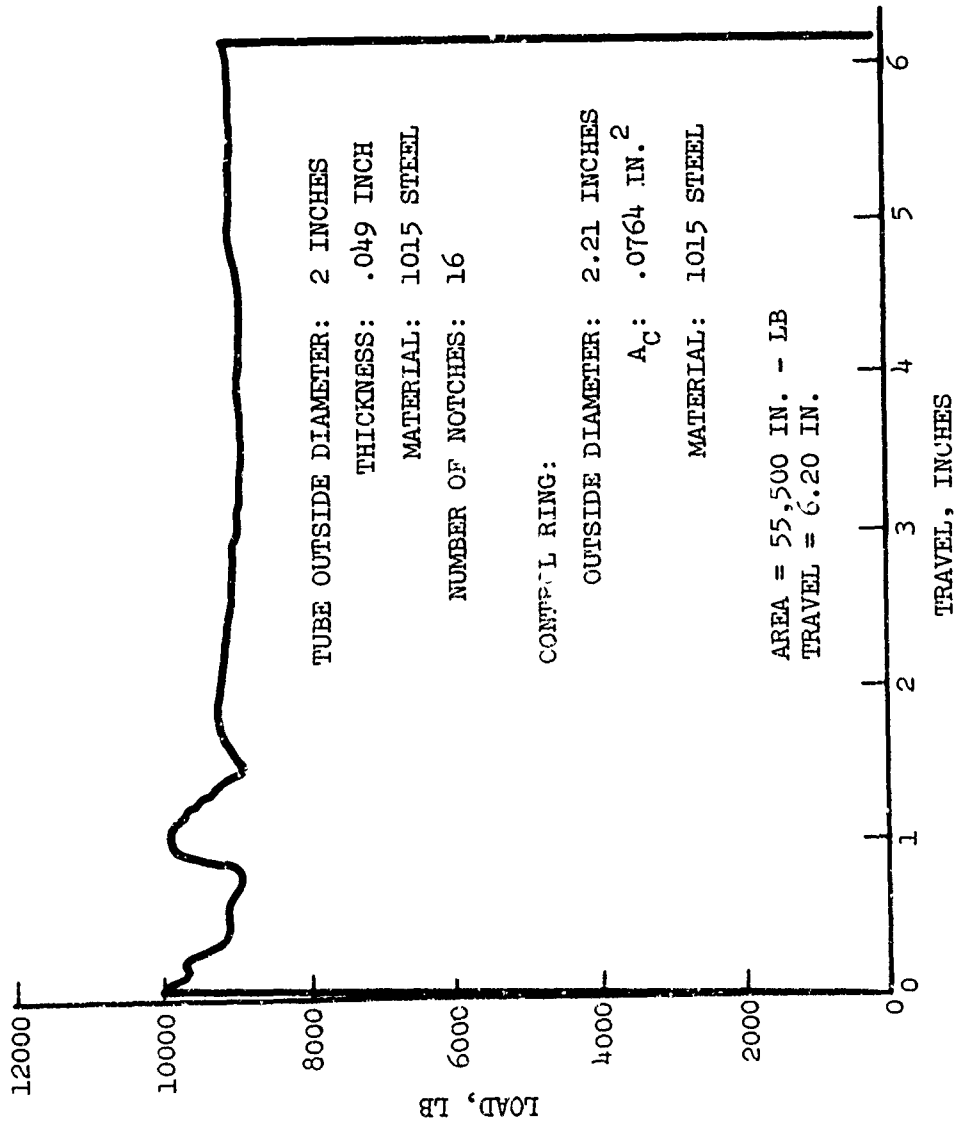
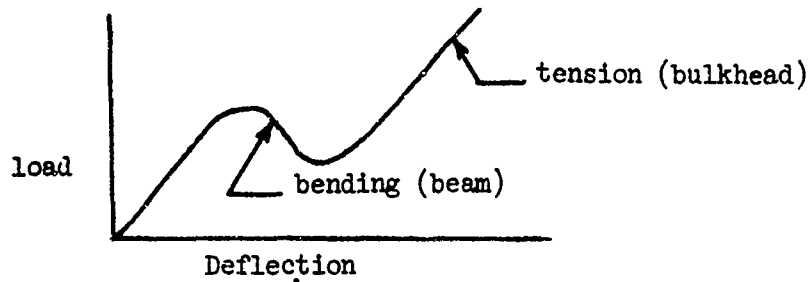


Figure 124. Frangible Tube Energy Curve (Reference 34).



The general discussion regarding this particular type of structural failure indicates that the load-deflection curve, in reality, consists of load-deflection curves of particular elements, each one of which may be of either the Type II or Type III category. One approach to developing a load-deflection curve for Type I elements is to superimpose the load-deflection characteristic of the individual elements in the sequence in which they occur. For example, in the UH-1H, the transmission mount can be idealized by a soft stiffness region representative of its rubber mount followed by a much higher stiffness region which represents the pylon support structure, the stiffness of which is important after the rubber mount has bottomed.

RESULTS OF THE PROGRAM

The results of the program are summarized as follows:

LITERATURE SURVEY AND CRITIQUE

A literature survey and critique of technical reports and publications are completed. Sixty reports are reviewed. The literature is discussed with regard to eight areas of applicability to the development of designer-oriented crashworthiness design procedures. A literature index is provided in Volume II which further divides each report into specific content and area of applicability. There are 29 such divisions. The basic contents of the literature are reviewed and commented upon. Some notable comments regarding the literature include:

- The analytical procedures and empirical data which are available in the literature are not oriented toward simplified design procedures because
 - 1) they are related to unique specimens or loading conditions.
 - 2) they require the use of complex computer programs.
 - 3) the empirical data is not related to analytical procedures.
- Analytical techniques and numerical methods of stability analysis and post-failure analysis are primarily concerned with the technique rather than the application of the techniques to practical design problems.

LOAD-SENSITIVITY STUDY

Program KRASH and an existing 31 mass model of the UH-1H, developed under a previous study contract with the U. S. Army Air Mobility and Research Laboratory (USAAMRDL), Fort Eustis, Virginia (Reference 1), is used to determine the sensitivity of the response, for several major structural elements, to changes in load-deflection characteristics in the post-failure region. Variations were made in the load-deflection characteristics for the engine, transmission, landing gear and fuselage. A total of 27 parameter variation cases are analyzed.

The results of the load-sensitivity study using the UH-1H math model indicate that during a vertical crash impact with a 95th percentile potentially survivable accident (42 ft/sec vertical velocity):

- The energy-absorption capability of the structural elements in question and their particular location within the airframe will influence the degree of refinement with which they are to be modeled.

- For "noncritical energy-absorbing structure" in the post-buckling region, the load-deflection characteristics do not require a sophisticated modeling representation.
- The "noncritical energy-absorbing structure" for the UH-1D/H aircraft modeled (i.e., landing gear, engine mount, transmission mount in the UH-1H) can be represented with three or less nonlinear load-deflection categories.
- The fuselage structure load-deflection characteristics including the bottoming spring stiffness exert a significant influence on the response of the major upper masses (engine and transmission) as well as the occupants due to the fact that the fuselage crushing is the primary absorber of energy in the airframe.

SUBSTRUCTURE ANALYSIS

A general procedure for determining the total load-deflection characteristics, including failure and post-failure behavior, for the structure selected for the test program is presented. The structural elements analyzed and tested in this study are representative of the multiweb construction of helicopter lower fuselage, which consists of stiffened panels and angle stiffeners in the region where a transmission pylon is supported. The general procedure for determining the load-deflection characteristics, including failure and post-failure behavior, for the structure includes a step-by-step process with the following sequence:

- Prediction of failure loads for stiffened panels
- Post-failure analysis of stiffened panels
- Main beam and bottom skin analysis
- Formulation of total substructure load-deflection curve

The procedure takes into account monolithic, wrinkling and interrivet failure modes. The basic equations are developed for a nondimensional L/ρ ratio of 20. For L/ρ ratios greater than 20, column effects are also included.

Although developed for angle type stiffened panels, the procedure is applicable to a variety of panel types, including:

- T-type stiffeners
- Formed angle stiffeners
- Extruded angle stiffeners
- Formed multicorner sections

- Formed hat stiffened panels
- Extruded Y stiffened panels

Individual load-deflection curves are presented for specimens 1 through 6 depicting:

- Lateral bulkhead crushing
- Side stiffener web crushing (representing major bulkheads at BL-14 and BL-14)
- Side stiffener beam bending

The individual load-deflection curves are superimposed upon each other to obtain a total load-deflection curve for the total structure. Predicted total load-deflection curves for all the different specimens are presented.

The simplified analytical technique developed in this study provides a reasonable representation of the load-deflection characteristics of multi-webbed angle stiffened structure typical of helicopter structure. While the method cannot accurately predict the failure behavior of each individual stiffener element it does satisfactorily reproduce the overall crushing characteristics and general deformation behavior of the structural segment. The assumption of a symmetric failure mode appears justified in a gross sense although some failure modes will be asymmetrical in nature. While asymmetrical failure modes will introduce a small error in the predicted load compared to loads based on the symmetric mode failure assumption, the representation of the peak failure load will not be impaired and the energy absorption capability of the structure will be sufficiently accurate for preliminary design purposes. The primary interest in the analysis presented herein is the development of analytical tools for preliminary design analysis and, as such, the emphasis is placed on adequate prediction of failure loads and energy absorption. The simplified analytical procedure does not account for structural imperfections. However, these imperfections influence the pre-failure region (pre- and post-buckled behavior) more than the post-failure region where the imperfections become small relative to the actual deflection of the structure.

The analytical technique described herein tends to predict a lower failure deflection value than recorded from the tests. However, the energy absorption contribution to the total crushing energy is extremely small and the small discrepancy in this region will not introduce any significant error nor detract from the analytical representation of the structure's crashworthiness capability. Furthermore, the analytical approach presented in this study implies that an upper bound yield stress is reached at failure which, in principle, is equivalent to obtaining the failure deflection from pre- and post-buckling stiffness calculations.

The literature evaluation indicates that the calculation of pre-failure stiffnesses and, consequently, deflections is a formidable task due to the effect of initial structural imperfections.

The analytical method is modified by the results of the test in the manner in which the post-failure curve is developed. The initial assumption of a fully warped flange resulting in a conservative (lower bound) plastic hinge moment is modified using an empirically developed exponential function (Equation 51) for angle stiffened panels. The modification results in improved agreement between test and analytically predicted failure deflection.

The analysis is intended to apply statically predicted load-deflection characteristics to crash simulation studies. For lightweight structure of the type used in helicopter fuselage design, the failures due to crippling would most likely be caused by a lowest mode, in which case, a statically predicted load-deflection curve, although slightly conservative, would suffice in lieu of a dynamic analysis. The test results show that the dynamic tests yield slightly higher (~ 5%) failure loads when compared to static tests (specimens 7, 8 and 9) for the type of structure tested in this program. However, there are situations where static failure modes do not occur under dynamic loads. Under this circumstance, the utilization of a statically predicted load-deflection curve for a crash simulation study may not provide sufficiently accurate responses. The problem of structures exhibiting deformation modes which are different under dynamic loading is discussed in References 86, 109 and 110.

SUBSTRUCTURE TEST PROGRAM

The substructure test program is established such that:

- Typical fuselage structure is represented.
- The effect of detail design changes on load-deflection characteristics is investigated.
- A representative crash loading condition is reproduced.
- The test data can be related to designer-oriented analytical procedures.
- The test data can be related to analytical modeling data requirements.

The specimens selected for test are representative of the transmission pylon support structure in the region bounded by BL + 14 to BL - 14, WL 9 to 22 and FS 102 to 180. Twelve specimens were fabricated for the test program. The specimen configurations and test conditions include:

static load

dynamic impact: 14 ft/sec \leq velocity \leq 30 ft/sec

four-edge support

two-line support

skin web thickness: .025 in. to .064 in.

angle stiffener thickness: .032 in. to .072 in.

specimen depth: 6.125 in. to 12.125 in.

number of angle stiffeners: 12 to 32

specimen weight: 13.6 lb to 31.25 lb

effect of lightening holes in bulkheads

The overall specimen dimensions are:

width = 18 in.

length = 46 in.

depth 6.125 in. or 12.125 in.

The test results indicate that, for these types of structural elements, static testing to determine load-deflection characteristics should yield sufficiently accurate results when compared to dynamic test results, but in a more economical manner. A static test can provide the desired information with regard to:

- Shape of the load-deflection curve
- Peak failure load (dynamically obtained failure loads are between 9% and 24% higher than the loads measured from static test and the loads from predicted static calculations, respectively)
- Deflection at which failure load occurs
- Energy absorption capability of the structure.

Figure 125 shows a comparison of the load-deflection response for two dynamic test conditions and a static test, all performed for a similar type specimen.

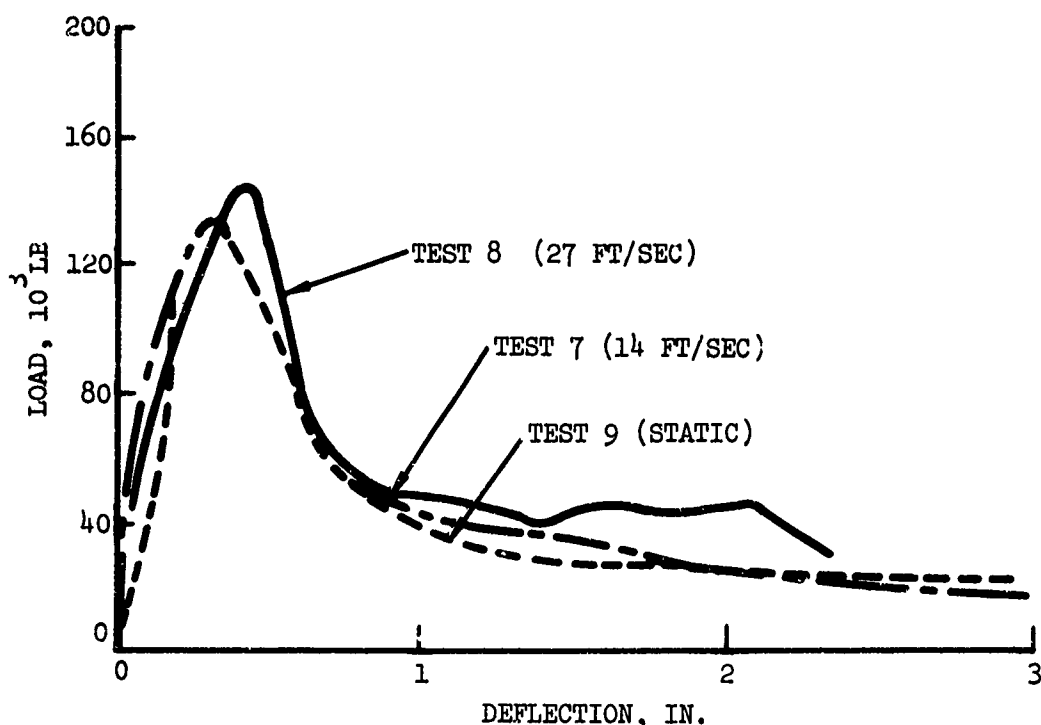


Figure 125. Comparison of Static and Dynamic Test Results.

A dynamic test has the advantage that the amount of springback from the maximum deflected value is immediately evident. With static test, the structure will relax slowly (up to several days) to its permanently deformed position. The springback could be as high as 40% of the maximum deflected value. However, under a static loading condition, the specimen experienced more deformation than under a dynamic impact, for an equal amount of input energy. Figure 126 depicts a possible percentage range of structural springback as a function of impact velocity for the type of specimens tested. The curve is based on a limited number of tests.

The static test, in addition to being more economical to run than a dynamic test, has the advantages of easier and more precise alignment of impact head with specimen, a more rapid test setup, and, generally, a lesser amount of instrumentation required.

If dynamic tests are to be performed, load cells should be installed in lieu of accelerometers to obtain a better definition of the load time history. The response from the accelerometers exhibits oscillations which include the frequency contents associated with the impact mass, structural specimen and test support structure. The interpretation of the accelerometer data can be difficult if the oscillations are severe. Load cells, in addition to providing a smoother continuous time history, can be used to indicate the alignment of the impact head with the specimen. In the tests conducted in this program, the load cells were placed below the support along each of the four edges, thus providing data regarding slight misalignment at impact.

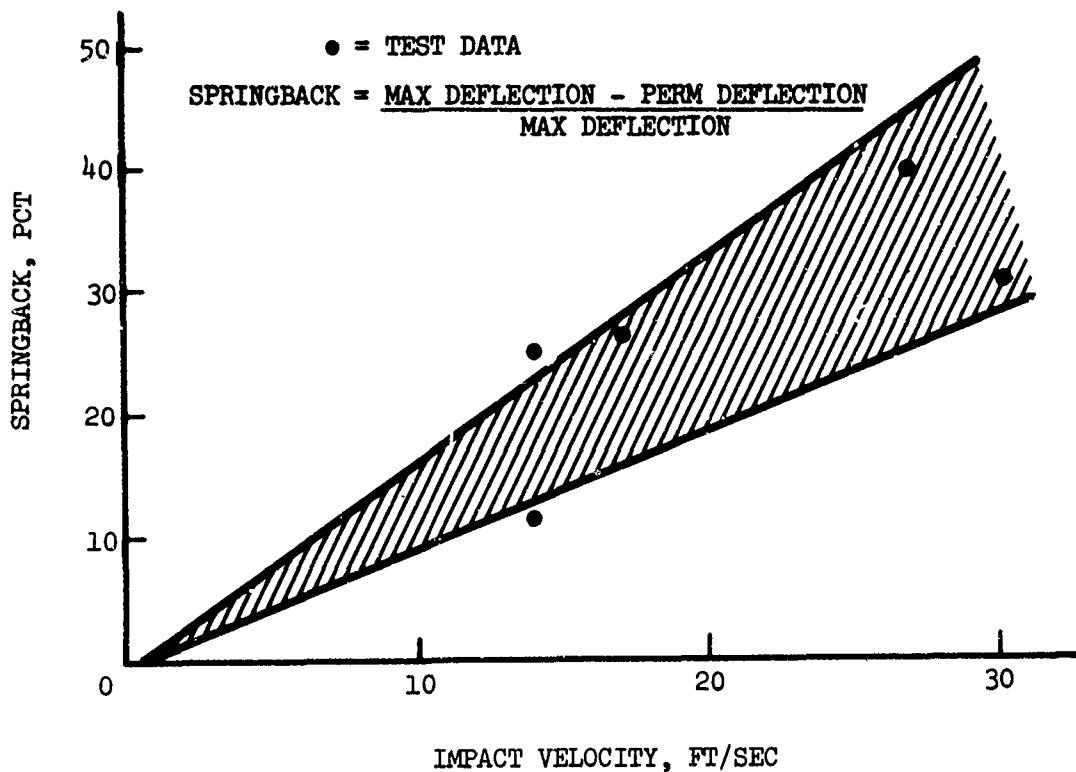


Figure 126. Percentage of Structural Springback Versus Impact Velocity.

The typical response of the type of structure tested in this study is a relatively sharp load buildup in the elastic region up to the peak failure load at approximately .25 inch of deflection. After failure, the load reduces at a rate less severe than the initial buildup until the deflection reaches approximately .75 to 1.0 inch. Thereafter, the load remains constant until the structure crushes to the point that it again stiffens. This latter point is approximately half the depth.

The test program demonstrated that representative aircraft structure can be fabricated and tested to either obtain or verify load-deflection characteristics within a reasonable budget, particularly if static tests are performed. The average specimen cost in this program, including dynamic testing, specimen fabrication, instrumentation, test support and data reduction, is between \$2500 and \$3000.

For each specimen, photographs of the post-test condition are included in the Test Program section. In addition, a motion-picture film combining footage from each of the tests and depicting the test setup, crushing of the structure, and the post-test condition of selected specimens has been prepared as part of the study described herein.

CORRELATION BETWEEN TEST AND ANALYSIS

A comparison of the predicted crushing characteristics versus test results is presented for all 12 specimens. Reasonable agreement between test and analysis is obtained. For the specimens supported on four edges (Specimens 1 through 11), the comparison of test and analysis using load cell data is:

- Peak failure load (percent error between - 10.6% and + 8.0%)
- Energy absorption (percent error between - 16.1% and - 1.5%)

For the dynamic tests (specimens 4, 5 and 6) using only accelerometer data the difference between analysis and test for the peak load varied from - 24% to + 6.8% and for energy absorption from - 1% to + 26%. For the line-supported specimen (No.12), the comparison of analysis and test showed a difference of approximately + 1.3% and - 27% for peak failure load and energy absorption, respectively.

The results of the correlation indicate that an analysis to determine load-deflection characteristics of multiweb constructed angle stiffened panels, typical of the UH-1H lower fuselage, is feasible using relatively simple techniques. The overall crushing behavior of the substructure can be predicted within reasonable accuracy although the failure mode of each individual stiffener cannot be consistently accounted for. The analytical procedure described herein is capable of satisfactorily determining the two most significant parameters for crushable structure, i.e., peak failure load and energy absorption capability. The approach, as developed in this study, has limitations with regard to accurately predicting the deflection at which failure occurs and the deflection at which post-failure stiffening occurs. Although the predicted failure deflection is a consistently lower value than that obtained from tests, it represents an extremely small percentage of the total crushing energy and this discrepancy is not significant as long as the peak failure load and load-deflection characteristics are reliably represented. The analytical assumptions regarding the mode of failure in the post-failure region and the hinge formulation at failure are generally considered valid in light of the test results. For example, although failures in the form of an asymmetrical mode shape as well as symmetric mode failures (as initially assumed) occur, the predicted energy absorption capability of the structure is, on the average, still very close ($\approx + 14\%$) to the test results. Assuming the asymmetric hinge formation sensitivity factor, shown in Figure 95, was applied to all specimens, the energy absorption would be raised approximately 15%. While improving some comparisons with test results, it would create a larger disparity for other comparisons. Although the failure modes experienced during the tests show both types (symmetric and asymmetric) of failures, the initial assumption of a symmetric failure is "on an average" reasonable.

The initial assumption of a conservative plastic hinge moment formation (fully warped angle stiffener flange) results in a lower predicted failure deflection than is observed during the test portion of the program. Therefore, a modified post-failure load-deflection curve is formulated. Although this improves the comparison between the test and analysis obtained failure deflections, the analytical values still tend to be consistently lower than the corresponding test value.

For the prediction of the pre-failure stiffness (pre- and post-buckling) in the analysis, it is assumed that the yield strain is reached at failure. Due to uncertainties regarding the initial structural imperfections and their effect on the post-buckled stiffness, the overall pre-failure stiffness is difficult to predict. The approach described herein, although approximate and resulting in a slightly higher elastic pre-failure stiffness, is considered adequate because: (1) the discrepancy is minor in relation to the total crushing energy and, (2) the analysis represents the proper failure load.

Figure 127 shows a summary of the comparison between test and analysis results for load and energy absorbed. A detailed discussion of the correlation between analysis and test is presented in the Correlation section.

In particular the validity of the following analytical assumptions is discussed in detail:

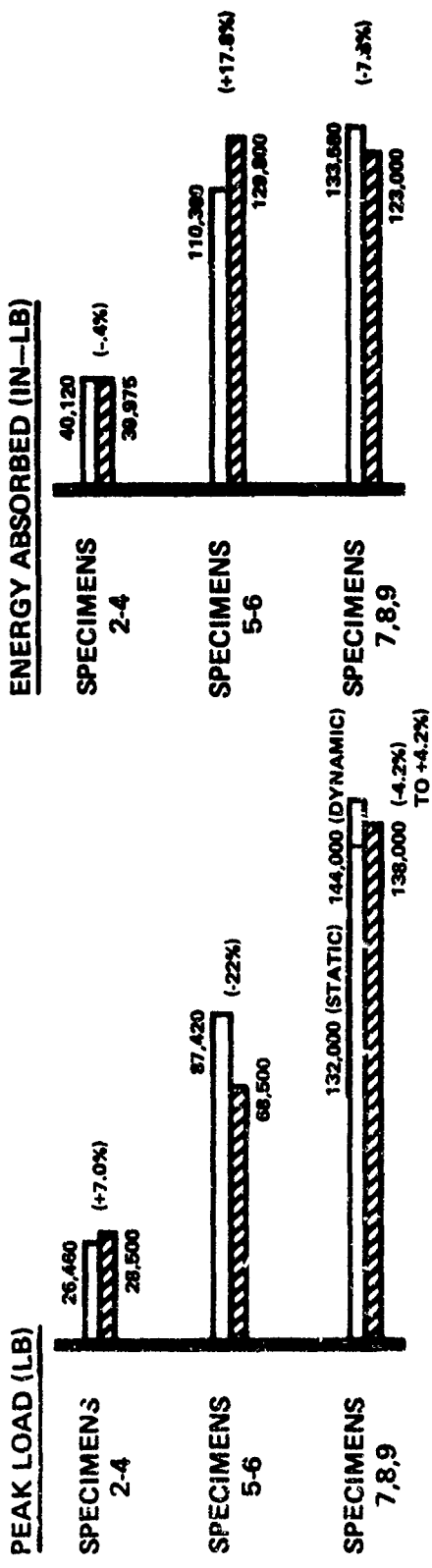
- Plastic hinge formation
- Empirical corrections to the post-failure load-deflection curve
- Determination of the deflection value at failure
- Strain data and failure modes

PROGRAM "KRASH" REFINEMENT

Program "KRASH" is refined to facilitate its usage by designers. The input data format is changed for ease of data input and subsequent data changes, such as is normally required for parameter tradeoff studies. The input format changes are divided into three categories:

- reordered data
- standardization of certain inputs
- allowance for more general KR curves

As a result of the format and associated programming changes, the program capability has been expanded to at least 80 masses and 100 internal beam



SPECIMEN	PERCENT ERROR BETWEEN PREDICTED AND TEST %	
	LOAD	ENERGY
1	-10.6	- 8.6
10	+ 2.5	-13.0
11	- 8.0	-16.1
12	+ 1.3	-27.1

TEST (VALUES SHOWN ARE THE AVERAGE OF APPLICABLE TESTS)
 ANALYSIS

Figure 127. Comparison of Test and Analysis Results.

elements and 120 Stiffness Reduction Curves simultaneously. The program capacity for lumped masses and internal beam elements was previously 40 and 80, respectively. However, program run time is still the same for problems of equal size.

The refined program KRASH has been exercised to show that results are in agreement with previously obtained results using the original version of the program (Reference 1). Case 31-52, which corresponds to the test condition described in Reference 1, was used as the verification case. An updated program source deck, listing, sample input and output are being submitted to the Fort Eustis Directorate.

Program capability for special impact conditions, not previously performed, is demonstrated using the refined program for the following:

- Three-directional velocity impact (~ 40 ft/sec combined impact - 27 ft/sec longitudinal, 23 ft/sec vertical and 18.5 ft/sec lateral)
- Upper mass penetration into a specified occupiable volume
- Simplified blade contact
- Utilization of load-deflection data obtained from specimen testing during this program

Energy balance equations are included in Volume II along with a sample energy balance data format. Volume II also contains a revised User's Guide and associated format revisions.

DESIGN PROCEDURES

Three means by which crashworthiness capability can be specified are presented, including:

- Buyer-specified velocity envelopes and/or peak accelerations
- Manufacturer-specified capability including procedures by which compliance is shown
- Specified procedures which must be adhered to

A discussion is presented in which the general approach for performing crashworthiness analysis, particularly during preliminary design, is described. Included in the general approach is:

- Identification of overall failure mode
- Identification of individual element failure modes

- Prediction of load-deflection curve for each element
- Prediction of substructure total load-deflection curve
- Simplified representation of load-deflection curves for typical structural elements

A detailed design procedure is included by which load-deflection characteristics of multiweb composite substructure, typical of fuselage design, can be formulated by designers. The procedure includes tables, figures, nomographs and equations and is presented in a step-by-step sequence. Included in the sequence is:

- Failure load analysis
- Beam bending analysis
- Composite load-deflection curve formulation

In conjunction with the detailed design procedure a comprehensive sample problem of a typical segment of the UH-1H lower fuselage is presented which illustrates the manner in which design procedure is applied.

Included in the design procedures section is a subsection which presents structural element modeling guidelines. Approximate load-deflection curves are presented for some typical Type I, II and III structural elements. In particular available pertinent data for the following structures are presented:

- Solid cross-section column
- Thin walled column
- Honeycomb panel
- Frangible tube

CONCLUSIONS

1. Currently available methods for analyzing the nonlinear behavior of structures are oriented toward emphasizing the analysis methods or solving classical types of problems rather than providing tools to be used in practical design applications.
2. A simplified, experimentally verified analytical technique for predicting crushing characteristics of one type of typical helicopter fuselage airframe structure has been developed. The technique is oriented toward designer usage. The technique is used to predict the peak failure load and energy absorption characteristics of the structure with satisfactory accuracy for preliminary design.
3. Tests of representative helicopter airframe structure have demonstrated that static tests provide satisfactory load-deflection data suitable for preliminary design such as peak failure load, failure deflection, energy absorption and curve shape when compared to similar data obtained from dynamic tests. However, dynamic tests provide immediate information regarding springback effects, which in a static test are not evident until relaxation takes place.
4. Load sensitivity studies have shown that the energy absorption capability of structural elements, as well as their particular location in the vehicle, influences the degree of accuracy with which they should be modeled. Modeling of post-buckling behavior for noncritical energy-absorbing regions can be approximated with simplified load-deflection curve representation.
5. Program KRASH, developed and verified under a previous Army study, now has the capability for 80 lumped masses and 100 internal beam elements. The program has been demonstrated "qualitatively" to be operational for analyses of three-directional velocity impacts, mass penetration into an occupiable volume, and simplified blade contact.

REFERENCES

1. Wittlin, G., Gamon, M. A., EXPERIMENTAL PROGRAM FOR THE DEVELOPMENT OF IMPROVED HELICOPTER STRUCTURAL CRASHWORTHINESS ANALYTICAL AND DESIGN TECHNIQUES, Lockheed-California Company; USAAMRDL Technical Report 72-72A, 72B, Eustis Directorate, U. S. Army Air Mobility Research and Development Laboratory, Ft. Eustis, Virginia, May 1973, AD 764985.
2. Turnbow, J. W., Carroll, D. F., Haley, J. L., Jr., Robertson, S. N., CRASH SURVIVAL DESIGN GUIDE, Dynamic Science; USAAMRDL Technical Report 71-22, Eustis Directorate, U. S. Army Air Mobility and Research Laboratory, Ft. Eustis, Virginia, Oct. 1971, AD 733358.
3. Reed, William, H., Avery, James P., Ph.D., PRINCIPLES FOR IMPROVING STRUCTURAL CRASHWORTHINESS FOR STOL AND CTOL AIRCRAFT, Aviation Safety Engineering and Research; USAAVLABS Technical Report 66-39, U. S. Army Aviation Materiel Laboratories, Ft. Eustis, Virginia, June 1966, AD 637133.
4. Greer D. L., et al, DESIGN STUDY AND MODEL STRUCTURES TEST PROGRAM TO IMPROVE FUSELAGE CRASHWORTHINESS, General Dynamics, Convair, FAA Technical Report DS-67-20, Federal Aviation Administration, Washington, D.C., October 1967, AD 666816.
5. Saczalski, K. J., Park, K. C., TRANSIENT RESPONSE OF INELASTICITY CONSTRAINED RIGID BODY SYSTEMS, to appear in Journal of Engineering for Industry, ASME Transactions, 1974.
6. Massonnet, C. E., and Save, M. A., PLASTIC ANALYSIS AND DESIGN, VOL. I, BEAMS AND FRAMES: Blusdell Publishers, New York, 1965.
7. Roark, R. J., FORMULAS FOR STRESS AND STRAIN, McGraw-Hill Publishers, New York, 1965.
8. Ayre, Robert S., Shock and Vibration Hdbk., Chap. 3, Vol. 1, TRANSIENT RESPONSE TO STEP AND PULSE FUNCTIONS., Hoppman, W. K., Chap. 9, Vol. I, EFFECTS OF IMPACT ON STRUCTURES, McGraw-Hill Publishers, New York, 1961.
9. Timoshenko, S., and Woinowsky-Krieger, S., THEORY OF PLATES AND SHELLS, McGraw-Hill Publishers, New York, 1959.
10. Tulk, F. D., BUCKLING OF CIRCULAR CYLINDRICAL SHELLS UNDER DYNAMICALLY APPLIED AXIAL LOADS, UTIAS Report 160, 1972.
11. Striklin, J. E., et al, LARGE DEFLECTION ELASTIC-PLASTIC DYNAMIC RESPONSE OF STIFFENED SHELLS OF REVOLUTION, TEES-RPT-72-25 and SLA-73-0128, 1972.

12. Becker, H., Gerard, G., HANDBOOKS OF STRUCTURAL STABILITY, PARTS I - V. NACA Technical Notes, TN 3781 - 3785, 1957.
13. Skogh, J., and Stern, P., POSTBUCKLING BEHAVIOR OF A SECTION REPRESENTATIVE OF THE B-1 AFT INTERMEDIATE FUSELAGE, Lockheed Palo Alto Research, AFFDL-TR-73-63, Air Force Flight Dynamics Laboratory, Air Force Systems Command, Wright-Patterson Air Force Base, Ohio, May 1973.
14. Atluri, S., PETROS 3: A FINITE-DIFFERENCE METHOD AND PROGRAM FOR THE CALCULATION OF LARGE ELASTIC-PLASTIC DYNAMICALLY-INDUCED DEFORMATIONS OF MULTILAYER VARIABLE THICKNESS SHELLS, BRL, U. S. Army Aberdeen Research and Development Center, Aberdeen Proving Ground, Maryland, Contract #DAADO5-68-C-0314, Nov. 1971.
15. Haftka, R. T., A KOITER-TYPE METHOD FOR FINITE ELEMENT ANALYSIS OF NON-LINEAR STRUCTURAL BEHAVIOR, AFFDL-TR-70-130, Vol. I, Air Force Flight Dynamics Laboratory, Wright-Patterson Air Force Base, Ohio, Nov. 1970.
16. Stilwell, W. C., and Ball, R. E., A DIGITAL COMPUTER STUDY OF THE BUCKLING OF SHALLOW SPHERICAL CAPS AND TRUNCATED HEMISPHERES, NASA CR 1998, June 1972.
17. Witmer, E. A., LARGE DYNAMIC DEFORMATIONS OF BEAMS, RINGS, PLATES AND SHELLS, AIAA Journal, Vol. I, No. 2, August 1963.
18. Perrone, N., ON A SIMPLIFIED METHOD FOR SOLVING IMPULSIVELY LOADED STRUCTURES OF RATE-SENSITIVE MATERIALS, Office of Naval Research, Wash., D. C., Journal of Applied Mechanics, ASME, September 1965.
19. Bodner, S. R., and Symonds, P. S., EXPERIMENTAL AND THEORETICAL INVESTIGATION OF THE PLASTIC DEFORMATION OF CANTILEVER BEAMS SUBJECTED TO IMPULSIVE LOADING, Brown University, Journal of Applied Mechanics, December 1962.
20. Hibbit, H. D., et al, A FINITE ELEMENT FORMULATION FOR PROBLEMS OF LARGE STRAIN AND DISPLACEMENT, Brown University, International Journal of Solids and Structures, 1970, Vol. 6, pp. 1069-1086.
21. Toridio, T. G., and Khozeimeh, K., INELASTIC RESPONSE OF FRAMES TO DYNAMIC LOADS, A.S.C.E. Proceedings, Engineering Mechanics Division, June 1971.
22. McDaniel, T. J., DYNAMICS OF STIFFENED CYLINDRICAL SHELLS WITH SPATIALLY VARYING CURVATURE, University of Dayton Research Institute, Air Force Materials Laboratory Report AFML-TR-72-134, Air Force Systems Command, Wright-Patterson Air Force Base, Ohio, July 1972.
23. Bendix Corp., Final Engineering Report, ENERGY ABSORBING CHARACTERISTICS OF CRUSHABLE ALUMINUM STRUCTURES IN A SPACE ENVIRONMENT, NASA-CR-65096, July 1965.

24. Kornhauser, M., STRUCTURAL EFFECTS OF IMPACT, Sparton Books, Inc., Baltimore, Md. 1964.
25. Fisher, L. J., Jr., LANDING-IMPACT-DISSIPATION SYSTEMS, NASA Technical Note D-975, December 1961.
26. McGehee, J. R., A PRELIMINARY EXPERIMENTAL INVESTIGATION OF AN ENERGY-ABSORPTION PROCESS EMPLOYING FRANGIBLE METAL TUBING, NASA Technical Note D-1477, 1962.
27. Kroell, C. K., A SIMPLE, EFFICIENT, ONE SHOT ENERGY ABSORBER, General Motors Research Laboratory, Warren, Michigan, Shock, Vibration and Associated Environments, Part III, Bulletin No. 30, 1962.
28. Weinberg, L. W. T., and Turnbow, J. W., Ph.D., SURVIVABILITY SEAT DESIGN DYNAMIC TEST PROGRAM, Aviation Safety Engineering and Research, USAAVLABS Technical Report 65-43, U.S. Army Aviation Materiel Laboratories, Ft. Eustis, Virginia, July, 1965, AD 621718.
29. Langhaar, H. L., THEORETICAL AND EXPERIMENTAL INVESTIGATIONS OF THIN-WEBBED PLATE-GRIDDER BEAMS, Transactions of ASME, October 1943.
30. Perry, D. J., AIRCRAFT STRUCTURES, McGraw-Hill Book Co., New York, 1950.
31. Jones, N., et al, THE DYNAMIC PLASTIC BEHAVIOR OF SHELLS, MIT Report 71-6, 1971.
32. Mitchell, B., THE DYNASORB ENERGY ABSORBER, Lockheed Report LR 16735, March 1963.
33. Mitchell, B., SHOCK ABSORPTION WITH ONE SHOT TUBES, Lockheed Report LR 16369, June 1963.
34. Mitchell, B., DESIGN NOTES FOR THE DYNASORB ENERGY ABSORBER, Lockheed Report LR 17201, December 1963.
35. Mitchell, B., ENERGY ABSORPTION AT HIGH SPEED VERTICAL LANDING, Lockheed Report LR 21023, November 1967.
36. Perrone, N., RESPONSE OF RATE SENSITIVE FRAMES TO IMPULSIVE LOAD, ASME Journal of Applied Mechanics, February 1971, pp. 49-62.
37. Jones, Norman, INFLUENCE OF STRAIN-HARDENING AND STRAIN-RATE SENSITIVITY ON THE PERMANENT DEFORMATION OF IMPULSIVELY LOADED RIGID PLASTIC BEAMS, International Journal of Mechanical Science, 1967 Vol. 9, pp. 777-796.
38. Ni, C. M., IMPACT RESPONSE OF CURVED BOX BEAM-COLUMNS WITH LARGE GLOBAL AND LOCAL DEFORMATIONS, Research Laboratories, General Motors Corp., Warren, Michigan, AIAA Paper 73-401.

39. O'Bryan, T. C., and Hatch, H. G., Jr., LIMITED INVESTIGATION OF CRUSHABLE STRUCTURES FOR ACCELERATION PROTECTION OF OCCUPANTS OF VEHICLES AT LOW IMPACT SPEEDS, NASA Technical Note D-158, 1958.
40. Jones, Norman, THE INFLUENCE OF LARGE DEFLECTION ON THE BEHAVIOR OF RAPID-PLASTIC CYLINDRICAL SHELLS LOADED IMPULSIVELY, Journal of Applied Mechanics, ASME June 1970, pp. 417-425.
41. D'Amato, R., STATIC POST-FAILURE STRUCTURAL CHARACTERISTICS OF MULTI-WEB BEAMS, WADC TR 59-112, February 1959.
42. Rawlings, B., ENERGY ABSORPTION OF DYNAMICALLY AND STATICALLY TESTED MILD STEEL BEAMS UNDER CONDITIONS OF GROSS DEFORMATION, International Journal of Mechanical Sciences, Pergamon Press, Ltd., 1967, Vol. 9, pp. 633-649, Printed in Great Britain.
43. Thompson, J. E., VEHICLE CRUSH PREDICTION USING FINITE-ELEMENT TECHNIQUES, Chrysler Corp., SAE Paper 73-157, January 1973.
44. Burgmann, J. B., and Rawlings, B., DYNAMIC PLASTIC ANALYSIS OF PIN-JOINTED FRAMES, International Journal of Mechanical Science, Pergamon Press, 1968, Vol. 10, pp. 967-980, Printed in Great Britain (Received 8 May 1968, and in revised form 30 July 1968).
45. Martin, J. B., MODE APPROXIMATION FOR IMPULSIVELY LOADED STRUCTURES IN THE INELASTIC RANGE, Proceedings of the Southampton 1969 Civil Engineering Material Conference.
46. Jensen, W. R., Falby, W. E., and Prince, N., MATRIX ANALYSIS METHODS FOR ANISOTROPIC INELASTIC STRUCTURES, AFFDL-TR-65-220, April 1966.
47. Isaakson, G., Armen, H., Jr., and Pipko, A., DISCRETE ELEMENT METHODS FOR THE PLASTIC ANALYSIS OF STRUCTURES, NASA CR 803, October 1967.
48. Stricklin, J. A., et al, NONLINEAR DYNAMIC ANALYSIS OF SHELLS OF REVOLUTION BY MATRIX DISPLACEMENT METHOD, AIAA Journal, Vol. 9, No. 4, April 1971, p. 629.
49. Owens, R. H., and Symonds, P. A., PLASTIC DEFORMATION OF A FREE RING UNDER CONCENTRATED DYNAMIC LOADING, ASME Journal of Applied Mechanics, December 1955, p. 524.
50. Lee, H., and Symonds, P. S., LARGE PLASTIC DEFORMATIONS OF BEAM UNDER TRANSVERSE IMPACT, ASME Journal of Applied Mechanics, September 1952, p. 308.
51. Prager, W., A NEW METHOD OF ANALYZING STRESSES AND STRAINS IN WORK-HARDENING PLASTIC SOLIDS, ASME Journal of Applied Mechanics, December 1956, p. 493.

52. Morino, L., Leach, J. W., and Witmer, E. A., AN IMPROVED NUMERICAL CALCULATION TECHNIQUE FOR LARGE ELASTIC-PLASTIC TRANSIENT DEFORMATIONS OF THIN SHELLS, Part 1, ASME Journal of Applied Mechanics, June 1971, p. 423.
53. Pifko, A. Isaakson, A FINITE-ELEMENT-METHOD FOR THE PLASTIC BUCKLING ANALYSIS OF PLATES, Grumman Aerospace Corporation, Bethpage, N. Y., AIAA Journal, Vol. 7, No. 10, October 1969.
54. Armen, H., Jr., Pifko, A., and Levine, H. S., FINITE ELEMENT ANALYSIS OF STRUCTURES IN THE PLASTIC RANGE, NASA CR 1649, February 1971.
55. Mallett, R. H., AUTOMATED METHOD FOR THE LARGE DEFLECTION AND INSTABILITY ANALYSIS OF THREE-DIMENSIONAL TRUSS AND FRAME ASSEMBLIES, AFFDL-TR-66-102, December 1966.
56. Przemieniecki, J. S., MATRIX METHODS IN STRUCTURAL MECHANICS, AFFDL-TR-66-80, Conference held October 26-28, 1965.
57. Berke, L., PROCEEDINGS OF THE SECOND CONFERENCE ON MATRIX METHODS IN STRUCTURAL MECHANICS, AFFDL-TR-68-150, Conference held 15-17 October 1968.
58. Symonds, P. S., SURVEY OF METHODS OF ANALYSIS FOR PLASTIC DEFORMATION OF STRUCTURES UNDER DYNAMIC LOADING, BU/NSRDC/1-67, Brown University, Providence, R. I., 1967.
59. Semonian, J. W., and Anderson, R. A., AN ANALYSIS OF THE STABILITY AND ULTIMATE BENDING STRENGTH OF MULTIWEB BEAMS WITH FORMED CHANNEL WEBS, NACA Technical Note TN 3232, 1954.
60. Semonian, J. W., and Peterson, J. P., AN ANALYSIS OF THE STABILITY AND ULTIMATE COMPRESSIVE STRENGTH OF SHORT SHEET STRINGER PANELS WITH SPECIAL REFERENCE TO THE INFLUENCE OF THE RIVETED CONNECTION BETWEEN SHEET STRINGERS, NACA Technical Report TR 1255, 1956.
61. Bleich, F., BUCKLING STRENGTH OF METAL STRUCTURES, McGraw-Hill Publishers, New York, 1952.
62. Newmark, N. M., A METHOD OF COMPUTATION FOR STRUCTURAL DYNAMICS, A.S.C.E. Proceedings, Engineering Mechanics Divisions, Vol. 85, EM-3, pp. 67-94, 1959.
63. Bushnell, D., et al, FINITE-DIFFERENCE ENERGY METHOD FOR NONLINEAR SHELL ANALYSIS, Journal of Computer & Structures, Vol. 1, 1971, pp. 361-387.
64. Koiter, W. T., Ph.D. Thesis, NASA TTF-10, 883, 1967, WPAFB, AFFDL-TR-70-25, 1970.

65. Sewell, M. J., A GENERAL THEORY OF EQUILIBRIUM PATHS THROUGH CRITICAL POINTS, Royal Society Proceedings, Series A, 306, pp. 201-223, 1968.
66. Tong, P., A NOTE ON POST-BUCKLING SOLUTION OF ELASTIC STRUCTURES, ASRL-TR 1444-4, MIT, January 1970.
67. Chu, K. H., and Gornens, A. J., ELASTIC BUCKLING OF BEAM FLANGE PLATES, EM-4, ASCE, pp. 1324-1336, August 1971.
68. El-Bayoumy, L., BUCKLING OF CLAMPED RECTANGULAR PLATES, ASCE, EM-4, pp. 1277-1288, August 1971.
69. Stein, M., THE PHENOMENON OF CHANGE IN BUCKLE PATTERN IN ELASTIC STRUCTURES, NASA Technical Note TN R-39, 1959.
70. Rhodes, J., and Harvey, J. M., THE LOCAL BUCKLING AND POST-LOCAL BUCKLING BEHAVIOR OF THIN-WALLED BEAMS, Aeronautical Quarterly, 22, 4, pp. 363-388, November 1971.
71. Rhodes, J., THE POST-BUCKLING BEHAVIOR OF THIN FLAT PLATES IN COMPRESSION WITH UNLOADED EDGES ELASTICALLY RESTRAINED AGAINST ROTATION, Journal of Mechanical Engineering Sciences, 13, 2, pp. 82-91, April 1971.
72. Graves, A., Smith, T. R., THE EFFECT OF INITIAL IMPERFECTIONS ON THE STRENGTH OF THIN WALLED BOX COLUMNS, International Journal of Mechanical Sciences, 13, 11, pp. 911-925, November 1971.
73. Hutchinson, S. W., and Koiter, W. T., POST-BUCKLING THEORY, Applied Mechanics Reviews, December 1970.
74. Sewell, M. J., A GENERAL THEORY OF EQUILIBRIUM PATHS THROUGH CRITICAL POINTS, Proceedings of Royal Society, Series A, 306, pp. 201-223, 1968.
75. Cox, H. L., THE BUCKLING OF PLATES AND SHELLS, The MacMillan Company, N. Y., 1963.
76. Chitner, A. H., THIN-WALLED STRUCTURES, John & Wiley & Sons, Inc., New York, 1967.
77. Mau, S. T., and Gallagher, R. H., A FINITE ELEMENT PROCEDURE FOR NON-LINEAR PRE-BUCKLING AND INITIAL POST-BUCKLING ANALYSIS, NASA CR-1936, January 1972.
78. Vos, Robert F., FINITE ELEMENT ANALYSIS OF PLATE BUCKLING AND POST-BUCKLING, Ph.D. Thesis, Rice University, Houston, Texas, 1970.
79. Roberts, T. M., and Ashwell, D. G., THE USE OF FINITE ELEMENT MID-INCREMENT STIFFNESS MATRICES IN THE POST-BUCKLING ANALYSIS OF IMPERFECT STRUCTURES, Journal of Solids and Structures, 7.7, pp. 805-823, July 1971.

80. Greer, D. L., et al, CRASHWORTHY DESIGN PROCEDURES, General Dynamics, CONVAIR, FAA Technical Report ADS-24, Federal Aviation Administration, Washington, D. C., November 1965, AD 623575.
81. Stein, M., LOADS AND DEFORMATIONS OF BUCKLED RECTANGULAR PLATES, NACA Technical Report, TR-R-40, 1959, Washington, D. C.
82. Gatlin, Clifford I., et al, ANALYSIS OF HELICOPTER STRUCTURAL CRASH-WORTHINESS, Dynamic Science, USAAVLABS Technical Report 70-71, 71B, Eustis Directorate, U.S. Army Air Mobility Research and Development Laboratory, Ft. Eustis, Virginia, January 1971, AD880680.
83. Sechler, E. E., and Dunn, L. G., AIRPLANE STRUCTURAL ANALYSIS AND DESIGN, Dover Publishers Inc., 1963, New York, N. Y.
84. Hutchinson, J. W., and Budiansky, B., DYNAMIC BUCKLING ESTIMATES, AIAA Journal 4, pp. 525-530, 1966.
85. Thompson, J.M.T., DYNAMIC BUCKLING UNDER STEP LOADING, IN DYNAMIC STABILITY OF STRUCTURES (Ed. by G. Herrmann), Pergamon Press, 1965.
86. Budiansky, B., DYNAMIC BUCKLING OF ELASTIC STRUCTURES: CRITERIA AND ESTIMATES IN DYNAMIC STABILITY AND STRUCTURES (Ed. by G. Herrmann), Pergamon Press, 1965.
87. Mayer, J., and Budiansky, B., ANALYSIS OF BEHAVIOR OF SIMPLY SUPPORTED FLAT PLATES COMPRESSED BEYOND THE BUCKLING LOAD INTO THE PLASTIC RANGE, NACA TN 3368, Washington, D. C., 1955.
88. Walker, A. C., FLAT RECTANGULAR PLATES SUBJECTED TO LINEARLY-VARYING EDGE COMPRESSIVE LOADING, in Thin-Walled Structures (Ed. by A. H. Chilner), John Wiley & Sons, Inc., New York, 1967.
89. Walker, A. C., THE POST-BUCKLING BEHAVIOR OF SIMPLY SUPPORTED SQUARE PLATES, Aero. Quarterly, Vol. XX, August 1, 1969, pp. 203-222.
90. Masur, E. F., BUCKLING, POST-BUCKLING AND LIMIT ANALYSIS OF COMPLETELY SYMMETRIC ELASTIC STRUCTURES, International Journal of Solids and Structures, 1970, Vol. 6, pp. 587-604.
91. Hutchinson, J. W., and Koiter, W. T., POST-BUCKLING THEORY, Applied Mechanics Review, December 1970, pp. 1353-1366.
92. Needham, R. A., THE ULTIMATE STRENGTH OF ALUMINUM ALLOY FORMED STRUCTURAL SHAPES IN COMPRESSION, Journal of Aeronautical Sciences, Vol. 21, No. 4, 1954, pp. 217-229.
93. Schuette, E. H., OBSERVATIONS OF THE MAXIMUM AVERAGE STRESS OF FLAT PLATES BUCKLED IN EDGE COMPRESSION, NACA TN 1625, 1949.

94. Semonian, J. W., and Peterson, J. P., AN ANALYSIS OF THE STABILITY AND ULTIMATE COMPRESSIVE STRENGTH OF SHORT SHEET-STRINGER PANELS WITH SPECIAL REFERENCE TO THE INFLUENCE OF RIVETED CONNECTION BETWEEN SHEET AND STRINGER, NACA Report 1255, 1956.
95. Stowell, E., A UNIFIED THEORY OF PLASTIC BUCKLING OF COLUMNS AND PLATES, NACA Report 898, 1947.
96. Dow, N. F., and Hickman, W. A., EFFECT OF VARIATION IN RIVET DIAMETER AND PITCH ON THE AVERAGE STRESS AT MAXIMUM LOAD FOR 24S-T3 AND 75S-T6 ALUMINUM-ALLOY, FLAT, Z-STIFFENED PANELS THAT FAIL BY LOCAL INSTABILITY, NACA TN 2139, 1950.
97. Dow, N. F., Hickman, W. A., and Rosen, B. W., EFFECT OF VARIATION IN RIVET STRENGTH ON THE AVERAGE STRESS AT MAXIMUM LOAD FOR ALUMINUM-ALLOY, FLAT, Z-STIFFENED COMPRESSION PANELS THAT FAIL BY LOCAL BUCKLING, NACA TN 2963, 1953.
98. Von Karman, T. L., Sechler, E. E., and Donnel, L. H., THE STRENGTH OF THIN PLATES IN COMPRESSION, Journal of Applied Mechanics Transcripts, A.S.M.E., Vol. 54, No. 2, 1932.
99. Marguerre, K., THE APPARENT WIDTH OF THE PLATE IN COMPRESSION, NACA Technical Memo 933, 1937.
100. Timoshenko, S. P., and Gere, J. M., THEORY OF ELASTIC STABILITY, 2nd Ed., McGraw-Hill Book Co., New York, 1961.
101. Neal, B. G., THE EFFECT OF SHEAR AND NORMAL FORCES ON THE FULLY PLASTIC MOMENT OF A BEAM OF RECTANGULAR CROSS-SECTION, Journal of Applied Mechanics, Vol. 28, 1961, pp. 269-274.
102. Vlasov, V. Z., THIN-WALLED ELASTIC BEAMS, English Translation by National Science Foundation, Second Ed., pp. 286-288, 335-368.
103. Hodge, P. H., Jr., PLASTIC ANALYSIS OF STRUCTURES, McGraw-Hill Book Co., New York, 1959.
104. Neal, B. G., THE PLASTIC METHODS OF STRUCTURAL ANALYSIS, Chapman & Hall, London, 1956.
105. Heimerl, G. J., and Woods, W., EFFECT OF BRAKE FORMING ON THE STRENGTH OF 23S-TITANIUM ALLOY SHEET, NACA Technical Note TN 1072, May 1946.
106. Haley, J., PRELIMINARY DRAFT, COST EFFECTIVENESS OF CRASHWORTHY STRUCTURAL FEATURES IN A 9-13 PLACE HELICOPTER, USAAVS Technical Report 72-1, U. S. Army Agency for Aviation Safety, Ft. Rucker, Alabama, 1972.

107. Walker, A. C., THE POST-BUCKLING BEHAVIOR OF SIMPLY-SUPPORTED SQUARE PLATES, The Aeronautical Quarterly, Vol. XX, 1969, pp. 203-222.
108. Kuhn, P., Petterson, J. P., and Levin, L. R., A SUMMARY OF DIAGONAL TENSION, PART I - METHODS OF ANALYSIS, NACA TN 2661, 1952, Washington, D. C., p. 32.
109. Lowe, W. T., et al, IMPACT BEHAVIOR OF SMALL SCALE MODEL MOTOR COACHES, Proceedings of the Institute of Mechanical Engineers, Vol. 186, No. 36, 1972, pp. 409-419.
110. Saczalski, K. J., and Park, K. C., AN INTERACTIVE HYBRID TECHNIQUE FOR CRASHWORTHY DESIGN OF COMPLEX VEHICLE STRUCTURAL SYSTEMS, To be presented at S.A.E. International Conference of Vehicle Structural Mechanics, Detroit, Michigan, March 26-28, 1974.
111. Hone, C. P., TORSIONAL-FLEXURAL BUCKLING OF AXIALLY-LOADED, THIN-WALLED, ELASTIC STRUTS OF OPEN CROSS-SECTION IN THIN-WALLED STRUCTURES, (Ed. by A. H. Chilver), John Wiley & Sons, Inc., New York, 1967.
112. ENGINEERING DATA, HEXCELL TECHNICAL SERVICE BULLETINS, TB 110 through TB 123, 1960 - 1968, Hexcell Products Inc., Berkeley, California.

LIST OF SYMBOLS

SUBSTRUCTURE ANALYSIS

A	area; for stiffened panel, area of stiffener plus area of sheet corresponding to stiffener spacing, in. ²
a	plate length, in.
A _s	area of stiffener, in. ²
A _w	area of web, in. ²
b _s	width of skin, in.
b _w	width of stiffener web, in.
C	constant (= 3.0)
c	number of cuts
d	rivet diameter, in.
E	modulus of elasticity, psi
e, e _o	distance to neutral axis, in.
f	number of flanges
f _{cr}	crush strength, lb
f _w	effective rivet off-set, in.
G	acceleration level
g	gravity term = 386.2 in./sec ²
H	distance, in.
I	moment of inertia, in. ⁴
I _o	moment of inertia about c.g., in. ⁴
K	eccentricity factor
KE	kinetic energy, in.-lb
K _w	wrinkling coefficient
L, l	one-half column length, in.
L'	effective length = L/\sqrt{C} , in.
M	effective moment, in.-lb

SUBSTRUCTURE ANALYSIS

M_p	plastic hinge moment, in.-lb
N/A	neutral axis
N	effective axial force, lb
N_p	plastic hinge axial force, lb.
P	rivet pitch, in.
P	applied axial force, lb
P_f	monolithic failure load, lb
P_{fw}	wrinkling failure load, lb
q	distributed load, lb/in.
S	stopping distance, core radius of given cross section, in.
s	distance from midcross-section of skin to neutral axis of stiffener, in.
T	ratio of σ/σ_{cy}
T_{cr}	ratio of critical stress (σ_{cr}) to yield stress (σ_{cy})
t_c	minimum core thickness, in.
t_s	skin thickness, in.
\bar{t}_w	stiffener thickness, in.
V	impact velocity, in./sec
W	weight, lb
w_e	effective half width of skin, in.
y	lateral deflection
Z	function of column length and end shortening, in.
α	defined in equation 51
η	plasticity reduction factor
$\bar{\eta}$	cladding reduction factor
π	$P_i = 3.14$
θ	$\tan^{-1} Z$
ρ	radius of gyration = $\sqrt{I/A}$, in.
γ	partial derivative

SUBSTRUCTURE ANALYSIS (Continued)

δu	incremental displacement, in.
δ, Δ, u	displacement, end shortening, in.
ν	Poisson's ratio
x	distance to c.g., in.
σ	compressive stress, psi
σ_b	stress at outermost fiber of sheet skin, psi
σ_{co}	column buckling stress, psi
σ_{cr}	buckling stress, psi
σ_{cy}	compressive yield stress, psi
$\bar{\sigma}_{cy}$	effective compressive yield stress, psi
σ_{cy_w}	effective compressive yield stress for stiffener web, psi
σ_{cy_s}	effective compressive yield stress for skin, psi
σ_e	Euler stress, psi
σ_f	cripling (or failure) stress, psi
σ_{fr}	failure stress of riveted panel, psi
σ_w	failure stress due to wrinkling mode, psi
σ_{20}	buckling stress at $L'/\rho = 20$

Subscripts:

b	bending
f	filler
i	i th segment
max.	maximum
min.	minimum
p	plastic state
s	skin or sheet
w	stiffener web

SUBSTRUCTURE ANALYSIS (Continued)

Constants (function of stiffened panel configuration)

β_f

β_g

g

m

n

PROGRAM "KRASH"

$[A_i]$	rotational transformation matrix from body axes to ground axes
$[A_i]^T$	transpose of A_i matrix
CE	total crash spring (external spring) energy absorbed
DE	total damping energy dissipated
DRI	dynamic response index
E_{TOT}	total system energy
FD_{ijl}	internal beam damping force (or moment) for the ij^{th} beam in the l^{th} direction
FSP_{ijk}	crash spring forces; spring ij in the k^{th} direction
F_{ijl}	force (or moment) at point j due to beam ij , in the l^{th} direction
I_{xi}, I_{yi}, I_{zi}	moments of inertia of lumped mass m_i about i^{th} body fixed axes
$I_{xyi}, I_{yzi}, I_{zxi}$	product of inertia of lumped mass m_i about i^{th} body axes
KE	total kinetic energy
l_{ik}	length of vector from m_i to ground contact point C'_{ik}
m_i	i^{th} lumped mass
N	number of lumped masses
PE	total potential energy
SE	total strain energy absorbed
$TERM_{ij}$	term in expression for crash spring energy

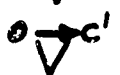
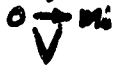
PROGRAM "KRASH" (Continued)

W_i	weight of i^{th} lumped mass
x_i, y_i, z_i	ground coordinates of m_i
u_i, v_i, w_i	i^{th} body axes component of absolute translational velocity vector of mass i
p_i, q_i, r_i	i^{th} body axes components of absolute angular velocity vector of mass i
$\left\{ \begin{matrix} X_{ci}, Y_{ci}, Z_{ci} \\ L_{ci}, M_{ci}, N_{ci} \end{matrix} \right\}$	crash (external) forces and moments, i^{th} body axes
$\Delta x'_i, \Delta y'_i, \Delta z'_i$	$= \left\{ \Delta v_{ci} \right\}$, incremental displacement of point i , i^{th} body axes
$\Delta \text{inp}_i, \Delta \text{inq}_i, \Delta \text{inr}_i$	incremental rotation of point i , i^{th} body axes
Δv_{ijl}	incremental displacement vector of point j with respect to point i , due to deformation of beam ij , in the l^{th} direction

USER'S GUIDE AND REFERENCE 1 TERMS

A_1, B_1, C_1	Terms used in Euler's equations of motion
$[A_1]$	Rotation transformation matrix from body axes to ground axes
$[\bar{A}_1]$	Matrix relating $(\phi_1, \sigma_1, \psi_1)$ to (p_1, q_1, r_1) in equation (92)
$[\dot{A}_1]$	Time derivative of $[A_1]$
$[A_1'']$	Rotation transformation matrix from ith body axes to c.g. axes
$[A_{1,j}]$	Rotation transformation matrix from beam ij axes to body i axes
$[A']$	Rotation transformation matrix from c.g. axes to ground axes
$[\bar{A}']$	Matrix relating (ϕ', σ', ψ') to (p', q', r') in equation (88)
C_{ik}	End point of kth spring on ith mass
C_{ik}^i	Ground contact point of kth spring on ith mass
dvc_{ijk}	Ground axes components of vector from m_1 to C_{ik}
dvc_{ijk}^i	Ground axes components of vector for C_{ik}^i to C_{ik}
$[D_i]$	Derivative matrix
$[D']$	Derivative matrix
$FM_{1,jkl}$	Running time sum of $\Delta FM_{1,jkl}$
$\overline{FM}_{1,jkl}$	Value of $FM_{1,jkl}$ at time of loading reversal
$FSP_{1,jk}$	Body i axes components of spring force at ground contact point C_{ik}
$FSPO_{ik}$	Axial compressive force in kth spring on ith mass
\overline{FSPO}_{ik}	Value of $FSPO_{ik}$ at time of loading reversal

USER'S GUIDE AND REFERENCE 1 TERMS (Continued)

$\dot{v}_{cp_{1jk}}$	Ground axes components of absolute velocity of ground contact point C_{1k}
	Velocity vector of C_{1k} with respect to m_1
	Velocity vector of C_{1k} with respect to ground
	Velocity vector of m_1 with respect to ground
W_i	Weight of i th lumped mass
W_{TOT}	Total vehicle weight
$x_{b_{1j}}, y_{b_{1j}}, z_{b_{1j}}$	Beam ij coordinates
$x_G, y_G, z_G (v_{G_j})$	Ground coordinates of initial ($t = 0$) c.g. position
$\dot{x}_G, \dot{y}_G, \dot{z}_G$	Ground axes components of initial ($t = 0$) c.g. velocity vector
$x_G'', y_G'', z_G'' (v_{GPP_{1j}})$	Helicopter axes coordinates of vehicle c.g. (point G)
$x_1, y_1, z_1 (v_{a_{1j}})$	Ground coordinates of m_1
$x_1^i, y_1^i, z_1^i (v_{iP_{1j}})$	Coordinates of m_1 in center-of-gravity coordinate system
$x_1'', y_1'', z_1'' (v_{iPP_{1j}})$	Coordinates of m_1 in helicopter coordinate system
x_{1j}, y_{1j}, z_{1j}	Ground coordinates of vector from point i to point j
$x_{1j}^i, y_{1j}^i, z_{1j}^i$	i th body coordinates of vector from point i to point j
$\left(\begin{matrix} X_{1j}^i & Y_{1j}^i & Z_{1j}^i \\ L_{1j} & M_{1j} & N_{1j} \end{matrix} \right)$	Total (summed over time) internal forces and moments at point i due to beam ij , i th body axes
$\left(\begin{matrix} X_{j1}^i & Y_{j1}^i & Z_{j1}^i \\ L_{j1} & M_{j1} & N_{j1} \end{matrix} \right)$	Total (summed over time) internal forces and moments at point j due to beam ij , j th body axes

USER'S GUIDE AND REFERENCE 1 TERMS (Continued)

$\begin{pmatrix} X_i, Y_i, Z_i \\ L_i, M_i, N_i \end{pmatrix}$	Total forces and moments on mass i , in i^{th} body axes
X_{Ai}, Y_{Ai}, Z_{Ai}	Aerodynamic forces, i^{th} body axes
$\begin{pmatrix} X_{Ci}, Y_{Ci}, Z_{Ci} \\ L_{Ci}, M_{Ci}, N_{Ci} \end{pmatrix}$	Crash (external) forces and moments, i^{th} body axes
X_{Gi}, Y_{Gi}, Z_{Gi}	Gravity forces, i^{th} body axes
$\begin{pmatrix} X_{Ii}, Y_{Ii}, Z_{Ii} \\ L_{Ii}, M_{Ii}, N_{Ii} \end{pmatrix}$	Internal forces and moments, i^{th} body axes
$XVOC_{ijk}$	Ground axes components of spring force at ground contact point C'_{ik} , positive up, left and aft
z_{MAX}^c	Vertical distance from c.g. to lowest C'_{ik}
Δ_i	Determinate expression used in equation (68)
ΔF_{ijk}	Incremental forces and moments at point j due to beam ij
ΔFM_{ijkl}	k^{th} incremental load due to l^{th} incremental deflection for beam ij
$\Delta \phi_{bij}, \Delta \theta_{bij}, \Delta \psi_{bij}$	Incremental rotations of point j with respect to point i , in beam ij axes
$\Delta \phi_i, \Delta \theta_i, \Delta \psi_i$	Incremental change in i^{th} mass Euler angles
Δt	Numerical integration time interval
Δv_{bij}	Six element vector made up of $\Delta x_{bij}, \Delta y_{bij}, \Delta z_{bij}, \Delta \phi_{bij}, \Delta \theta_{bij}, \Delta \psi_{bij}$
$\overrightarrow{\Delta v}_{bij}$	Incremental displacement vector of point j with respect to point i , due to deformation of beam ij
$\overrightarrow{\Delta v}_{di}$	Incremental displacement vector of point j with respect to point i

USER'S GUIDE AND REFERENCE 1 TERMS (Continued)

$FSPO_{y1k}$	Final value of $FSPO_{1k}$ in input table of s_{1k} vs. $FSPO_{1k}$
G	Center-of-gravity of total vehicle
H	Origin of helicopter coordinate system (F.S.O, B.L.O, W.L.O)
$He_{x1}, He_{y1}, He_{z1}$	Angular momenta of m_i due to rotation of masses internal to m_i
I_{x1}, I_{y1}, I_{z1}	Moments of inertia of lumped mass m_i , about i th body fixed axes
$I_{xy1}, I_{yz1}, I_{zx1}$	Products of inertia of lumped mass m_i , about i th body fixed axes
ke_{1k}	Linear unloading stiffness for k th spring
$[K_{1j}]$	Six by six linear stiffness matrix for beam ij
$[KR_{1j}]$	Six by six diagonal stiffness reduction matrix for beam ij
l_{1k}	Length of vector from m_i to ground contact point C'_{1k}
$\bar{l}_{x1}, \bar{l}_{y1}, \bar{l}_{z1} (\bar{l}_{1k})$	Free length of k th spring on i th mass
l_{c1}	Aerodynamic lift constant
LIFT ₁	Aerodynamic lift on m_i , positive up, in ground axes
m_i	i th lumped mass
mu_{1k}	Ground-spring friction coefficient for k th spring on i th mass
N	Total number of lumped masses
\bar{h}_{1k}	Unit vector triad fixed in i th body coordinate system
$\bar{n}_x, \bar{n}_y, \bar{n}_z$	Unit vector triad fixed in ground coordinate system
O	Origin of ground coordinate system

USER'S GUIDE AND REFERENCE 1 TERMS (Continued)

P_i, Q_i, R_i	ith body axes components of absolute angular velocity vector of mass i
p', q', r'	c.g. axes components of initial(t=0) vehicle angular velocity vector
$[pL_i]$	Contact point velocity matrix used in equation (60)
s_{ik}	Axial external spring compression, kth spring on ith mass
\bar{s}_{ik}	Value of s_{ik} at time of loading reversal
s_{Fik}	Final value of s_{ik} in input table of s_{ik} vs. $FSPO_{ik}$
s_{ik}	kth spring axial compression measured relative to current load stroke curve origin
s_{ik}''	Horizontal shift of s_{ik} coordinates with respect to S_{ik} coordinates
t	Time
$[T_{ij}]$	Static balance matrix used in equation (30b)
u_i, v_i, w_i	Body i axes components of absolute translational velocity vector of point a_i
vb_{ij}	x_i, y_i, z_i
vb_{ij}	Running time sum of Δvb_{ij}
\bar{vb}_{ijl}	Value of vb_{ijl} at time of loading reversal
\bar{v}_{ik}	Magnitude of ground plane contact point velocity
vb_{ijl}^i	lth total beam deflection measured relative to current load-stroke curve origin
vb_{ijl}''	Horizontal shift of vb_{ijl}^i coordinates with respect to vb_{ijl} coordinates
vc_{ijk}	Ground coordinates of point C_{ik}

USER'S GUIDE AND REFERENCE 1 TERMS (Continued)

$\overrightarrow{\Delta v}_{1j}$	Incremental displacement vector of point j with respect to point i, due to rotation of mass i
$\Delta x_{b_{1j}}, \Delta y_{b_{1j}}, \Delta z_{b_{1j}}$	Coordinates of $\overrightarrow{\Delta v}_{1j}$ in beam ij axes
$\Delta x_1, \Delta y_1, \Delta z_1$	Incremental displacement of point i, ground axes
$\Delta x_{1j}, \Delta y_{1j}, \Delta z_{1j}$	Incremental displacement of point j with respect to point i in ground axes
$\begin{pmatrix} \Delta X_{1j}, \Delta Y_{1j}, \Delta Z_{1j} \\ \Delta L_{1j}, \Delta M_{1j}, \Delta N_{1j} \end{pmatrix}$	Incremental internal forces and moments at point j due to beam ij, in beam ij axes (elements of ΔF_{1j} vector)
$\begin{pmatrix} \Delta X_{1j}^0, \Delta Y_{1j}^0, \Delta Z_{1j}^0 \\ \Delta L_{1j}^0, \Delta M_{1j}^0, \Delta N_{1j}^0 \end{pmatrix}$	Incremental internal forces and moments at point j due to beam ij, ground axes
$\begin{pmatrix} \overline{\Delta X}_{1j}, \overline{\Delta Y}_{1j}, \overline{\Delta Z}_{1j} \\ \overline{\Delta L}_{1j}, \overline{\Delta M}_{1j}, \overline{\Delta N}_{1j} \end{pmatrix}$	Incremental internal forces and moments at point i due to beam ij, ground axes
$\begin{pmatrix} \Delta X_{1j}^i, \Delta Y_{1j}^i, \Delta Z_{1j}^i \\ \Delta L_{1j}^i, \Delta M_{1j}^i, \Delta N_{1j}^i \end{pmatrix}$	Incremental internal forces and moments at point i due to beam ij, i th body axes
$\begin{pmatrix} \Delta X_{j1}^i, \Delta Y_{j1}^i, \Delta Z_{j1}^i \\ \Delta L_{j1}^i, \Delta M_{j1}^i, \Delta N_{j1}^i \end{pmatrix}$	Incremental internal forces and moments at point j due to beam ij, j th body axes
ϕ_1, θ_1, ψ_1	Euler angles from ground axes to body axes (time varying)
$\phi_{1j}, \theta_{1j}, \psi_{1j}$	Euler angles from ith body axes to beam ij axes (constant)
ϕ^i, θ^i, ψ^i	Euler angles from ground axes to c.g. axes (constant); initial (t=0) attitude of vehicle
$\phi_i'', \theta_i'', \psi_i''$	Euler angles from c.g. axes to ith body axes (constant)